Time-Resolved Imaging of Magnetisation Dynamics in Nanoscale Magnonic Structures

Submitted by **Toby Charles Davison**, to the University of Exeter
as a thesis for the degree of Doctor of Philosophy in Physics,
May 2012.

I certify that all material in this thesis which is not my own work has been identified and that no material has previously been submitted and approved for the award of a degree by this or any other University.

.....

Abstract

In this thesis the results of several different experimental techniques are presented. Time-resolved scanning Kerr microscopy and time-resolved optically pumped scanning optical microscopy measurements were made in Exeter on bi-component anti-dot lattices and permalloy films respectively. Magnetic transmission x-ray microscopy measurements were performed on cobalt nanostructures at the Advanced Light Source at the Lawrence Berkeley National Laboratory in Berkeley, California, USA.

Time-resolved Kerr microscopy was used to study bi-component 400nm anti-dot lattices with a 1μm lattice constant. At 200 Oe the mode frequencies were obtained using time-resolved measurements. The mode frequencies of the cobalt filled anti-dots (binary sample) are 3 and 4.4 GHz. The 4.4 GHz mode has propagating character; the 3 GHz mode has non-propagating character. The mode frequencies of the air –filled anti-dot arrays (anti-dot reference sample) are 3.84 and 4.72 GHz. The 3.84 GHz mode has propagating character; the 4.72 GHz mode has non-propagating character. The alteration of the internal field by the air-filled anti-dots lowers the propagating mode frequency compared to the binary sample. Scanning Kerr microscopy was used to study the spatial character of the anti-dot modes. By fitting the spatial character the effective damping parameter(s) were determined. The effective damping parameter for the binary sample was 0.023 and 0.044 for the 4.4 and 3.04 GHz modes respectively. The 3.04GHz mode exists through the cobalt filled anti-dots leading to a high effective damping. The effective damping parameters for the anti-dot reference sample 0.026 and 0.028 for the 3.84 and 4.72 GHz modes respectively.

Time-resolved optically pumped measurements have been performed on a continuous 20nm permalloy film. This is a new experimental technique developed during my PhD. Early

data acquired on the optical microscope is compared with data measured later and attempts are made to explain the discrepancies. With a 500 Oe out-of-plane field initial time resolved signals show an oscillation at 17 GHz, the origin of the oscillation is unknown and is thought to originate from a magnon or phonon contribution. The experiment overlapping sub-micron pump and probe spots makes acquiring consistent time-resolved signals a difficult challenge. Images revealing circular lobe shapes are observed, the origin of these images is not fully understood. Later measurements are compared to the early measurements. In the recent measurements, images of spin waves with a wavelength and frequency of 2.5 μm and 4 GHz respectively are observed. These values are not reconcilable with the wavelengths and frequencies of 1μm and 17GHz seen in the images and time-resolved signals respectively. Recent measurements also revealed a strong dependence on the pump focus position on the measured images.

Lastly, magnetic transmission x-ray microscopy measurements are presented on 700nm cobalt anti-dot structures overlaid on continuous permalloy films of thicknesses ranging from 20 to 60nm. The magnetic ground states of the nanostructures are investigated using L_3 edge x-ray absorption and x-ray magnetic circular dichroism as a magnetic contrast mechanism. The reversal fields are determined and consistent with hysteresis loops measurements in Exeter. The dipolar fields from the complex shape of the cobalt anti-dots are expected to modulate the magnetic ground state of the permalloy. Reversal of the permalloy occurs suddenly over a consistent field window, starting and finishing between 13 ~ 17 Oe respectively. The reversal process in the cobalt occurs gradually and full saturation is not observed until fields of up to 350Oe.

Acknowledgements

The work presented in this Thesis is the cumulative sum of efforts from many of my colleagues, co-workers and friends. It would be unfair to say it was my own single effort and I am thankful for their much needed contribution to this Thesis and all the work that has been associated with my studies in the past few years. The list of people to thank is too long to be explicitly mentioned, minor discussions, comments and interactions on all levels with all people has in some way influenced me in one way or another to complete the work presented here. I would like to thank peers Mr Max Marcham and Mr Tom Duckworth from the Magnetic materials group. They have been there since I, having started at the same time and are my closest associates and friends within the group, who always brightened a situation with unforgettable humour. They were always available as a sounding board for my frustrations and worries, and were always available for playing football and 'walks around the pitches'. On an experimental basis, I would like to thank Dr. Yat-Yin Au who designed much of the experimental apparatus I used and his much needed guidance on matters experimental and practical. The School of Physics workshop has been an invaluable asset for experimental work, being able to advise, mill and drill apparatus into working order, namely I would like to thank Matt Wears and Russell Edge for their help and guidance on all matters practical and mechanical. Their common sense approach to practical work was a refreshing insight that remained useful and carried over to my experimental work in the lab. I would also like to thank and acknowledge the School of Physics and the rest of the magnetic materials group for their encouragement and help over the years. Last but not least, I would like to thank my supervisor Dr. Volodymyr Kruglyak, who always had valuable insight to my experiments and whose persistence and supervision has led me to this point here.

List of Contents

List of Publications

1. Y. Au, T. Davison, E. Ahmad, P. S. Keatley, R. J. Hicken, and V. V. Kruglyak, *Excitation of propagating spin waves with global uniform microwave fields***,** Applied Physics Letters **98**, 122506 (2011)
2. Y. Au, E. Ahmad, O. Dmytriiev, M. Dvornik, T. Davison, and V. V. Kruglyak, *Resonant microwave-to-spin-wave transducer,* Applied Physics Letters, **100**, 182404 (2012)

List of Figures

List of Tables

Declaration

The work presented in this thesis is the joint effort of many people. The contribution to the work is outlined below and is also done so throughout the main text of this thesis.

Chapter 1 – Introduction

The introduction to the work in this thesis, the brief history of magnetism and the outline of research is my own. Details published by authors from the literature used in this chapter has been acknowledged.

Chapter 2 – Background Theory

The material in the background theory chapter has been compiled by myself. The concepts and principles presented in chapter 2 are not the result of my work. The reference material used in chapter 2 has been acknowledged.

Chapter 3 - Experimental Setup and Development

The experimental design of the field-pumped time-resolved Kerr microscope is due to Prof. Rob Hicken, Dr. Paul Keatley, and Dr. Volodymyr Kruglyak. The refinement of the drawings and assembly of the time-resolved Kerr microscope was performed by Dr. Yat-Yin Au. The experimental design of the time-resolved optically pumped scanning optical microscope is due to Dr. Volodymyr Kruglyak, with the construction drawing produced by Dr. Yat-Yin Au. Assembly of the time-resolved optically pumped scanning optical microscope was performed by myself and Dr. Yat-Yin Au.

Machining of part for both microscopes was performed by Mr. Russell Edge in the machine workshop in Exeter. The alignment and maintenance of the shared optics and opto-

mechanics beyond the microscopy probe stations was performed by myself with assistance of Dr. Thomas Isaac, Dr. Yat-Yin Au, Mr. Rostislav Mikhaylovskiy, and Dr. Mykola Dvornik. The software for data acquisition for both experiments was written by Dr. Yat-Yin Au and Dr. Mykola Dvornik.

Chapter 4 - Time-Resolved Scanning Kerr Microscopy measurements of Cobalt and Air filled Anti-dot structures

The electrically connected two-dimensional Co- and air-filled anti-dot lattices for the time-resolved scanning Kerr microscopy measurements in Exeter were designed and fabricated by Mr. Georg Dürr from the Technical University of Munich and Marco Madami from the University of Perugia, who (with their colleagues) have also performed their preliminary characterization using Vector Network Analyser Ferromagnetic Resonance and Brillouin Light Scattering measurements and micromagnetic simulations. I was taught how to use and operate the Kerr microscope by Dr. Yat-Yin Au. Data presented in this thesis from experiments on the binary and air-filled anti-dot lattices using the time-resolved scanning Kerr microscope were acquired by myself.

Chapter 5: Time-resolved Optically pumped Scanning Optical Microscope measurements of a Permalloy film

The 20nm thick continuous permalloy film was fabricated by Dr. Ehsan Ahmad in Exeter. Data presented in this thesis from experiments on the permalloy film using the time-resolved optically pumped scanning optical microscope were acquired by myself.

Chapter 6: Magnetic Transmission X-ray Microscopy (M-TXM) of Cobalt Nano-structures

The cobalt/permalloy nanostructures measured at the Advanced Light Source in California were fabricated in Exeter by Dr. Ehsan Ahmad. The measurements were possible thanks to beam line scientist Dr. Peter Fischer and beam line postdoc Dr. Mi-Young Im. I am grateful to Dr. Mi-Young Im for showing us how to operate parts of the microscope. Data on the beam line were collected by myself and Dr. Mykola Dvornik from Exeter and Mr. Michal Mruczkiewicz from the Adam Mickiewicz University in Poznan, Poland. The software for image analysis was written by Dr. Mykola Dvornik. The data analyses were performed by myself.

Chapter 1: Introduction

What is Magnetism? This question has fascinated people ever since Thales of Miletus (*circa* 634-546 BC) first described the phenomenon as the attraction of Iron by 'lodestone', the naturally occurring mineral magnetite, Fe_3O_4 [1]. Over the last 2,500 years the phenomenon of magnetism has been used extensively in practical applications such as navigation and more recently sensors, motors and credit cards. In parallel with this, it has also been explored theoretically and light has slowly been shed on its quantum mechanical origin. This historical rendition is based on books by Segre [1,3], Verschur [4] and Livingstone [5].

The most primitive magnetic phenomena, being physical attraction between magnetic materials has been observed since time-immemorial. Magnetism is so often synonymous with 'attraction' it has even entered the popular English lexicon. Yet, even today it is still a non-trivial question why two magnets attract one another. The concept of spin magically emerging from Dirac's relativistic quantum mechanics of the electron in the 1920's is an example of this [2]. It is simply taken for granted and accepted that 'spin' exists, we base our entire understanding of magnetism on the concept of spin and how this 'intrinsic' electron angular momentum gives rise to the spin magnetic moment. The electron's spin magnetic moment is also complemented by the electrons 'orbital' magnetic moment that exists due to the electrons orbital angular momentum and its motion around the nucleus.

Not until the scientific revolution which started in Europe in the 16^{th} and 17^{th} centuries was magnetism studied in greater quantitative detail. The first scholarly treatment of magnetism was by Frenchman Peter Peregrinus [3] in 1269, who compiled a list of facts of magnetism and

how to make instruments from lodestone. Three centuries later, William Gilbert (1544-1603), a medical doctor, wrote his treatise *De Magnete* in 1600. He postulated that the earth itself is a giant magnet, with a field similar to that of a bar magnet and that the geographic poles do not coincide physically with the earth's magnetic poles. This explained earlier observations from navigators such as Columbus, who noted discrepancies between the compass needle and the stars. It was later Carl Friedrich Gauss (1777-1855), who made more detailed measurements of the earth's magnetic field in 1835 [4].

Hans Christian Oersted (1777-1851) noticed in 1819 the force an electric current exerted on a magnetic needle generated from a near-by wire. A year later, Jean-Baptiste Biot (1774-1862) and Felix Savart (1791-1841) derived the form of the magnetic field around a current carrying wire and then between 1820 and 1825 Andre Marie Ampere (1775-1836) studied forces between current carrying wires. This lead to the famous eponymous laws we now know after them.

Several years later, Classical Electromagnetism peaked with the work of two of the greatest physicists of the 19th Century, the English experimentalist Michael Faraday (1791-1867) and the Scottish theorist James Clerk Maxwell (1831-1879) [5]. In 1831 Faraday discovered electromagnetic induction and in 1845, he discovered the (Magneto-Optical) Faraday Effect, evidence for a direct connection between magnetism and light. The analogous effect to the Faraday Effect is the (Magneto-Optical) Kerr Effect in reflection, discovered by Scottish physicist John Kerr (1824-1907) in 1876. Faraday's efforts culminated in his book *Experimental Researches in Electricity* and he invented electric motors, generators and transformers, all of which became cornerstones of industrialised nations.

Maxwell cemented Faraday's ideas of electricity and magnetism into a firm mathematical footing with the eponymous Maxwell equations in 1864, developed in his book *Treatise on Electricity and Magnetism*. This was the inception of the electromagnetic field as Maxwell concluded that light is an electromagnetic wave [2].

It was at the beginning of the 20th century that an atomistic picture of magnetism started to develop [4]. In 1913, the Dane Niels Bohr (1885-1962) postulated that the electron angular momentum is quantised and that orbital magnetic moments arise from orbiting electron currents. The famous experiment in 1921 by Otto Stern (1888-1969) and Walther Gerlach (1889-1979) showed the splitting of a beam of Ag atoms in an inhomogeneous magnetic field due to the quantisation of the orientation of the electrons spin. Wolfgang Pauli (1900-1958) in 1925 asserted that no two electrons are able to exist in the same quantum state simultaneously, a statement later to be coined by Dirac the 'Pauli Exclusion principle'.

The three year period from 1925 to 1928 saw an enormous leap forward in physics. It saw the genesis of Quantum mechanics by Werner Heisenberg (1901-1976) and Erwin Schrodinger (1887-1961) and the introduction of the electron's spin. The electron 'spin' had been mentioned before, but it was Paul Dirac's (1902-1984) celebrated relativistic quantum mechanical theory of an electron in an external electromagnetic field in 1928 that saw 'spin' emerge without being explicitly assumed [6]. That same year saw Heisenberg's formulation of a spin-dependent model for the exchange interaction [7]. The archaic molecular field proposed by Weiss was now replaced by the exchange interaction. This introduction of the strong and short ranged exchange interaction was the birth of modern magnetism and has its origins in both Quantum theory and Relativity.

In a series of papers starting in 1932, Louis Neel (1904-2000) developed the concept of antiferromagnetism [8]. Neel's ideas of antiferromagnetic and ferrimagnetic spin alignments were later verified by neutron diffraction experiments. In the mid 1930's band theory was first applied to magnetic systems by Neville F. Mott (1905-1996) [9], John C. Slater (1900-1976) [10, 11] and Edmund C. Stoner (1899-1968) [12]. Today further developments of this theory form the foundation of modern magnetism.

Studies of magnetism today is largely driven by the fast moving pace of information technology, especially data storage and memory applications, fundamental research still continues on 'novel' magnetic structures such as magnonic crystals [13], where a periodic modulation of material magnetic properties is deliberately contrived to yield properties not found in conventional homogeneous magnetic structures. This so-called magnonic crystal is a magnetic metamaterial, which gains its properties from sub-wavelength structuring, rather than from the material band structure directly. This newly emerging field of 'magnonics' [14] looks to use spin waves for applications such as magnonic logic, spin wave computing and spin wave filters.

In this Thesis the results of different experimental techniques have been presented. Both static and Time-Resolved data are shown. Here 3 different experimental chapters span a variety of experimental techniques and a variety of samples in which the experiments were used to characterise them. Field and optical pumping were both performed in Exeter, while (static) Magnetic Transmission X-ray Microscopy (M-TXM) was performed at the Advanced Light Source (ALS) in Berkeley, California, USA.

In Chapter 2 the essential background of magnetism is discussed, the chapter describes the spin and orbital moments, the energetics of magnetism including the competing energy terms

and the Landau-Lifshitz-Gilbert equation, the exchange interaction and the spin-orbit coupling. The focus of this chapter is ferromagnetism. The Magneto-Optical Kerr effect (MOKE), spin wave dispersion and spin waves in periodic magnetic structures are also described, followed by a description of synchrotron radiation.

In Chapter 3 the experimental setup of both the Time-Resolved Scanning Kerr Microscope (TRSKM) and the Time-Resolved Optically-Pumped Scanning Optical Microscope (TROPSOM) is described. Both the Kerr microscope and TROPSOM use the same lock-in detection scheme, the method of detecting the Kerr signal using a polarising beamsplitter and twin photodiodes is also discussed. The Tsunami laser system and Millennia Pro pump laser are also described and provide the essential ingredient of laser light to both experiments. Brief aspects of laser theory, including spontaneous and stimulated emission, and population inversion are described. The Millennia resonant optical cavity, second harmonic generation and brief aspects of the Tsunami folded cavity are also discussed. In this chapter the development of the time-resolved optically pumped scanning optical microscope is also described.

In Chapter 4 Time-Resolved Scanning Kerr Microscopy was used to study square lattice arrays of cobalt disks embedded in a permalloy film (Cobalt filled anti-dots) and an identical reference sample without the cobalt disks, having air gaps instead (air filled anti-dots). Here spin wave modes were studied propagating in the magnonic crystal after being excited by a coplanar waveguide; comparison of propagating spin waves modes in both the cobalt-permalloy sample and the permalloy reference is made. Also, the propagation length of the spin wave modes is inferred from the field-pumped measurements. This chapter also describes the experimental methodology used in the measurements.

In Chapter 5 optically-pumped measurements are made on a continuous 20nm permalloy film using the time-resolved optically pumped scanning optical microscope. The optically pumped microscope is a new pioneering technique that was developed during my PhD, essentially being an optical analogue of the field pumped Kerr microscope described in Chapter 3. The optically pumped microscope is still in its infancy, being in an early stage of development, a long road of refinement lies in its future for it to be able to achieve its maximum potential.

In Chapter 6, X-ray microscopy (M-TXM) measurements at the Advanced Light Source are presented on cobalt nanostructures atop a permalloy continuous film. Here, the element specificity and high spatial resolution inherent to pulsed x-ray sources is used to study the magnetic ground state of the nanostructures to sub-100nm resolution. The effect of the dipolar fields from the cobalt nanostructures on the permalloy film is studied and the results are presented.

In Chapter 7, a summary of the Thesis is given, providing an overview of the measurements made and conclusions drawn.

Chapter 2: Background Theory

2.1 Introduction

In this Chapter, the fundamental ideas of magnetism and the background theory of the Thesis is presented. The Chapter starts with a discussion of different types of magnetism, magnetic moments and precessional motion. The Landau-Lifshitz-Gilbert (LLG) equation of motion, the effective magnetic field and magneto-optical effects, such as the Kerr effect is described. This is followed by discussion of the dispersion of spin waves and spin waves in periodic magnetic structures. This is by no means an exhaustive summary and further reading can be sought in the reference material.

Despite the modern interest and research currently taking place in the field of magnetism, magnetic phenomena have been known to man for several thousand years. However, until recent times, the only use magnetism was the compass needle for navigation. Today, many areas of our lives are dependent on a wide range of magnetic devices and technologies. From medical applications, such as magnetic resonance imaging (MRI) to the generation of electricity in the National grid, magnetism plays a key role. Other everyday applications of magnetism include VHS tapes, floppy disks, audio cassettes, hard disk drives, credit, debit and ATM cards, older style cathode-ray television and computer monitors, speakers, microphones, electrical motors, generators, transformers and in transportation, the so-called Maglev trains.

Modern research in magnetism focuses on structures typically in the nanoscale regime. Over the last several decades the size of ‘small’ magnetic structures has come down from the micro to the nanometre scale. Continuous and patterned thin films and arrays produced by a

variety of nano-fabrication techniques are the subject of much research today in magnetism. The application of this research will be to improve existing technologies, such as data storage, and perhaps bring about new spin wave based technologies.

2.2 Magnetism of matter

There are many different magnetic states that exist in matter; here only several of them will be described.

The most common magnetic material is Iron. Similar magnetic properties are also shared by nickel and cobalt. This 'well known' magnetism is ferromagnetism. However, all ordinary substances show magnetic effects, although very weak, being orders of magnitude smaller than ferromagnetism. This small magnetism is of two kinds, diamagnetism and paramagnetism.

Below, the origin of magnetism is discussed following Ref 15-16. In many substances, the atoms have no permanent magnetic moment $\boldsymbol{\mu}$, or rather, all the magnetic moments in the material cancel, so the net magnetic moment is zero. In this sense, we would say its 'non-magnetic'.

$$\boldsymbol{\mu}_{\text{net}} = \sum_i \mu_i = 0 \qquad (2.2.1)$$

In a material the total net moment is the sum of all the magnetic moments. From a classical point of view, when a magnetic field is applied, small extra currents are generated at the atoms. From Lenz's law, the induced magnetic moments are induced opposite to the applied

field. The resulting susceptibility is negative, so the induced magnetisation lies anti-parallel to the applied external field. This is the principle of diamagnetism. The material becomes magnetized in an opposite polarity and is thus repelled.

$$\mathbf{M} = \chi\mathbf{H} \tag{2.2.2}$$

For small fields equation 2.2.2 represents the linear relation between the magnetisation **M** and applied magnetic field **H**. If magnetisation and magnetic field are not co-linear, χ is a second-rank tensor, which relates the respective components of the applied field and the magnetisation. It is the determinant of the tensor that dictates its sign. There are substances for which the atoms have a permanent net magnetic moment. So besides the small diamagnetic effect, the moments can be aligned with an external field. Paramagnetism is weak because the magnetic ordering of the moments is small compared to thermal motions at room temperature. The paramagnetic susceptibility is positive; the magnetization lies parallel with the applied field **H**.

$$\mathbf{M} = N < \boldsymbol{\mu} >_{average}$$

$$= \frac{1}{V}\sum_i \mathbf{m}_i \tag{2.2.3}$$

From equation (2.2.3) the magnetisation, **M**, is the magnetic moment per unit volume, *V*. *N* is the average number of magnetic moments per unit volume. The magnetic moment, like the

magnetisation is a vector quantity. Given all materials exhibit diamagnetic behaviour, the total susceptibility of a paramagnet is a sum from both contributions given by 2.2.4,

$$\chi = \chi_{dia} + \chi_{para} \tag{2.2.4}$$

Contrasting with the weak behaviour of dia and paramagnetism, a strong coupling between magnetic moments results in a new type of magnetism. This strong coupling between moments leads to an ordered magnetic state. This ordering allows a stable spontaneous magnetization to exist at room temperature. This strong coupling is due to the exchange interaction, which is a short range isotropic phenomenon. It aligns the local moments to one another and is a consequence of the quantum mechanical origin of magnetism. The new classes of ordered magnetic states are Ferromagnetism, Anti-ferromagnetism and Ferrimagnetism. If the magnetic moments are aligned parallel to one another, the substance is a ferromagnet and a net magnetisation is present in zero field. In anti-ferromagnetic materials, neighbouring magnetic moments align anti-parallel and the net magnetization is zero. In ferrimagnetism the magnetic moments on different sub-lattices have different magnitude, but opposite alignment. Strictly, ferrimagnetism is a special case of anti-ferromagnetism, where the moments are unequal.

However, these magnetic properties are temperature dependent. Above a certain temperature there is a magnetic phase transition, the strong coupling between the magnetic moments is removed and the material becomes paramagnetic. As the material gets heated, the ordered magnetic state is perturbed by random thermal motion and zero spontaneous magnetisation results. This is the Curie and Neel temperature for a ferromagnet and anti-

ferromagnet respectively. It is impossible to understand the magnetism of materials using classical physics. Such effects are purely Quantum Mechanical.

2.3 Magnetic Moments and Angular Momentum

Below a discussion of magnetic moments and angular momentum following Ref 17-18.

Consider an electron in motion around an atom, say the hydrogen electron. Let the orbital angular momentum of any given electron be $\hat{\mathbf{L}}$, let its magnetic moment be $\hat{\boldsymbol{\mu}}$. The orbital magnetic moment and orbital angular momentum are related by,

$$\hat{\boldsymbol{\mu}}_{orbital} = -\frac{e}{2m_e}\hat{\mathbf{L}}, \tag{2.3.1}$$

where e is the electronic charge and m_e is the electron mass. The magnitude of the angular momentum observable is $\hbar\sqrt{l(l+1)}$, where l is the angular momentum quantum number and $\hbar$ is the rationalized Planck constant. Equation 2.3.1 describes the magnetic moment of the electron and can be written as,

$$|\boldsymbol{\mu}|_{orbital} = \frac{e}{2m_e}\hbar\sqrt{l(l+1)} \tag{2.3.2}$$

The magnetic moment of the electron and its angular momentum lie anti-parallel to one another, due to the negative electron charge. Equation 2.3.2 is true for orbital motion. The electron also possesses a spin angular momentum, which is not associated with any type of external motion

but is an intrinsic property of the electron. The 'intrinsic spin angular momentum' has no intuitional understanding. Due to the electron spin, the electron has both an orbital and a spin magnetic moment. The spin magnetic moment of the electron is given by,

$$\hat{\boldsymbol{\mu}}_{Spin} = -g\frac{e}{2m_e}\hat{\mathbf{S}}, \tag{2.3.3}$$

where g is the Lande factor and $\hat{\mathbf{S}}$ is the spin operator. The magnitude of the spin observable is $\hbar\sqrt{s(s+1)}$, where s is the spin quantum number. The spin magnetic moment can be written as,

$$|\boldsymbol{\mu}|_{Spin} = -g\frac{e}{2m_e}\hbar\sqrt{s(s+1)} \tag{2.3.4}$$

Both the spin magnetic moment and the orbital magnetic moment are given in terms of a set of quantum numbers. Quantum numbers describe the quantum state of a system and they quantize the spin and angular momentum states.

The spin magnetic moment is larger than the orbital magnetic moment. The orbital angular momentum can be 'quenched' and averages to zero, resulting in the spin moment contributing to the atomic magnetic moment and hence magnetisation. Atoms with unfilled outer shells possessing net moments are due to unpaired electron spins. Atoms with unfilled outer shells can bond to other atoms with unfilled outer shells, combining the two net spins anti-parallel to yield zero net moment.

Only a few elements show ferromagnetic behaviour at room temperature. These are the 3d transition metals (Fe^{26}, Co^{27} , Ni^{28}). In these elements the 3d transition band is not filled and

the atom has a net spin moment. The exchange integral then determines the parallel or anti-parallel alignment of the moments. This is the cause of the spontaneous magnetisation.

For the rest of the chemical elements it is the Pauli Exclusion Principle and Hund's Rules that prevent any net moment from occurring. For elements with filled shells, degenerate electrons have to exist in different quantum states, doing so by having different spin quantum numbers. Two 'neighbouring' electrons will have opposite spins and spin magnetic moments. No net moment results.

2.4 Precession of Atomic Moments

Below this discussion of precession follows Ref 15.

The consequence of having a magnetic moment proportional to the angular momenta is that an atomic magnet placed in an external field will precess. From the previous section we saw that there are two contributions to the magnetic moment of an electron, the orbital and spin angular momentum.

For a freely suspended magnetic moment, $\boldsymbol{\mu}$, experiencing an external field, $\mathbf{B}$, the precession is caused by torque $\boldsymbol{\tau}$,

$$\boldsymbol{\tau} = \boldsymbol{\mu} \times \mathbf{B} \tag{2.4.1}$$

This torque causes $\boldsymbol{\mu}$ to precess about the applied field direction. Using equation (2.3.1) to relate the magnetic moment to the angular momentum, we can write,

$$\frac{d\mathbf{L}}{dt} = -\frac{e}{2m_e}\mathbf{L}\times\mathbf{B} \tag{2.4.2}$$

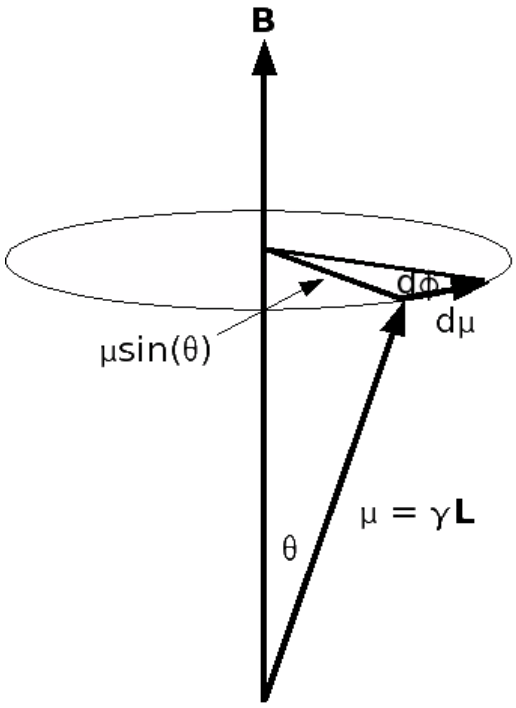

Figure 2.4.1. Precession of the angular momentum about the field axis along a constant energy trajectory. [19]

2.5 Landau-Lifshitz-Gilbert Equation

Below this discussion of the Landau-Lifshitz equation follows Ref 20.

A phenomenological approach to discussing the precessional motion of the magnetisation in an external magnetic field is the Landau-Lifshitz equation. In the absence of damping, the precessional motion describes a cone that traces a constant energy trajectory. In the absence of damping the equation describing the magnetisation is,

$$\frac{\partial \mathbf{M}}{\partial t} = -\gamma \mathbf{M} \times \mathbf{H}_{eff}, \tag{2.5.1}$$

where γ is the gyromagnetic ratio and $\mathbf{H}_{eff}$ is the effective magnetic field. When parallel, the torque is zero. The torque generated by the field is minimized and the energy is lowered by aligning the moments with the effective field. Equation 2.5.1 is known as the Landau-Lifshitz equation. The Landau-Lifshitz equation can be written in a more general form that includes a damping term which can be suitably chosen

$$\frac{\partial \mathbf{M}}{\partial t} = -\gamma \mathbf{M} \times \mathbf{H}_{eff} + \mathbf{R}(\mathbf{M}, \mathbf{H}_{eff}), \tag{2.5.2}$$

where $\mathbf{R}(\mathbf{M},\mathbf{H}_{eff})$ is a damping term that is a function of the effective field and the magnetisation. Either the Landau-Lifshitz damping term $\mathbf{R}_{\mathrm{LL}}$ or the Gilbert damping term $\mathbf{R}_{\mathrm{G}}$ can be used and are equivalent for small damping.

$$\mathbf{R}_{LL} = -\frac{\lambda}{M^2}\left(\mathbf{M} \times \left(\mathbf{M} \times \mathbf{H}_{eff}\right)\right) \tag{2.5.3}$$

$$\mathbf{R}_{G} = \frac{\alpha}{M}\left(\mathbf{M} \times \frac{\partial \mathbf{M}}{\partial t}\right), \tag{2.5.4}$$

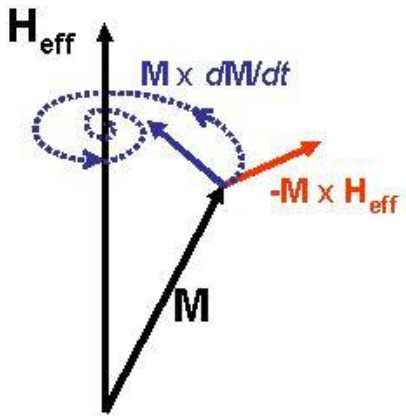

Figure 2.5.1 - The trajectory of the magnetization in the presence of damping. As energy is lost from the precessional motion the magnetization trajectory spirals in toward the effective field, finally coming to rest parallel to the effective field. In this configuration there in no net torque on the magnetization and it is in an energetically favorable magnetic groundstate.

where λ and α are the Landau and Gilbert damping constants respectively. The Landau-Lifshitz equation containing the Landau damping term is usually just called the Landau-Lifshitz equation (LL), while the Gilbert damping term usually names the equation as the Landau-Lifshitz-Gilbert (LLG) equation. Figure 2.5.1 shows the relative orientation of the terms in equation 2.5.5.The Landau-Lifshitz-Gilbert equation, using equation 2.5.2 and 2.5.4,

$$\frac{\partial \mathbf{M}}{\partial t} = -\gamma \mathbf{M} \times \mathbf{H}_{eff} - \frac{\alpha}{M}\left(\mathbf{M} \times \frac{\partial \mathbf{M}}{\partial t}\right), \tag{2.5.5}$$

with $\gamma = g\frac{\mu_B}{\hbar}$ and μ_B is the Bohr magneton. The first term $\mathbf{M} \times \mathbf{H}_{eff}$ describes the precession of the magnetization under the influence of the effective field, the second (damping) term $\mathbf{M} \times \frac{\partial \mathbf{M}}{\partial t}$

describes how the magnetization vector 'spirals' in toward the axis of the field direction as time progresses. Eventually the dynamical magnetization 'relaxes' into a position parallel to the effective field. The phenomenological constant α, the so-called damping parameter stands for unspecified dissipative phenomena in the dynamics. The LLG equation can also be used to describe the propagation of spin waves (or magnons from a quasi-particle point of view). The cross products show that propagation of spin waves is governed by the torques generated by the effective magnetic field on the magnetisation. The LLG equation is the cornerstone of describing magnetization dynamics.

2.6 Energetics of Magnetism

Below the discussion of Energetics of Magnetism follows Ref 15 and Ref 21.

The magnetic state of a material is determined by different energy terms that 'compete' to minimize their energy at the cost of the others. The magnetic free energy is the sum of relevant magnetic energy terms of the system. The stable magnetic states are local energy minima within this parameter space. In the last section we saw from the LLG equation, how the magnetisation precession is governed by the effective magnetic field $\mathbf{H}_{eff}$ and how the Landau-Lifshitz equation is a torque equation. The effective magnetic field is defined as the functional derivative of the magnetic free energy density *w* with respect to the magnetisation [21].

$$\mathbf{H}_{eff} = -\frac{\delta w}{\delta \mathbf{M}} \tag{2.6.1}$$

The total magnetic energy density is the sum of all the contributing factors in the system.

The Exchange interaction, Zeeman interaction, Magnetostatic and Anisotropy terms are generally the most considered, but others also may be included. The sample shape, crystalline structure, applied magnetic field and the exchange interaction lend themselves to the final effective magnetic field and sample magnetisation.

$$w = w_{exchange} + w_{Zeeman} + w_{magnetostatic} + w_{anisotropy} \tag{2.6.2}$$

Below the energy terms in equation 2.6.2 are discussed.

The exchange interaction is short ranged, isotropic and responsible for the magnetic order in ferromagnets, ferrimagnets and anti-ferromagnets. The exchange interaction results from the Pauli-exclusion principle and is of electrostatic origin, being a consequence of the quantum mechanical origin of magnetism. Exchange energy is very 'expensive' on the system and has a very strong influence on the local magnetic moments, **m**. The exchange length determines the range to which the exchange interaction is 'felt' in the material, having a range of 5-10nm.

$$w_{exchange} = A(\nabla \mathbf{m})^2 , \tag{2.6.3}$$

where A is the exchange constant and M_S is the saturation magnetisation. [21].

The Zeeman energy is the potential energy of the magnetisation with respect to the applied magnetic field. It is the larger scale analogue of the potential energy an individual magnet moment experiences in an applied magnetic field. An applied magnetic field exerts torque on individual moments, this torque attempts to align the moments with the field. As the

torque orientates the moments it does work moving the moments into a lower magnetic potential energy. The Zeeman energy is given by,

$$w_{Zeeman} = -\mathbf{M} \cdot \mathbf{H}_{applied} \tag{2.6.4}$$

The magnetostatic or Dipolar Energy is a long range interaction that leads to creation of preferential directions of magnetisation dependent on the sample shape and geometry. Also called shaped anisotropy, the magnetostatic energy attempts to minimize the effective surface and volume magnetic charges, in doing so the stray fields produced by the material are minimized. It costs energy to create stray fields in space and usually the material forms domains to counter this. Domains minimize the magnetostatic energy because of the flux closure of the stray field lines. Ideally two magnetic moments would lie anti-parallel to one another; this however is at strong odds with the exchange interaction which would enjoy the moments to be parallel to one another. The demagnetizing field is determined by solving the magnetostatic Maxwell equations. The magnetostatic energy density is given by,

$$w_{magnetostatic} = -\frac{1}{2}\mathbf{M} \cdot \mathbf{H}_{demag} \tag{2.6.5}$$

Magneto-crystalline anisotropy is the preference for the magnetisation to be orientated along particular crystallographic axes. The origin of the magneto-crystalline anisotropy is the spin orbit interaction. The energy depends on the direction of the magnetisation relative to the lattice axes. The magnetocrystalline anisotropy depends on the crystallographic structure of the material, not on the samples geometrical shape.

The axis along which the magnetisation tends to lie when no external field is present is called an easy axis. The axis along which it is most difficult to magnetize along is called a hard axis. The

magnetocrystalline energy is defined as the work required aligning the magnetisation along a certain direction from the easy axis. It is usual to express the anisotropy energy in a power series of trigonometric functions of the angles the magnetisation makes with the principal axes of the crystal. Usually the first few terms will be sufficient. For a uniaxial anisotropy, the magnetocrystalline energy density can be written as,

$$w_{magnetocrystalline} = K_1 \sin^2 \theta \qquad (2.6.6)$$

In equation 2.6.6 K_1 is an anisotropy constant and has dimensions of energy density. θ is the angle between the magnetisation and the easy axis. Equation (2.6.6) must be independent of a change of sign of θ and will only contain even terms in the expression.

2.7 The Spontaneous Magnetisation

(This section is based on the pages from [22])

In 1907 Pierre Weiss (1865 - 1940) recognized that properties of some materials with a strong response to a magnetic field, such as Iron, require the existence of a *spontaneous magnetisation*, that is, a magnetisation that exists in the absence of an applied field. Localized regions of the material or domains retain a net magnetisation, the magnetisation directions of the domains can be macroscopically aligned by an externally applied magnetic field.

Weiss understood that atoms must carry a magnetic moment in order to sustain the spontaneous magnetisation. The problem lay in explaining how atomic moments persist in staying aligned macroscopically against thermal fluctuations. Initially, one might think that the alignment is

generated by the field from the atomic dipoles, at typical distances of atoms in a crystal lattice of r = 0.15nm and moments of $\mu = 1\mu_B$, the dipolar fields $\mu_0 H_D \approx 1T$, the dipolar interaction of atomic moments of $1\mu_B$ then leads to magnetic order at temperatures of 1K. Compared to the Curie temperature of around 1000K for Fe, Ni and Co and their alloys, the field generated from atomic dipoles is too weak to explain ferromagnetism. Table 2.7.1 below shows the Curie temperatures of the common ferromagnetic transition metal elements.

Element	T_C (K)	$\mu_0 H_W$ (T)
Fe	1043	1553
Co	1388	2067
Ni	631	949

Table 2.7.1 - Measured Curie temperatures T_C for elemental transition metals and the Weiss fields H_W calculated from the Molecular field expression for spin s=1/2 and $H_W = K_B T_C / \mu_B$ (Data taken from [22])

In order to account for the large Curie temperature, Weiss postulated a molecular field existed in ferromagnets to account for the spontaneous magnetisation. The magnitude of this so-called *molecular* or *Weiss* field would have to be of the order of 1000T. The Weiss field would then be able to generate the spontaneous magnetisation by aligning the atomic dipoles against thermal fluctuations. We see from table 2.7.1 that Weiss fields are enormous, too large to be generated experimentally. This Weiss field is now known to be generated from the quantum mechanical exchange interaction.

2.8 The Exchange Interaction

(This section follows material from [23])

In the previous section, the alignment of the atomic moments was generated by an internal molecular field proposed by Weiss, which is proportional to the magnetisation $H_W \approx \lambda_W M$. Above the Curie temperature T_C, the thermal energy $k_B T$ is greater than the interaction energy $\mu_B H_W$ and the magnetic ordering is lost. The strength of the Weiss field can be estimated by $k_B T \approx \mu_B H_W$. For Fe, $T_C = 1043K$, $H_W = 10^7$ Oe or 1000T. The magnetic field produced by the dipolar fields is $\approx \mu_B / a^3 \sim 10^3$ Oe, where 'a' is the material lattice parameter. As seen in the previous section the dipolar fields are too weak to account for the atomic alignment of the spontaneous magnetisation. An understanding of magnetic moments and their interaction was not fully understood until the advent of Quantum mechanics in the 1920's. The quantum theory of magnetism first revealed itself in atomic and molecular spectroscopy. Historically the concept of electron spin with half integer angular momentum was proposed by Uhlenbeck and Goudsmit [24] and was incorporated into wave mechanics by Heisenberg and Jordan in 1926 [25]. The key to this development was the understanding of atomic spectra by means of quantum theory. In the process, two of the most important concepts of physics and chemistry emerged. These are the concepts of exchange and spin-orbit coupling.

The exchange interaction is the strongest magnetic interaction and is the origin of the alignment of the spin system. The spin-orbit interaction creates 'orbital' magnetism, coupling the spin system to the lattice and gives rise to magnetocrystalline anisotropy. The concept of 'exchange' was originally derived from the interpretation of the emission spectra of atoms with two unpaired electrons such as neutral helium. Helium contains two electrons in the central field of two protons. In order to properly treat the electronic and spin structure of atoms one cannot use the conventional Schrodinger equation, since it does not describe spin. In principle, one

needs to use the relativistic Dirac equation. Dirac found that spin 'magically' emerges out of his theory without any such explicit assumptions. A starting point is the time-dependent Pauli equation 2.8.1 [26]. The Pauli equation is the non-relativistic Schrodinger equation with a term added for the spin and can be written as,

$$(H_e + H_S)\psi(r,t) = E\psi(r,t) \tag{2.8.1}$$

where H_e is the electronic Hamiltonian for an atom at the origin with a nuclear charge $q_n = Ze$ and electrons with a charge $q_e = -e$

$$H_e = \sum_{i=1}^{N}\left(\frac{\mathbf{p}_i^{\,2}}{2m_e} - \frac{Ze^2}{4\pi\varepsilon_0|r_i|}\right) + \sum_{i<j}\left(\frac{e^2}{4\pi\varepsilon_0|\mathbf{r}_j - \mathbf{r}_i|}\right) \tag{2.8.2}$$

The first term in equation 2.8.2 is the electronic kinetic energy, and the Coulomb interaction between the electrons and the nucleus. The last term is the Coulomb interaction between the electrons themselves and gives rise to the exchange interaction. The second term in the Pauli equation H_S represents the non-relativistic expression for the spin energy. It can be written in the form of 2.8.3,

$$H_S = \frac{e\hbar}{m_e}\mathbf{S}\bullet\mathbf{B} \tag{2.8.3}$$

In 2.8.3, **S** is the atomic spin and **B** is the magnetic induction. This term gives rise to the spin-orbit interaction. The central field felt by an electron comes not only from the nucleus, but has a screening contribution from an averaged electron-electron field. The central field Hamiltonian effectively decouples the motion of the individual electrons from one another, so the position of each electron is not correlated with the position of any other electron. The total

eigenfunction is a product of individual one-electron orbitals; it needs to be properly anti-symmetrized. It is clear that one-electron functions are incomplete since they do not include spin. The spin dependence can be written as $\chi(s_z)$ and the one-electron spin orbitals are given by 2.8.4.

$$\psi(\mathbf{a}) = \psi(\mathbf{r},\mathbf{s}) = R_{n,l}(r)Y_l^{\,m}(\theta,\phi)\chi(s_z) \tag{2.8.4}$$

The total eigenfunction of the central field Hamiltonian consists of the product of the individual electron orbitals. For a two-electron system we get,

$$\psi(\mathbf{a},\mathbf{b}) = \psi_1(a)\psi_2(b) \tag{2.8.5}$$

Because electrons are indistinguishable, 2.8.5 must be identical to 2.8.6,

$$\psi(\mathbf{a},\mathbf{b}) = \psi_2(a)\psi_1(b) \tag{2.8.6}$$

A solution must therefore be of the form of 2.8.7,

$$\psi(\mathbf{a},\mathbf{b}) = \frac{1}{\sqrt{2}}\left[\psi_1(\mathbf{a})\psi_2(\mathbf{b}) \pm \psi_2(\mathbf{a})\psi_1(\mathbf{b})\right] \tag{2.8.7}$$

The plus sign in 2.8.7 represent a symmetric total wavefunction, the minus sign an antisymmetric wavefunction.

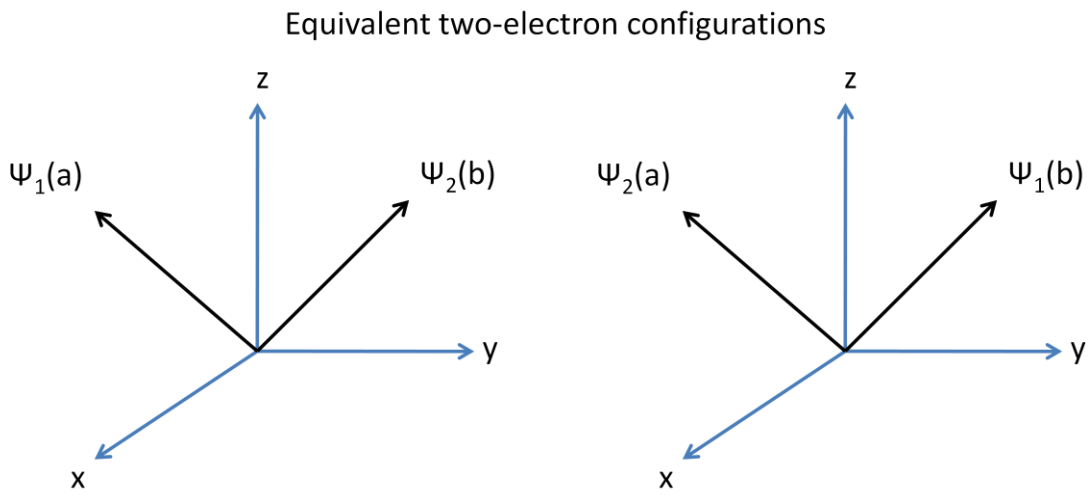

Figure 2.8.1 - The two electrons are labeled by subscripts 1 and 2 and their spatial and spin coordinates are given by vectors a and b. Since electrons are indistinguishable the configuration describe by $\psi_1(a)$ and $\psi_2(b)$ must be identical to that described by $\psi_2(a)$ and $\psi_1(b)$.

Starting with the He groundstate wavefunction, both electrons occupy the 1s orbital, the spatial part of the wavefunction is symmetric because both electrons share the same orbital and have quantum numbers *nlm* = 100. The spin part therefore has to be antisymmetric, giving the electron pair different spin functions α and β. The groundstate wavefunction is given by 2.8.8.

$$\psi_{GS}(\mathbf{a},\mathbf{b}) = \psi_{Sym}(\mathbf{r}_1,\mathbf{r}_2)\chi_{AS}(\mathbf{s}_1,\mathbf{s}_2) \tag{2.8.8}$$

$$\chi_{AS}(\mathbf{s}_1,\mathbf{s}_2) = \frac{1}{\sqrt{2}}\left|\alpha\beta - \beta\alpha\right| \tag{2.8.9}$$

Equation 2.8.8 is the solution to the central field equation and gives the He groundstate energy. Denoting an electron in a 1*s* orbital as *nlm* = 100 and another electron in an excited state as *nlm*, the central field wavefunction will have two possible forms given by 2.8.10 and 2.8.11; this gives the singlet and triplet excited state respectively.

$$\psi_{ES}{}^{S}(\mathbf{a},\mathbf{b}) = \frac{1}{\sqrt{2}}\left[\psi_{100}(\mathbf{r}_1)\psi_{nlm}(\mathbf{r}_2) + \psi_{100}(\mathbf{r}_2)\psi_{nlm}(\mathbf{r}_1)\right]\bar{\chi}_{AS}(\mathbf{s}_1,\mathbf{s}_2) \tag{2.8.10}$$

$$\psi_{ES}{}^{T}(\mathbf{a},\mathbf{b}) = \frac{1}{\sqrt{2}}\left[\psi_{100}(\mathbf{r}_1)\psi_{nlm}(\mathbf{r}_2) - \psi_{100}(\mathbf{r}_2)\psi_{nlm}(\mathbf{r}_1)\right]\bar{\chi}_{AS}(\mathbf{s}_1,\mathbf{s}_2) \tag{2.8.11}$$

Using the Schrodinger equation for the central potential $H^0(r_1,r_2)$, the same energy is obtained using either 2.8.10 or 2.8.11. This energy is given by $E_{ES} = E_{100} + E_{nlm}$. Remaining is the contribution from the electron-electron interaction $H_{e\text{-}e}(\mathbf{r}_1,\mathbf{r}_2)$. Perturbation theory gives a correction $E_{e\text{-}e}$ to E_{ES} given by equations 2.8.12 and 2.8.13 for the singlet (anti- parallel spin alignment) and triplet (parallel spin alignment) states respectively.

$$E_{e-e}{}^{S} = \left\langle \psi_{ES}{}^{S}(\mathbf{a},\mathbf{b}) \middle| H^1(\mathbf{r}_1,\mathbf{r}_2)\psi_{ES}{}^{S}(\mathbf{a},\mathbf{b}) \right\rangle = I + J \tag{2.8.12}$$

$$E_{e-e}{}^{T} = \left\langle \psi_{ES}{}^{T}(\mathbf{a},\mathbf{b}) \middle| H^1(\mathbf{r}_1,\mathbf{r}_2)\psi_{ES}{}^{T}(\mathbf{a},\mathbf{b}) \right\rangle = I - J \tag{2.8.13}$$

The energies *I* and *J* have a simple physical meaning. The *Coulomb integral* '*I*' represents the electrostatic Coulomb repulsion between the electron densities $|\Psi_{100}(\mathbf{r}_1)|^2$ and $|\Psi_{nlm}(\mathbf{r}_2)|^2$ and has a positive sign, opposite to the negative sign of the electron-nuclear Coulomb attraction. The other quantity '*J*' is called the *exchange integral* and reflects the energy associated with a change of quantum states between two electrons. The *exchange energy* $\Delta E = 2J$ corresponds to the singlet-triplet splitting. If *J* is positive, the spins are parallel. If *J* is negative, the spins lie anti-parallel.

2.9 The Spin-Orbit Coupling

(This section follows from [27])

In the last section the exchange interaction was discussed and revealed to be the strongest of the magnetic interactions, it has the shortest range and is isotropic. It was the sign of the

exchange integral that determines whether the spins are parallel or antiparallel. In a ferromagnet the exchange integral is positive and the spins are orientated parallel. In addition to the exchange interaction there is the spin-orbit (SO) interaction, it is about 10 – 100 times smaller than the exchange interaction, but by no means less important. As the name suggests the SO interaction describes the coupling of the spin **s** with the orbital angular momentum **L** to a new total angular momentum **J = s + L**.

Semi classical approach to the spin-orbit energy

The SO coupling can be pictured using classical concepts in a magnetostatic model. An approximate expression can be found for the interaction of the spin **S** with the orbital angular momentum **L**. The capital letters for **S** and **L** to indicate that they may already represent the sum of coupled momenta. The orbital angular momentum is pictured to arise from a current loop created by the electron as seen in figure 2.9.1

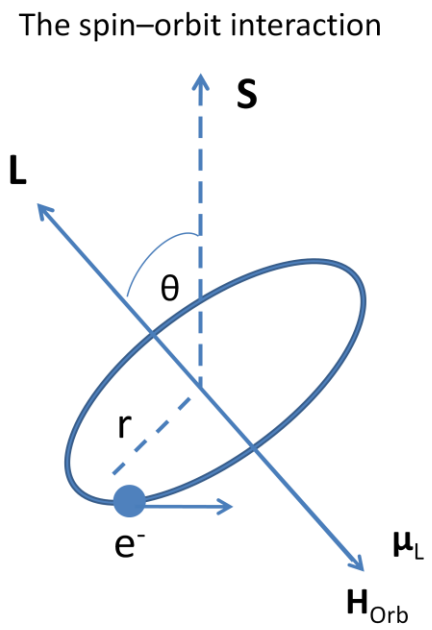

Figure 2.9.1 – Simple picture for deriving the spin-orbit coupling energy in the semi-classical picture. **L** is the orbital angular momentum of the electron, **S** the spin angular momentum**,** $\boldsymbol{\mu}_L$ is the magnetic moment arising from the orbital angular momentum. Note that the electron motion is opposite to the current loop it generates.

Using $-\boldsymbol{\mu}\bullet\mathbf{H}$ for the energy of a magnetic dipole in a magnetic field, the interaction energy of the spin moment $\boldsymbol{\mu}_S$ with the magnetic field generated at the loop centre by the current loop $\mathbf{H}_{Orb}$ can be calculated. The spin moment $\boldsymbol{\mu}_S = -\, e\, \mu_0\, \mathbf{S} / m_e$, where **S** is in units of h-bar.. The field and the orbital moment $\boldsymbol{\mu}_L$ are linked by 2.4.2 and the orbital moment and the orbital angular momentum **L** are linked by 2.3.1. The orbital field is given by equation 2.9.2.

$$\mathbf{H}_{Orb} = \frac{\boldsymbol{\mu}_L}{2\pi\mu_0 r^3} = -\frac{e\mathbf{L}}{4\pi m_e r^3} \qquad (2.9.2)$$

Using $-\boldsymbol{\mu}\bullet\mathbf{H}$ and 2.9.2 an expression for the spin-orbit energy E_{SO} is given by equation 2.9.3

$$E_{SO} = -\frac{e^2}{4\pi\varepsilon_0 m^2{}_e c^2 r^3}\mathbf{L}\bullet\mathbf{S} \qquad (2.9.3)$$

The orbital field $\mathbf{H}_{Orb}$ can be remarkably strong, if a spin-half moment of one Bohr Magneton μ_B is assumed, a simple relation between the spin-orbit energy and the magnetic field strength results.

Quantum mechanical spin-orbit Hamiltonian

It was just seen how a semi-classical treatment of the spin-orbit interaction may be given to estimate the spin-orbit energy and orbital field, now a brief visit to the spin-orbit Hamiltonian will be made. From the electrons point of view the nucleus appears to rotate around it and the moving nuclear charge appears as a current to the electron producing a magnetic field given by 2.9.6

$$\mathbf{B}^* = -\frac{\mathbf{v}\times\mathbf{E}}{2c^2} \qquad (2.9.6)$$

Using $\mathbf{E} = -\nabla\varphi$ and the classical expression for linear momentum $\mathbf{p} = m_e\mathbf{v}$ equation 2.9.6 can be written in the form of equation 2.9.7.

$$\mathbf{B}^* = \frac{1}{2m_e c^2}\mathbf{p}\times\nabla\phi \qquad (2.9.7)$$

The spin-orbit Hamiltonian may be written as 2.9.8

$$H_{SO} = \frac{e\hbar}{2m^2{}_e c^2}\mathbf{s} \bullet \mathbf{p} \times \nabla \phi$$

$$= \xi_{nl}(r)\mathbf{s} \bullet \mathbf{L} \qquad (2.9.8)$$

The expectation value of ξ(r) from 2.9.8 is the *spin-orbit parameter* or the *coupling constant* and has the dimensions of energy. The spin-orbit interaction energy is comparatively small for the *3d* transition metals, having the magnitude 10 – 100meV, this is weaker than the exchange interaction ~1eV and this accounts for the small orbital moments of Fe, Ni and Co.

The essence of the spin-orbit interaction is that the electron's spin and orbital motion are connected by 2.9.8, the spatial part of the electron's wavefunction 'senses' the lattice and its anisotropy, consequently the spin moment feels influenced by symmetry directions in the lattice via the spin-orbit coupling. According to the definition of the magnetostatic energy, the energy given by 2.9.3 corresponds to the energy gain one experiences if the spin **S** is turned from a perpendicular to a parallel orientation to **L,** as depicted in figure 2.9.1. If we now imagine that the orbital moment prefers to 'lie' along a specific bonding or lattice direction, the orbital moment is 'locked-in' by the lattice. This is the magnetocrystalline anisotropy energy. In solids, the spin-orbit interaction is responsible for the magnetocrystalline anisotropy.

2.10 Magneto-optical Kerr Effect

(This section follows [28])

In the last two sections the exchange interaction and the spin-orbit (SO) coupling were discussed from a microscopic level. In this section the magneto-optical Kerr effect (MOKE) is

discussed and is an important experimental technique for studying magnetic materials within static and dynamic approaches. Magneto-optical effects ultimately manifest themselves on a microscopic level being described by quantum mechanics; macroscopic descriptions use a more phenomenological approach in terms of the dielectric tensor of the medium. Here the latter will be discussed in the following.

In 1845 Faraday discovered that the polarization vector of linearly polarized light is rotated upon transmission through a sample that is exposed to a magnetic field parallel to the propagation direction of the light [29]. About 30 years later, Kerr observed that when linearly polarized light is reflected from a magnetic solid its polarization plane also rotates over a small angle with respect to the incident lights polarization [30].

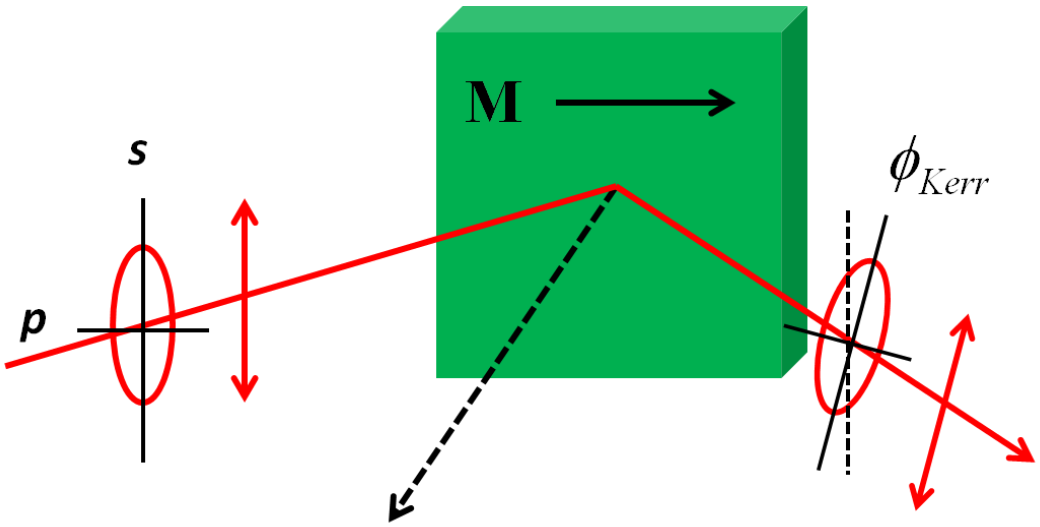

Figure 2.10.1 – Schematic illustrating the Kerr rotation Φ_K and the Kerr ellipticity ε_K. Incident p or s-polarised light becomes elliptically polarized upon reflection from a magnetic material. The Kerr ellipticity and rotation are proportional to the magnetization to first order, therefore, by measuring changes in the polarization of reflected light from the material, changes in the magnetization can be detected.

This discovery has become known as the magneto-optical Kerr effect (MOKE). Since then many other magneto-optical effects have been discovered, such as the Zeeman, Voigt and Cotton-Mouton effects. These effects have in common that the interaction of polarized light with a magnetic solid depends on its polarization.

The quantum mechanical understanding of the Kerr effect began in 1932 when Hulme proposed that the Kerr effect could be attributed to the spin-orbit interaction [31]. The symmetry between left and right-hand circularly polarized light is broken by the spin-orbit coupling in a magnetic solid. This leads to different refractive indices for the two kinds of circularly polarized light, the reflected light has an elliptical polarization. The major elliptical axis is rotated by the so called Kerr angle from the original axis of polarization. The first systematic study of the frequency dependence of the Kerr and Faraday effects was developed by Argyres [32]; later Cooper presented a more general theory using some simplifying assumptions [33]. The very powerful linear response techniques of Kubo gave general expressions for the conductivity tensor [34] which are now widely used. The first ab initio calculation of MO properties was made by Callaway and co-workers in the mid 1970s, they calculated the conductivity tensor elements σ_{xx} and σ_{xy} for bulk Fe and Ni, obtaining results in good agreement with experiment [35, 36]. The following section gives a classical description of magneto-optical effects.

Magneto-optical effects refer to a change in the polarization state of light upon interaction with media possessing a net magnetic moment; this also includes the complementary differential absorption of left and right circularly polarized light (circular dichroism). In the visible these magneto-optical effects result from electron excitations in the conduction bands. Near x-ray absorption edges magneto-optical effects can be enhanced by core-to-valence

electron transitions allowed by transition symmetry. Using symmetry considerations it can be shown that all magneto-optical phenomena are caused by the symmetry reduction caused by the magnetic ordering [37]. For the optical properties this symmetry reduction has consequences when the SO interaction is included. To calculate magneto-optical properties the spin-orbit coupling and magnetism have to be described simultaneously with the material electronic band structure.

Classical phenomenological approach to the Magneto-optical Kerr effect

The interaction of electromagnetic radiation with a magnetic medium is described classically by the Maxwell equations. In cgs units the Maxwell equations are given by 2.10.1 to 2.10.4 inclusive.

$$\underline{\nabla} \bullet \mathbf{D} = \rho \tag{2.10.1}$$

$$\underline{\nabla} \bullet \mathbf{B} = 0 \tag{2.10.2}$$

$$\underline{\nabla} \times \mathbf{H} - \frac{\partial \mathbf{D}}{\partial t} = \mathbf{J} \tag{2.10.3}$$

$$\underline{\nabla} \times \mathbf{E} + \frac{\partial \mathbf{B}}{\partial t} = 0 \tag{2.10.4}$$

D is the electric displacement, related to the electric field **E** caused by the polarization **P** of the medium. **B** is the magnetic induction, **H** the macroscopic magnetic field and ρ and **J** are the macroscopic charge and current densities. The Maxwell equations are complemented by a set of

constitutive equations, which introduce material specific parameters such as the electrical conductivity **σ,** the relative permittivity ε_r and the relative permeability μ_r.

$$\mathbf{D} = \varepsilon_0 \varepsilon_r \mathbf{E} = \varepsilon_0 \mathbf{E} + \mathbf{P} \tag{2.10.5}$$

$$\mathbf{B} = \mu_0 \mu_r \mathbf{H} = \mu_0 (\mathbf{H} + \mathbf{M}) \tag{2.10.6}$$

$$\mathbf{J} = \sigma \mathbf{E} \tag{2.10.7}$$

Equations 2.10.5 to 2.10.7 inclusive are the so-called constitutive equations, **M** is the magnetization, ε_0 and μ_0 are the permittivity and permeability of free space respectively. In general the relative permittivity ε_r is a function of both space and time variables, which relate the displacement field **D**(**r**,t) to the electric field $\mathbf{E}(r', t')$ at past times consistent with causality, given by 2.10.8.

$$\mathbf{D}(\mathbf{r}, t) = \int_{-\infty}^{t} \int \varepsilon(\mathbf{r}, \mathbf{r}', t') \mathbf{E}(\mathbf{r}', t') dt' d\mathbf{r}' \tag{2.10.8}$$

In the following, only the frequency dependence is considered ε_r (ω), the spatial dependence of the relative permittivity is neglected. The effect of the relative permeability tensor μ_r (ω) at optical frequencies is usually small and it can be assumed that μ_r (ω) = ***I***, where ***I*** is the kronecker delta. It should be mentioned that for high electric or magnetic fields the relative permittivity and permeability may depend on the field strength, in such cases higher order terms in a Taylor expansion of the material properties lead to the appearance of non-linear effects [38]. The relative permittivity ε_r (ω) and optical conductivity σ (ω) are complex quantities.

$$\varepsilon = \varepsilon_1 + i\varepsilon_2 \tag{2.10.9}$$

$$\sigma = \sigma_1 + i\sigma_2 \tag{2.10.10}$$

Equations 2.10.9 and 2.10.10 are related by equation 2.10.11.

$$\varepsilon = 1 + i\frac{\sigma}{\omega} \tag{2.10.11}$$

In the absence of a spontaneous magnetization or external magnetic field and in the general case of an anisotropic material the relative permittivity $\varepsilon_r(\omega)$ is a symmetric tensor, after transforming to its principal axes has three components. For simplicity, consider a material of cubic structure with magnetization aligned along the z axis. Above the Curie temperature T_C the crystal has cubic symmetry and all three components of the permittivity tensor are equal. When the magnetization **M** parallel to the z axis appears below T_C the symmetry is lower and $\varepsilon_r(\omega)$ becomes equation 2.10.12

$$\varepsilon(\mathbf{M},\omega) = \begin{pmatrix} \varepsilon_{xx} & \varepsilon_{xy} & 0 \\ -\varepsilon_{xy} & \varepsilon_{xx} & 0 \\ 0 & 0 & \varepsilon_{zz} \end{pmatrix} \tag{2.10.12}$$

The remaining symmetry of the system depends on the orientation of the magnetisation. For cubic systems the effective symmetry is tetragonal, trigonal or orthorhombic depending on whether the magnetisation is aligned along the [001], [111] or the [110] axes respectively [39].

The components of the relative permittivity tensor depend on the magnetisation and have to satisfy the Onsager relations.

$$\varepsilon_{\alpha\beta}(-\mathbf{M},\omega) = \varepsilon_{\beta\alpha}(\mathbf{M},\omega) \tag{2.10.13}$$

where α, β = x, y or z. The Onsager relations mean that the diagonal components of the permittivity tensor are even functions of **M** and the nondiagonal elements are odd functions of **M**. To first order in **M** we get 2.10.14,

$$\varepsilon_{xy} \approx M\ , \qquad \varepsilon_{zz} - \varepsilon_{xx} \approx M^2 \tag{2.10.14}$$

In the absence of external currents (**J** = 0) and charges (ρ = 0) equations 2.10.1 to 2.10.7 inclusive reduce to equations 2.10.15 and 2.10.16.

$$\nabla \times \mathbf{E} = -\mu_0 \frac{1}{c}\frac{\partial \mathbf{H}}{\partial t} \tag{2.10.15}$$

$$\nabla \times \mathbf{H} = \varepsilon_0 \varepsilon_r \frac{1}{c}\frac{\partial \mathbf{E}}{\partial t} \tag{2.10.16}$$

Assuming the incident light is a plane wave such a substitution can be made for **E** and **H** into 2.10.15 and 2.10.16. Plane waves have the form,

$$\mathbf{E}(\mathbf{r},t) = \mathbf{E}_0 \exp\left[-i(\omega t - \mathbf{q}\bullet\mathbf{r})\right] \tag{2.10.17}$$

$$\mathbf{H}(\mathbf{r},t) = \mathbf{H}_0 \exp\left[-i(\omega t - \mathbf{q}\bullet\mathbf{r})\right] \tag{2.10.18}$$

In 2.10.17 and 2.10.18, ω and **q** are the frequency and wavevector of the incident light. After substituting plane waves 2.10.17 and 2.10.18 into 2.10.15 and 2.10.16, one arrives at a secular equation of the form,

$$\begin{pmatrix} N^2 - \varepsilon_{xx} & -\varepsilon_{xy} & 0 \\ \varepsilon_{xy} & N^2 - \varepsilon_{xx} & 0 \\ 0 & 0 & \varepsilon_{zz} \end{pmatrix} \begin{pmatrix} E_x \\ E_y \\ E_z \end{pmatrix} = 0 \tag{2.10.19}$$

where **N** is a unit vector directed along **q**. When the light propagates along the z direction parallel with **M**, $E_z = 0$, while the condition for non-zero solutions of E_x and E_y yields eigenvalues,

$$n^2_{\pm} = \varepsilon_{xx} \pm \varepsilon_{xy} \tag{2.10.20}$$

This gives the normal modes of the light as 2.10.21 and 2.10.22,

$$D_+ = \varepsilon_0 n_+^{\,2}(E_x + iE_y) \tag{2.10.21}$$

$$D_- = \varepsilon_0 n_-^{\,2}(E_x - iE_y) \tag{2.10.22}$$

The optical normal modes are right and left circularly polarized light waves with complex refractive indices n_+ and n_- respectively. Phenomenologically, one can think of the magnetisation dependent elements of the relative permittivity tensor inducing circular birefringence in the incident polarisation. The incident linearly polarized light can be considered as a superposition of two circular polarizations of opposite handedness, both of which experience a different refractive

index upon reflection, both polarizations undergo a phase change with respect to each other and the net superposition of the reflected beam is elliptically polarized. It is the angular difference between the initial polarisation and the semi-major axis of the elliptical polarisation state that is referred to as the Kerr rotation.

Magneto-optical Kerr effect geometries

Depending on the orientation of the magnetization vector relative to the reflective surface and the plane of incidence of the light beam, three different types Kerr geometries are distinguished as seen in figure 2.10.2, longitudinal, polar and transverse.

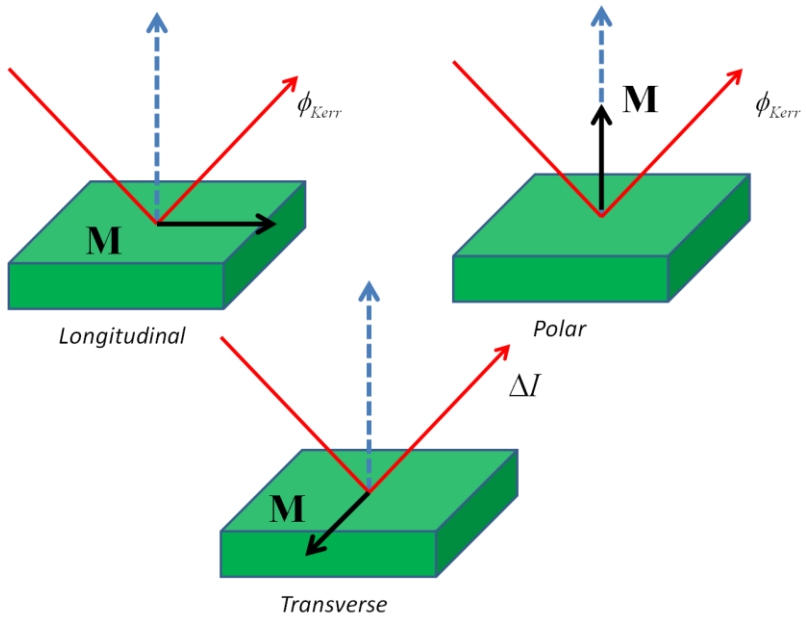

Figure 2.10.2 – The three principal MOKE geometries, longitudinal, polar and transverse. The geometry depends on the orientation of the magnetization with respect to the plane of incidence of the light.

In the polar geometry the magnetization vector **M** is orientated perpendicular to the sample surface and lies in the plane of incidence. In the longitudinal geometry the magnetization **M** is parallel to the sample surface and lies in the plane of incidence. In both geometries either 'p' or's' polarized light may be used. The magnetization dependent Kerr rotation is measured for both longitudinal and polar configurations, the strength of which depends on the frequency of the probing light and the reflecting material via the conductivity tensor. The conductivity tensor depends on the refractive index of the material which in turn depends on the frequency of the incident light. In the transverse geometry, the magnetization **M** is perpendicular to the plane of incidence and lies in the sample plane. Since only r_{pp} has a dependence on the magnetization p-polarised light must be used to detect the magnetisation **M**. For s-polarised light the lights electric field is parallel to **M** so the magneto-optical effect is null. In the transverse geometry only a magnetization dependent change in intensity ΔI can be measured.

Magneto-optical Kerr effect reflection coefficients

Using the Jones matrix formalism, one can relate the incident and reflected electric fields of the light by the matrix of reflection coefficients,

$$\begin{pmatrix} E_S \\ E_P \end{pmatrix}_{\text{Re } flected} = \begin{pmatrix} r_{ss} & r_{sp} \\ r_{ps} & r_{pp} \end{pmatrix} \begin{pmatrix} E_S \\ E_P \end{pmatrix}_{Incident} \qquad (2.10.23)$$

Equation 2.10.23 relates the incident and reflected electric fields from a reflecting media in terms of optical reflection coefficients r_{ij}. The Kerr rotation and ellipticity is given by 2.10.24 and 2.10.25 for p-polarised light.

$$\Phi_K = -\mathrm{Re}\left[\frac{r_{sp}}{r_{pp}}\right] \tag{2.10.24}$$

$$\varepsilon_K = \mathrm{Im}\left[\frac{r_{sp}}{r_{pp}}\right] \tag{2.10.25}$$

For s-polarised light the Kerr rotation and ellipticity are given by 2.10.26 and 2.10.27 respectively.

$$\Phi_K = \mathrm{Re}\left[\frac{r_{ps}}{r_{ss}}\right] \tag{2.10.26}$$

$$\varepsilon_K = \mathrm{Im}\left[\frac{r_{ps}}{r_{ss}}\right] \tag{2.10.27}$$

For a non-magnetic material, r_{ps} and r_{sp} are zero, r_{pp} and r_{ss} are non-zero and complex. For a ferromagnetic material r_{ps} and r_{sp} are non-zero and complex. This results in s (or p) polarised incident light inducing p (or s) polarised reflected light. In general the diagonal reflection coefficients r_{ss} and r_{pp} are not equal, which can lead to a net rotation of the polarization if the incident light is not exactly p or s-polarised, even in the case of zero magnetization. For the benefit of measuring the changes arising from the magnetization, only either p or s-polarised light is used in magneto-optical experiments.

2.11 Spin wave Dispersion

This section follows from ref 40.

From section 2.5, the Landau-Liftshitz-Gilbert equation (equation 2.5.5) is used to describe the dynamical magnetization of a magnetic material. Due to the damping term in the equation, any excitation of the initial magnetization is followed by a loss of this energy from the magnetic system and the amplitude of the magnetization decays in time.

$$\frac{\partial \mathbf{M}}{\partial t} = -\gamma \mathbf{M} \times \mathbf{H}_{eff} - \frac{\alpha}{M}\left(\mathbf{M} \times \frac{\partial \mathbf{M}}{\partial t}\right) \tag{2.5.5}$$

Spin waves are dynamical excitations of the magnetization and are described the Landau-Liftshitz-Gilbert equation. Like electromagnetic waves in media and electron waves in crystalline solids, spin waves are described by their dispersion relation. By solving the Landau-Liftshitz-Gilbert equation one can determine the dispersion relation and hence how spin waves travel with wave vector and/or applied magnetic field. In a non-periodic system, such as a continuous thin film with an in-plane magnetic field H_x, the Landau-Liftshitz-Gilbert equation can be solved in the 'macrospin' approximation to yield Kittel type dispersion. The macrospin approximation neglects any non-uniformity of magnetization and the spins precess together in phase. The Kittel equation is given by equation 2.11.1

$$\left(\frac{\omega_k}{\gamma \mu_0}\right)^2 = H_x\left(H_x + M_S - \frac{2K_Z}{\mu_0 M_S}\right) \tag{2.11.1}$$

Here M_S is the saturation magnetization and K_z represents the out-of-plane anisotropy. If solutions to equation 2.5.5 are to admit dynamics beyond uniform precession, it is important to distinguish between two different interactions between moments, the dipolar and exchange interactions.

Solving 2.5.5 in the magnetostatic limit yields a manifold of dynamical solutions for a magnetic thin film. They are classified by their propagation direction with respect to the applied magnetic field. Modes whose frequency lies above the uniform precession frequency generally tend to localise at the surface of the film and have a wave vector pointing orthogonal to the magnetic field. The geometry with **k** and **H** perpendicular is called Damon-Eshbach geometry. The relationship between the mode frequency and applied field for a film of thickness 't' is given by equation 2.11.2

$$\left(\frac{\omega_{DE}}{\gamma\mu_0}\right)^2 = H_x\left(H_x + M_S - \frac{2K_Z}{\mu_0 M_S}\right) + \frac{M_S{}^2}{4}\left(1 - \exp\left(-2|k_{DE}|t\right)\right) \qquad (2.11.2)$$

When **k** and **H** are parallel, spin waves feature a lower precession frequency compared to their Kittel precession. This gives rise to 'negative' dispersion as the wave travels 'backwards' in phase. This type of propagating behaviour is called a backward-volume mode. Figure 2.11.1 illustrates both Damon-Eshbach and backward-volume type modes in the dipolar regime. There is a manifold of modes in between the Damon-Eshbach and backward-volume geometries corresponding to the area between the dispersion curves for both modes respectively.

The wavelength of spin waves varies between 10 μm in the dipolar regime, where the dipolar fields are the dominant coupling mechanism to the exchange regime where wavelengths can be 1nm. Their frequencies span the GHz and the THz ranges respectively. At wavelengths below 100 nm, the dispersion is dominated by the exchange interaction and we speak of 'exchange' spin waves. The magnetostatic energy is neglected and for a chain of precessing spins coupled by the exchange interaction the dispersion has a 1 – cos(kr) behaviour. A consequence of neglecting the anisotropic dipolar coupling in the exchange limit, is that the

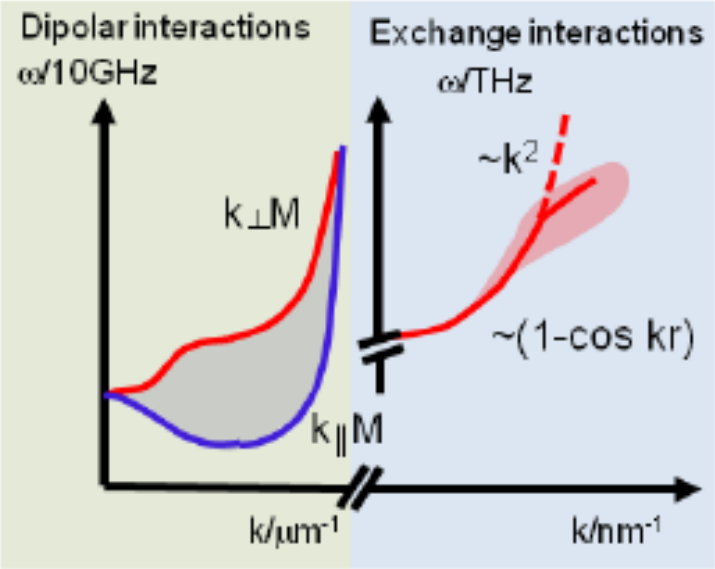

Figure 2.11.1 – In the dipolar regime, long wavelength GHz spin waves can have either Damon-Eshbach (k and M perpendicular) or Backward-volume (k and M parallel) dispersion. When the dipolar coupling is neglected short wavelength THz spin waves, called exchange spin waves are described by quadratic dispersion. Figure taken from [40].

dispersion does not depend on the direction of magnetisation. For small k in the exchange limit the dispersion is quadratic in k. In this region, the energy of a magnon increases quadratically with momentum analogous to free electron behaviour. High-energy THz spin waves are heaviliy damped and travel very short sub-micron distances in magnetic media.

2.12 Spin waves in periodic magnetic structures

The dispersion of spin waves in a non-periodic (continuous) structure was complicated by the anisotropy of the dispersion on the applied field direction. When a medium is subject to a dynamical excitation, the periodic system's response function determines the modes which can propagate via the dispersion relation ω(k), this in turn determines the available density-of-states. For weak potentials, Bloch states can be constructed from plane waves and the dispersion can be

calculated. In periodic dielectrics and in crystalline media this approach is applied to photons and electrons respectively. The same concepts for electrons and photons are applied to spin waves to form Bloch states in a magnonic crystal. Using the Bloch theorem a magnonic bandstructure of a periodic ferromagnetic system can be deduced. A theoretical *ansatz* was developed by Puszkarski et al [41]. Two methods, the effective media approximation and the plane wave method are discussed.

Effective Media approximation

A simple approximation can be used to estimate the dispersion relation of periodic structures such as an anti-dot lattice. The effective media approximation replaces the heterogeneous structure of the anti-dot lattice with a uniform continuous film. The film parameters are effective magnetic parameters. Using volume weighted averaged parameters; the effective saturation magnetization and exchange length are given by equation 2.12.1 and 2.12.2 respectively.

$$M_S = fM_S^{Co} + (1-f)M_S^{Py} \tag{2.12.1}$$

$$l_{Exc} = fl_{Exc}^{Co} + (1-f)l_{Exc}^{Py} \tag{2.12.2}$$

Where '*f*' is the anti-dot filling fraction, defined as the ratio of the cobalt dot to the are of the unit cell: $f = \pi R^2 / a^2$, where *'a'* is the lattice parameter and *'R'* is the dot radius. Exchange length is defined in the standard way: $\sqrt{\frac{A}{\mu_0 M_S^2}}$. 'A' is the exchange constant of the material. To determine the dispersion relation for the structure, the Damon-Eshbach dispersion for a thin film can be used modified for effective parameters (equation 2.11.2) for propagation perpendicular to the bias field [42]. The measured dispersion relation for the permalloy and

cobalt dot / anti-dot structures discussed in Chapter 4 reveals quantization of the modes. The effective media approximation does not model periodicity and the resulting dispersion is continuous. The quantization of the dispersion is explained by adding periodicity. The plane wave method allows one to consider the periodicity of the structure itself and is discussed in the next section.

The Plane wave method

The spin wave dispersion relation can be calculated using the plane wave method. The plane wave method considers the structural periodicity which is subject to time-harmonic excitations. The Landau-Liftshitz equation is used, neglecting the magnetocrystalline anisotropy, $\mathbf{H}_{\text{eff}}$ can be written as equation 2.12.3

$$\mathbf{H}_{eff}(\mathbf{r},t) = \mathbf{H}_0 + \mathbf{H}_{ex}(\mathbf{r},t) + \mathbf{H}_{ms}(\mathbf{r},t) \tag{2.12.3}$$

$\mathbf{H}_0$ is the applied field, and the exchange field is given by $\mathbf{H}_{ex} = \nabla l_{ex}^2 \nabla \mathbf{m}(\mathbf{r},t)$. In bi-component magnonic crystals, such as the anti-dot / dot lattices presented in chapter 4, the spatial periodicity of the exchange length l_{ex} and the saturation magnetization M_{S}, must be considered [43]. To solve the Landau-Liftshitz equation, the dynamical magnetization takes the Bloch form in equation 2.12.4.

$$\mathbf{m}(\mathbf{r},t) = \sum_{G} \mathbf{m}_k(\mathbf{G}) \exp(i(\mathbf{G}+\mathbf{k})\mathbf{r}) \exp(i\omega t) \tag{2.12.4}$$

‘**G**’ is a reciprocal lattice vector and the wavevectors ‘**k**’ lie in the first Brillouin zone. The Landua-Lifshitz equation is cast in reciprocal space and solved as an eigenvalue problem for

the frequencies ω and $\mathbf{m_k}(\mathbf{G})$, being eigenvalues and eigenvectors, respectively. The solution is obtained by using standard numerical procedures for solving real matrix eigenvalue problems.

2.13 Ultrafast Magnetisation Dynamics

The magnetisation of a solid reacts to external disturbances such as disturbances in temperature and magnetic fields on many timescales ranging from millions of years in geomagnetism, to years in magnetic storage media, milli and microseconds in AC-transformers and nanoseconds in magnetic data writing and reading. Magnetisation changes on these timescales and their relation to the size of magnetic structures such as magnetic domains and domain walls have been prominent subjects in magnetism because of the multitude of applications. This section follows ref [44]. Over the last 30 years, the development of magneto-optics with pulsed lasers has opened up a new field, *ultrafast magnetisation dynamics*. Typically, ultrafast studies employ pulsed lasers for both excitation of the sample and probing the ensuing changes of the magnetisation in so-called pump-probe experiments. Such experiments now have a time resolution below one picosecond (10^{-12} s), well in to the femtosecond (10^{-15} s) range [45]. The timescales in the picosecond and femtosecond range are of great interest because they naturally correspond to the timescales over which important magnetic energies interact, shown in figure 2.13.1. The field of ultrafast magnetisation dynamics is typically interested in exploring magnetic processes faster than 100ps. The classical description of magnetization dynamics using the LLG equation and thermodynamics becomes less applicable toward these shorter timescales, as quantum effects become more significant. Due to time-energy correlation, magnetic interactions of differing strengths operate over different time scales; the greater the interaction energy the faster interaction occurs. For *3d* systems, the

exchange energy has the order $E \approx 3 \times 10^{-1}$ eV, the spin-orbit energy 10^{-2} eV $\leq E \leq 10^{-1}$ eV and the magnetic anisotropy energy 10^{-6} eV $\leq E \leq 10^{-3}$ eV.

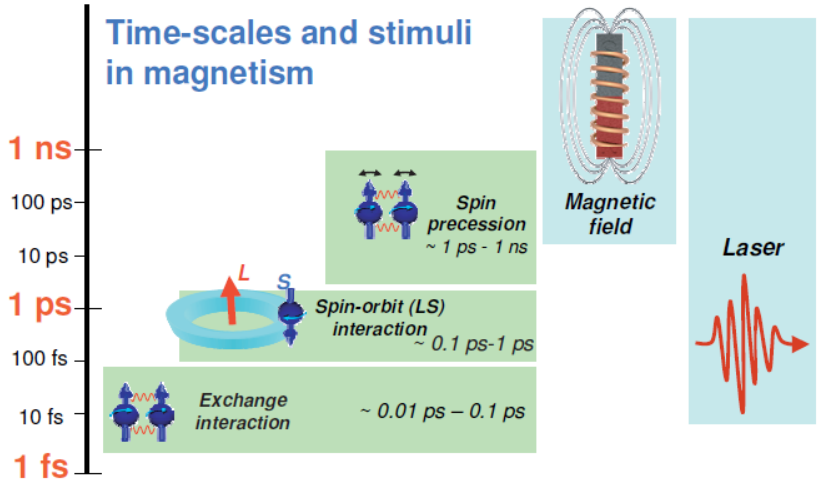

Figure 2.13.1 - Typical time scales in magnetism as compared to magnetic field and laser pulses. The short duration of the laser pulses makes them an attractive alternative to manipulate the magnetisation. (Reproduced from [46])

In order to ensure fast and homogeneous deposition of the laser pulse energy, the film thickness is usually the order of the optical absorption length, usually several tens of nanometres. If a magnetic field pulse is used for excitation, the penetration depth is determined by the skin effect. A ferromagnetic body can store excitation energy in three different forms: the energy of the electrons, the energy of phonons and as a change of the magnetic order i.e the spin system. This reflects itself as a change of the spontaneous magnetisation of the sample material. Figure 2.13.2 shows the heat reservoirs in a ferromagnetic metal. All three reservoirs may be separately excited, indicated by the arrows. The deposition of energy in a specific reservoir initially leads to a nonequilibrium distribution, indicated by two shades. An effective temporary equilibrium

temperature may or may not be reached before it finally equilibrates with the other reservoirs after a characteristic time τ_i.

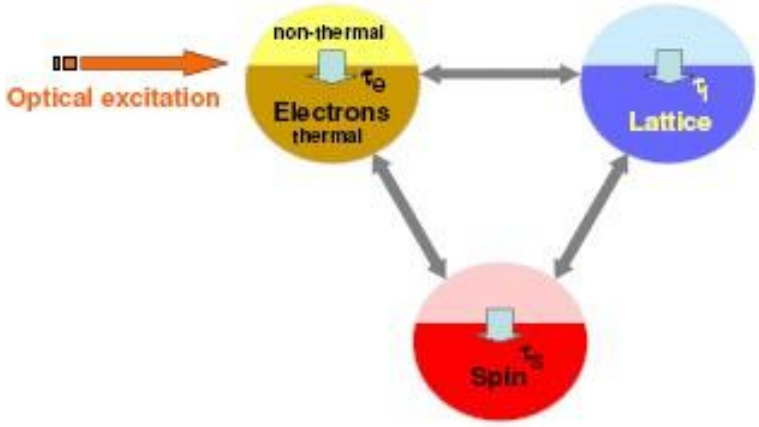

Figure 2.13.2 –The electron, spin and lattice systems act as 3 energy baths for the redistribution of the incident pulse energy. The electron, lattice and spin relaxation time is given by τ_e, τ_l and τ_s respectively. Each energy reservoir has its own specific heat capacity and temperature associated with it, also coupling constants between the interacting energy baths describe the efficiency of energy and angular momentum transfer between the electron, spin and lattice systems.

It is of key importance to realise that both energy and angular momentum need to be exchanged and conserved between the energy storage reservoirs; here angular momentum is the essence of the magnetisation. The flow of angular momentum to and from the spin system determines the spin and consequently the magnetisation dynamics [47].

When a metal film is heated with an ultrashort femtosecond optical pulse, there are generally four steps that are considered to occur, which may potentially overlap in time. (1) When the pulse arrives the pulse energy is deposited within the skin depth of the metal (*circa* 20nm), absorption of the energy occurs via interband and intraband optical transitions, exciting electron-hole pairs in a highly non-equilibrium electron gas. (2) As a consequence of electron-

electron interactions, the non-equilibrium electron gas then thermalizes to a Fermi-Dirac distribution in around 500fs. (3). The hot electron gas relaxes from its initial non-equilibrium state to the equilibrium state, having passed the excitation energy of the pulse to the lattice via electron-phonon interactions within 1-10ps. Lastly (4) this energy propagates in the medium via conventional heat propagation until it is completely dissipated. Phenomenologically, the above processes are incorporated into the so-called three temperature model [47]. In which the electron, lattice and then spin systems are ascribed individual temperatures. Heat capacities are assigned to the three interacting baths and coupling constants can be found to relate the mechanisms of interaction of these three reservoirs [48].

It was Beaurepaire [49] that initially provided experimental evidence of the ultrafast demagnetization that occurs on a subpicosecond time scale after the arrival of an ultra short pulse. It is within these timescales that there is an ultrafast demagnetization of the sample, where due to the temperature increase the magnetic ordering is lost or reduced. The extent of the rise of the electron temperature and demagnetisation depends on the intensity of the incident pulse. After demagnetisation, the magnetisation slowly recovers, with a timescale dependent on the intensity of the pulse and the 'hot' electron temperature. Not only does the incident pulse cause demagnetisation, but other phenomena such as magnetisation reversal and precession of the magnetisation may take place during these timescales.

2.14 Synchrotron radiation

(This section is based on [50])

It is well known from Maxwell's equations, equations 2.10.1 to 2.10.4 inclusive, that an accelerating charged particle emits electromagnetic radiation. When moving at relativistic speeds, this radiation is emitted in a narrow cone on a tangent to the path of the particle. Synchrotron radiation is generated when relativistic electrons are accelerated in a magnetic field. There are three types of magnetic structures commonly used to produce synchrotron radiation: bending magnets, undulators and wigglers. Bending magnets cause a single curved trajectory as depicted in figure 2.14.1. The result is a fan of radiation around the bend. Undulators are periodic magnetic structures with relatively weak magnetic fields; this magnetic periodicity causes the electron to undergo harmonic motion as it moves in the axial direction. The weak magnetic fields cause the amplitude to be small and the resulting spectrum can be very narrow.

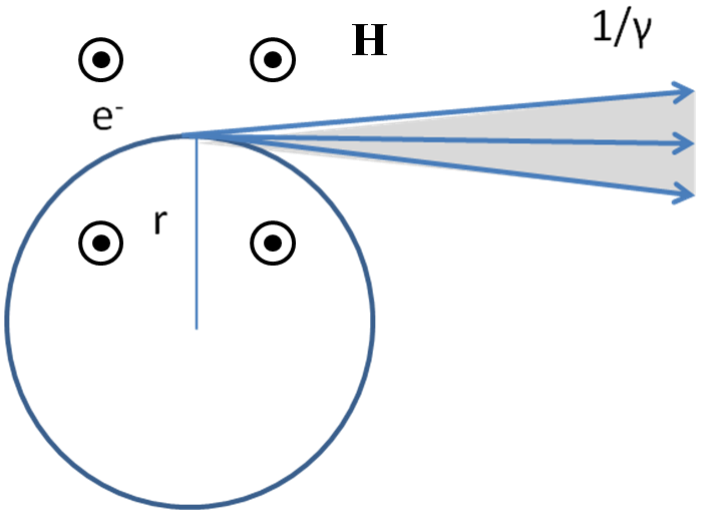

Figure 2.14.1 – Bending magnet radiation occurs when a relativistic electron travels in a uniform magnetic field, executing circular motion with acceleration directed toward the centre. The radiation is directed tangentially outward in a narrow radiation cone, giving the appearance of a sweeping searchlight. The radiation spectrum is broadband, analogous to a 'white-light' x-ray bulb. The emission angle is given by $1/\gamma$, where $\gamma = (1 - (v/c)^2)^{-1/2}$.

Wigglers are identical to undulators, but have much stronger magnetic fields, meaning the cone angle and radiated power is much larger. The spectrum of wigglers is much broader than the narrow undulator radiation, similar to the bending magnet spectrum. Historically, synchrotron radiation was first observed as energy loss in electron storage rings. The first synchrotrons for scientific use were circulars rings, utilizing parasitic beam ports that harnessed otherwise lost radiation. The resulting radiation from such sources was bend magnet radiation, being very broadband it is the x-ray analogue of the white light bulb. Over time, however, purpose built sources have been constructed (second generation facilities). The newest synchrotrons (third generation facilities) are composed of many straight sections specifically optimized to produce high brightness undulator and wiggler radiation.

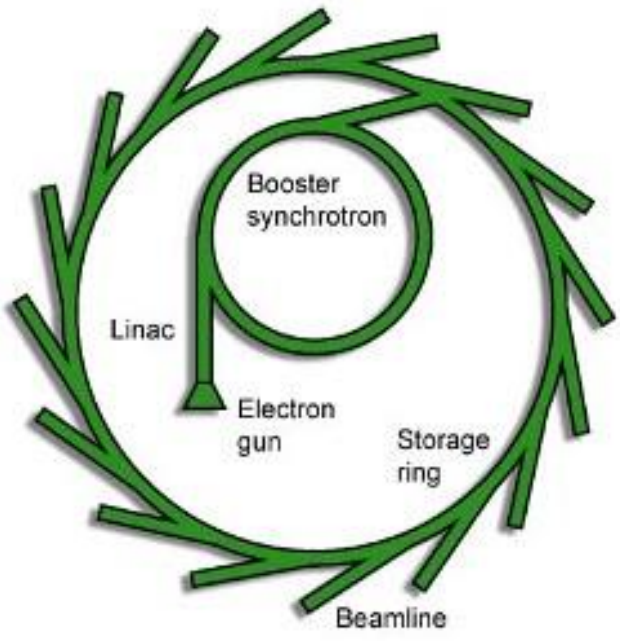

Figure 2.14.2 – Simple schematic of a synchrotron source, showing the linear accelerator (LINAC), booster synchrotron, storage ring and the beamlines tangential to the storage ring.

In figure 2.14.2 relativistic electrons are injected into the storage ring from a linear accelerator (LINAC), after passing through the booster synchrotron. The booster synchrotron increases the electron kinetic energy from the LINAC until the kinetic energy is sufficient to enter the storage ring magnet settings. Various magnetic lenses keep the electrons travelling along the desired trajectory. Synchrotron radiation is produced as the electrons pass through bending magnets, undulators or wigglers.

Facility	ALS	APS
Electron energy	1.90 GeV	7.00 GeV
γ	3720	13,700
Current (mA)	400	100
Circumference (m)	197	1100
RF frequency	500	352
Pulse duration (FWHM) (ps)	35-100	170
Bending magnet radiation		
Bending magnetic field (T)	1.27	0.599
Critical photon energy (keV)	3.05	19.5
Critical photon wavelength	0.407nm	0.0636nm (0.636 Angstrom)
Bending magnet sources	24	35

Table 2.14.1 – Typical parameters for synchrotron radiation at two complementary storage ring facilities. The two facilities are complementary in that one is optimized for soft x-rays (ALS) and the other is optimized for hard x-rays (APS). The Advanced Light Source (ALS) is operated by Lawrence Berkeley National Laboratory in California. The Advanced Photon Source (APS) is operated by Argonne National Laboratory in Illinois. Data taken from [50].

Electron beam energy lost to synchrotron radiation is replenished with a radio-frequency accelerator, which is a cavity with an axial electric field oscillating at the frequency of arrival of sequential electron bunches.

Table 2.14.1 lists for convenience synchrotron and bending magnet parameters, where γ is the 'gamma-factor' from special relativity. The ALS is optimised for 'soft' x-rays, that is, with a wavelength between 10 to 0.1nm, soft x-rays are weakly penetrating of matter and strongly absorbed by air. Contrasting with the ALS, the APS is optimised for 'hard' x-rays. Hard x-rays have a wavelength between 0.1 to 0.01nm and are highly penetrating of matter.

Characteristics of Bending Magnet Radiation

As an electron traverses a curved path, radiation is emitted tangentially as seen in figure 2.14.1, in a narrow radiation cone of half-width $\theta \sim 1/2\gamma$. For electrons circulating in a ring, the photon energies and wavelengths can be estimated using the Heisenberg uncertainty principle ΔE $\Delta\tau \geq h/4\pi$, where $\Delta\tau$ is the (rms) time duration during one detects radiation and ΔE is the uncertainty (rms spread) in observed photon energies.

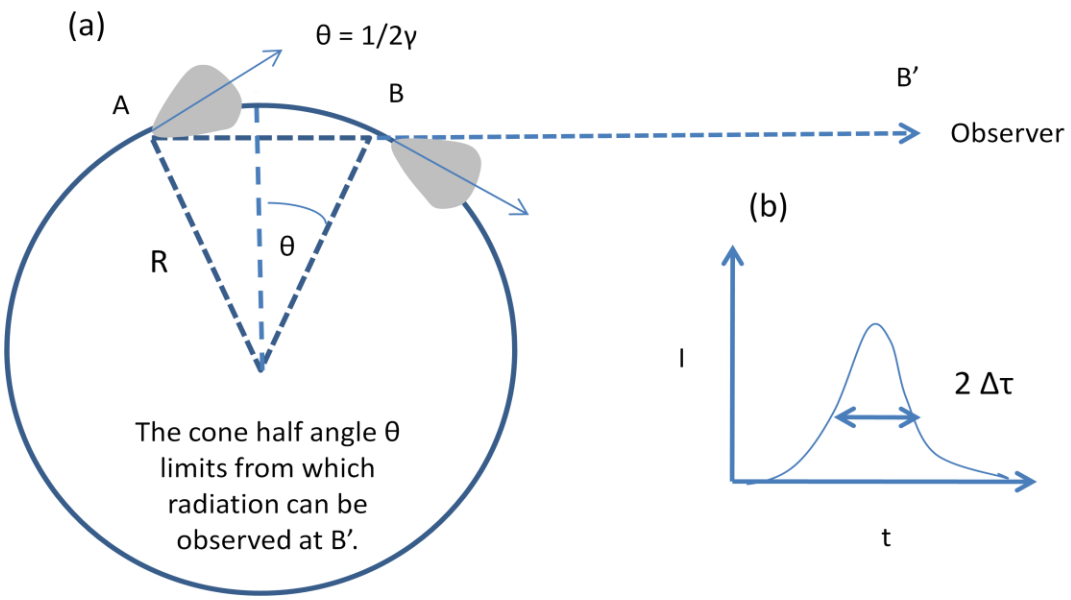

Figure 2.14.3 – (a) Schematic of bending magnet radiation illustrating the 'searchlight' effect, similar to that of a headlight of a train on a circular track. This is a general feature of radiation from highly relativistic electrons. The grey patches indicate the radiation cone of the electrons at point A and B having angular width θ. In (b) the pulse width of the observed radiation pulse is determined by the transit time differences between radiation and electrons at points A and B.

The detected pulse duration 2 Δτ emitted by a short bunch of electrons following a circular trajectory of radius R is estimated by considering the detector at point B′. As the electron bunch comes within an angle $\theta \sim 1/2\gamma$ of the horizon at point A, the detector is in the path of emitted photons. These photons will be detected at B′ after a transit time of the light τ_r. The radiation will continue to be detected until the electron bunch reaches point B, after point B the angular width of the radiation cone is not sufficient to be detected at B′. The electron bunch will reach point B after the transit time taken to traverse the bend, τ_e. The pulse width shown in fig 2.14.3(b) is the difference between these two transit times, i.e. the detector at B′ detects radiation after a time τ_r and stops detecting radiation at τ_e.

$$2\Delta\tau = \tau_e - \tau_r$$

$$2\Delta\tau = \frac{arc.length}{v} - \frac{radiation.path}{c}$$

$$2\Delta\tau \cong \frac{2R\theta}{v} - \frac{2R\sin\theta}{c} \qquad (2.14.1)$$

Noting that θ ~ 1/2γ and using a small angle approximation for sinθ and substituting v= β c, equation 2.14.1 becomes equation 2.14.2,

$$2\Delta\tau \cong \frac{R}{\gamma\beta c}\left(1-\beta\right) \qquad (2.14.2)$$

Noting that $\gamma = 1/\sqrt{1-\beta^2}$ and that as the velocity approaches c, β tends to unity, so 1 – β ≈ 1 / $2\gamma^2$. The expression for the duration of the radiation pulse becomes,

$$2\Delta\tau \cong \frac{R}{2c\gamma^3} \qquad (2.14.3)$$

This can be expressed as the anticipated photon energy spread using Heisenberg's uncertainty principle and the radius of curvature. The uncertainty principle is given by,

$$\Delta E.\Delta\tau \geq \frac{\hbar}{2} \qquad (2.14.4)$$

Combining 2.14.4 with 2.14.3, we get the rms spread of the photon energies given by equation 2.14.5.

$$\Delta E \geq \frac{2\hbar c\gamma^3}{R} \tag{2.14.5}$$

To better appreciate the photon energies implied by equation 2.14.5, the radius of curvature *R* can be replaced by an expression involving γ and the magnetic field. For electrons crossing a perpendicular magnetic field, as in a bend magnet, the relativistically correct form of the equation of motion can be written as equation 2.14.6.

$$\mathbf{F} = \frac{d\mathbf{p}}{dt} - e\mathbf{v} \times \mathbf{B} \tag{2.14.6}$$

Where $\mathbf{p} = \gamma m\mathbf{v}$, m is the electron rest mass and **B** is the magnetic flux density. For an electron in motion in a uniform magnetic field, the electron energy and γ are both constant, only the direction of **v** changes and not is magnitude. The equation of motion (2.14.6) can now be written as 2.14.7.

$$\gamma m \frac{d\mathbf{v}}{dt} = -e\mathbf{v} \times \mathbf{B} \tag{2.14.7}$$

Since the magnitude of **v** is constant, so is the magnitude of the acceleration, equal to evB / γ*m* in a plane perpendicular to **B**. This corresponds to motion along a circle with a centripetal acceleration v^2 / R, so the scalar equation of motion becomes,

$$\gamma m\left(-\frac{v^2}{R}\right) = -evB \tag{2.14.8}$$

Solving for the radius of curvature, we get,

$$R = \frac{\gamma m v}{eB} \tag{2.14.9}$$

Or for highly relativistic electrons 2.14.9 becomes,

$$R = \frac{\gamma m c}{eB} \tag{2.14.10}$$

Putting 2.14.10 into 2.14.5 the rms spread of photon energies from bend magnet radiation becomes,

$$\Delta E \geq \frac{2e\hbar B\gamma^2}{m} \tag{2.14.11}$$

Equation 2.14.11 depends on the electron charge to mass ratio e / m and the product B γ^2. If we substitute values for e, h and m, equation 2.14.11 indicates photon energies in the keV range (nanometer wavelengths) for typical values of γ and B found in modern storage rings. γ is several thousand and B is 1T or more.

Synchrotron Timing Structure

In the last section the bending magnet radiation produced by relativistic electrons which travel at almost the speed of light (0.9999c) was discussed. The electron beam in the storage ring is not a continuous beam, but is composed of bunches of electrons. The spacing of these bunches is set by the RF power used to restore power to electrons, to compensate the power lost by synchrotron radiation. The RF is fed to a microwave cavity operating in a mode with an axial electric field, synchronized so that slower electrons receive a small acceleration and faster electrons experience a small deceleration. Using this technique, a sequence of potential wells is

set up, which traps electrons into ‘buckets’ or groups that travel around the storage ring at almost the speed of light.

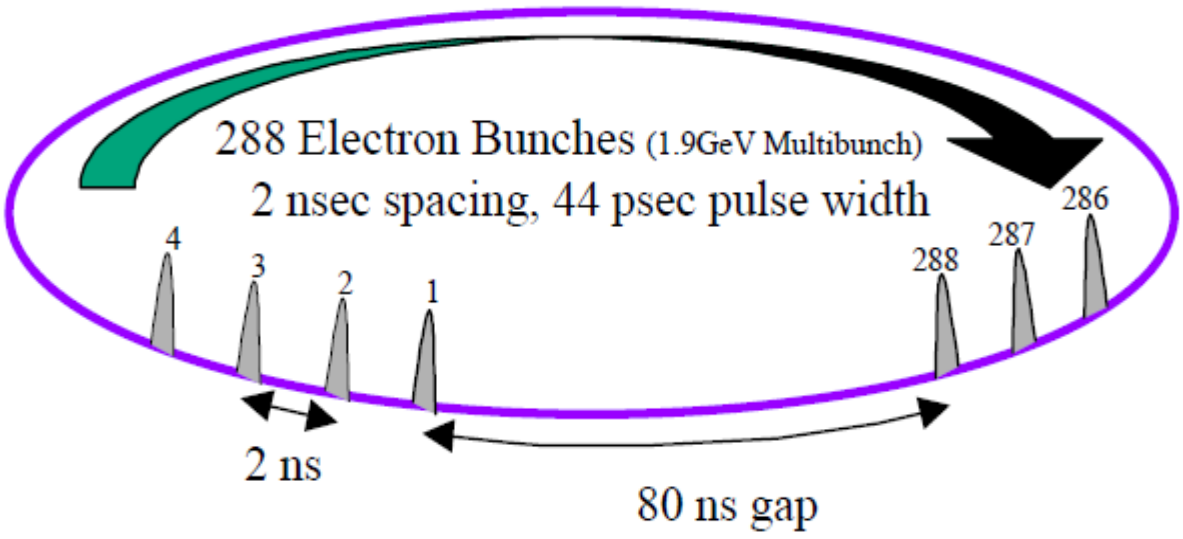

Figure 2.14.4 – Illustration showing the timing structure of the synchrotron storage ring. In table 2.14.1, the synchrotron RF frequency is 500MHz, this gives a 2 ns spacing between bunches, the temporal duration of the bunches is several tens of ps. The radiation pulsewidth that enters the beam line has the same duration as the electron pulse width. Figure reproduced from [51].

The bunch-to-bunch separation is equal to the RF wavelength. Figure 2.14.4 shows the ALS storage ring in multi-bunch operation, in total there are 328 buckets. By properly timing of the electron injection into the ring any sequence of filled buckets can be obtained. The ALS electron kinetic energy is 1.9GeV, ring circumference is 197 m and the beam current is 400mA. For the case illustrated in fig 2.14.4, the RF frequency is 500 MHz which produces a bunch-to-bunch separation of 60cm or 2ns temporally. Only 288 of the 328 buckets are filled for the given beam energy and bending magnet fields. Each of the electron bunches has a near Gaussian pulse shape with a nominal 40ps FWHM pulse duration. The current timing structure of synchrotrons

does not yield a temporal duration of more than several tens of picoseconds; this gives an upper limit to the allowed temporal resolution in time-resolved x-ray experiments. For static imaging experiments the time-resolution is not important.

2.15 Interaction of Polarised Photons with Matter

In the last section it was seen that modern synchrotron sources are capable of producing x-rays with a variety of properties from highly relativistic electrons using various insertion devices such as undulators, wigglers and bending magnets. This section describes the interaction of polarized x-ray photons with matter. In 1895 Rontgen (1845 - 1923) discovered more or less accidentally, what he soon called x-rays. Very shortly afterwards, his discovery became a worldwide sensation, unprecedented in the history of physics [52]. Experiments on x-rays were being run in almost every major laboratory in the world. A considerable amount of work was aimed at understanding the physical properties of these new rays and their interaction with matter. Now x-rays are known to be very high frequency radiation, beyond visible light and past the ultraviolet, having frequencies of the order $10^{16} – 10^{19}$ Hz.

In 1975 the theoretical work of Erskine and Stern showed that X-ray absorption could be used to determine the x-ray magnetic circular dichroism (XMCD) in transition metals when left and right-circularly polarized x-ray beams are used [53]. In 1985 Thole predicted a strong magnetic dichroism in the $M_{4,5}$ x-ray absorption spectra of the magnetic rare-earth materials, for which they calculated the temperature and polarization dependence [54]. A year later this XMCD effect was confirmed experimentally by Van der Laan at the Tb $M_{4,5}$ absorption edge of terbium

iron garnet [55]. The next year Schutz measured the K-edge absorption of iron with circularly polarized x-rays and found an asymmetry in absorption of about 10^{-4} [56]. A theoretical description for XMCD at the Fe K-edge was given by Ebert using a spin-polarised version of relativistic multiple scattering theory [57]. In 1990 Chen et al. observed a large magnetic dichroism at the $L_{2,3}$ edges of a Ni film [58]. Full multiplet calculations for 3d transition metal $L_{2,3}$ edges by Thole and van der Lann were confirmed by several measurements on transition metal oxides [59]. What was considered at first to be a rather exotic technique, XMCD has now developed into an important measurement technique. Whereas optical and MO spectra are often swamped by too many transitions between occupied and empty valence states, x-ray transitions have the advantage that the core state has a localized wave function which offers element specificity and site symmetry.

X-ray Absorption (Attenuation)

(This section follows [60])

The importance of x-ray absorption is evident from Rontgen's first experiments, shown by his famous photograph of the x-ray image of his wife's hand which shows the preferential absorption of bone over that of tissue. Empirically it was found that when x-rays encounter matter, the transmitted x-ray intensity $I = c\ \varepsilon_0\ E^2$ falls off exponentially with distance through the material. This fact is easily derived if we assume the material has a characteristic length λ_z over which the transmitted intensity falls to 1 / e. The quantity $\mu_z = 1 / \lambda_z$ with dimensions of inverse length is called the linear x-ray absorption coefficient and enters into equation 2.15.1 to describe the transmitted intensity.

$$I = I_0 \exp(-\mu_z z) \tag{2.15.1}$$

The incident intensity at z = 0 is I_0. The x-ray cross-section σ^{abs} is defined as the number of photons absorbed per atom divided by the number of incident photons per unit area. The number of photons absorbed in a thin sheet *dz* is *I(z)dz* and the number incident on the material is *I(z)* ρ_a *dz*, where ρ_a is the atomic number density (atoms / volume).

$$\mu_z = \rho_a \sigma^{abs} = \frac{N_A}{A} \rho_m \sigma^{abs} \tag{2.15.2}$$

Equation 2.15.2 relates the linear absorption coefficient and the absorption cross section. Where ρ_m is the mass density (Kg / m^3), N_A is Avogadro's number, 6.023 x 10^{23} atoms / mole and A is the atomic mass number. The quantities ρ_m, A and ρ_A are listed for the *3d* transition metals in table 2.15.1.

Element	ρ_m (kg / m^3)	A (g / mol)	P_a (atoms / nm^3)	V_a (cubic angstrom)
Fe (bcc)	7874	55.845	84.9	11.8
Co (hcp)	8900	58.933	90.9	11.0
Ni (fcc)	8908	58.693	91.4	10.9

Table 2.15.1 – Bulk properties of 3d metals Fe, Ni and Co. Listed are the mass density ρ_m at room temperature, the atomic mass number A, the atomic number density ρ_a and the atomic volume V_a.

X-ray Magnetic Circular Dichroism (XMCD)

Dichroism has two related but distinct meanings in optics. A dichroic material is either one which causes visible light to be split up into distinct beams of different wavelengths, such as a dichroic filter (not to be confused with dispersion), *or* the preferential absorption of light owing

to its polarization state. The term dichroism is used more generally to describe the polarization dependent absorption of light. The origin of dichroism is anisotropies in the charge or spin distribution in the material. The latter case is referred to as magnetic dichroism and can be of linear or circular polarization type. Here we briefly discuss the principles of magnetic dichroism in the x-ray region and X-Ray Magnetic Circular Dichroism (XMCD). X-ray absorption spectroscopy (XAS) utilizes the energy dependent absorption of x-rays to obtain information about the elemental composition of the sample; in addition to this, the XAS of different circular polarizations is central to the XMCD spectrum.

In the x-ray absorption process core electrons are excited into empty states above the Fermi energy and thereby probe the electronic and magnetic properties of the empty valence states. In the following we are concerned with the spectra of the magnetic 3d transition metal elements Fe, Co and Ni. Their magnetic properties are largely determined by the 3d valence electrons. Since x-ray absorption spectra are governed by dipole selection rules, the d-shell properties are best probed by L-edge absorption studies. This is a transition from a 2p core electron to a valence 3d transition. The name of the 'edge' depends upon the core electron which is excited, the principal quantum number n = 1, 2, 3… corresponds to the K, L and M edges respectively. For instance, excitation of the 1s electron occurs at the K-edge, while excitation of a 2s or 2p electron occurs at the L-edge. The L-edge x-ray absorption spectra of the transition metals and oxides are dominated by two main peaks separated by about 15 eV, called the L_3 and L_2 peaks respectively, as shown in Fig. 2.15.1.

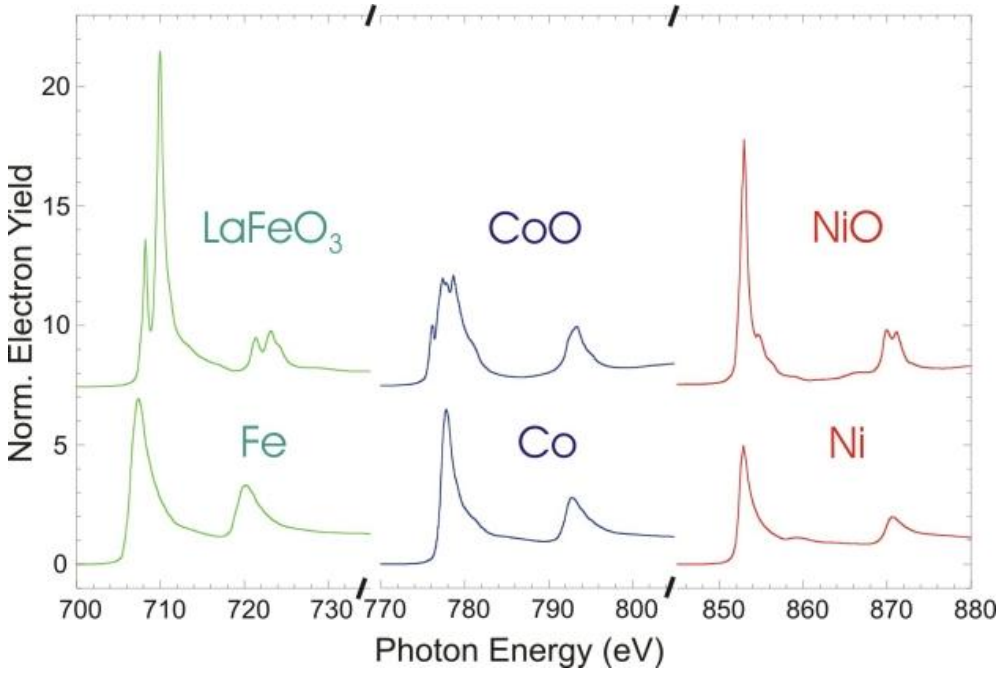

Figure 2.15.1 – X-ray absorption spectra (XAS) for the *3d* transition metals Fe, Ni and Co at the L-edge for a given photon polarization. The lower curves are for the pure elements, the upper curves are for the metal oxides. The two main structures in the spectra are the L_3 edge and the higher energy L_2 edge. The L_3 edge for Fe, Co and Ni is 707, 778 and 853eV respectively. Image taken from [61]

The two main peaks in the XAS spectra of figure 2.15.1 arise from the spin-orbit interaction of the 2p core shell and the total intensity of the peaks is proportional to the number of empty 3d valence states. The metal spectra mainly show two broad peaks, reflecting the width of the empty d-bands. The oxide spectra exhibit considerable fine structure, called multiplet structure. The elemental transition metals are ferromagnetic and their magnetic properties are best studied with X-Ray Magnetic Circular Dichroism (XMCD) spectroscopy, while the oxides are usually antiferromagnetic and are studied with X-Ray Magnetic Linear Dichroism (XMLD) spectroscopy. For magnetic transitions metals the d shell has a spin moment which is given by the imbalance of spin-up and spin-down electrons at the Fermi level. In order to measure the difference in the number of d holes with up and down spin, we need to make the x-ray absorption

process spin dependent. This is done by use of right or left circularly polarized photons which transfer their angular momentum to the excited photoelectron.

Two-step model for the XMCD Intensity

XMCD can be described by a two step model. In the first x-ray absorption step, conservation of angular momentum requires a transfer of the angular momentum of the incident circularly polarized x-rays to the excited photoelectrons. If the photoelectron is excited from a spin-orbit split level, e.g., the $2p_{3/2}$ (L_3 edge), the angular momentum of the photon can be transferred to the spin through the spin-orbit coupling and the resulting photoelectron(s) are spin polarized. The spin polarization is opposite for incident x-rays with positive ($+\hbar$) and negative ($-\hbar$) spin. Also since the $2p_{3/2}$ (L_3) and $2p_{1/2}$ (L_2) levels have opposite spin-orbit coupling ($l + s$ and $l - s$ respectively), the spin polarization will be opposite at the two edges. The photoelectron spin quantization axis is identical to that of the photon spin, i.e., it is parallel or antiparallel to the x-ray propagation direction.

In the second step, the exchange split valence shell with a different spin-up and spin-down population acts as a 'detector' for spin of the excited photoelectrons. Since spin flips are forbidden in electric dipole transitions, spin flips are not allowed during a transition ($\Delta\mathbf{S} = 0$) so spin-up (spin-down) photoelectrons from the p core shell can only be excited into spin-up (spin-down) d hole states. Hence the spin-split valence shell acts as a 'detector' for the spin of the excited photoelectron and the transition intensity is simply proportional to the number of empty d states of a given spin. The quantization axis of the valence shell "detector" is given by the magnetization direction. The L_3 and L_2 resonance intensities and their differences for parallel and

anti-parallel orientation of photon spin and magnetization directions are quantitatively related by sum rules to the number of d holes and the size of the spin and orbital magnetic moments.

In the two-step model of XMCD the first step consists of circularly polarized x-rays generating photoelectrons with a spin and/or orbital momentum from a localized inner atomic shell, second, the 3d shell serves as a detector of the spin or orbital momentum of the photoelectron. For maximum effect, the photon spin needs to be aligned with the magnetization direction.

In figure 2.15.2 (a) the L_3 edge transition is depicted from the core 2p state to the valence 3d band, circularly polarized light (σ^+, σ^-) is sensitive to the spin type and a given helicity is only able to excite a spin up (down) core electron into a spin up (down) valence state. The vertical axis is energy and the horizontal axis is the density-of-states (DOS).

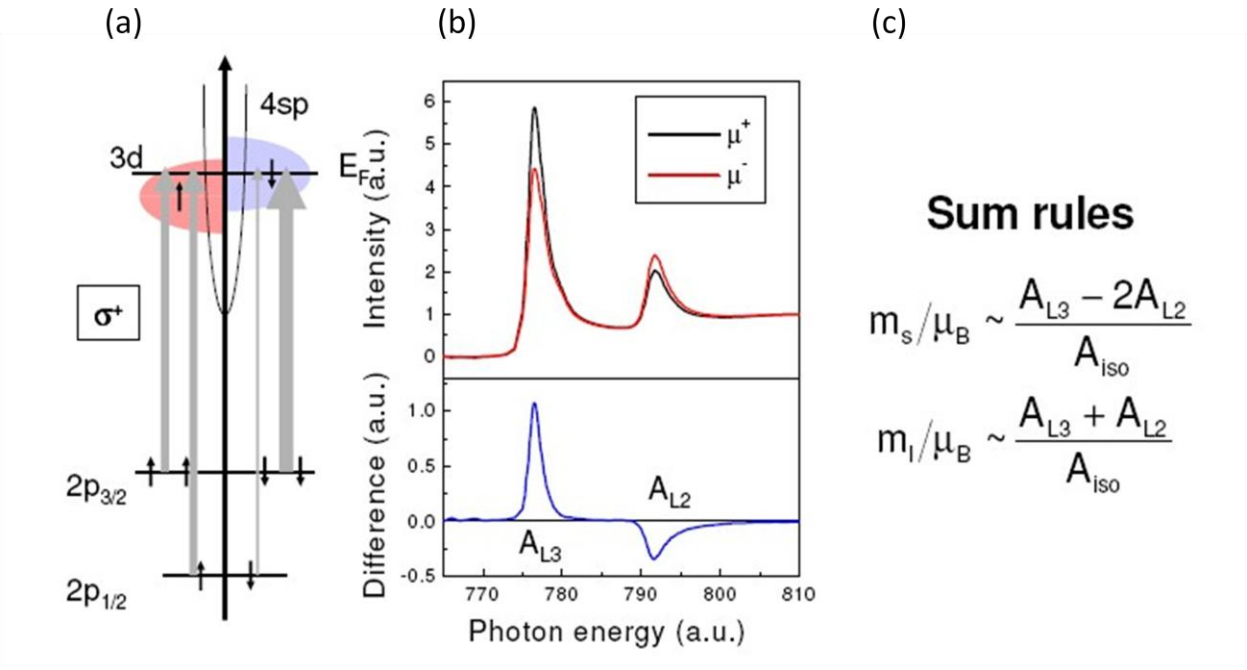

Figure 2.15.2 – Figure showing (a) a schematic of density-of-states (DOS) (horizontal axis) verses energy for the L_3 absorption edge transitions, (b) the XAS spectra for two opposite orientations of the sample magnetisation (top) and the difference or XMCD spectra. Lastly, (c) shows how the 'sum rules' realte the areas under the ZMCD spectra to the ratio of the orbital and spin moments of a ferromagnet. Figure taken from [62]

The net sample magnetization is given by the net spin polarization at the Fermi energy. In figure 2.15.2 (b) is the XAS and XMCD spectra for Co is shown, having an L_3 edge resonance of 778eV. The XAS has been taken with the same x-ray polarization and sample moments μ^+ and μ^- is reversed by an external field. The μ^+ (top) curve shows a larger resonant absorption than μ^-, illustrating the effect the relative absorption is dependent on the orientation of the local magnetic moment with the incident photon angular momentum. The bottom curve of 2.15.2 (b) is the difference of the μ^+ and μ^- curves or the XMCD spectra, the net area under the curve denoted by A_{L3} and A_{L2} is related only to the magnetic dichroism. The XMCD spectrum is defined as the

difference of two XAS spectra taken with oppositely circularly polarized light. The sum rules in (c) relate the convergent area of the XMCD spectra to the spin (m_s) and orbital (m_l) moments of the material, μ_B is the Bohr magneton.

The size of the dichroism depends on three important factors: the degree of the circular photon polarization, P_{circ}, the expectation value of the magnetic moment of the 3d shell $\langle \mathbf{m} \rangle$ and the angle between the photon angular momentum $\mathbf{L}_{Ph}$ and the magnetic moment **m** as seen in equation 2.15.1

$$I_{XMCD} \propto P_{circ} \mathbf{m} \bullet \mathbf{L}_{Ph} \propto P_{circ} \langle m \rangle \cos\theta \tag{2.15.1}$$

For the maximum XMCD effect the direction of magnetization **M** of the sample and the photon spin angular momentum $\mathbf{L}_{pho}$ are chosen to be collinear. An equivalent method is to fix the photon polarization and reverse the magnetization using an external field, in practice this is more feasible since altering the polarisation can also change the sample illumination and change the signal size. In terms of the XAS signal the XMCD spectrum is defined as,

$$I_{XMCD} = XAS_{H+} - XAS_{H-} \tag{2.15.2}$$

A more advanced discussion of XMCD can be found in the reference material [60].

By tuning the polarization of the x-ray photons, magnetic sensitivity to the spin orientation can be achieved, being sensitive to either ferromagnetic or antiferromagnet spin alignment. Similarly by tuning the x-ray energy to a specific material absorption edge, elemental specificity can be achieved. This gives the opportunity to study a composite sample literally element by element. Also, due to the inherently short wavelength of soft x-rays (~ 1nm) the

spatial resolution is high for microscopy purposes, spatial resolutions down to 20nm are approaching fundamental magnetic length scales such as the exchange length. It is the available element specificity, magnetic specificity and high spatial resolution that makes x-ray methods a popular choice to study magnetic structures on the nanoscale. One drawback of the timing structure of synchrotrons is that the current temporal resolution is not as high as with contemporary pulsed optical laser sources. Future developments aim to improve synchrotron temporal resolution.

2.16 Summary

In this chapter the background theory of the thesis and magnetism has been presented. Initially, descriptions of different magnetic states in matter, including diamagnetism, paramagnetism and the ordered magnetic states of ferro, anti-ferro and ferrimagnetism were described. Then magnetic moments, angular momentum and the precession of atomic magnetic moments were described, leading up to the Landau-Lifshitz equation. The Landua-Liftshitz Gilbert equation of motion is used to describe precessional dynamics of the magnetisation and is of similar importance in magnetism as the Schrödinger equation is in non-relativistic quantum mechanics. The magneto-optical Kerr effect responsible for the measurement of the dynamical magnetisation in pump-probe experiments was described phenomenologically, leading up to discussion of spin wave dispersion and their behaviour in periodic magnetic structures. The spin wave dispersion describes the propagation characteristic of spin waves in a magnetic material and is key to understanding the behaviour of spin waves in novel magnetic structures. Periodic magnetic structures allow tailoring of artificial magnetic properties such as tunable bandgaps and selective propagation of spin waves. A description of ultrafast magnetisation dynamics

following absorption of an ultrafast optical pulse was described, finally followed by synchrotron radiation and X-ray magnetic circular-dichroism.

Chapter 3: Experimental Setup of the Time-resolved Kerr microscope and Time-Resolved optically-pumped Scanning optical microscope

3.1 Introduction

In this chapter the experimental setup of the time-resolved Kerr microscope and the time-resolved optically pumped scanning optical microscope is discussed. The development of the time-resolved optically pumped scanning optical microscope is also described. A description of the Tsunami laser system including the Millennia Pro pump laser is given after the initial description of the time-resolved Kerr microscope. The Tsunami laser system is used for both the Kerr and the optical microscope setups, providing pump and/or probe light to both experimental techniques.

3.2 Experimental setup of the Time-Resolved Kerr microscope

The setup of the time-resolved scanning Kerr microscope is shown in figure 3.2.1. A tuneable Tsunami oscillator outputs 100fs optical pulses at 80 MHz with a central wavelength of 800nm. Using a beta barium borate doubling crystal these pulses undergo second harmonic generation (SHG) and become frequency doubled to 400 nm. After passing through a delay line, which mechanically adjusts the arrival of these 'probe' pulses, the blue beam passes a communal beam splitter common to both the field-pumped Kerr microscope and the optically pumped microscope. The blue probe beam enters the field-pumped microscope. The periscope assembly directs the beam through a polariser to a beam splitter from which it then enters the microscope

objective. The same objective then collects the focused light from the sample which passes back to the beam splitter and to a balanced optical detector. The objective used has a numerical aperture (NA) of 0.75, which in the diffraction limited case yields a spot size of order λ. The light entering the objective is linearly polarised and in this geometry is sensitive to the out-of-plane component of magnetisation, the reflectivity changes and stroboscopic changes are measured by the detector mounted at the top of the probe station.

Scanning is achieved due to the objective being mounted on a scanning xyz stage allowing images to be taken and correct focusing to be achieved. Figure 3.2.2 is complete drawing of the Kerr microscope and the aforementioned optics can be seen. The temporal resolution is achieved in the experiment by the mechanical delay line and the inherent temporal duration of the 100 fs pulse. Using lock-in detection only dynamic changes of the out-of-plane magnetisation are measured. Kerr imaging is not sensitive to the absolute value of the magnetisation.

Figure 3.2.1(a) schematically shows the electrical plumbing of the Kerr microscope and the optical path from the Ti:sapphire oscillator to the probe objective and finally the optical bridge detector. The master clock synchronises the 80 MHz optical pulses with the RF generator so both outputs are phase locked. A 3 KHz square wave modulates the exciting pulse train and acts as the lock-in amplifier's reference frequency. This square wave acts as an electrical 'chopper'. This is done to impart a characteristic frequency of 3 KHz to changes in the sample which the lock-in amplifier can detect and measure. Figure 3.2.1(b) shows the layout of the optical table, showing the Millennia seed laser, Tsunami and the location of the optically and field-pumped microscope.

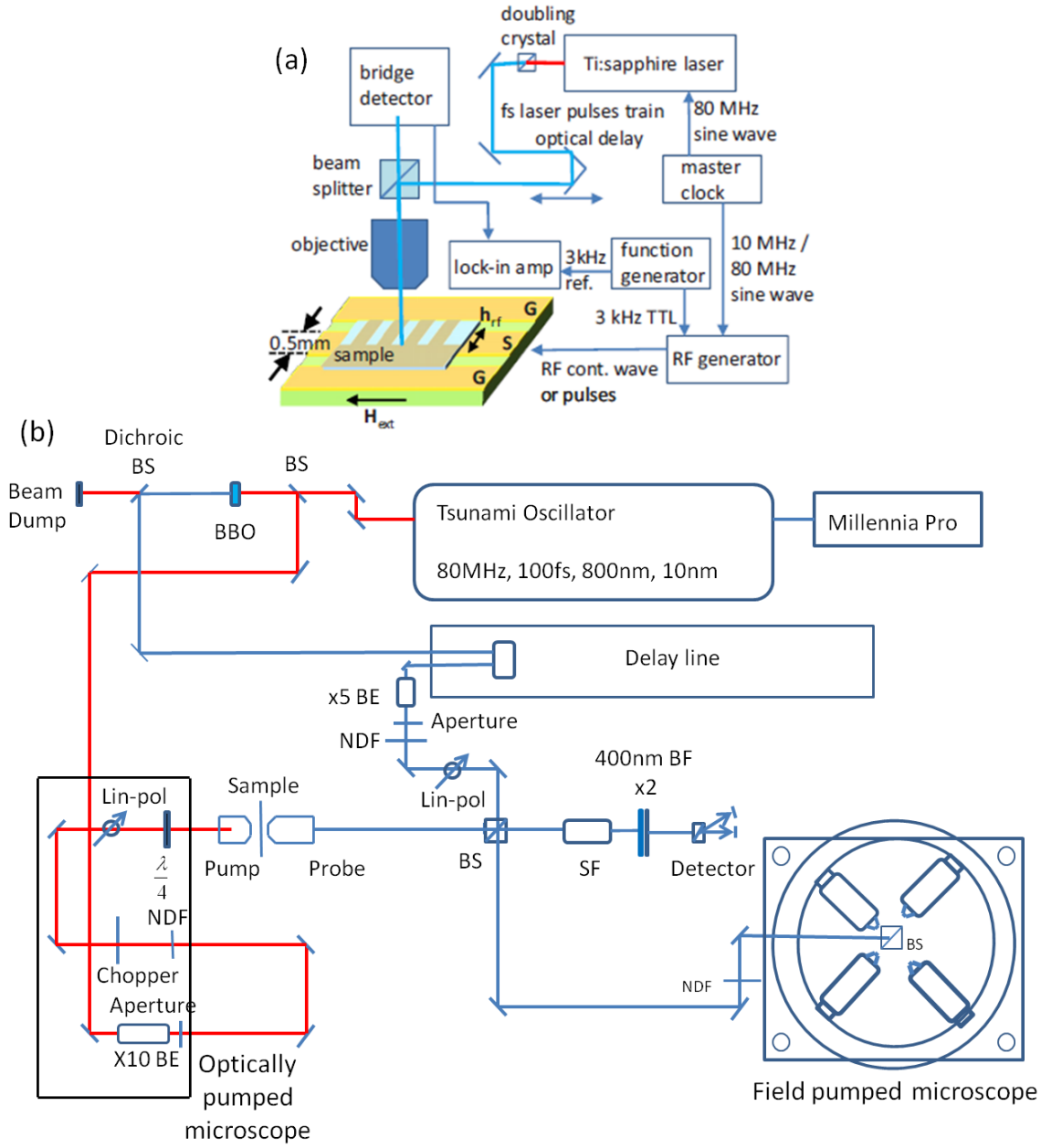

Figure 3.2.1 – The optical table is used for two independent experiments. (a) Shows the TRSKM electrical plumbing schematically integrated into the optical probe path. Panel (b) shows the layout of the experiments as they appear on the optical table itself, the dark rectangle around the optically-pumped microscope is a shed built around the microscope to prevent scattered IR pump light flooding the detector. BS = beam splitter, SF = spatial filter, NDF = neutral density filter and BF = bandpass filter. Figure 3.2.1 (a) is taken from [63]

The optically-pumped microscope uses both beams for an 800 nm pump and 400 nm probe. The field-pumped microscope uses the 400 nm probe beam only. Its 'pump' methods are electrical and can be either pulsed excitation utilising a Picosecond pulse labs 3600 pulse generator or a continuous wave (CW) excitation using a microwave generator, which drives the magnetisation at a preset frequency using a GHz sine wave. Using pulsed excitation, the Picosecond pulse labs 3600 locks to a sine wave input and delivers pulses with a temporal duration of 70 ps, 6V amplitude and at a rep rate of 80 MHz. A total time delay of 12.5 ns can be achieved before the new field pulse arrives. A solitary retro reflector is mounted on the delay line giving a total of 4 ns of delay, for longer-lived signals electronic 'phase' delay can be used to delay the field pulses giving up to 12.5 ns total delay. In principle, a second retro reflector can be mounted onto the delay line in a double retro reflector configuration; this method would provide a total of 8 ns temporal delay. This method was not used in this study.

Figure 3.2.2 is a Solidworks drawing of the Kerr microscope, drawn by Dr. Yat-Yin Au during the design phase of the microscope. The periscope assembly where the 400 nm probe beam enters can be seen on the left hand side, then passing the polariser and beamsplitter to enter the probe objective. The Magnet ring (bottom) and balanced optical detector (top) can clearly be seen. The sample itself sits beneath the objective on a coplanar waveguide that feeds to either the pulse generator or CW generator via SMA cable. The sample is surrounded by the 4 pole pieces of the quadrupole magnet geometry which can generate a maximum field of 1 KOe in any direction in the plane of the sample.

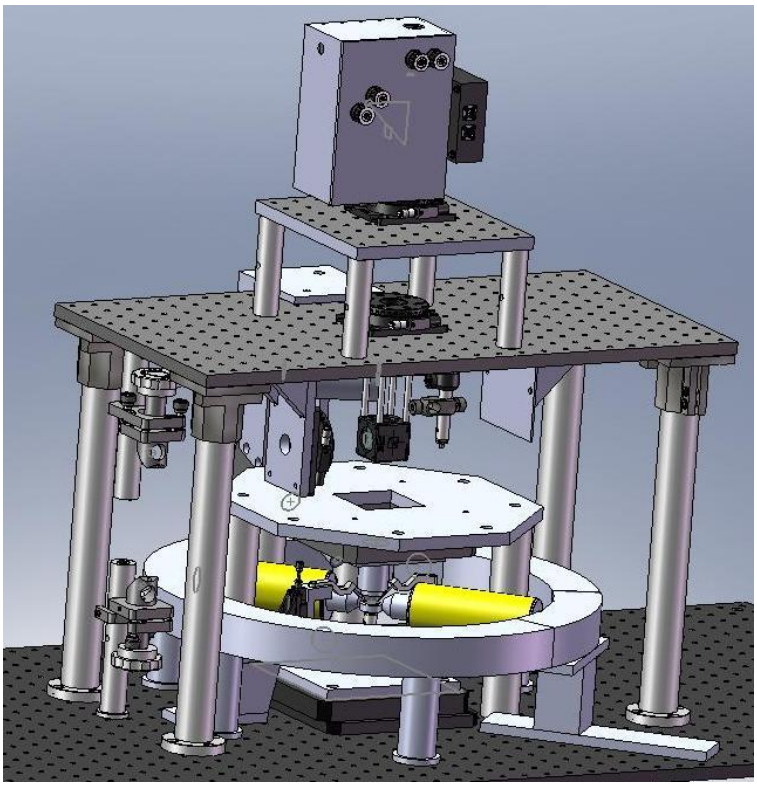

Figure 3.2.2 – Drawing in Solidworks showing the Kerr microscope (TRSKM) drawn by Dr. Yat-Yin Au

A schematic of the optical bridge detector is shown in figure 3.2.3. The optical detector consists of a polarising beam splitter and two photodiodes, conventionally labelled ‘A’ and ‘B’. Strictly, the photodiodes lie outside the detector, connected by optical fibre couplers, inside the detector itself are focusing lenses to direct the individual outputs to a commercial Thorlabs PDB210A balanced detector. No operational detail is lost in pretending the photodiodes are inside the detector. The polarising beamsplitter splits light according to its polarisation, splitting the incident beam into two beams of orthogonal polarisation. The polarising beam splitter can be rotated in a plane normal to the incident beam; by rotating the polarising beam splitter the amount of light on each photodiode is varied, when the light on each diode is the same the bridge is said to be ‘nulled’ and the ‘A’ and ‘B’ photodiode voltages are equal and the ‘A-B’ voltage is zero.

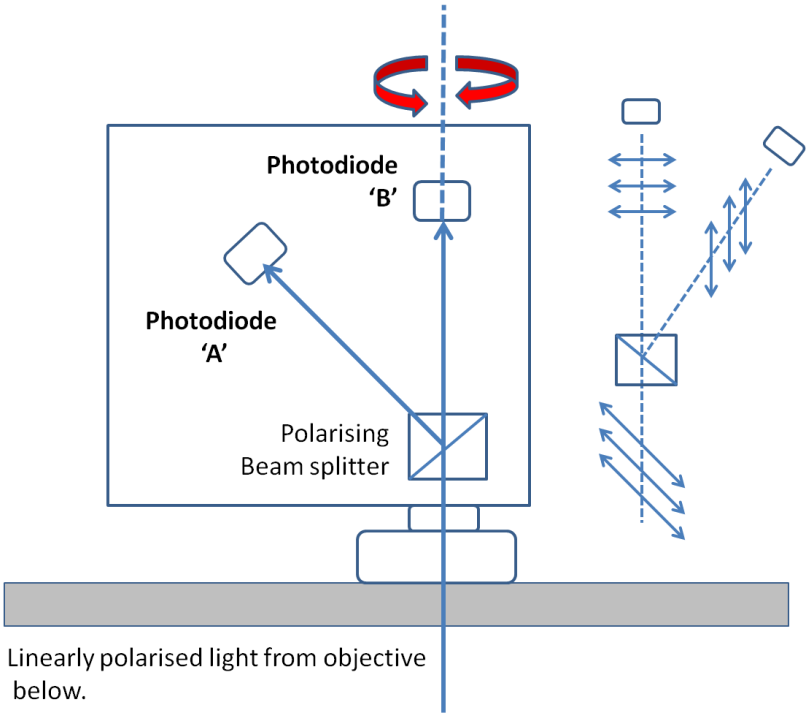

Figure 3.2.3 – Internal schematic of the detector used to measure the Kerr rotation from the sample. The detector can be rotated about a vertical axis to 'null' the bridge. The graphic right of the detector illustrates the polarizing beam splitter splitting an arbitrary linear polarization being split into two orthogonal components.

Throughout the course of measurements any rotation of the polarisation from this 'balanced' condition will lead to a non-zero net voltage from the detector that is measured and recorded. The diode voltages themselves, in addition to the 'difference' voltage, are also recorded. This allows reflectivity images of the sample to be recorded. For dynamic measurements the 'A-B' rotation signal is small and is measured using lock-in detection, this signal is then referred to as an 'AC' signal. For larger signals that can be measured without using lock-in detection, the signal is called a 'DC' signal.

The Tsunami laser system

(Taken from the Newport Spectra Suite user manuals [64], [65])

The Tsunami laser system consists of a Millennia Pro CW pump laser and a Tsunami laser cavity. The Millennia Pro supplies the energy and powers the Tsunami laser system with a 15 W 532 nm (green) pump beam and the Tsunami system then generates the pulsed femtosecond (fs) optical output from inside its folded cavity.

The Millennia Pro uses an X-cavity design to minimise its footprint on the optical table. Inside, the Millennia Pro consists of an optical resonator (neodymium yttrium vanadate laser crystal, Nd:YVO_4 or 'vanadate' for short), guiding optics directing light from the diode pump light and the lithium triborate (LBO) frequency-doubling crystal. The vanadate gain medium is end-pumped by two fibre-coupled modules. In the X-cavity, the near-infrared (NIR) 1064 nm beam from the vanadate crystal is focused into the lithium triborate (LBO) crystal which undergoes second-harmonic generation (SHG) and generates the frequency doubled 532 nm output beam. The LBO crystal is non-critically phase matched and kept in an oven designed to keep the crystal at an optimum SHG temperature. The cavity end mirror in the frequency-doubling limb of the cavity has high-reflective coatings for both near-infrared and green wavelengths, this utilises back reflected near-infrared to undergo SHG upon a second pass of the LBO crystal. The frequency-doubled green beam is able to exit the cavity via a dichroic output coupler to the Tsunami.

Contained inside the Tsunami is the Ti:sapphire rod and the resonator cavity optics. Such optics include the pump beam mirrors, rod focusing mirrors, an output coupler (OC), a high reflector (HR), beam folding mirrors, the dispersion control elements and the tuning control

elements. The Tsunami laser system can be operated in a picosecond (ps) or femtosecond (fs) configuration. In the fs configured system intracavity prisms are used for dispersion control, whereas a Gires-Tournois Interferometer (GTI) performs the dispersion control in a ps configured system. Also, operating in fs mode, a slit is used for wavelength selection in the output beam compared to a birefringent filter for ps mode. Here the fs configuration is always used. The Tsunami is also accompanied by a Lok-to-Clock control unit that allows phase locking of the output pulses to either the internal 80 MHz Tsunami source or an external source, such as a RF synthesizer clock. The latter is done for operation of the field-pumped microscope.

Brief aspects of Laser Theory

Light sources such as incandescent bulbs radiate a broad spectrum of blackbody radiation, given by the Planck distribution. The amount and frequency of the light emitted by blackbody sources is determined entirely by the temperature of the emitting material, at room temperature most of the radiative power is in the infrared (*circa* 10 μm), as the temperature increases the emitted light moves to higher frequencies as the molecular vibrational motion increases. The light emitted by lasers is characteristically different to light emitted by such sources, rather than originate from vibrational or thermal motion, laser light arises from quantum mechanical electron transitions from lower to higher excited states. Laser light possesses a well defined phase, coherence and wavelength relationship between its photons, unlike 'thermal' sources which are broad, phase and coherence relationships random, lasers generate light with identical phase and high coherence, the resulting output beam is singularly directional, (usually) monochromatic and coherent. Radiant absorption and emission take place between bound electronic states; transitions take place when an electron moves from one quantum state to

another, this happens when an electron absorbs or emits energy, usually in the form of an external photon.

Spontaneous and Stimulated emission

Consider a transition from a lower level E_1 to a higher level E_2, this transition can only take place if the incident photon energy is equal to this energy difference, given by equation 3.2.1.

$$E_2 - E_1 = \hbar\omega \tag{3.2.1}$$

Where $\hbar$ is the rationalised Planck constant and ω is the frequency of light. Likewise, when an electron falls into a lower energy state it will emit a photon equal to the energy difference of the initial and final states. An electron in an excited state may decay randomly after a given time period, this is called spontaneous decay and will emit a photon with a frequency given by equation 3.2.1. An excited electron can also be 'prompted' to decay by interacting with a passing photon of energy $E_2 - E_1$, causing the emission of a second photon.

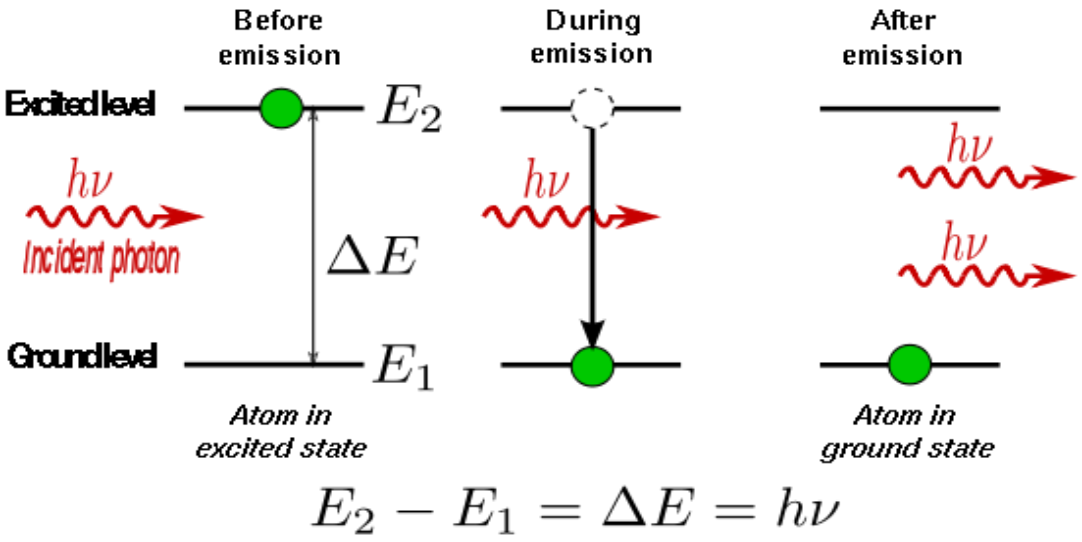

Figure 3.2.4 – Schematic showing the ground and excited state for the case of stimulated emission. An incident photon of the correct energy perturbs an excited electron state, stimulating it to fall to a lower energy state; simultaneously an identical photon to the first is emitted. Image taken from [66].

This is called stimulated emission, as shown in figure 3.2.4; the second stimulated emission photon has an identical phase, frequency and direction to the first. Contrasting with stimulated emission, spontaneously emitted photons have no directional or phase relationships between them.

Population Inversion

A laser is designed to utilize and take advantage of absorption and both spontaneous and stimulated emission phenomena, using them to create conditions favorable for the amplification of light. The net absorption of the gain medium is the difference between the rates of emission and absorption for a particular frequency. It can be shown that the rate of excitation from E_1 to E_2 is proportional to both the number of electrons in the lower level N_1 and the transition probability. Similarly, the rate of stimulated emission is proportional to the population of the

excited level N_2 and its transition probability. The transition probability depends on the number of incident photons and the 'cross-section' of the transition. The absorption coefficient depends on the difference of the populations of the two states N_1 and N_2 and the number of incident photons.

For a material in thermal equilibrium the Boltzmann distribution describes the populations of the ground and excited states. Since the rate of absorption is always greater than that of emission, the absorption coefficient is always positive. If for a two-level system enough photons of the correct frequency are added, the populations can be changed until $N_1 = N_2$ and the absorption coefficient becomes zero as the emission and absorption rates become equal. For a two-level system it is impossible to drive N_2 to be greater than N_1 because every excited state is matched by a state in the ground state.

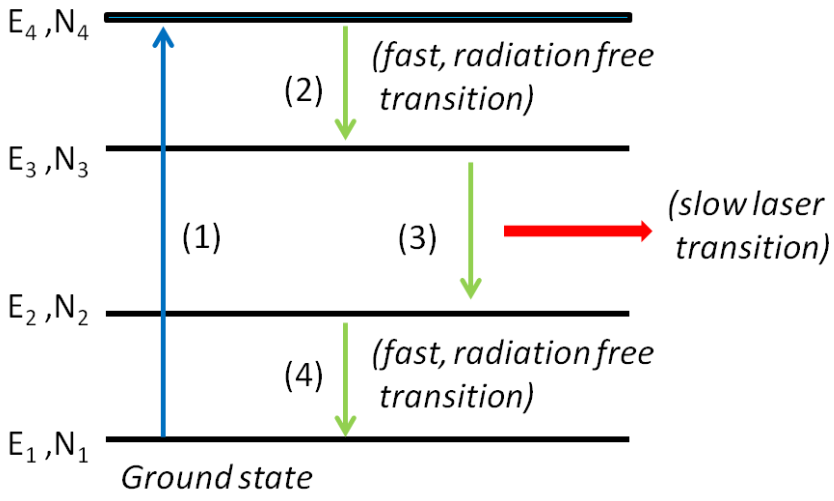

Figure 3.2.5 – A four-level transition scheme with energies E_1, E_2, E_3, E_4 and state populations N_1, N_2, N_3 and N_4 respectively. (1) denotes the pumping transition, (2) denotes a fast non-radiative transition and (3) denotes a fast non-radiative transition. Fast is relative to the lifetime of the metastable transition state (3).

A model four-level system is shown in figure 3.2.5. An incident photon of sufficient frequency excites or 'pumps' an electron from E_1 to E_4, denoted by the pump transition (1) in figure 3.2.5. If the transition probability from E_4 to E_3 is greater than the transition probability from E_4 to E_1 and the excited state lifetime of E_4 is very small, the excited state E_4 will decay to E_3 almost immediately, shown by (2) in figure 3.2.5. Provided E_3 is metastable, meaning the excited state will live for a fairly long time compared to shorter lived states, the population N_3 will start to rise and its population will grow as excited states decay and cascade from above. After some time, the metastable state E_3 will decay to E_2 and in doing so will emit a lasing photon, denoted by (3). Finally for the excited states at E_2 to return to the groundstate E_1, the energy state must be unstable (4), by having a shorter lifetime than state E_3 a population inversion will exist between the metastable state E_3 and the lower energy state E_2. Under these conditions the absorption coefficient is negative and light is amplified as it propagates, in what is called the 'active' medium. The greater the population inversion that can be achieved the greater the gain.

The Millennia Resonant Optical cavity

To sustain lasing action, the gain medium must be in a resonant optical cavity. A resonant optical cavity can be formed between two mirrors providing feedback to the active medium, this is caused by photons emitted parallel to the cavity axis which become back-reflected into the gain medium which interact with excited energy states causing stimulated emission to occur. Stimulated emission produces secondary photons in this process, with identical energy, phase and direction. One photon becomes two, two photons becomes four, four become eight and so on, this process continues geometrically until equilibrium is reached between the excitation and radiative transition processes.

Power	15 W
Wavelength	532 nm
Spatial mode	Tem_{00}
Beam diameter at $1/e^2$ points	2.3 mm ± 10%
Beam divergence, full angle	< 0.5 mrad ± 10%
Polarisation	> 100:1 vertical
Power stability	± 1%
Beam pointing stability	≤ 2 μrad/ ^{0}C
Noise	< 0.04% rms

Table 3.2.1 – Millennia Pro 10s J specifications from the Millennia Pro S-series User manual.

The Millennia Pro laser head uses an X-cavity design resonator as shown in figure 3.2.6. In this design fibre-coupled light at 1064 nm enters the resonator and is used to end pump the Nd:YVO_4 or vanadate 'rod'. The vanadate crystal is the driving engine of the Millennia laser, it absorbs the diode laser light and emits its own light at the same wavelength, which is resonated and confined in the Millennia cavity. The vanadate crystal produces a very high gain, being able to produce close to 20 W of near diffraction-limited infrared power and converts more than 50% of the light from the lasing diode.

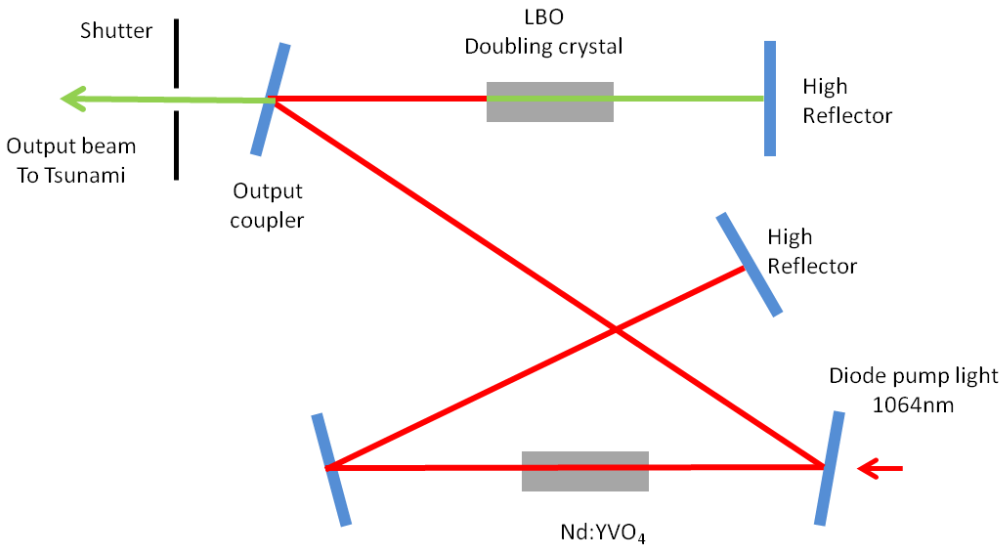

Figure 3.2.6 – Schematic showing the optical design of the Millennia Pro laser head.

Frequency doubling

The high output power from the vanadate medium is turned into visible light via second-harmonic generation or frequency doubling in a non-linear medium. SHG is achieved using a 90 deg, non-critically phase matched and temperature tuned LBO crystal. Although LBO has a lower non-linear coefficient than other materials, it has several advantages: the non-critical phase matching means that the fundamental and second harmonic beams are collinear, simplifying alignment, also there is no spatial 'walk-off' of both the fundamental and second harmonic beams which helps to preserve the mode quality, lastly the crystal's SHG performance is easily optimised by changing the temperature of the crystal with no need to realign the laser cavity itself. The second harmonic power is given by,

$$P_{2\omega} \propto \frac{d^2{}_{eff} P^2{}_{\omega} l^2[\varphi]}{A} \qquad (3.2.2)$$

Where d_{eff} is the effective non-linear coefficient, P_{ω} is the power of the first harmonic, l is the effective crystal length, A is the cross-sectional area of the optical beam in the crystal and φ is the phase-matching factor. From equation 3.2.2, it can be seen that the power of the second-harmonic depends on the square of the input power, very high conversion efficiencies can be achieved by maximizing the intensity falling on the LBO medium.

Ti: sapphire Laser Theory

The Tsunami laser head is the Ti:sapphire rod and the resonator cavity optics. Such optics include the pump beam mirrors, rod focusing mirrors, an output coupler (OC), a high reflector (HR), beam folding mirrors, the dispersion control elements and the tuning control elements. The laser action of Ti:sapphire is generated by the Ti^{3+} titanium ion. Ti:sapphire is a crystalline material produced by introducing Ti_2O_3 into a melt of Al_2O_3. A boule of material is grown from this melt where Ti^{3+} ions are substituted for a small percentage of the Al^{3+} ions. Resultantly, the electronic ground state of the Ti^{3+} ion is split into a pair of vibrationally broadened levels.

Absorption processes occur over a broad range of wavelengths from 400 to 600 nm as shown in figure 3.2.7. Fluorescence transitions take place from the lower vibrational levels of the excited state to the upper vibrational levels of the ground state, the resulting emission spectra is also shown in figure 3.2.7.

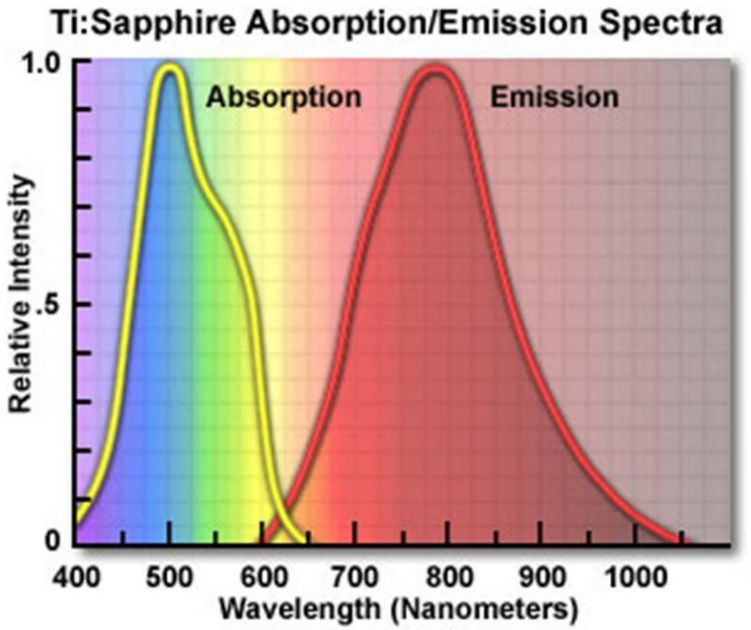

Figure 3.2.7 – Absorption and emission spectra for Ti:sapphire. The width of the absorption spectrum allows the Ti:sapphire to be pumped by a broad range of pump lasers, while the emission spectrum width allows many modes to be combined to form ultrashort pulses. Image taken from [67]

The fluorescence band extends from 600 nm up to over 1000 nm, however, lasing action is only possible at wavelengths longer than 670 nm because the long wavelength side of the absorption spectra overlaps with the short wavelength end of the emission spectra, as seen in figure 3.2.7. The tuning range is further reduced by an additional weak absorption band that overlaps the fluorescence spectrum. The origin of this is related to the presence of Ti^{4+} ions, but also depends on the material growth techniques and the concentration of Ti^{3+} ions in the Ti:sapphire material. The tuning range is further altered by mirror coatings, pump power, losses due to tuning elements and atmospheric absorption due to water vapour and oxygen. To get continuous wave wave pumping the unsaturated round-trip CW gain must exceed the round-trip loss from all sources. A high CW gain is achieved by having a high population inversion density

and a long enough length of Ti:sapphire material. The former can be achieved by having a high pump intensity and a high concentration of Ti^{3+} ions. Losses in the Ti:sapphire laser come from mirror coatings and residual loss in the Ti:sapphire material itself, the latter is proportional to the rod length and the Ti^{3+} concentration.

The Folded Cavity

Since the Tsunami is a mode-locked (ML) laser, the cavity length required to allow a repitition rate of 80 MHz means that it has a longer cavity length than its continuous wave cousins. The femtosecond configuration consists of a ten-mirror and folded cavity shown in figure 3.2.8. While folding a cavity optimises space and reduces the laser footprint on the optical table, such a configuration makes the pumping process more complex. Such a problem occurs when optics such as a focusing mirror, used at an angle other than normal incidence creates astigmatism in the beam unless corrected by additional optics, such as, in this case a Brewster-angle rod. In folded cavities where the astigmatism is not eliminated the output beams are elliptical and difficult to focus. However astigmatism exists in the laser rod itself, the pump beam must be astigmatic for efficient coupling between the pump and intracavity beam. A concave focusing mirror used at the correct angle induces astigmatism in the pump beam, matching the Tsunami cavity mode.

In figure 3.2.8, the pump beam steering is controlled with P_1, which directs the beam from the 532 nm Millennia pump laser onto the pump beam focus mirror P_2. P_2 directs the pump beam through the cavity focus mirror M_3 and focuses the pump beam on the Ti:sapphire rod. Mirrors M_2 and M_3 are the cavity focus mirrors, which focus and centre the beam waist in the Ti:sapphire lasing medium. Mirrors M_4 and M_5 are the cavity fold mirrors, they fold the beam on

itself, leading the beam onto Pr1. Prisms Pr1 through Pr4 inclusive compensate for positive GVD within the cavity. Each prism is mounted on small translation stages to allow the necessary adjustment.

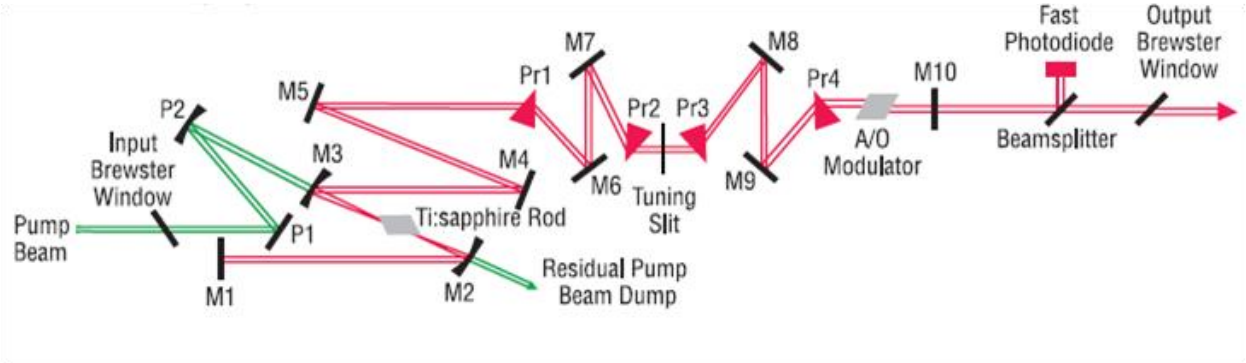

Figure 3.2.8 – Schematic of the fs cavity layout of the Tsuanmi ultrafast laser system. The incident CW pump beam from the Millennia Pro enters from image left and after being 'processed' in the laser itself emerges as a wave train of optical pulses. Schematic taken from [68]

The wavelength tuning slit is labeled as the tuning slit in figure 3.2.9 and sits between Pr2 and Pr3 which control the intracavity dispersion. Both the slit and prisms Pr2 and Pr3 are controllable externally. The prism mirrors M_6 through M_9 direct the beams through the GVD compensation prisms to the acoustic-optic modulator (AOM). The AOM allows the laser to sustain a reliable mode-lock for extended periods and is driven by a regeneratively derived RF signal. The output coupler (OC) M_{10} is the second of two cavity end mirrors, the other one being M_1 and rather than reflect all the light back into the cavity which is what M_1 does, M_{10} allows a small percentage of light to pass as the output beam. Before this happens, the beam traverses a beamsplitter which sends a portion of the outgoing beam onto a photodiode, the signal from

which goes to the accompanying electronic control box, model 3955, which is used to help mode-lock the laser on start-up.

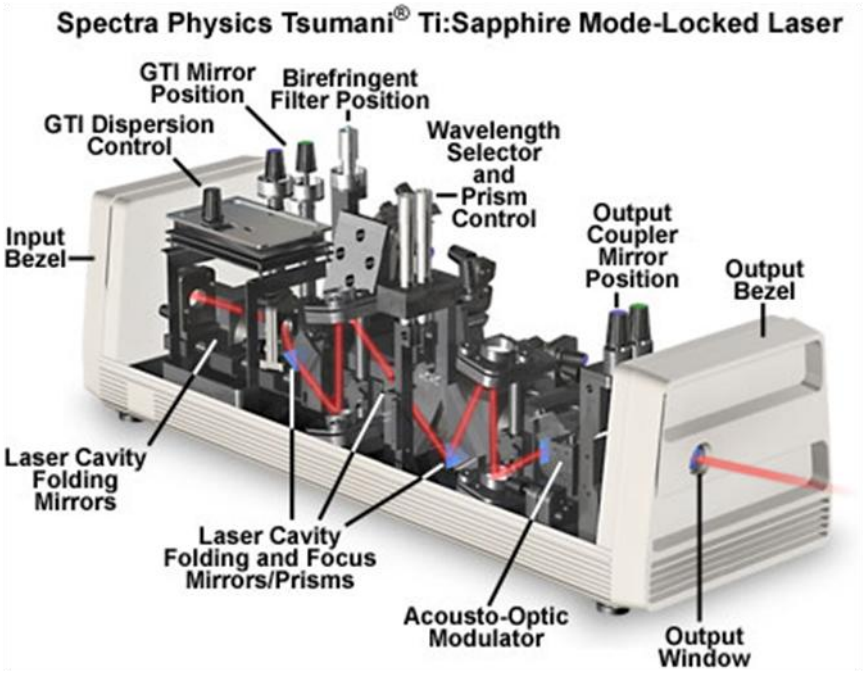

Figure 3.2.9 – Tsunami seen with the top cover removed. Millennia Pro pump light enters from the rear and after passing the 'guts' of the Tsunami emerges from the output window to the optical table. Image taken from [69]

Figure 3.2.8 shows a schematic of the internal optics of the Tsunami, figure 3.2.9 is an image of the Tsunami laser system itself with the top cover removed. The internal folded cavity configuration can be clearly seen. The externally accessible controls to the user are the output coupler mirror positioner, the wavelength selector and prism controller, the birefringent filter position, the GTI mirror position and the GTI dispersion control. The latter three are used in the ps configuration.

Wavelength Selection

For selection of wavelength in the fs configuration a prism and slit sequence is used. This arrangement of prisms and a slit allows a region in the cavity where the wavelengths are spatially spread. An adjustable slit is positioned at this point in the beam and the output wavelength is chosen by moving the slit horizontally in the vertical plane. To change the bandwith and consequently the pulsewidth of the output pulse, the slit width can be adjusted to the desired amount.

Pulse width Selection

In addition to the ability to change wavelength, the pulsewidth and spectrum can also be controlled by altering the intercavity dispersion compensation. The pulse width tuning characteristics of the Ti:sapphire laser are influenced by the Ti:sapphire material itself and the cavity parameters. It is most convenient to change the cavity parameters rather than the lasing material itself, doing this the net group velocity dispersion (GVD) of the cavity can be altered. The optical components in the laser cavity usually introduce positive GVD, causing a temporal spreading of the optical pulse, additionally further temporal spreading is caused in the Ti:sapphire rod by self-phase modulation (SPM) of the pulse. SPM arises from the interaction of the short intense optical pulses with the lasing material, where it experiences an intensity dependent refractive index. To obtain the best temporal resolution and smallest pulse width these intracavity phenomena must be compensated. To overcome additional GVD from the optics and SPM by the lasing medium, pairs of prisms are used to introduce negative GVD. By varying the position of the prism and adjusting the amount the prism enters into the beam path, the amount of negative GVD can be adjusted to compensate that gained in the cavity. Table 3.2.2 is a list of nominal operational parameters of the Tsunami laser system.

Repetition rate	80 MHz
Noise	< 0.2%
Stability	< 5%
Spatial mode	TEM_{00}
Beam diameter ($1/e^2$)	< 2 mm
Beam divergence (full angle)	< 1mrad
Polarisation	> 500:1 vertical
Pulse energy	34 nJ
Average power	2.7W at 800nm
Tuning range	700 – 1080 nm

Table 3.2.2– Tsunami specifications from [65], the high rep rate of 80 MHz gives a smaller pulse energy of 34nJ per pulse than other lower rep rate sources. Output pulses from the laser have vertical polarization and an operating beam power of 2.7 W.

3.3 Experimental Setup of the Time-resolved optically pumped scanning optical microscope

The Time-resolved optically pumped scanning optical microscope uses the Tsunami laser system to provide the 'pump' and 'probe' light used in the experiment. The Millennia Pro pump laser and the Tsunami ultrafast laser system were described in section 3.2. The Tsunami laser system provides laser light to both experiments on the optical table. The field-pumped microscope only uses frequency doubled 400 nm light as its probe, while the optically pumped microscope uses both 800 and 400 nm as its pump and probe respectively. In principle, both experiments could be run simultaneously, in practice however, due to the confined space available to the users and only one work station computer to run both experiments, this is not

done. The use of the Tsunami beam is rationed between the optical and the Kerr microscope. Figure 3.2.1 is a schematic map of the Tsunami optical table, showing the Tsunami system, the optically pumped and Kerr microscope and the laser beam paths.

Frequency doubled 'probe' light is directed to either the optical microscope or the Kerr microscope probe station. Depending on which setup is being used, the appropriate beam is blocked by a beam dump. 400 nm light enters the probe objective and is reflected from the sample, this beam returns to the communal beam splitter and the detector, which sits behind a spatial filter and two bandpass filters. The probe objective is a high numerical aperture (NA = 0.8) objective, which can focus down to a sub-micron 400 nm spot diameter. The probe beam power can be adjusted by a neutral density filter. The 800 nm pump beam enters a 10x beam expander and pinhole, the pinhole allows a well defined circular cross-sectioned beam to enter the objectives for best focusing. Before passing a mechanical chopper, the pump beam is attenuated with a neutral density filter. This prevents modulating unused pump light, which can cause disruption in the detector channel. The mechanical chopper is a rotating wheel with equally spaced cut notches, the beam passes through it and by spinning the beam is 'cut' or 'chopped', modulating the pump beam at the reference frequency set by the chopper controller. The reference frequency is set by the user and is sent as an input to both lock-in amplifiers. The reference frequency was 1.9 KHz. Before entering the pump objective, the modulated pump beam traverses a linear polarizer and a quarter-wave plate ($\lambda / 4$) set at an angle of 45 deg to the incident polarization. The linear birefringence of the quarter-wave plate at this angle generates circularly polarized light which then enters the pump objective. The pump objective has a high numerical aperture (NA = 0.75), able to focus light down to an 800 nm spot.

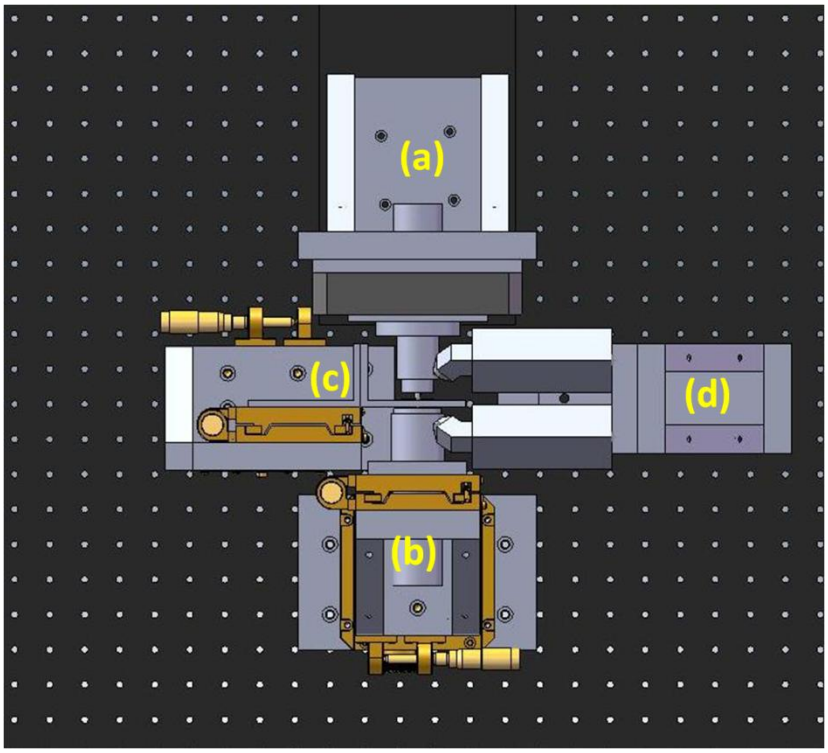

Figure 3.3.1 – Solidworks drawing showing a plan view of the optically pumped microscope. (a) is the 300 mm translation stage that the probe objective is mounted on, on the stage the probe objective is mounted on a 300 μm xyz stage. Probe light enters from the top of the image and is focused to the sample position, (c) designates the sample holder stages which allow motion in x and y in the sample plane. (b) is the pump objective stage mount, a Newport 25 mm stage allows movement parallel with the incident pump beam, manual stages allow the pump objective to be moved horizontally and vertically in the sample plane. Circularly polarized pump light enters from the bottom of the image through the pump objective to the sample position. A custom electromagnet was made specifically for the optically pumped microscope; due to the unconventional geometry the electromagnet can only produce 200 Oe per amp. Drawn by Dr Yat-Yin Au.

Figure 3.3.1 shows a Solidworks drawing of the optically pumped microscope, the sample sits on a specially made holder and is positioned between the pump and probe objective. Manual stages seen at position (c) allow the sample to be moved in its own plane, the objectives

move toward the sample itself. The 300 mm stage that the probe objective sits on allows coarse adjustment and the retraction of the probe objective to allow sample changing. Once the probe objective is close to the focus position, the xyz PI stage is used to perform fine alignment until the focus position is found. Once the probe is focused, the pump is ready to be focused, relative to the probe the pump is much harder to focus. Like the probe, it is crudely focused using a screen the far side of the communal beam splitter and a CCD camera. Finer focusing comes from making minor adjustments to the 25 mm Newport stage position, which can move the pump objective toward or away from the sample and then performing DC intensity scans across the 300 μm range. The 800 nm spot on the sample is revealed and the focus position can be adjusted based on the shape and size of the pump spot. Such a DC intensity scan is shown in figure 3.3.2. In figure 3.3.2 (a) a 40 x 40 μm scan is performed to find the pump spot location. Once found at a position of 145(x), 145(y), a smaller 10 x 10 μm scan is performed and from figure 3.3.2 (b) the pump spot shape can be seen and the central width is about 1 μm wide. The probe light leaves the probe objective from the sample and after passing the communal beam splitter has to pass a spatial filter and two 400 nm bandpass filters, before entering the simple bridge detector. In figure 3.3.3, a schematic of the spatial filter is shown. The spatial filter is a pinhole and two lenses, light entering the spatial filter is focused by a focusing lens down to a small spot which is able to pass a pinhole only 50 μm wide. After this a re-collimating lens then re-collimates the beam. The purpose of the spatial filter here is to help reduce some of the un-wanted pump light entering the detector.

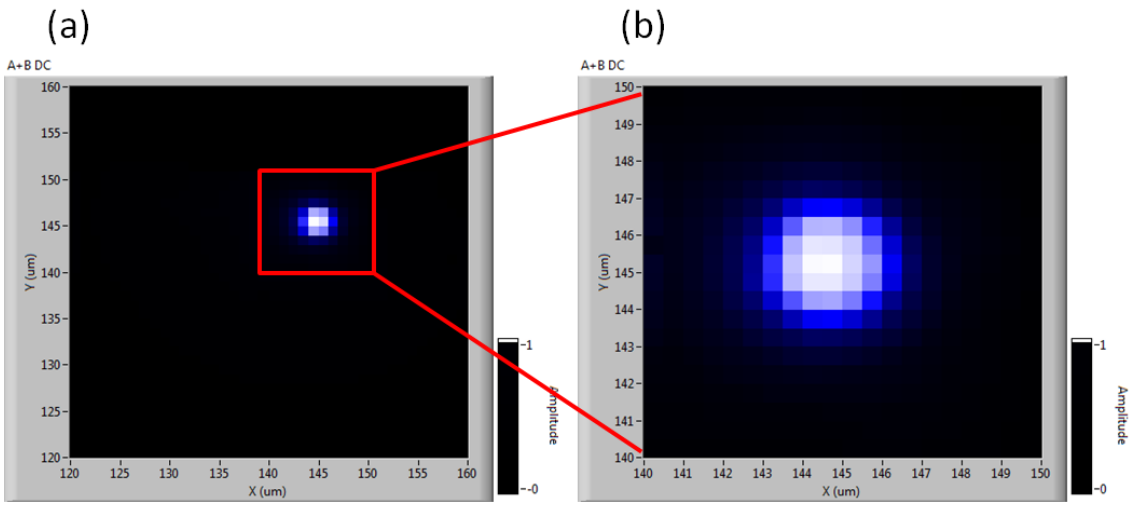

Figure 3.3.2 – Reflectivity intensity scans used to find the near-infrared spot. The axes are in microns, the horizontal axis is 'x' and the vertical is 'y'. It can be seen from (b) that the spot shape is symmetrical and Gaussian, with a central width of 1um. The spot here is in good focus. Once the near-infrared spot location is determined the probe spot can be positioned on or scanned around the pump irradiated region.

If reflectivity scans were performed without the spatial filter in figure 3.3.3, it would not be possible to determine the spot size within the 10 x 10 μm scan region. Infrared light would be able to enter the high numerical aperture probe objective and enter the detector in the proximity of the pump spot. The appearance of the spot in this case would be a larger smearing of the pump spot, the spatial filter in essence is the same as moving the detector much further back, only when the probe is exactly over the spot itself is pump light able to be measured in the detector.

For stroboscopic measurements, it is imperative to block any pump light getting into the detector; since the pump light is modulated. The experimental geometry means that pump light on the sample is collected into the light cone of the probe objective, any un-absorbed pump light heads straight for the detector (*circa* 1mW), potentially swamping the true pump-probe signal.

To attenuate the 800nm pump light, two 400nm bandpass filters are used, each with an optical density of 3.

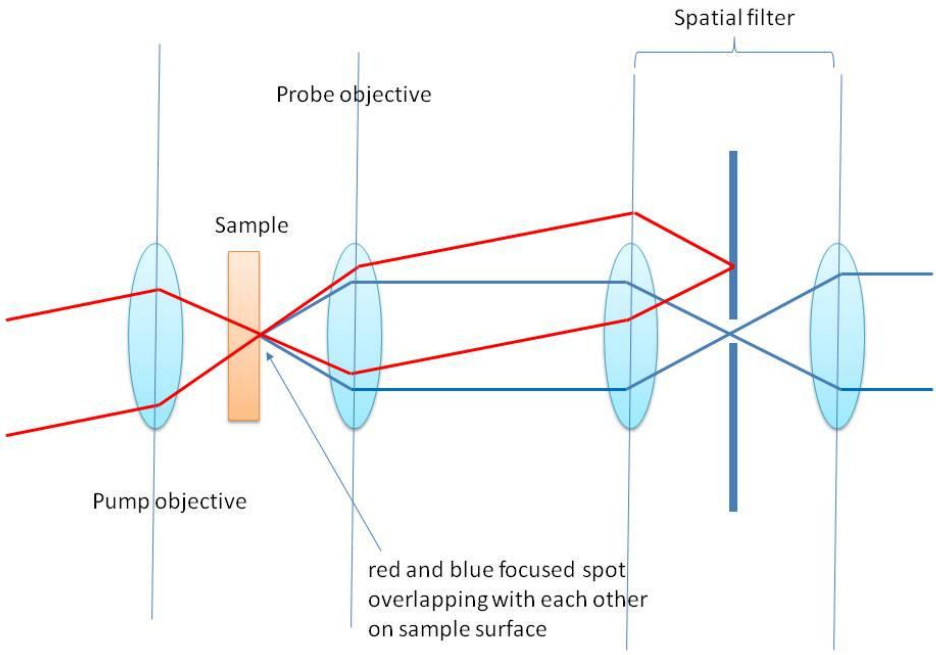

Figure 3.3.3 – Depiction of the spatial filter blocking all light that is not exactly collinear with the probe beam path. In addition to finding the pump spot, the spatial filter is also blocks unwanted pump light entering the detector.

The electrical plumbing of the optical microscope is simpler than the Kerr microscope because the pump and probe optical pulses are already synchronized with one another, since they leave the same source. The detector outputs are fed into two lock-in amplifiers and a digital-to-analogue converter (DAC). The DAC and lock-in signals are sent via GPIB to the computer work station. The chopper reference signal acts as a reference frequency input for the lock-in amplifiers.

3.4 Experimental Development of the Time-resolved optically pumped scanning optical microscope

Once the optically pumped microscope had been designed and built, the zero-time delay position and the signal itself had to be found. The location of the signal on the stage, its amplitude and its duration are unknown. The signal could exist and the experiment may not be working as intended, then there is the task of fault finding. The equipment and apparatus could be working and the signal is absent. In addition to this, is the challenge of overlapping two small spots, around 1 μm and 0.5 μm for the pump and probe respectively. Time-resolved scans for long delays revealed noise with strange backgrounds. Many variables were open to adjustment, the stage step size could be too large and one could fly right over the signal, the lock-in sensitivity might not be appropriate or the signal might not be on the stage at all. The pump and probe paths were measured and time-resolved scans were ran in the predicted region of the delay line and for a long time no signal was seen. This section describes some of the changes that were made, some in hindsight more useful than others.

Large steps forward have been made to narrow down the possible sources of noise in the system and many improvements have been undertaken. Identifying the largest sources of noise is still a real challenge. Large drifts are seen in the DC channels that arise from the stability of the laser's spectrum and power. Also, as pump powers are increased to further excite the sample, it becomes harder to isolate the Bridge Detector from this pump light.

Fabricated for 'test' focusing of the microscope and used for performing scanning was the Gold e-beam sample fabricated by Dr. Ehsan Ahmed. Since the test sample is non-magnetic, an old GdFeCo film was used for finding the zero-time delay position. The GdFeCo film can

lose its magnetic properties due to oxidation on the film surfaces. Yttrium iron garnet (YIG) square arrays were inserted and scans were performed before finally decided to return and look for the reflectivity signal in the gold 'test' sample. After many scans on this sample it was then discovered that some of the connecting BNC cables between the detector and the lock-in amplifiers were faulty and did not pass a signal, despite having a DC resistance of 0.2 Ohms. At this point there were some 'homemade' BNC cables of incorrect length being used. The fault here was the coaxial centre pin had become loose in the BNC connector. In the interest of more reliable and shorter BNC cables, some were ordered from Thorlabs. Finally, a 20 nm thick permalloy (NiFe) film was mounted into the optical microscope after being unable to observe a reflectivity signal in the gold test sample. Early tests on the permalloy had been made using too high a probe power and the film had been ablated away during DC scans. Further time-resolved scans were mistakenly made on the remaining glass. No signal was seen. Damage tests of the film were made to determine at what powers damage is done in the focus position. Damage powers of the permalloy film were found for 400 and 800 nm light.

Static Kerr and Faraday hysteresis loops have been measured using the 'claw' magnet and both the simple bridge and the balanced detector. At first, the balanced detector was unable to see any hysteresis loop. After some modification to the balanced detector, a loop could then be observed. All the time resolved scans tried up to this point were done with a balanced detector that could not measure a hysteresis loop. The sections below briefly discuss some of the changes made to the probe station in efforts to help find the signal.

Mains filtering

The over table sitting above the optical table was overrun with power cables and wires. RF sensitive equipment such as the lock-ins and the Bridge Detector were powered from normal mains sockets. The mass of cables was reorganized and in addition to this, mains filters to power sensitive units like the lock-ins and bridge detector were used. To accommodate shorter cables, the top boards were removed from the over table and sections were cut to allow cables to pass from the optical table to the lock-ins without excess length. Eliminating unwanted length will help to keep any pick-up/ interference from the surroundings to a minimum.

Old home-made BNC cables

For scans performed on the Gold, GdFeCo and YIG samples, several BNC cables running from the detector to the lock-ins were found to have loose coaxial centre pins. A first test to investigate the cables integrity was performed by looking at the DC resistance with a multi-meter, which found 0.2 Ohms. To further test the cable, the cable was connected to a photodiode to observe the 100 Hz mains flicker from the table lamp. Other 'working' BNC cables were tried and the 100Hz was clearly seen. To avoid using homemade cables of an unknown quality, cables were ordered from Thorlabs. These cables replaced all cables in use on the optical table and were chosen to be of correct length. The cables were tested using a signal generator, including the ordered t-connectors and were found to pass signal well.

Chopper stability and vibration

The chopper, when first used was quickly seen as providing an unstable reference frequency for the lock-ins. Set originally to 1 KHz, the chopping frequency could drift by several tens of Hz, typically around 30 or 40Hz (3-4%). Higher frequencies were used to look for the stability at around 1.7 KHz. Over several weeks, as the chopper had been on for longer and

longer periods of time the stability was seen to improve greatly as a result of being ‘run-in’. Now the chopper reams stable over about 10 Hz (1%). This stability seems to be present now for any frequency. Ultimately, this chopper was found not to be stable enough and a new more stable chopper was substituted and used.

Signal backgrounds arising from stray light entering the detector

External stray light can enter the balanced detector through the two small holes in the die cast housing that hold the balanced detector. These holes are not shielded from the surrounding environment and it is possible for light to enter. The silicon photodiodes have about 5 times the responsivity to 800 nm light than 400 nm light. The detector is therefore more sensitive to infrared light we cannot see. Stray light should not affect the stroboscopic channels as it carries no modulation.

A series of black foil partitions were erected to stop unwanted stray or scattered 400 and 800 nm light from entering the detector region, the foil partitions prevent light travelling horizontally across the table. Figure 3.2.1 shows the modern layout of the pump and probe beam paths. In an earlier incarnation, it was discovered by accident that light was being modulated and scattered around the inside of the box enclosure sitting over the optical table. About 1 W of unused pump light was modulated. Rearranging the beam path and altering the position of the chopper and neutral density filters alleviated the problem.

The Balanced Detector

Initially, a commercial Thorlabs PDB210A Silicon balanced detector with a 1MHz bandwidth was used. To incorporate this into the probe station, an aluminum body and housing

was constructed. This housing included the polarizing beam splitter and the detector could rotate about the horizontal axis to allow the bridge to be nulled. Supported at one end by a nylon stud which could rotate in an aluminium support and at the other it is connected to the frame by the 'Martock' screw device. This screw has a small wheel that allows you to make precise turns of the housing, turns of a degree or smaller. The rotation of the Nylon stud in the aluminum frame is not smooth for all angles of rotation. When the bridge detector is orientated so the rotating housing is level and horizontal it is easy to turn, when the housing is the rotated to around 45 degrees or larger the motion becomes stiffer. The Martock screw was never able to turn the housing in this position, it was not broken, it did not have the strength to turn the housing when it is at these stiffer angles. 45 degrees is the position at which the DC A-B signal should be zero. This problem was eventually solved by placing paper between the front support of the Bridge Detector and the frame. This raises the front end to allow rotation to be much smoother. It is now improved such that the 'Martock' screw now rotates the housing.

In addition to this, the bridge detector has had sections of the box which holds the balanced detector removed. This makes the large area photo detectors visible and much easier to align the incident beam onto them. A paper aperture has also been added to the front of the detector to make alignment easier. It turns out all of this was for not, because after extensive trials it was deemed that the commercial balanced detector was unsuitable due to its high bandwidth and insufficient transimpedance gain. After discovering this, the simple custom built bridge detector currently used in the same lab had to be borrowed to perform any measurements at all. This detector was fully working and went into service.

Moving the Probe station

To facilitate the spatial filter in the detector channel, the probe station was moved 4 inches along the optical table. This was done so that the spatial filter can fit along with the detector and a focusing screen. The spatial filter is used to help determine the pump spot size and shape and is equivalent to moving the detector further away. The moving of the probe station required the alteration of the 800 nm beam path and the recalculation of the pump and probe beam paths. The total length of the pump (800 nm) path is 297.5cm. The total length of the probe (400 nm) path with the stage in the close position is 266 cm. The 31.5 cm difference should put the pump-probe overlap position 15.75cm down-stage.

400 nm Damage Threshold of 20nm Py

In the probe path a 5-times beam expander was used to expand the beam and then use an aperture to 'section' off a small homogeneous circular section that would then give the best focus in the probe objective. The beam power was thought to be too low and the signal was thought to increase with probe beam power. To increase the beam power, the beam expander was removed from the beam path. The circular cross-section of the beam was lost and it became a more irregular shape. The total beam power into the objective was 20 mW, after performing scans with this power the permalloy had been ablated away. Further damage tests revealed that in the focus position 3 mW is sufficient to cause damage and leave a hole in the 20 nm thick permalloy film. Despite the high fluence of 20 mJ/cm^2 (which is roughly double the damage threshold for an opaque film), a large fraction of the 400 nm light is transmitted through the film itself due to its thickness. In figure 3.4.1, reflectivity scans are shown of the permalloy film sample surface for various probe powers into the objective. To perform the reflectivity scans the probe power was set to 500 μW, the probe position was set to the centre of the scan region (150, 150 μm) and the

probe power was increased. After allowing the spot to 'sit' for several moments, the power was reduced to 500 μW and an intensity scan was performed to check for damage. Any damaged area has a lower reflectivity and will appear as a dark region. For powers less than 2 mW in figure 3.4.1, there is no probe damage and the background is of uniform reflectivity, perturbed only by noise in the detector. From 3 mW an above damage is visible and as the power becomes greater than damage increases and the contrast improves.

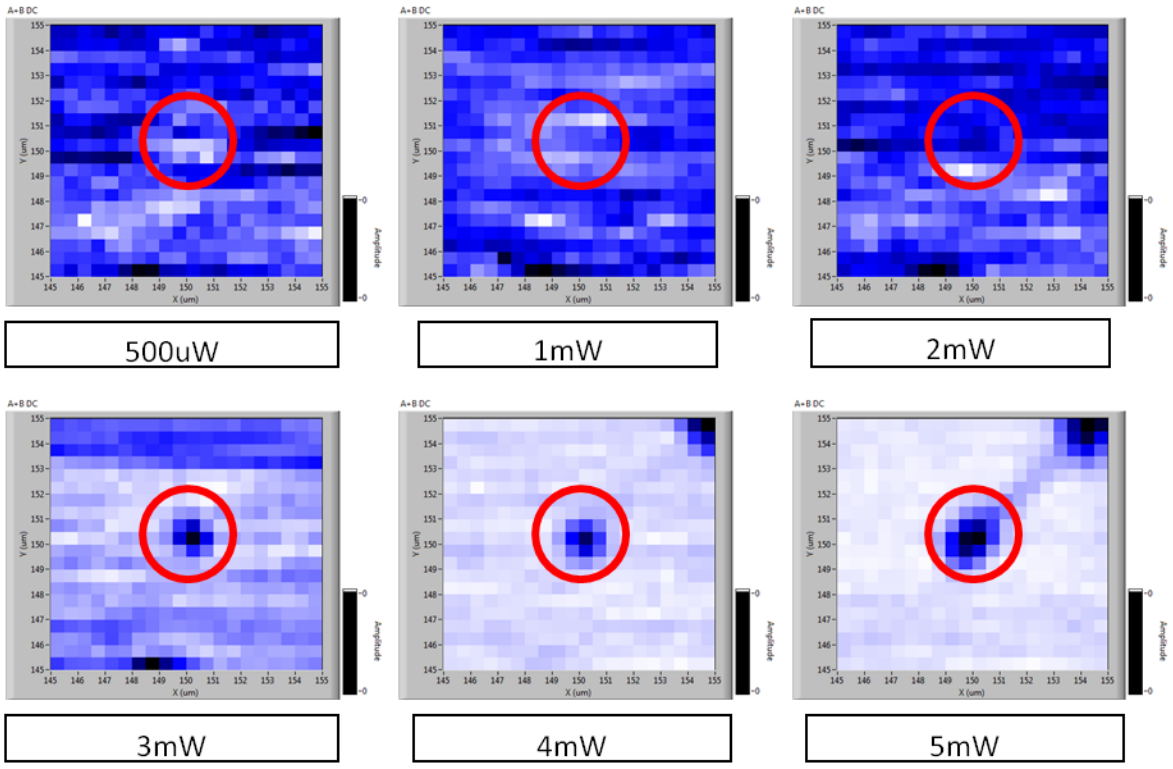

Figure 3.4.1 – The 10 x 10μm scan region of permalloy continuous film chosen for probe damage testing. The horizontal and vertical scales are in microns. The raster scan finishes in the top corner of the image, in this position the power was increased and then moved to image centre. At 5mw the damage track caused by the moving probe is visible; at this power damage was being caused as the probe spot swiftly

moves over the sample. Conventional powers used in the probe station are about an order of magnitude less than the minimum damage power of 3mW.

800nm Damage Threshold of 20nm Py

In the 800 nm pump path a 10-time beam expander expands the beam and an aperture allows a small section through to the pump objective. The un-used expanded beam is wasted; the pump channel has more power than the 400 nm probe beam. If the beam expander was removed, there would be around a watt of power into the pump objective. As the stage position is varied, the spot shape changes from a defocused cloud about 10 μm across to a spot several microns across featuring a halo like feature, shaped like a crescent. As the focus position was further changed the brightness of this halo like feature increased. Figure 3.4.2 shows several reflectivity scans of the pump spot for various pump objective positions.

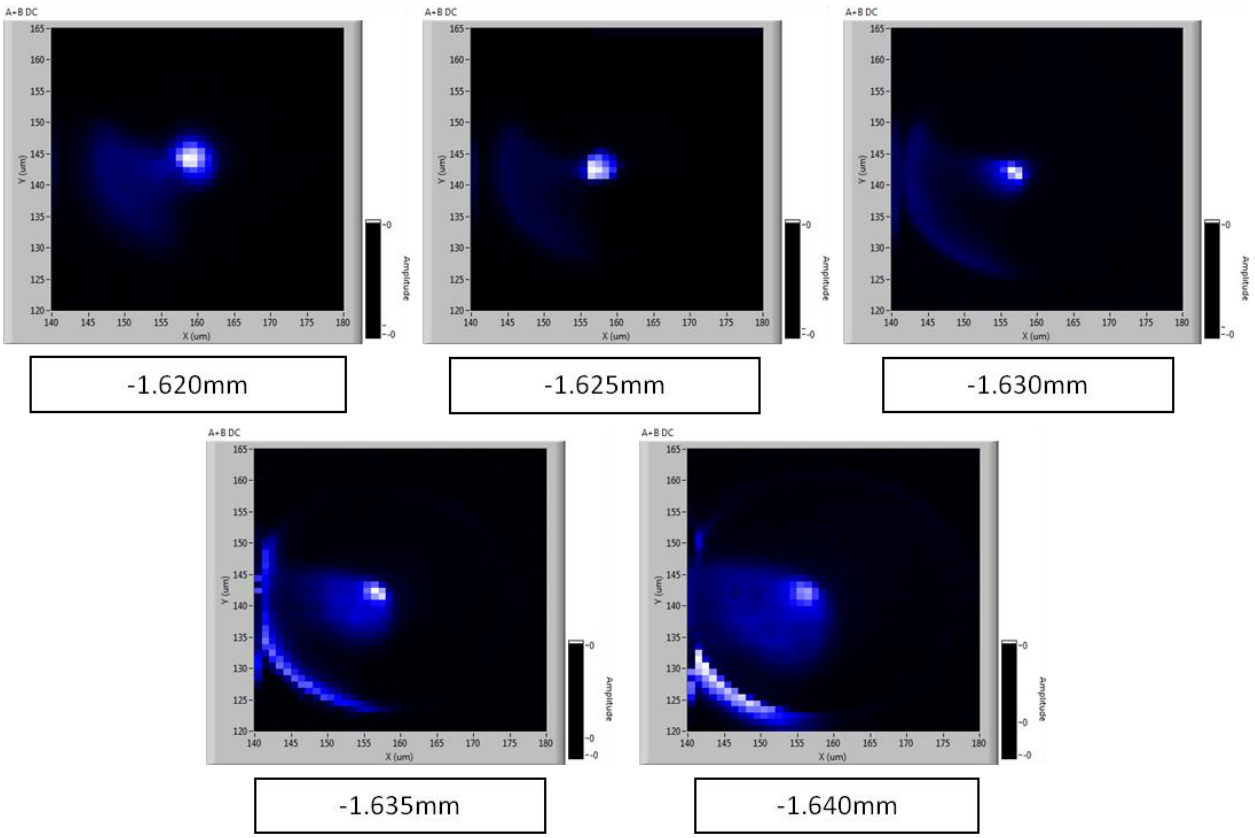

Figure 3.4.2 – Reflectivity images of the pump spot for various positions. The values in mm are relative to the origin of the Newport 25mm stage on which the probe objective is mounted. The scans are 40(x) x 45(y) μm and show a marked change in the pump spot shape for a 20μm range. At -1.620 mm the majority of the spot intensity is located in the central region, as the stage position moves to greater '–ve' values the intensity distribution migrates to the circular periphery and at -1.640 mm it appears that most of the intensity is located in the crescent shaped fringe.

The pump spot shape is sensitive to the pump position. The probe station is located under the lab air conditioners and despite being in a partially enclosed box, it suffers greatly from thermal drifts. Thermal expansion and contraction of the probe station often ruins the effort spent aligning the pump and probe objectives. Below in figure 3.4.3 are DC scans showing damage caused.

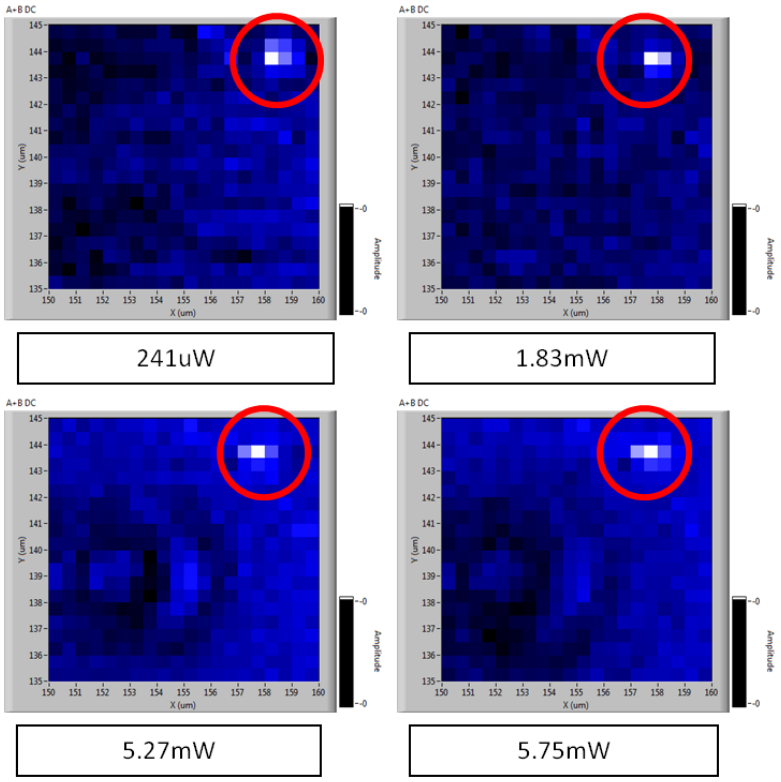

Figure 3.4.3 – 10 x 10 μm reflectivity scans of the 20nm permalloy region exposed to pump illumination for various powers. For pump powers above 5 mW into the pump objective damage appears from pump exposure. The damage does not appear neatly due to irregularities in the pump spot shape, this arises from the difficulties of focusing and when focused the effect of temperature fluctuations causing defocusing of the objective. The circled region in all the above images denotes a few very bright pixels which saturate the rest of the image; this is why the damage region and film appear with similar contrast. The origin of this artifact is unknown.

The damage threshold for the 20 nm permalloy film was 5 mW at 800 nm. Although operating pump powers are several factors less than 5 mW, there is typically about 1 mW of power directed toward the detector itself. The simple bridge is sensitive to several tens of nano-Watts at pump frequencies where the silicon diode responsivity is high. Measures to attenuate

the pump light include bandpass filters and the spatial filter. The optical density of the bandpass filters is 6 at 800 nm and the transmittance of the bandpass filters at 400nm is 55%.

Performance of the balanced detector and the simple bridge

To compare the performance of the balanced detector and the simple bridge used for measurement the transimpedance gain of the balanced detector is determined and compared to the simple bridge's output vs input characteristics. After adjustments to the balanced detector's housing body, it is now easier to align with respect to the incident probe beam, but its gain characteristics are thought to be too low when compared to the simple bridge. By measuring the output voltage as a function of the input power for both detectors, the performance can be determined from the gradient of the straight line. Since the balanced detector only has an A-B or RF output and lacks an A+B, only the difference output of both detectors will be compared. By using a CW He:Ne laser and an low-extinction ratio plane polariser to control the power to the detector the output can be read off using a Fluke multimeter. The power is increased in increment steps and the voltage is noted accordingly, by plotting and fitting the straight line its gradient can be found. The gradient tells us the output voltage (V) per unit input power (μW).

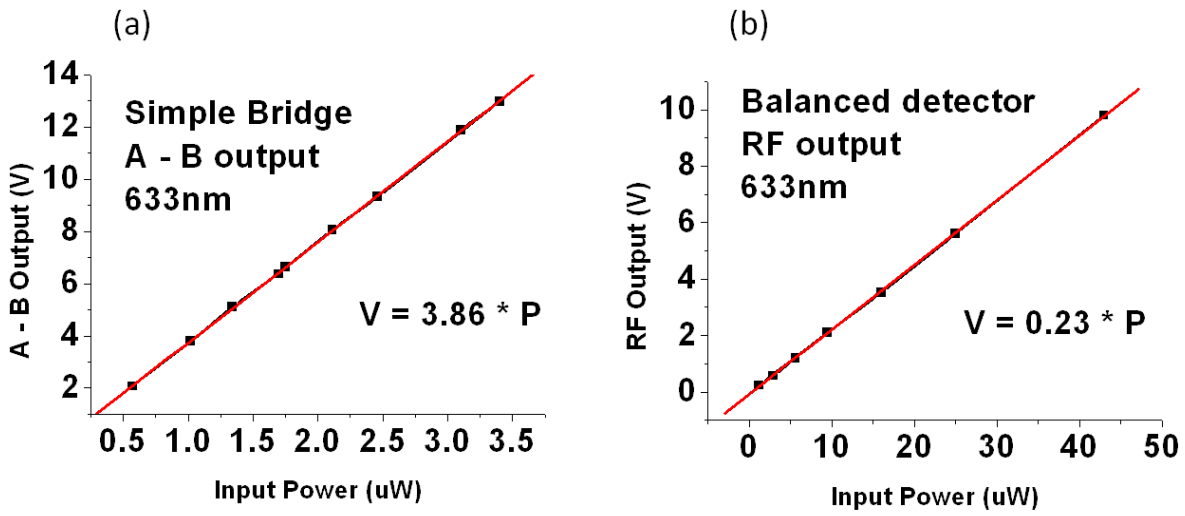

Figure 3.4.4 – Comparison of the difference outputs of the simple bridge (a) and the balanced detector (b). The simple bridge generates 3.86 V for every microwatt of incident power, compared to 0.23V for the balanced detector. The (red) line is the fit to the (black) data points.

The gradients of figure 4.3.5 are directly related to one another because the simple bridge and the balanced detector both use Silicon diodes and the Silicon diode responsivity is 0.45 A/W at 633 nm. The simple bridge has a gain (3.86 / 0.23) 16.8 times greater than the balanced detector. This gives the balanced detector a transimpedance gain of 511kV/A and the simple bridge an equivalent transimpedance gain of 8600kV/A.

3.5 Summary

In this chapter the experimental setup and development of the Kerr microscope and the time-resolved optically pumped scanning optical microscope have been discussed. The Tsunami laser system plays an integral part to both experiments. Aspects of its operation, including stimulated and spontaneous emission, population inversion and second harmonic generation are

described, followed by a brief discussion of the Millenia Pro and Tsunami oscillator cavity layouts. Then, the experimental development of the time-resolved optically pumped scanning optical microscope was described. Many of the changes and improvements to the optically pumped microscope have also been described.

Chapter 4: Time-Resolved Scanning Kerr Microscopy measurements of Cobalt and Air filled Anti-dot structures

4.1 Introduction

In this chapter the results of Time-Resolved Scanning Kerr Microscopy (TRSKM) measurements are presented on two magnonic crystals, both consisting of anti-dots patterned into a continuous permalloy (NiFe) film. The first binary sample features cobalt cylinders (dots) filling the permalloy antidots, forming a square cobalt dot lattice. The second sample is identical to the first, however it does not contain cobalt dots, the anti-dots are air filled. This sample acts as a reference to the binary sample; comparison is made of the mode propagation characters and the spin wave decay length. This study is part of a wider collaborative project within the European MAGNONICS project. Both samples were fabricated by Mr. Georg Dürr from the Technical University of Munich and Marco Madami from the University of Perugia. who (with their colleagues) have also performed characterization using Vector Network Analyser Ferromagnetic Resonance (VNA-FMR) and Brillouin Light Scattering (BLS) measurements and micromagnetic simulations.

Spin waves in confined magnetic structures have been investigated for several decades and the idea to consider periodically modulated magnetic structures can be dated back to 1976 [70] in which the authors studied experimental insertion loss of magnetostatic spin waves in selectively etched epitaxial yttrium iron garnet (YIG) films. More recently, magnetic metamaterials or materials with periodically varying magnetic properties in one, two or three dimensions are called magnonic crystals. The periodicity tailors the magnonic bandstructure, giving rise to band gaps and the possibility of building spin wave filters with narrow

transmission or rejection bands [71]. Magnonic bandgaps have been observed in a variety of periodic geometries. *Nikitov et al* [72] studied the propagation of spin waves in a multilayered structure, each layer having identical thickness but differing magnetisations. They observed forbidden zones or 'stop bands' in the wave spectrum where wave propagation is prohibited. *Vasseur et al* [73] deduced the theoretical two-dimensional spin wave spectra of square arrays of Fe cylinders in a ferromagnetic EuO background. They observe gaps in the magnonic bandstructure revealing the width of the gap is dependent on the square lattice parameter. The understanding and control of spin wave dynamics is ultimately geared toward the building of magnetism based logic devices. Spin wave logic devices use spin waves rather than electrons for information processing [74]. The aim of magnonics is to modify spin wave propagation in artificially patterned magnetic media which have a periodicity comparable to the magnon wavelength. Periodicity is handled by periodically varying the material constants such as saturation magnetisation and relative permeability, additionally a more correct physical picture can be obtained if the inhomogeneity of the internal field is considered. The formation of magnetic surface charges at the boundaries creates spatially nonuniform demagnetising fields, which locally reduce or intensify the internal field. This gives rise to the magnonic equivalent of a periodic potential in solids. This confinement of magnetic potential creates localised modes in magnonic crystals.

Studies of two-dimensional anti-dot structures have received much attention in recent years [75, 76, 77, 78]. The anti-dot lattice, which is a periodic array of holes in a ferromagnetic film, has attracted interest due to the potential for ultrahigh density memory storage [79, 80], magnonic crystal based information processing [81,82] and nano-optics with spin waves in multiple connected magnon waveguides [83, 84]. Neusser et.al [75] used All-Electrical Spin

wave Spectroscopy (AESWS) and Brillouin light scattering (BLS) to study 120 nm diameter permalloy anti-dot lattices for various size square lattice parameters varying from 300 to 4000 nm. For lattice periods less than 400 nm, high spin wave group velocities up to 6km/sec were seen. They found by adjusting the in-plane 400 Oe field they could control the spin wave mini-band responsible for the propagation of the 'fast' spin waves. Tacchi et.al [76] used the dynamical matrix method to calculate the band diagram for square arrays of saturated 600 nm diameter nano-disks (55 nm edge-to-edge seperation). They used Brillouin light scattering along different directions through the Brillouin zone at a field of 1KOe. The four-fold symmetry of the geometrical lattice was found to reduce in the presence of an external field and equivalent Brillouin zone directions were characterised by different dispersion relations and spin wave propagation. *Neusser et. al* [78] showed multiple resonances in permalloy anti-dot lattices (lattice constant 490 nm, hole diameter 240 nm) depending on the applied field direction with respect to the in-plane lattice. The applied field direction determines the extended or localized nature of the mode, in the case of the applied field being parallel to the anti-dot lattice edge the excited mode is extended orthogonal to the field direction. For field directions not orientated along a line of anti-dot symmetry, inhomogeneous mode characters were observed.

This chapter presents measurements on binary (PyCo) dot structures and the anti-dot reference samples, which are studied described additionally elsewhere [85]. *Duerr et al* [85] combined all-electrical spin wave spectroscopy and Brillouin light scattering to study the same samples which were studied here in this chapter using time-resolved Kerr microscopy. The dot/antidot sample(s) are based on a 300 µm by 120 µm large Py mesa, deposited by electron gun evaporation on a GaAs substrate. It is 24 nm thick. A square lattice of circular holes was exposed and developed in a resist layer (PMMA) on the mesa. This mask was used for Argon

milling of 8 nm deep troughs into the permalloy. Subsequently the holes were filled with 15 nm thick cobalt nanodisks (so-called dots) by electron gun evaporation without breaking the vacuum. After lift-off processing, a bi-component nanodisk/antidot system was obtained. Two characteristic spin wave modes are observed extending through the lattice perpendicular to the applied field. Their spatial positions depend on the presence of the cobalt disks, as they reverse the polarity of the internal field. Both samples underwent Time-resolved scanning Kerr microscopy in Exeter to compare the resonant mode characters. The measurements were performed at a field of 200 Oe, with the field parallel to the coplanar waveguide.

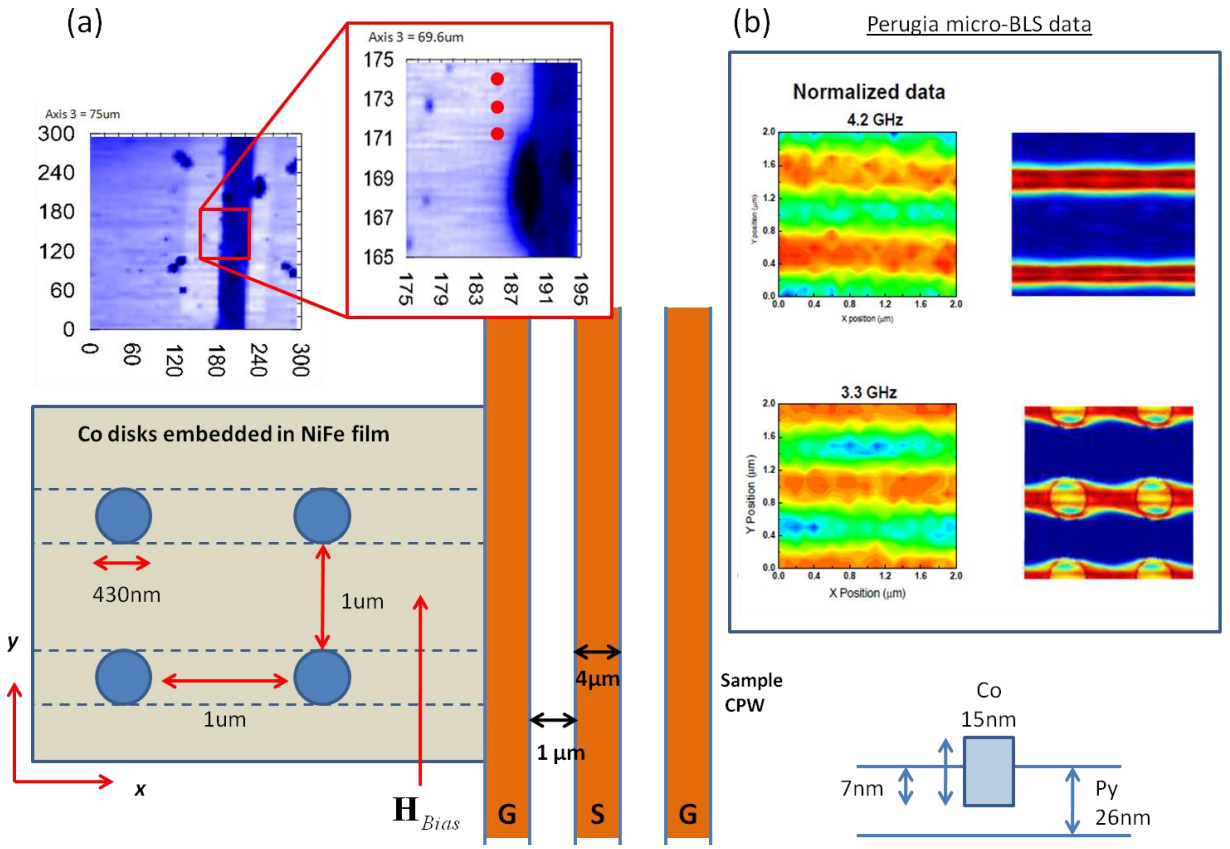

Figure 4.1.1 - Schematic layout of the binary and anti-dot lattices respectively, with a reflectivity image of the permalloy-cobalt binary sample (a). Micro-focus Brillouin light scattering intensity images are shown on the left and comparison with simulations on the right. Both measurements and simulations were performed by Mr. Georg Dürr from the Technical University of Munich and Marco Madami from the University of Perugia

In figure 4.1.1 (a) a schematic depicts the sample and waveguide geometry. The waveguide is labelled ground (G), signal (S) and ground (G) respectively. The square grey shaded region represents the permalloy (NiFe) film and the round (blue) dots represents the positions of the cobalt and air-filled anti-dots in the binary disk and anti-dot sample respectively. The disks are 430 nm in diameter and 15 nm high. The continuous permalloy film they are embedded in is 26 nm thick, the disks sit proud of the surface by 8 nm. The cobalt disks are separated by 1 μm. The reflectivity images in 4.1.1(a) show a large 300 x 300 μm scan of the sample and coplanar waveguide, the coplanar waveguide is the solid blue strip running vertically. The light white area is the location of the cobalt dots and permalloy film, outside of this region is the Galium-Arsenide substrate. In figure 4.1.1 (b) micro-focus Brillouin light scattering intensity images are shown on the left and comparison with simulations on the right. The images have the same orientation as the schematic in figure 4.1.1 (a); the 200 Oe field is applied normal to the extended mode profiles. The two observed modes at 4.2 and 3.3GHz discussed in [85] can be seen to extend either between or through the cobalt dots depending on the frequency. The data presented in this chapter is complementary to the work in [85].

Time-resolved scanning Kerr microscopy is being used to measure the binary Cobalt dot and air-filled anti-dots to determine the stationary or propagating character of the excited modes. Kerr microscopy reveals phase information about the excited modes, which appears as contrast in the measured Kerr images. Are these modes propagating from the waveguide or do they have a stationary character that is ‘driven’ by the CPW? Figure 4.1.2 shows BLS intensity measurements along the ‘furrows’ of the mode profile shown in the experimental data in figure 4.1.1(b). The experimental data can be similarly fitted to both a propagating character which falls off exponentially or as one over distance squared, indicating a stationary character in which the

mode is driven by the sample coplanar waveguide. The cobalt dots augment the dispersion relation of spin waves that can exist and propagate in the binary sample. Spin waves in un-patterned permalloy have been extensively studied. By embedding cobalt or air-filled dots into the permalloy it is not clear how this periodic modulation will change the spin wave dynamics. TRSKM is a polarisation technique which is sensitive to the phase of the spin wave and different orientations of the dynamic magnetisation.

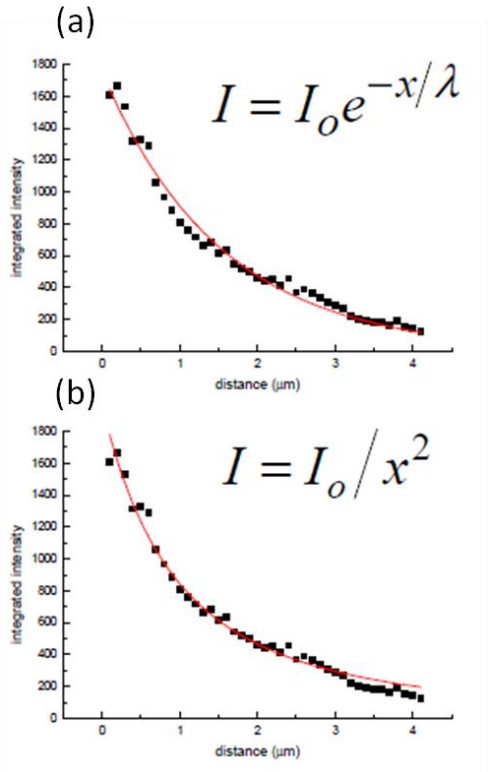

Figure 4.1.2 – Perugia micro-Brillouin light scattering data showing the mode intensity along the extended mode with position from the waveguide. The intensity can be equally described by an exponentially decaying propagation (a) or a stationary mode character profile falling off in a quadratic fashion (b).

By scanning over a region successive images can be taken at different time delays corresponding to a period of precession. This method gives a spatial distribution of the phase of the spin waves and thus it can be determined whether the observed modes have propagating or stationary character.

Experimental Results

After the experimental description has been given in the last chapter, the experimental results of the binary and anti-dot reference sample are presented. The first sample to be measured by time-resolved Kerr microscopy was the binary sample. The applied field value stayed constant throughout the measurements at 200 Oe. There was no investigation of any field dependent behaviour of either sample. To extract the resonance frequency, the sample is excited with field pulses using a Picosecond Pulse Labs (PSPL) model 3600 pulse generator connected to the sample waveguide. The temporally short 70ps pulses are spectrally broad and deposit multiple excitation frequencies into the magnetic ground state. At a field of 200 Oe the 'on-resonance' dynamic eigenmodes of the structure are excited. Time-resolved signals were performed at sub-micron intervals using pulsed excitation parallel to the waveguide, in this manner the probe spot traverses over and in-between the regions which contain the cobalt dots. The time-domain signal is converted into the frequency domain by performing the fast-Fourier transform (FFT). The FFT spectrum reveals two modes, a main peak and a smaller adjacent peak. Following the time-resolved signals Kerr imaging was performed using continuous wave (CW) excitation at the mode frequency identified from the Fourier spectra. By scanning the probe spot over the lattice region at preset time-delays, corresponding to $\boldsymbol{\pi/4}$ phase of a precession cycle, a series of consecutive images can be obtained. The images contain phase and magnitude information, which is required to understand the character of the mode(s). Compiling

consecutive images together using Image-J, an animated movie can be made revealing the temporal evolution of the distribution of magnetization (Kerr signal) within the scan region. Additionally, the mode profiles from the Kerr imaging were fitted to extract the spin wave decay length and wavelength. The aforementioned process is the experimental methodology and was conducted identically on both samples, here it has been explained for the binary sample and the process is repeated for the anti-dot ref sample.

4.2 The patterned Binary (PyCo) sample

The continuous permalloy film is 26 nm thick, with 15nm high Co cylinders embedded into the film to a depth of 7nm. The cobalt cylinders are 430 nm in diameter. The cylinders or 'dots' are arranged in a square lattice with a separation of 1 μm.

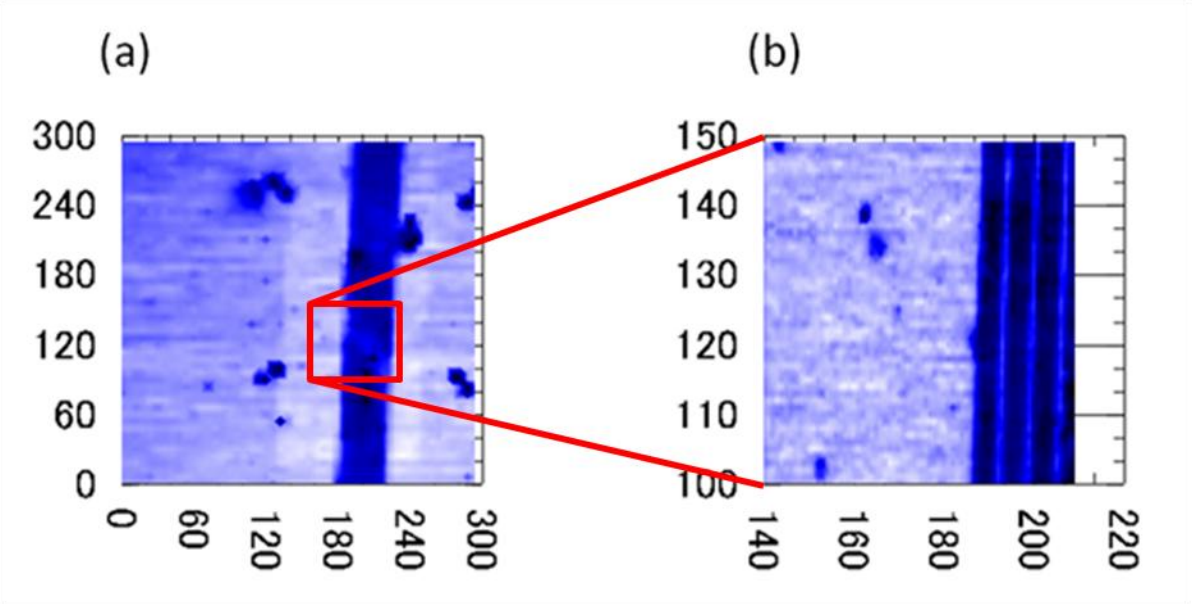

Figure 4.2.1 – Large area 300 x 300 μm DC reflectivity scan of the Binary dot sample (a), the step size is 6 μm. The dark blue rectangular region right of centre is the sample coplanar waveguide; four alignment

marks can be seen. The white region either side of the sample waveguide denotes the cobalt dot region, outside of this is the gallium-arsenide substrate. A smaller area DC scan reveals the ground-signal-ground line of the sample coplanar waveguide (b), the striplines are each 4 μm wide and separated by 1 μm.. The axis in (a) and (b) are in microns.

To ensure the probe spot is on the binary region, measurements are made within the alignment marks. The true demarcation of the binary region is not known, only by obtaining the Fourier spectra from the time-resolved signals is it possible to determine the sample composition under the probe spot.

Time-Resolved response of The Binary Sample

Time-resolved scans were performed at 0.5 μm intervals over several lattice constants. In principle, smaller step sizes between time-resolved signals scans could be taken. In practice, the probe spot size under the Abbe diffraction limit is 0.4 μm and in-plane drifts can be of the order of a micron or more. The dots are not directly observable in both reflectivity and Kerr images, due to their size; they can only be inferred via the Fourier spectra. The spot size under ideal conditions is the order of the wavelength of light (*circa* 400 nm), in practice, however, scanning at intervals much smaller than the spot size will increase the total duration of measurement and not increase the spatial resolution.

The spatial stability of the system is the limiting factor of the measured image quality; it has to be stable to the step size (0.5μm) for the consecutive scans to have a consistent meaning. In figure 4.2.2 the sample is excited by a spectrally broad pulsed field. The time-resolved signals reveal a ‘wave packet’ shape uncharacteristic of a typical impulse response, having their maximum signal at around 1ns. The probe is not positioned on the sample waveguide, but

laterally separated from the waveguide by several microns. The signals do not fully decay in the available 4 ns delay time and by 'chopping' or terminating the signal prematurely spectral resolution is reduced.

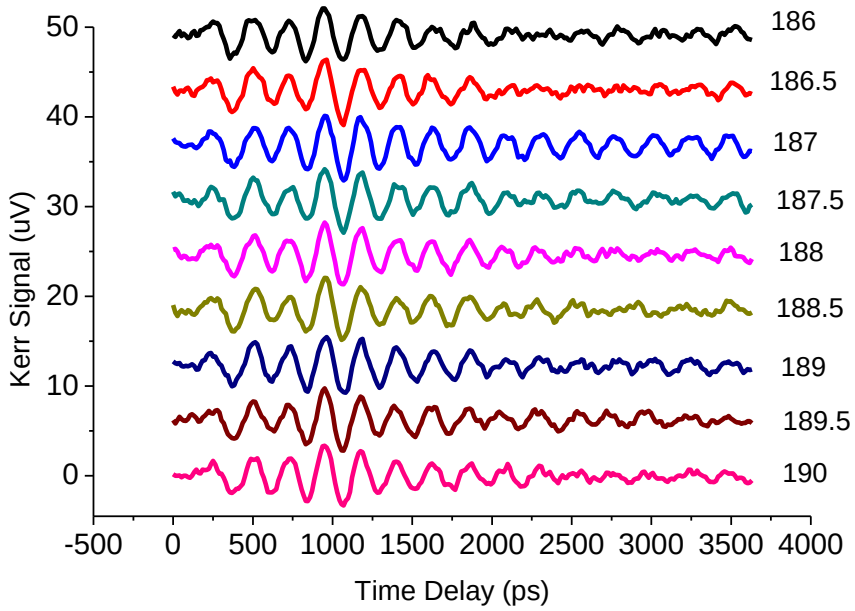

Figure 4.2.2 – Time-resolved signals of the binary region, showing the lock-in polar Kerr signal in μV versus the temporal pump-probe delay. The numbers right of the time resolved signals represent the 'y' coordinate of the scan position in microns. The time-resolved signals can be compared with their Fourier spectra in figure 4.2.3.

In figure 4.2.3, the Fourier spectra are shown for pulsed excitation, a dominant large amplitude 4.4 GHz peak is seen in all the mode profiles. A smaller amplitude 3 GHz peak periodically appears and disappears as the probe spot traverses across the lattice. The 4.4 GHz mode is associated with the un-patterned permalloy. The 3 GHz mode is associated with the cobalt dots. The probe is scanned 'blindly' due to the inability to resolve the dots in the

reflectivity images. The two mode frequencies of interest of the cobalt binary sample are the 4.4 and the 3 GHz modes respectively.

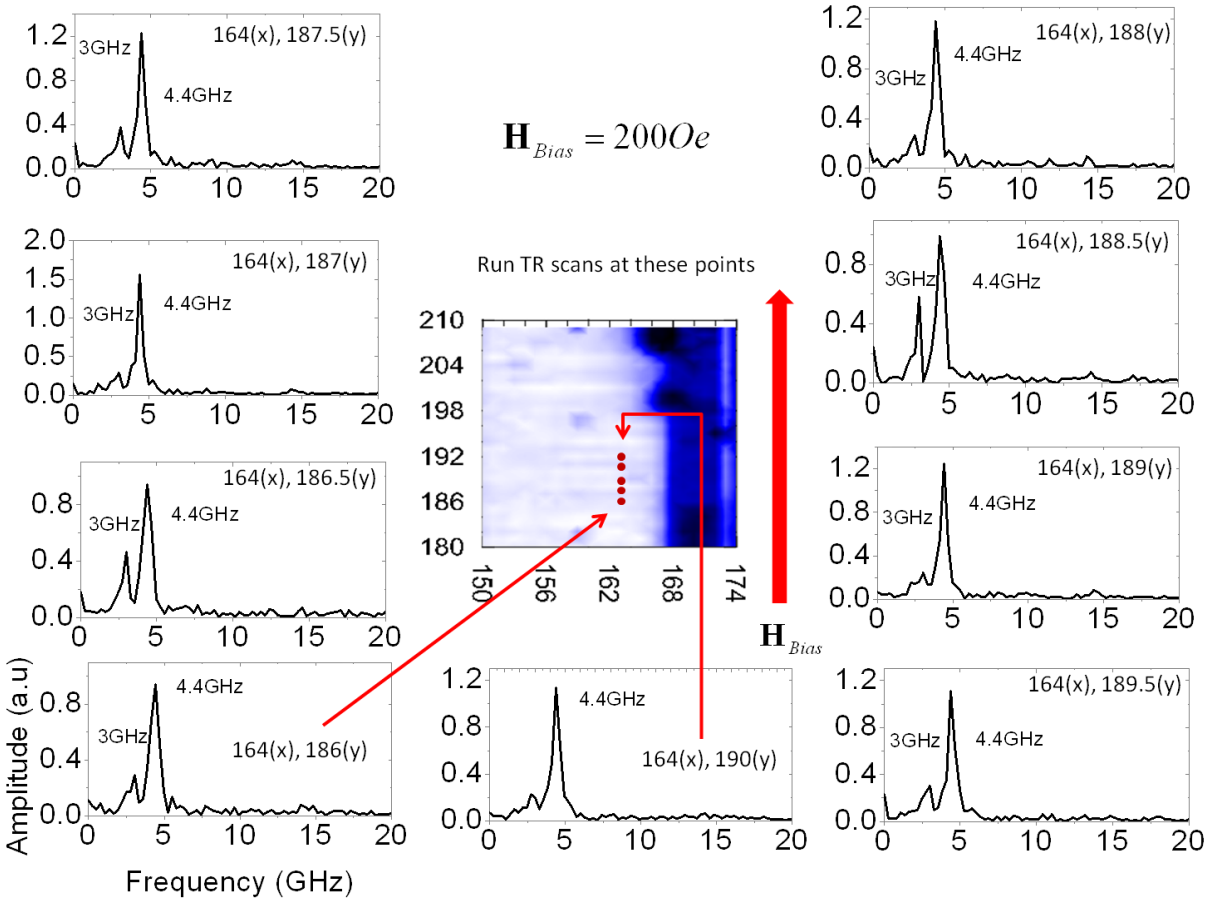

Figure 4.2.3 – Time-resolved scans are performed here 0.5μm apart parallel to the coplanar waveguide using pulsed excitation. The probe positions are several microns from the waveguide due to the rapid attenuation of the pulsed field with distance. The Fourier spectra are shown for points measured parallel to the waveguide. The departure from the straight edge of the waveguide in the reflectivity image in Figure 4.2.3 is most likely to be dirt or debris accumulating in the sample surface.

There is a discrepancy between the Brillouin light scattering mode frequencies (4.2 and 3.3GHz respectively) compared to the mode frequencies presented in the data above at the same field of 200 Oe (4.4 and 3 GHz respectively). The field calibration and the truncated time-resolved signals can help explain this. The Hall generator used in the field-pumped Kerr microscope typically has several percent experimental error. The inherent uncertainty in the field calibration and the reduced spectral resolution in the time-resolved signals are most likely to be responsible for this *circa* 10% discrepancy. The mode frequencies shown in figure 4.2.3 prove to be 'on-resonance' for the Kerr imaging shown in the next section.

The spatial Kerr Imaging of the Binary sample

From the Fourier spectra shown in figure 4.2.3, the mode frequencies are determined as 4.4 and 3 GHz respectively. In this step of the methodology, a microwave generator is used to drive the binary sample at the determined mode frequencies. In the presented Kerr images, two 50 x 30μm scans are performed at 3 and 4.4GHz, juxtaposing the bare un-patterned permalloy with the patterned region of the binary sample. This is followed by two smaller area 2 x 15μm scans on the binary sample imaging the mode profiles on a smaller length scale. To be consistent with the chronology of measurement the large area 50 x 30μm scans are presented first.

The 4.4GHz mode – 50 x 30μm scan

For the larger area 50x30μm Kerr imaging, the demarcation between the patterned cobalt anti-dot region and the un-patterned Permalloy film was unknown. A series of 'exploratory' time-resolved scans were performed along the waveguide at intervals of several 10's of microns. The Fourier spectra lost its lower frequency peak at 3 GHz when the probe spot left the patterned region. In figure 4.2.4 (a) the red rectangle shows the region over which the 50 x 30 μm scans

were performed. The region overlaps the sample region (white) and the GaAs substrate. Extended exposure to the focused probe beam has damaged the substrate, shown by the darkened region. The probe spot is positioned within a few microns from the waveguide, indicated by the circle dot in figure 4.2.4(b).

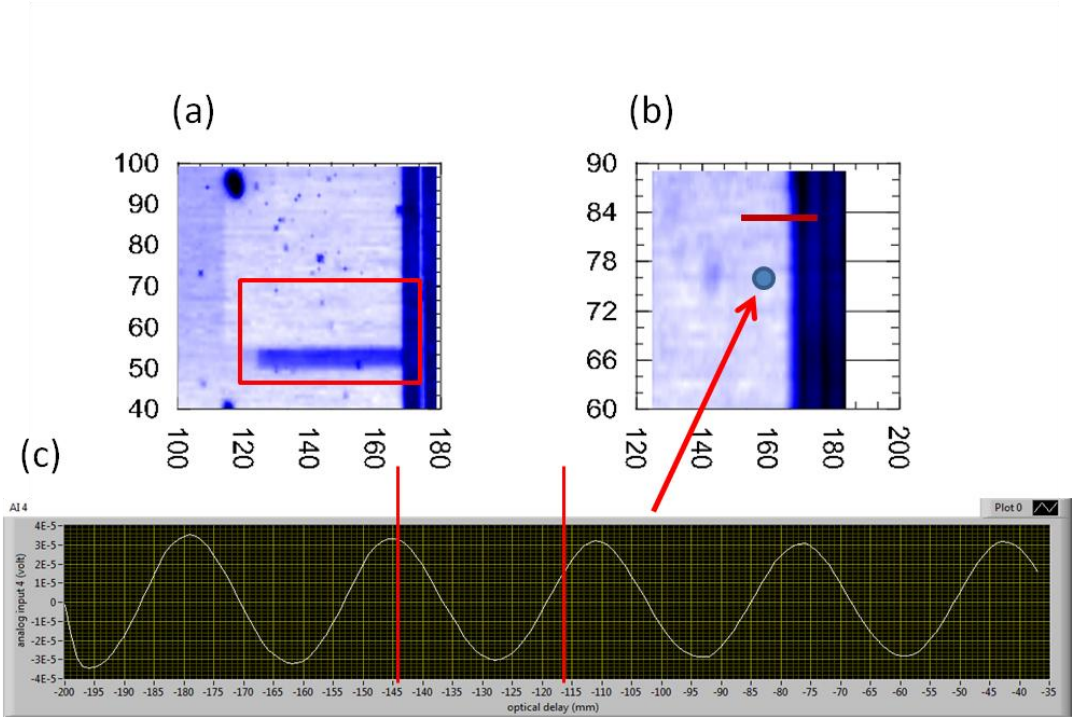

Figure 4.2.4 – The red rectangle in (a) denotes the scanned region of the sample. The scan region overlaps some of the gallium-arsenide substrate and the dark blue region at rectangle bottom is the burning of this region from the optical probe. Driving the sample with continuous wave excitation at 4.4 GHz, the probe beam is positioned close to the sample waveguide denoted by the dot in figure 4.2.4(b). The (red) line in figure 4.2.4 (b) denotes the line scan used by the auto-focus program. The time-resolved signal observed at the position of the dot in figure 4.2.4(b) is shown in figure 4.2.4(c). The red vertical lines designate stage delay start and finish points of the scan.

The horizontal axis in figure 4.2.4(c) is stage delay position in mm and the vertical axis is the lock-in Kerr signal voltage in μV. The signal amplitude typically is tens of microvolts. A sinusoidal signal is observed in 4.2.4(c), stage delays chosen over a cycle of precession are chosen at 8 points, corresponding to $\boldsymbol{\pi/4}$ radians apart.

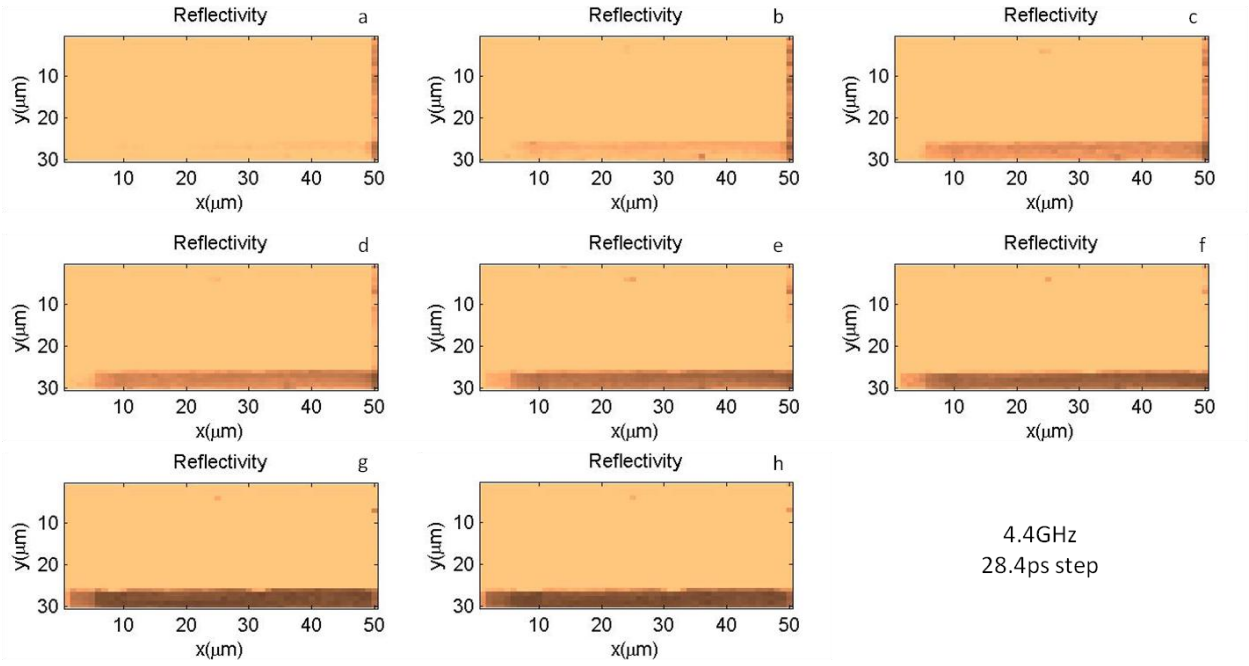

Figure 4.2.5 – The DC reflectivity images for the 50 x 30 μm scan region at $\boldsymbol{\pi/4}$ or 28.4 ps apart (a - h). The edge of the waveguide can be seen at the right edge of each image and is included to determine the amount of drift between successive images. The GaAs substrate is sensitive to optical exposure and the progression of the burning can be seen in subsequent images.

In figure 4.2.5 the DC reflectivity images at each time delay 'a' through 'h' are shown, corresponding to stage positions of -145, -140, -136, -133, -127, -122, -119 and -116mm respectively. Images 'a' to 'h' corresponds to one cycle of precession at 4.4GHz, the temporal step between each image is just over 28ps.

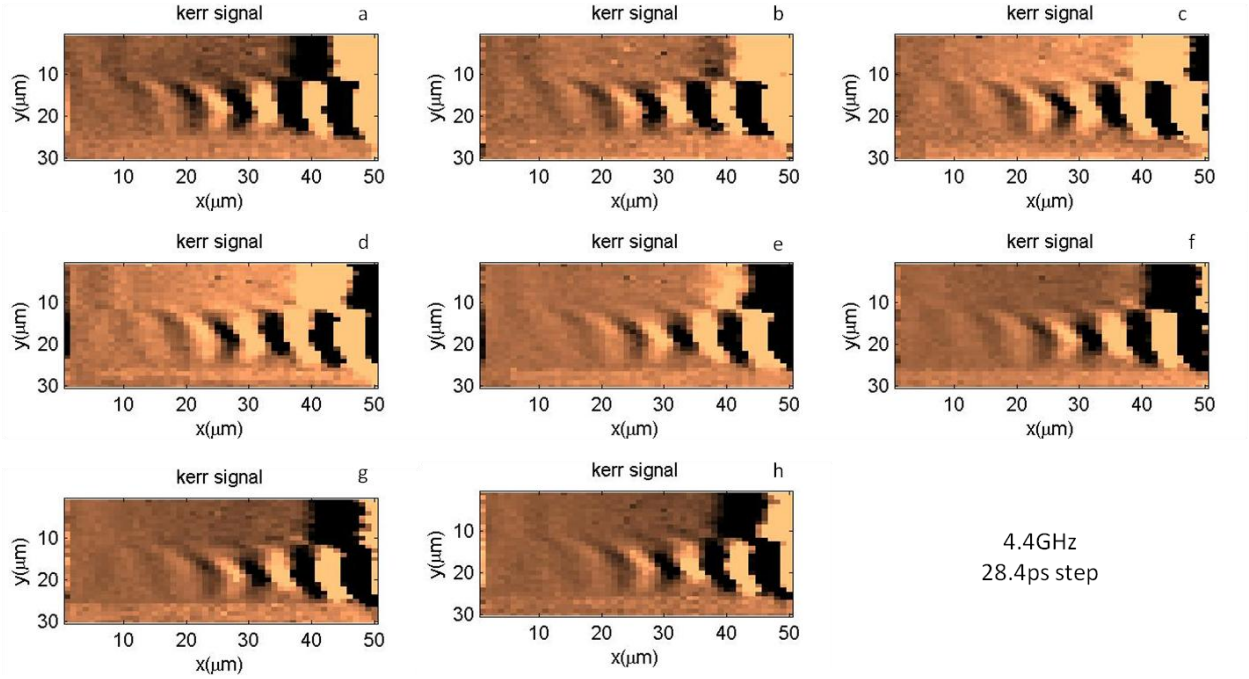

Figure 4.2.6 – The set of Kerr images corresponding to the reflectivity images in figure 4.2.5. The Kerr images are recorded simultaneously with the reflectivity images. The burnt rectangular strip can be seen image bottom, the dark and light ripples represent propagating spin waves in the bare permalloy, propagating to a distance of 40 μm. The binary region is image top, the distance to which any dynamics travel is much shorter. The microwave power is 18dBm and a 200Oe field is parallel to the waveguide.

The 50 x30 μm Kerr signals shown in figure 4.2.6 juxtaposes the contrasting behaviour of two different regions of interest on the sample. To limit drifts the step size is 1 μm. The Kerr scans reveal clear peaks and troughs, shown by the dark and light regions in the images (between 15 and 25 μm on the y axis). This region is the un-patterned permalloy film and spin waves are propagating for a distance of 40 μm. Contrastingly, above this region, between 0 to 15um on the vertical 'y' axis is the binary region containing the patterned region. Here the spin waves travel

no more than 10 μm. It is clear from figure 4.2.6 the distance which spin waves travel in the binary region is reduced. The data in figure 4.2.6 has been plotted from a different angle in 3 dimensions shown in figure 4.2.7.

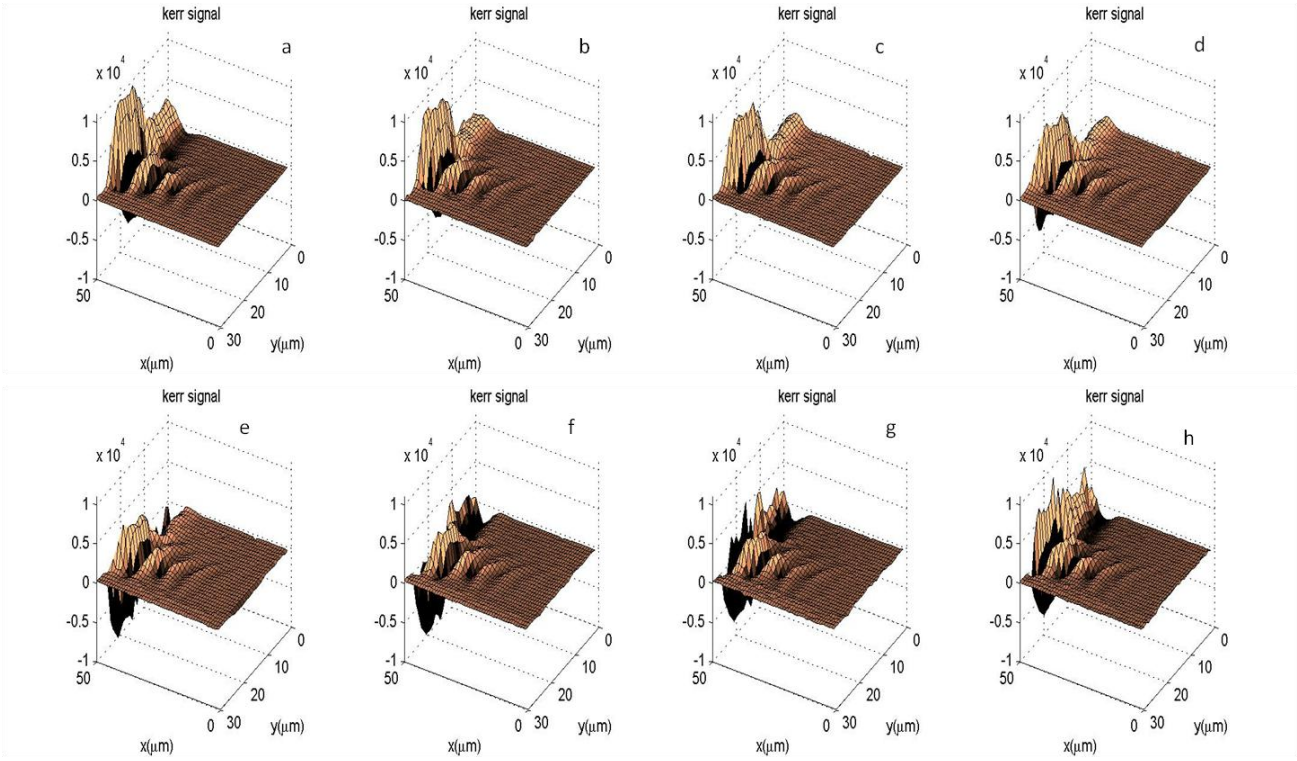

Figure 4.2.7 – Figure 4.2.6 has been re-plotted to further show the contrasting behaviour of the two regions. The un-patterned permalloy is located image front. What is clear is the different distances spin waves travel in both regions of the sample. Images 'a' to 'h' correspond to the same stage delays in figure 4.2.5 and 4.2.6 respectively.

The 3.04GHz mode – 50 x 30um scan

The large area 50 x 30 μm scan at 4.4 GHz in figure 4.2.6 contained such contrasting dynamics of the un-patterned permalloy and the patterned region containing cobalt dots. To

investigate what happens at the lower mode frequency in this region the scan was repeated at 3.04GHz. For completeness the reflectivity images have been included for the 3.04GHz scan.

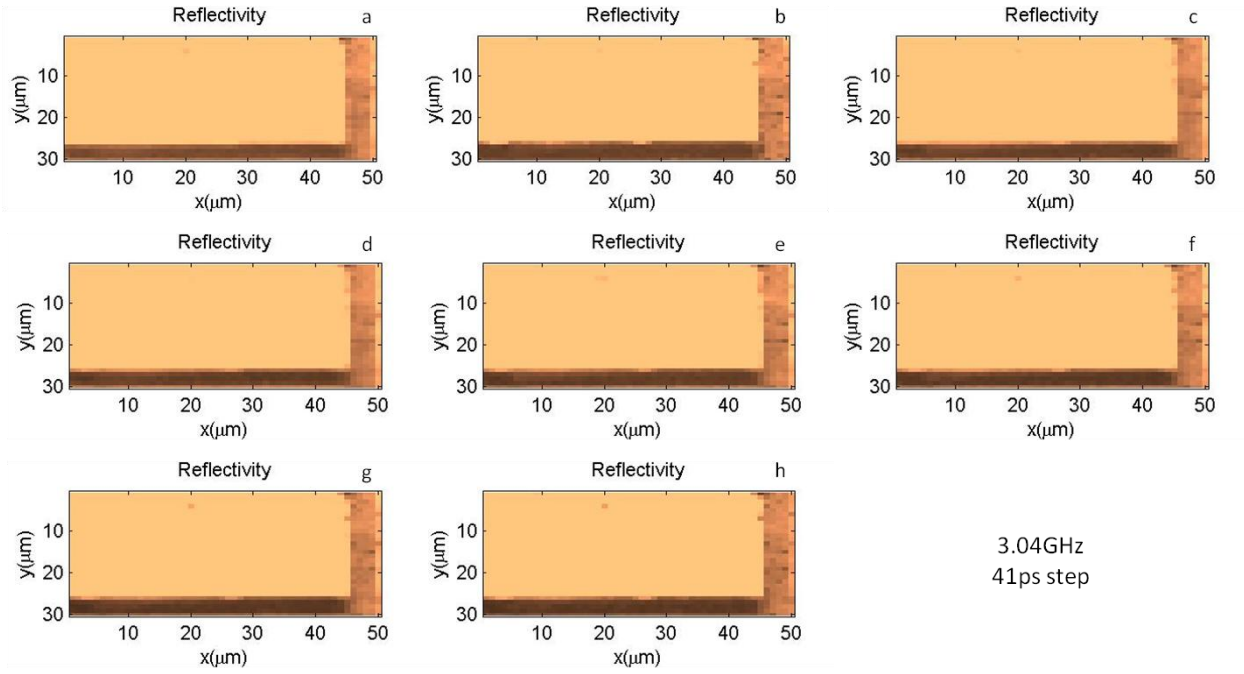

Figure 4.2.8 – Reflectivity scans for the 3.04 GHz mode, the ground line of the sample waveguide can be seen image right and the burn track from previous scans can be observed. The waveguide ground line is 4 μm wide. The microwave frequency is not exactly 3GHz, this is because the microwave frequency needs to be an integer multiple of the laser repetition rate of 80 MHz.

The letters ‘a’ to ‘h’ in figures 4.2.8 and 4.2.9 correspond to delays of -163, -155, -150, -146, -140, -133, -130 and -125mm respectively.

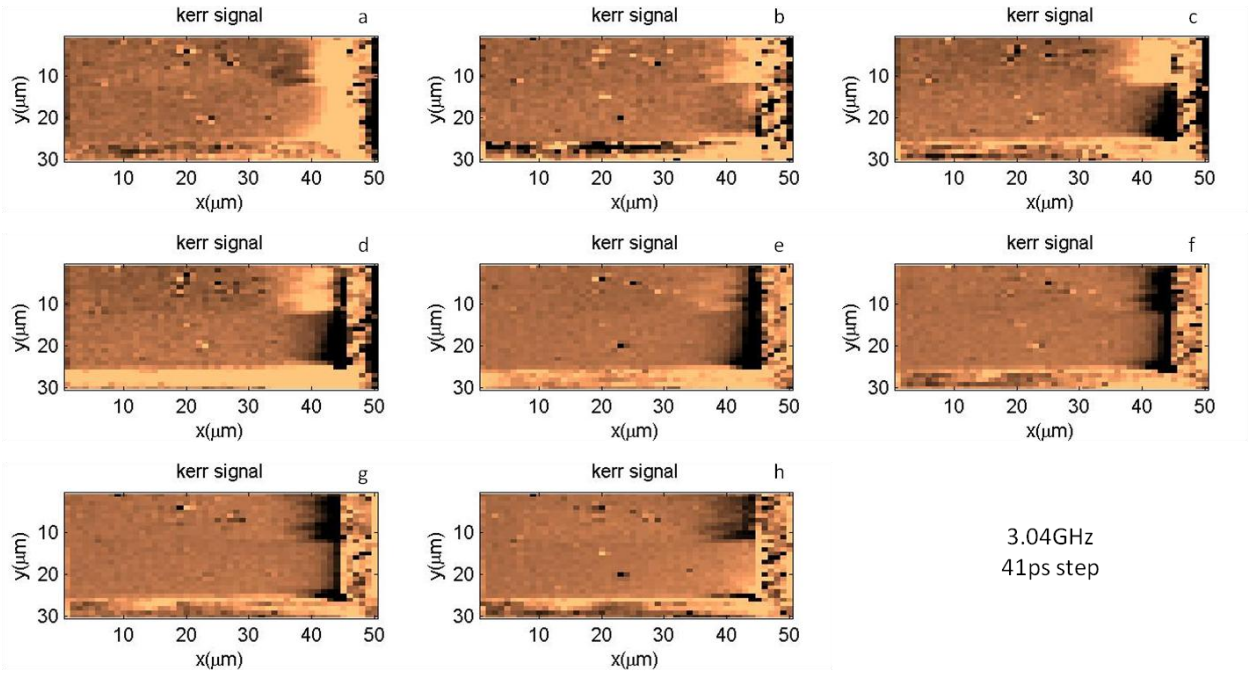

Figure 4.2.9 – The Kerr images at 3.04GHz and microwave power of 18dBm. A striking contrast is seen between these images and those of figure 4.2.6. In the un-patterned region no propagating spin waves are seen. The permalloy is off-resonance at this frequency seen from the Fourier spectra in figure 4.2.3. The patterned region shows a short range (*circa* 10 μm) disturbance extending out from the waveguide, from the images there appears to be no phase variation (colour contrast) in this region. A lack of phase contrast or variation suggests that a wave is non-propagating.

The 4.4GHz mode – 2 x 15um scan

In figures 4.2.4, 4.2.5, 4.2.6, 4.2.8 and 4.2.9 the waveguide is located in the right of the image, by switching axis the waveguide now appears at the top of the image, shown by the DC reflectivity images in figure 4.2.10 (a) and (b). In figure 4.2.6, the spin wave propagation distance is reduced in the patterned binary region compared to the un-patterned permalloy region, 10 μm Vs 40 μm respectively.

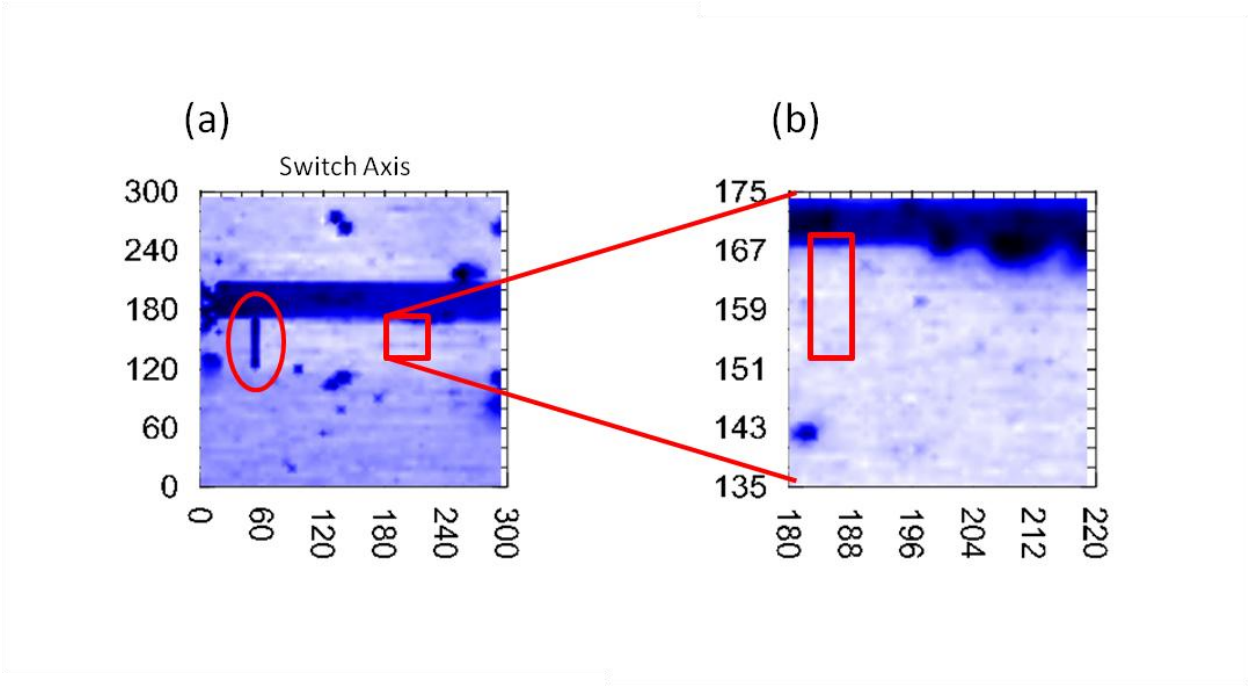

Figure 4.2.10 – In (a) a large area 300 x 300 µm scan of the sample region in switched axis mode, This changes the raster scan direction to help prevent drift for the long and narrow 2 x 15 µm scan. Scanning is performed across the narrow edge of the rectangle, making the scan less sensitive to drifts than by scanning along the long edge. The circle mark in figure 4.2.10 (a) denotes the burnt region that was formed by the previous 50 x 30 µm scans. The red rectangle in (b) denotes the 2 x 15 µm scan region.

Performing scans with a smaller scan size, more detail is observed. The scan size of 50 x 30 µm scan had a step size of 1 µm in both in-plane directions. The 2 x 15 µm scans have a step size along the narrow and long edges of 0.125um and 0.5um respectively.

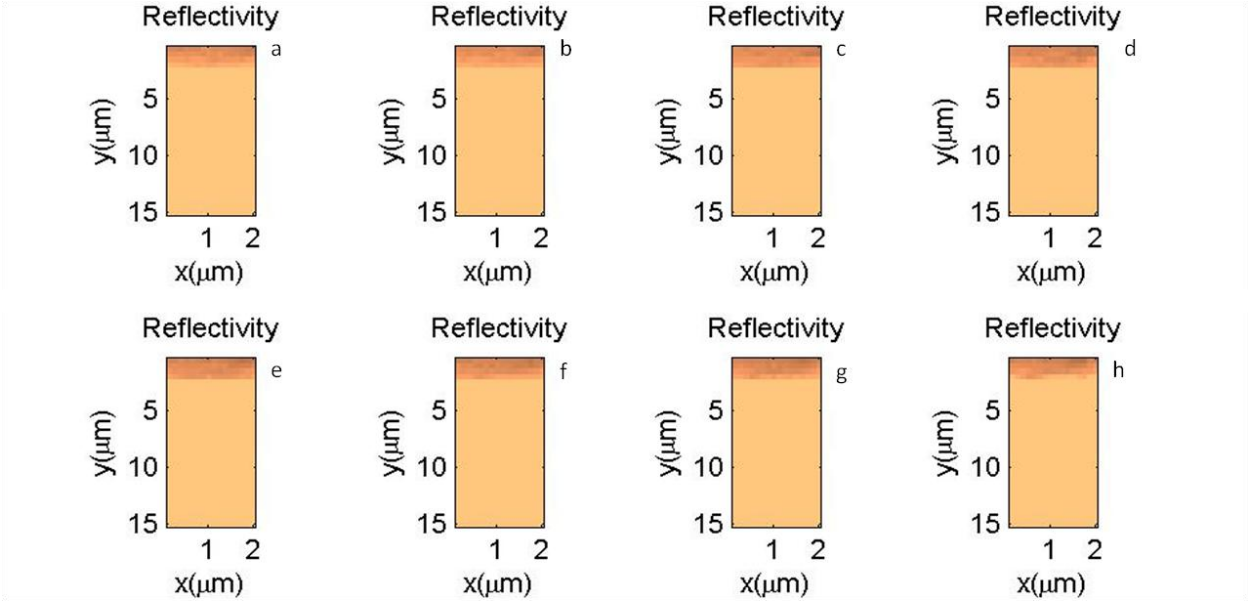

Figure 4.2.11 – Reflectivity images of the 4.4 GHz microwave excitation. In the 2 x 15 μm scans the step sizes in the x and y directions are 0.125 and 0.5um respectively. The reflectivity images are stable to a micron in the 'y' direction. To obtain images with minimal drift can take multiple attempts; usually scans were performed during the night to ensure the ambient environment was as stable as possible.

The corresponding stage delays for images 'a' to 'h' in figures 4.2.11, 4.2.12 and 4.2.13 are -171, -166, -162, -160, -153, -148, -145 and -142mm. The animated movie (not presented) comprising images 'a' through 'h' in figure 4.2.12 and 4.2.13 shows the 4.4 GHz mode to be propagating. The mode propagates preferentially between the cobalt dots and the patterning reduces the propagation distance by about a factor of four. In section 4.5, data from the 4.4 GHz scans are fitted to determine the wavelength and decay constant.

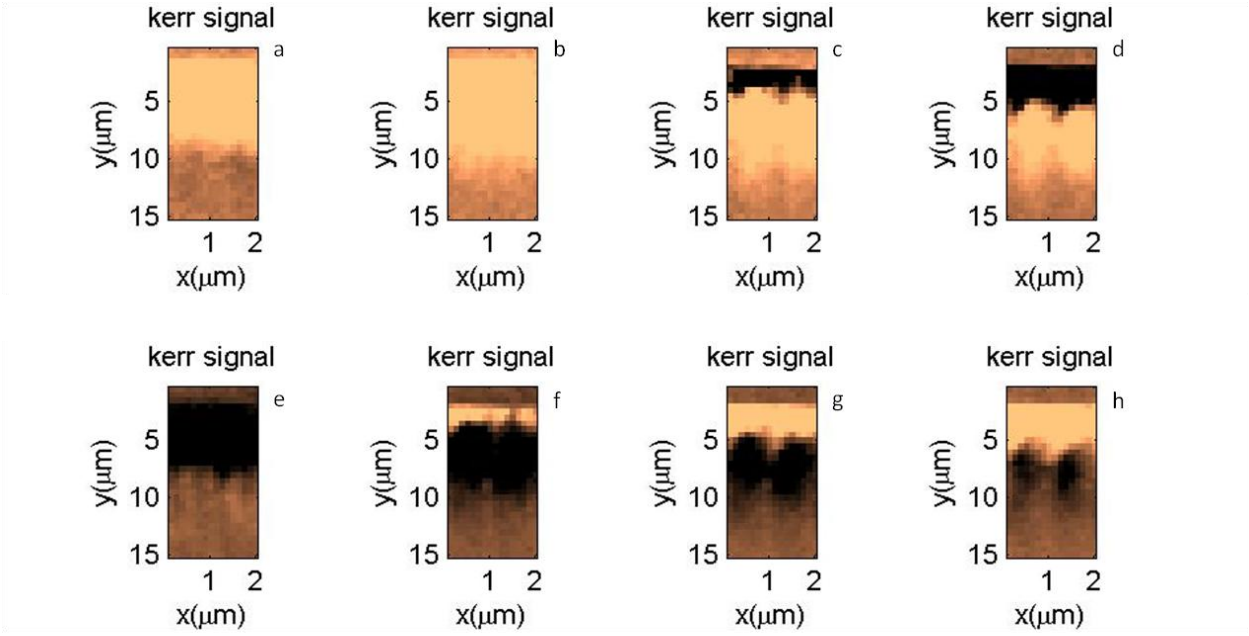

Figure 4.2.12 – The Kerr signals ‘a’ to ‘h’ for at 4.4 GHz and 18 dBm microwave power. The appearance of two ‘stripe’ like streaks can be seen with a spatial separation of 1 μm, which is equal to the lattice constant. This mode appears between the cobalt dots in the inset simulations of figure 4.1.1. Along the length of the streaks, the colour representing phase variation can be seen, suggesting that the 4.4GHz mode propagates from the waveguide. The propagation distance qualitatively is 10 μm.

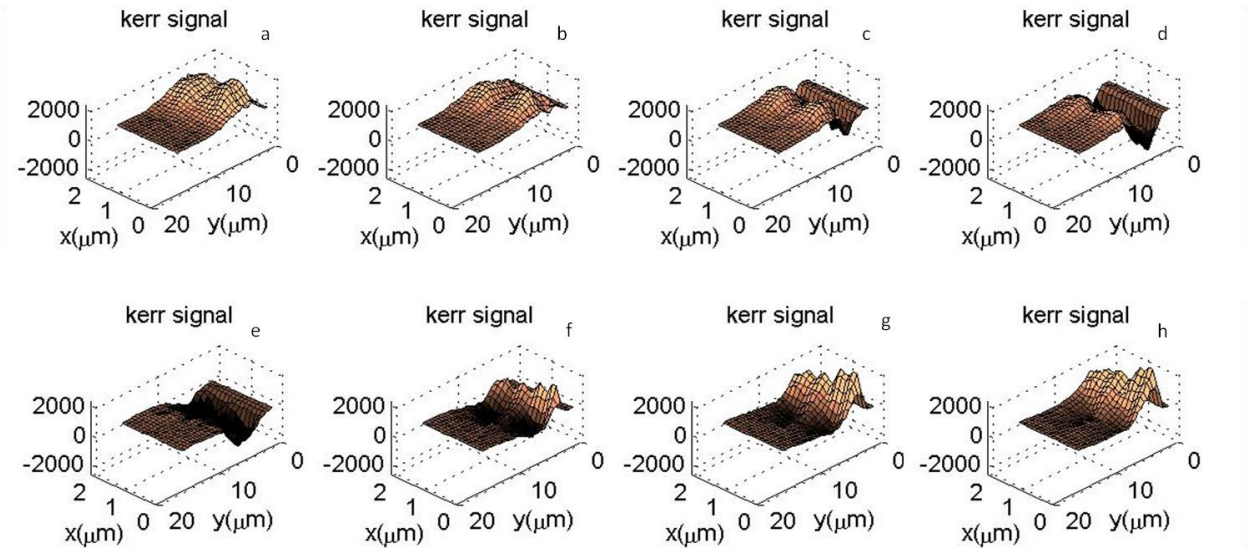

Figure 4.2.13 – 3 dimensional AC Kerr images re-plotted from figure 4.2.12. From this vantage point twin peaks can be observed, moving away from the waveguide in images ‘a’ to ‘h’, the phase contrast information in figure 4.2.12 and the forward moving humps in this figure show the 4.4GHz mode to be propagating.

The 3.04GHz mode – 2 x 15um scan

It was seen in the last section that the character of the 4.4GHz mode in the patterned region is propagating. In this section the same process is repeated for the 3.04GHz mode. In figure 4.2.16, Kerr images of the 3.04GHz excitation are presented. The ‘furrows’ in the images are kinked due to horizontal drifts during the scan of the order 0.5 μm. In figure 4.2.15, images ‘a’ to ‘h’ reveal little drift in the ‘y’ direction, it is not possible to determine drift in the orthogonal ‘x’ direction.

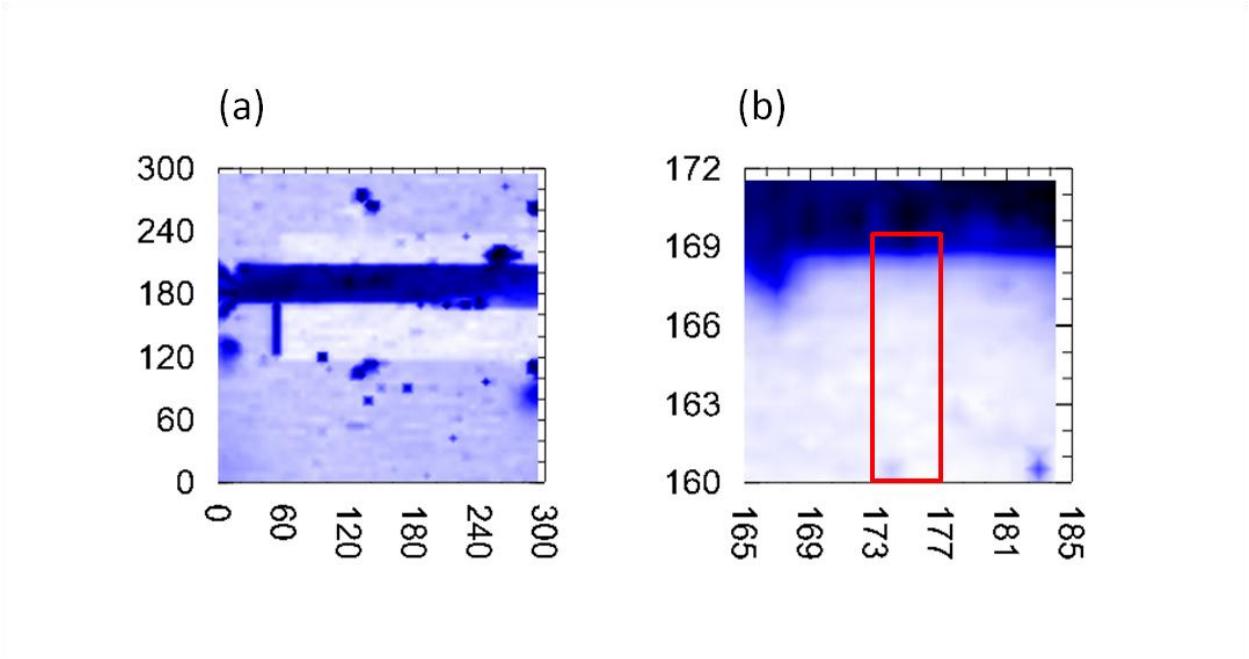

Figure 4.2.14 – In 4.2.14 (a), a 300 x 300 μm scan is used to obtain a 'strategic' overview of the sample. In (b) the highlighted region showing scan region for the 3.04 GHz excitation.

The stage delays corresponding to images 'a' to 'h' in figure 4.2.15 and 4.2.16 are -198, -193, -188, -182, -175, -170, -164, and -158mm respectively. An alternative view of figure 4.2.16 is plotted in figure 4.2.17. A constant phase relationship observed along a furrow shown in figure 4.2.16 (a) indicates a standing or a driven wave created by the sample waveguide.

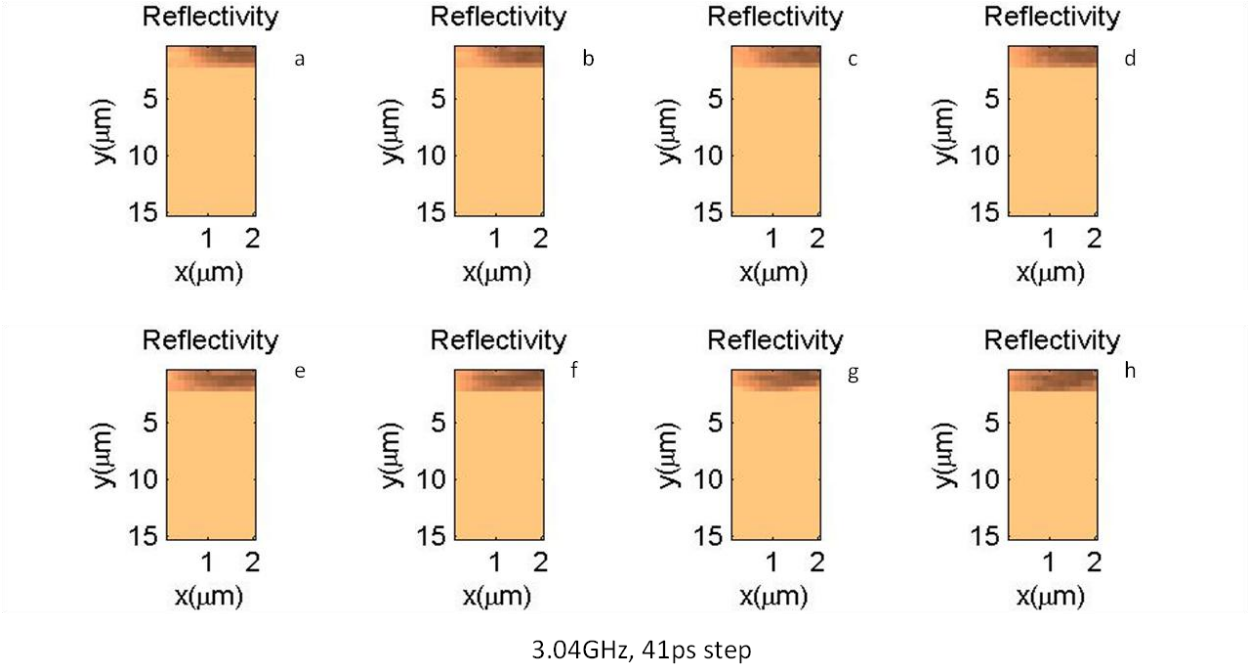

Figure 4.2.15 – Reflectivity scans of the region highlighted in figure 4.2.14 (b).

In figure 4.2.16 (b - d) inclusive, a dark region of opposite phase moves out from the waveguide following the furrow. For an unknown reason, the left hand furrow in 4.2.16 (e) is darker than the right side.

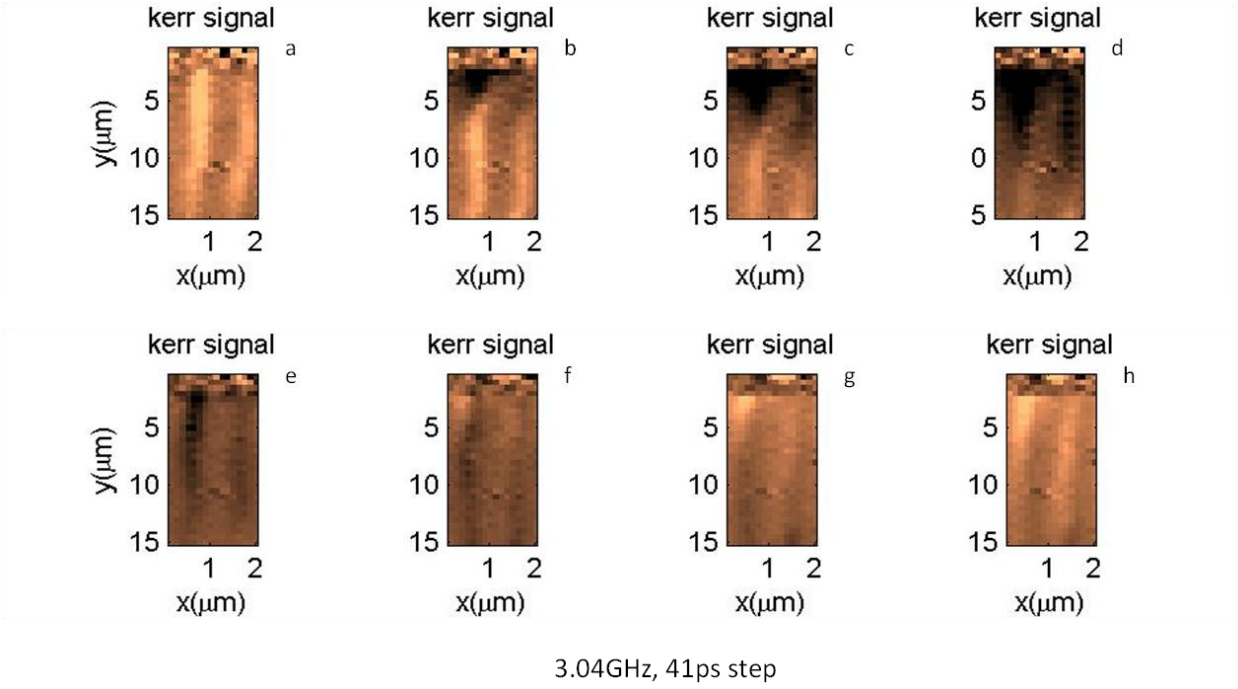

Figure 4.2.16 – Kerr images at 3.04 GHz, 18 dBM and 200 Oe parallel to the waveguide. Image 'a' shows uniform (light) phase contrast along its furrows, 'b' through' show a change in phase (dark) advancing away from the CPW. Then images 'e' to 'h' show uniform phase along the furrow length.

The animated movie of figure 4.2.16 and 4.2.17 (not shown) reveals the 3.04 GHz mode to be a propagating mode with a long wavelength (several tens of microns) but with a very short decay length as it propagates in the binary region. The mode at 3.04GHz can only exist in the patterned region. In figure 4.2.9 no propagation is observed into the un-patterned permalloy.

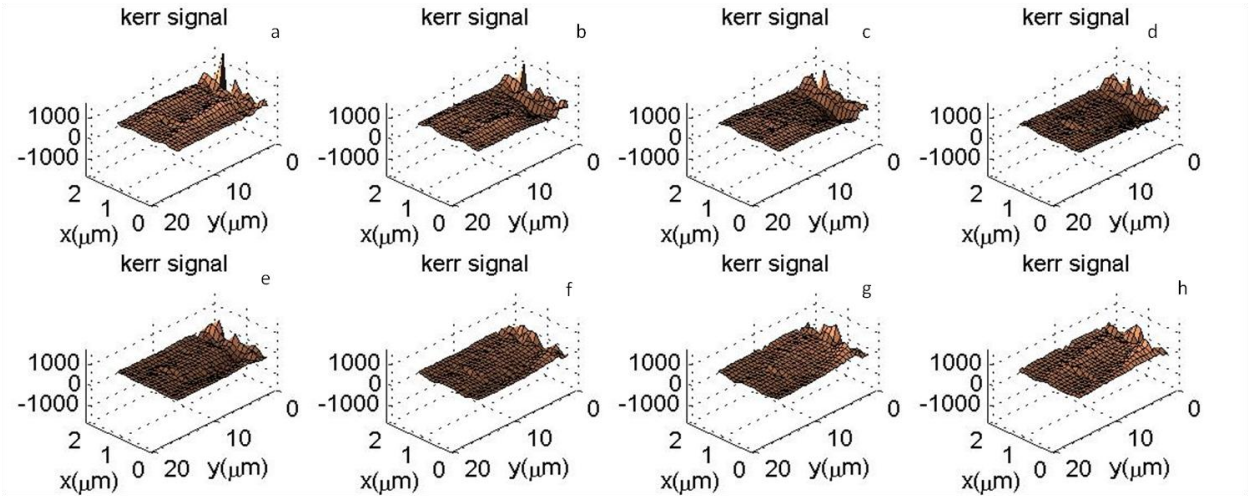

3.04GHz, 41ps step

Figure 4.2.17 – The alternative view of figure 4.2.16. The furrows seen in the previous figure are clear, however, the overall mode character is not. The character exhibited of the 3.04GHz mode remains elusive.

4.3 The patterned air-filled Anti-dot reference sample

In the last section, the time-resolved signals and Kerr images of the patterned binary sample were presented. Here, in this section the same approach is undertaken for the air-filled anti-dots. In a region centered between the alignment marks in figure 4.3.1 (b), time-resolved scans were performed at a series of points parallel to the sample waveguide. The time-resolved scans are shown in figure 4.3.2.

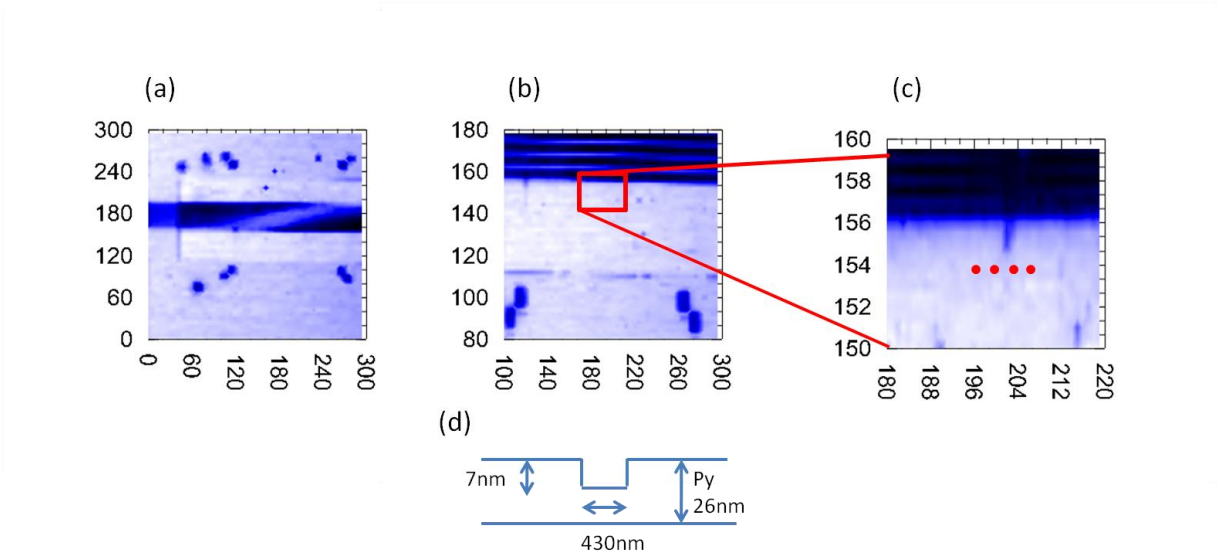

Figure 4.3.1 – Reflectivity scans of the anti-dot ref sample (a), (b) is centre of the alignment marks where the air filled anti-dots are located. In (c) the dots represent schematically where time-resolved scans probed the air-filled anti-dots. Sample dimensions are identical to cobalt filled dots of the binary sample in figure 4.4.1 (c).

The Anti-dot Reference Time-resolved signal

The corresponding Fourier spectra are shown in figure 4.3.3. The mode spectra are more complicated than the binary sample; primarily by the emergence of an additional peak around 6.5GHz. The origin of this peak is not investigated and its position dependent behaviour implies relation to the anti-dots.

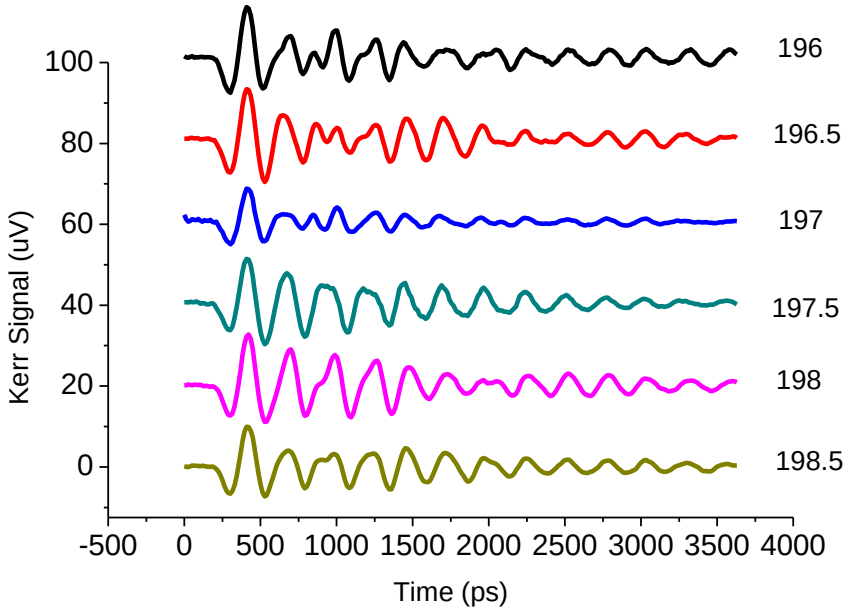

Figure 4.3.2 – Time-resolved scans for the air-filled anti-dots for pulsed excitation at 0.5 μm intervals at a field of 200 Oe. The numbers rights of the time-resolved signals are the 'x' or horizontal coordinate of the scan position, the 'y' position was kept at 156 μm.

A dominant peak at 3.84GHz is present for all probe positions; a second mode at 4.7GHz varies its amplitude with the TR scan position. The mode frequencies taken from 4.3.3 are 3.85 and 4.7GHz respectively.

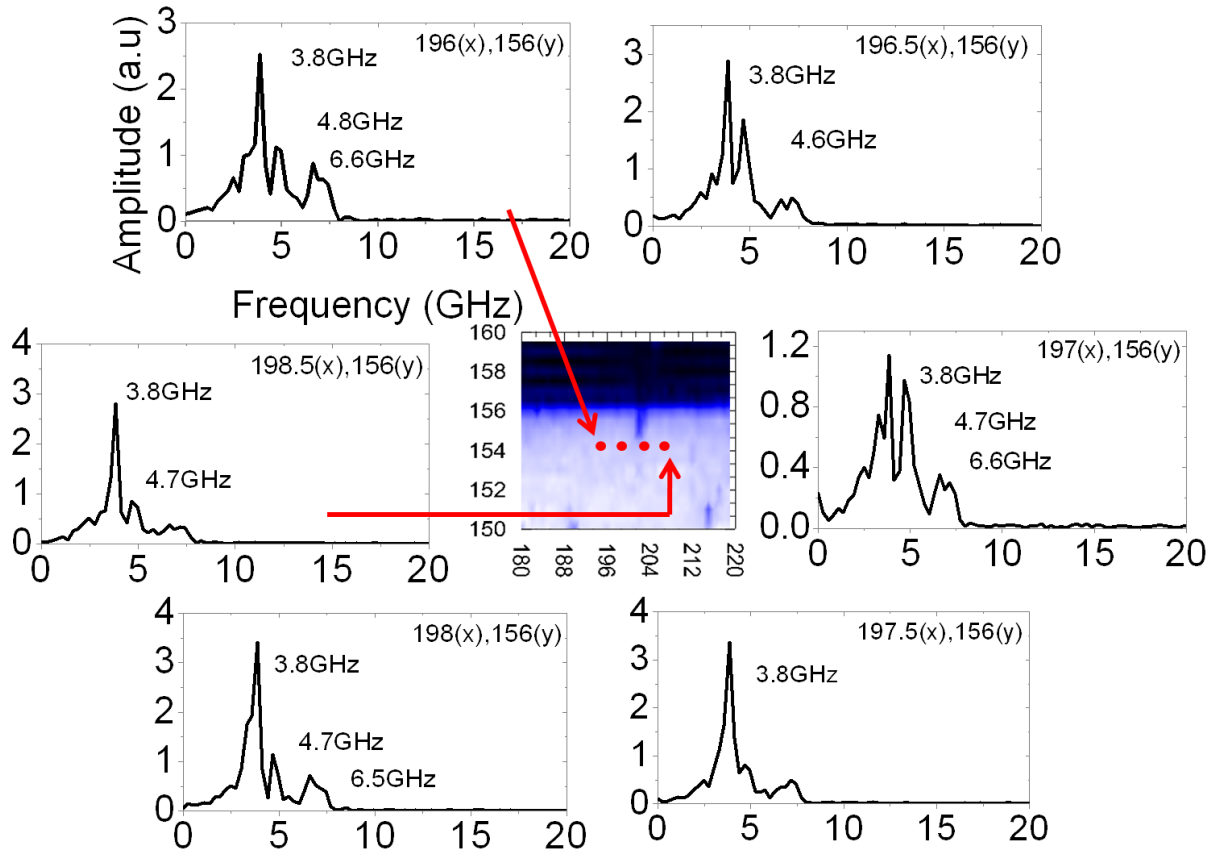

Figure 4.3.3 – Fourier spectra of the time-resolved scans in figure 4.3.2.The two modes of interest are at 3.85 and 4.70 GHz, an additional higher frequency mode at 6.56 GHz is also observed.

The spatial Kerr Imaging of the Anti-dot Ref sample

Following the time-resolved signals, Kerr imaging is performed using continuous wave excitation at the extracted resonant frequencies. Scans of 2 x 15 μm are performed at 3.85 and 4.70 GHz. In figure 4.3.4 (b), the scan region is denoted by the (red) rectangle.

The 3.85GHz mode – 2 x 15 μm scan

The lattice constant of the air-filled anti-dots is identical to the previous sample, hence the same size 2 x 15 μm scans are used to image the modes. Larger area (20 x 20um) scans were performed and are not shown.

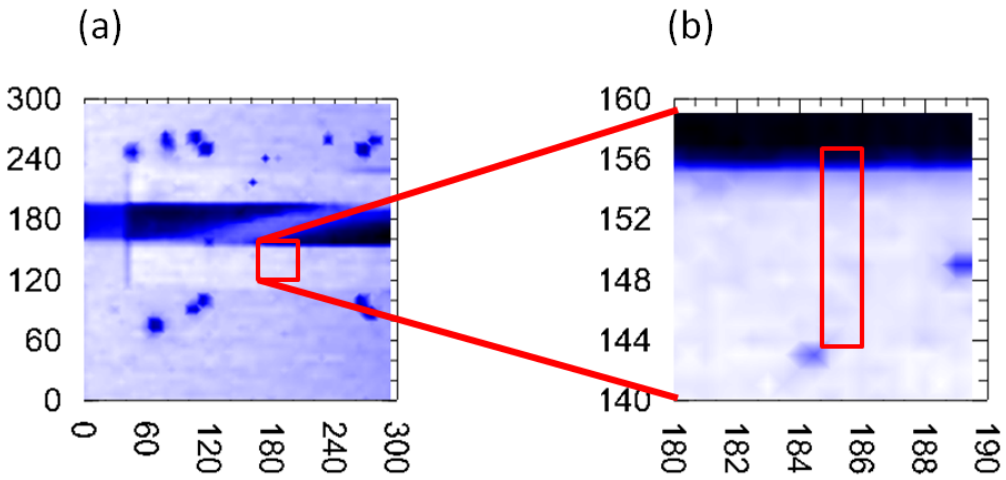

Figure 4.3.4 – The region of the anti-dot sample where Kerr imaging was performed at both 3.85 and 4.7 GHz, shown by the (red) rectangle in (b). The continuous wave time-resolved signal was acquired from 186(x), 153(y) in figure 4.3.4 (b).

The reflectivity images are shown in figure 4.3.5. The waveguide is located at the top of the images. The ground and signal lines of the waveguide are too wide to explain the visible striations in figure 4.3.5 (a - h). The edge of the waveguide is not observed to shift from one reflectivity image to another, indicating that drift is not responsible for this. The stage delay

positions for figure 4.3.5 and figure 4.3.6 ‘a’ to ‘h’ are -237, -230, -227, -223, -216, -212, -208 and -204mm respectively.

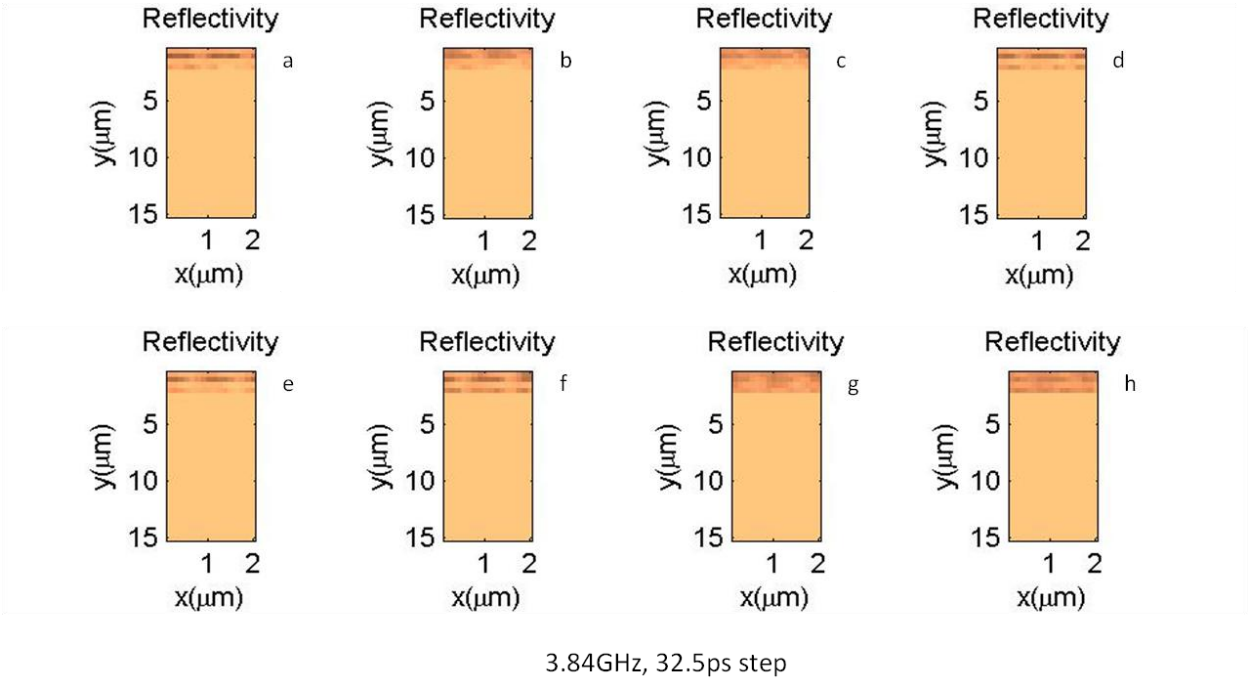

Figure 4.3.5 – Presented reflectivity images for images ‘a’ to ‘h’. The cause of the variation of the top region is unknown.

The Kerr images for the 3.84GHz mode are shown in figure 4.3.6. The step size is 0.125 μm (along ‘x’) and 0.5 μm (along ‘y’). The Abbe diffraction limit gives a spot no smaller than 0.82 λ or 330 nm for 400 nm light. The microwave driving frequency is 3.84 GHz and the microwave power is 18 dBm. The applied bias field is 200 Oe orientated parallel to the waveguide. The Kerr images in figure 4.3.6 show a clear evolution of phase along the stripe(s). In figure 4.3.6 ‘a’ to‘d’ dark regions move out from the waveguide. As the mode amplitude decays, light regions indicating opposite phase appear in figure 4.3.6 ‘e’ to ‘h’. The images in

figure 4.3.6 indicate the 3.84 GHz mode has propagating character. An alternative view of figure 4.3.6 is shown in figure 4.3.7. The amplitude progresses outward from the waveguide in figure 4.3.7 ‘a’ to ‘c’. The rapid attenuation indicates a short decay length. The short propagation distance is imparted by the geometrical patterning in the permalloy, rather than the filling material in the anti-dots.

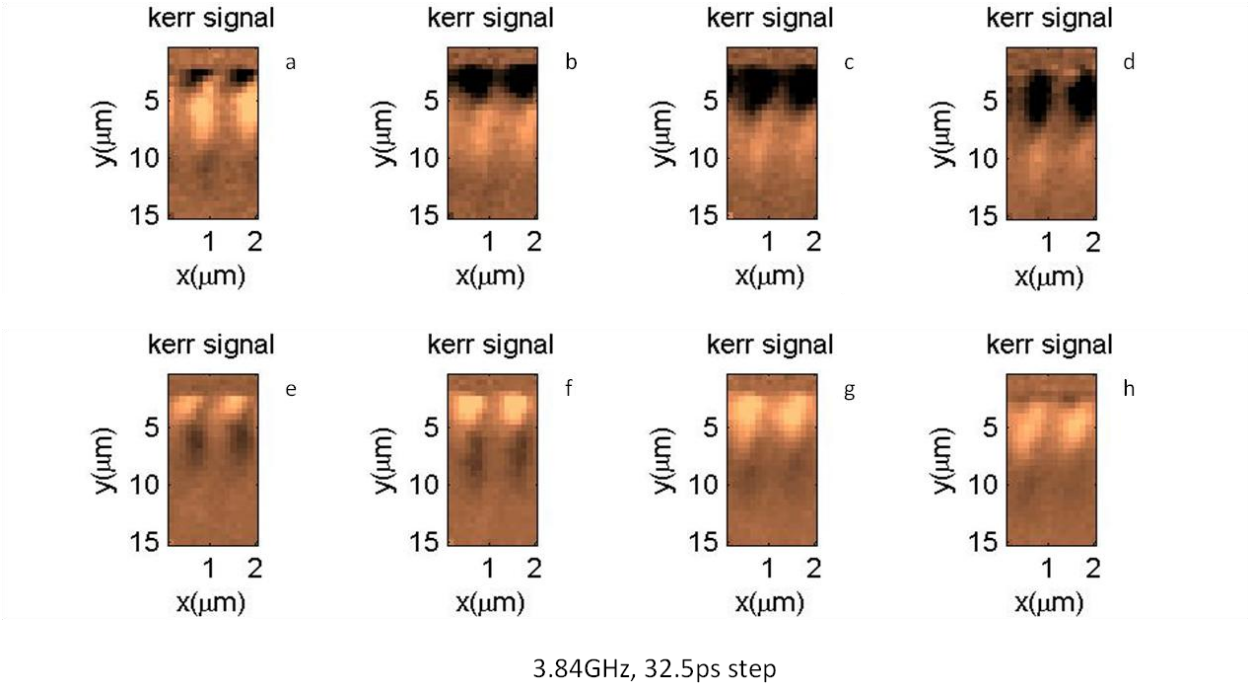

Figure 4.3.6 - Kerr images of the region denoted in figure 4.3.4 (b) driven at a frequency of 3.84 GHz and 18 dBm microwave power.

The phase variation along the mode length in figure 4.3.6 indicates a character of propagating type. The distance travelled in figure 4.3.6 and 4.3.7 is qualitatively no more than 10 μm. Later, this mode is fitted to extract the wavelength and decay constant.

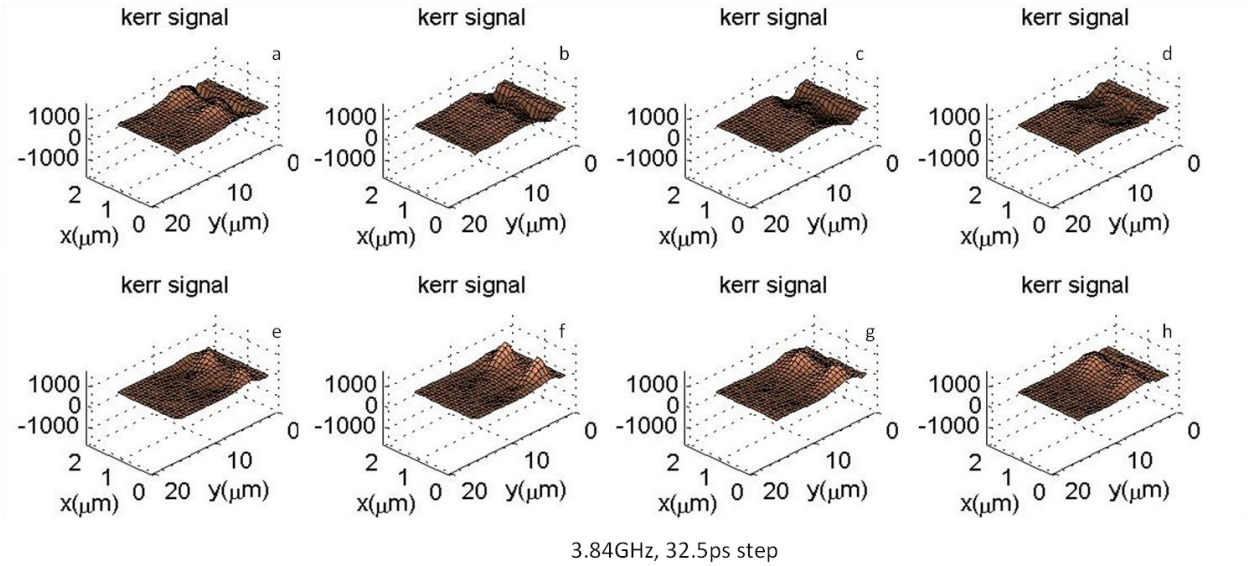

Figure 4.3.7 – Alternative 3 dimensional view of the data presented in figure 4.3.6. The two furrows, thought to propagate between the anti-dots can be seen, the short distance the amplitude travels indicates a short decay length in the patterned region.

The 4.70GHz mode – 2 x 15 μm scan

So far, the 3.85GHz mode has been observed to have a propagating character. Qualitatively, the phase contrast in the images indicates this; however nothing can be said about the wavelength and the decay constant of the sample. The same can also be said for the cobalt binary sample. The patterning of the cobalt filled dots and the air-filled anti-dot decreases the decay length, so spin waves do not travel more than about 10 μm. Also, it is not possible without further data manipulation to say anything about the wavelength, other than that it is longer than the region over which the spin waves decay, otherwise several periods would be visible. Here in this section, the second mode of the air-filled anti-dot lattice is imaged at the higher frequency of 4.70GHz. This region is shown in figure 4.3.4 (b)

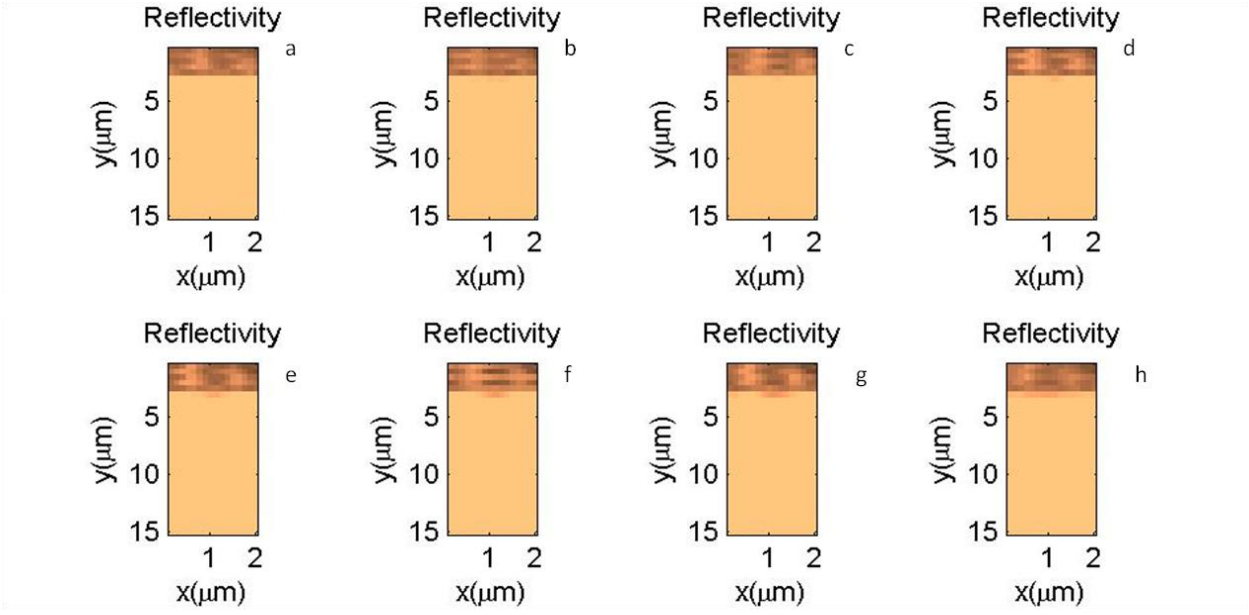

Figure 4.3.8 – The reflectivity scans for the second mode at 4.70 GHz. Due to the clarity of the waveguide edge the intensity contrast on the waveguide is likely to be generated by dirt or dust on the waveguide itself. The sharp edge also indicates the probe focus is stable throughout the scan.

The corresponding Kerr images of figure 4.3.8 are shown in figure 4.3.9. In figure 4.3.9, the contrast along the furrow regions is uniform throughout figure 4.3.9 ‘a’ to ‘h’. The constant phase suggests the mode is not propagating. The image background in figure 4.3.9 close to the waveguide is in anti-phase with the mode stripes, seen in images ‘a’ to ‘h’. The background is composed of permalloy, which at 4.7 GHz is being driven off-resonance. From figure 4.3.3 the permalloy resonance is at 3.85 GHz. Both regions are subject to the driven excitation at 4.7 GHz and consequently posses different phases relative to one another.

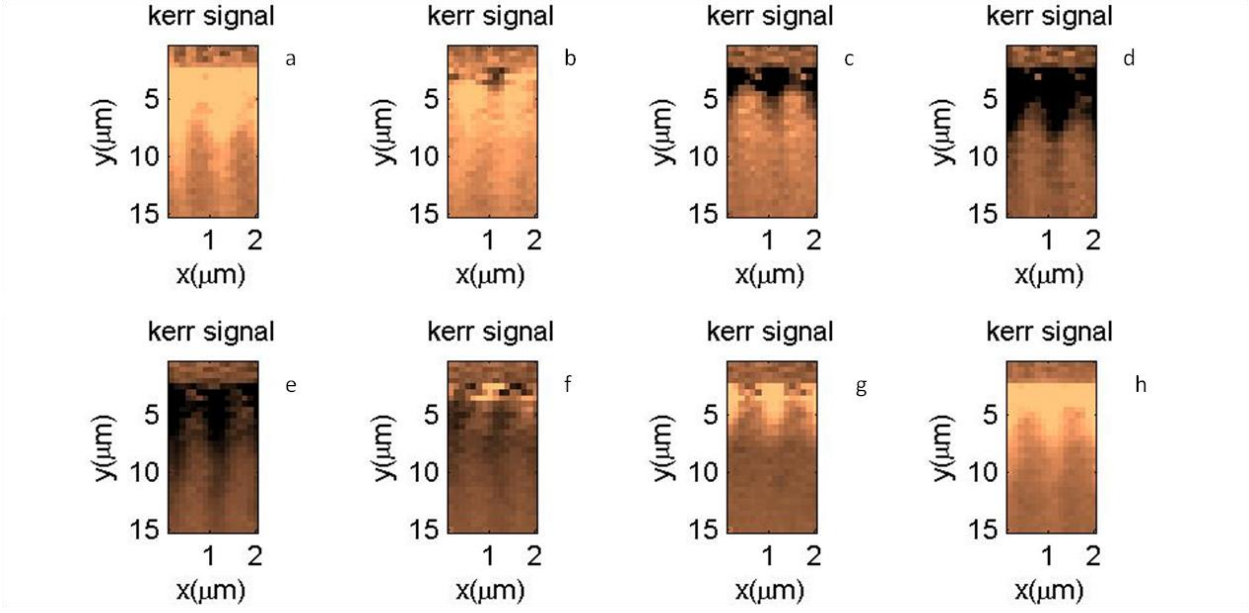

Figure 4.3.9 – Kerr images of the second mode at 4.72GHz. The frequency set on the microwave generator has to be an integer multiple of 80MHz. The closest integer multiple is 4.72 GHz.

Figure 3.4.10 shows an alternative 3 dimensional view of the data presented in figure 4.3.9. The mode at 4.72GHz has driven character. For the images in figure 4.3.9 and 4.3.10, the lack of phase variation along the mode stripes means the entire region is uniformly driven by the microwave field. The sinusoidal excitation is directly driving the magnetisation and the amplitude of the mode depends on the local field from the waveguide which decays rapidly with distance. At distances greater than 10 μm from the waveguide the microwave field is almost completely diminished.

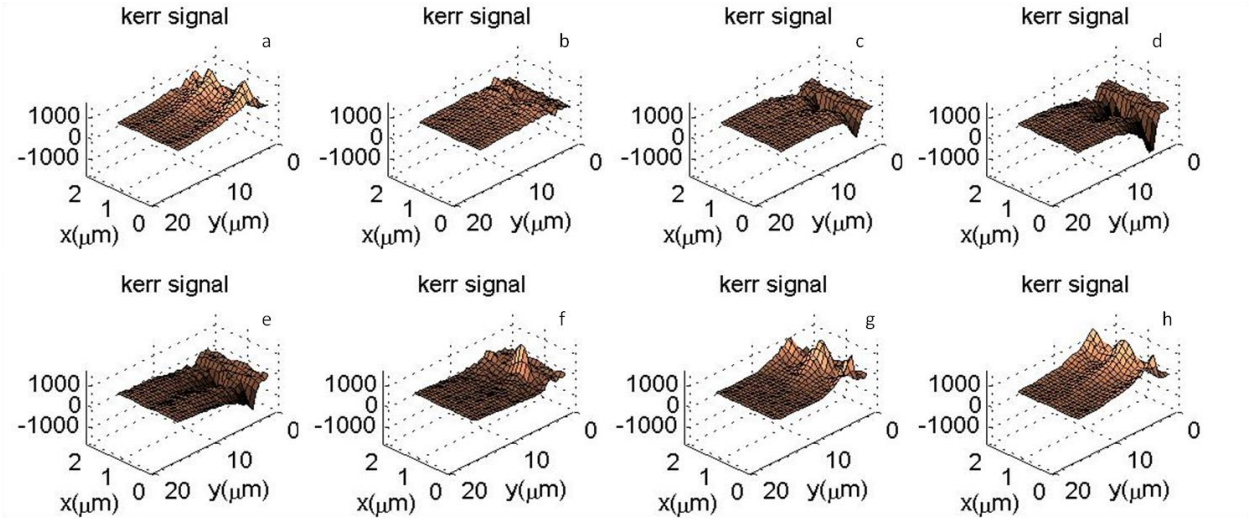

Figure 4.3.10 – Alternative view of figure 4.3.9.

4.4 Fitting of the Spatial Modes

The Binary Sample

Qualitatively, the presented Kerr images provide information whether a mode is propagating or not by the observed phase variation. Additionally, one can estimate the total propagation distance and in the case of un-patterned permalloy in figure 4.2.6 this distance is 40 μm. In the patterned sample regions, this distance is reduced to about 10 μm. It is not possible to estimate the wavelength qualitatively from the images, except for the unpatterned region in figure 4.2.6, where it is roughly 10μm. To determine the decay constant and wavelength, the spatial profiles were fitted to a damped sinusoid, given by equation 4.4.1

$$\phi_{Kerr} = Ae^{-\frac{x}{d}} \cos 2\pi \left[\frac{(x - x_{Shift})}{\lambda} - \frac{t}{T} \right] \tag{4.4.1}$$

Where ‘A’ is the amplitude,‘d’ is the decay constant, ‘x_{Shift}’ is the phase factor, ‘t’ is the time delay the given scan is at, ‘T’ is the period of the microwave frequency. In figure 4.4.1, the 30 x 50 μm scan from figure 4.2.6 is shown with the fitted data of the 4.4GHz spin waves propagating in permalloy. The fitting was performed by choosing a profile through the mode, a line scan, along which a damped sinusoid was fitted for each of the 8 images ‘a’ to ‘h’ respectively. From figure 4.4.1, the best fit for the wavelength and decay constant are 7.5 μm and 9μm respectively.

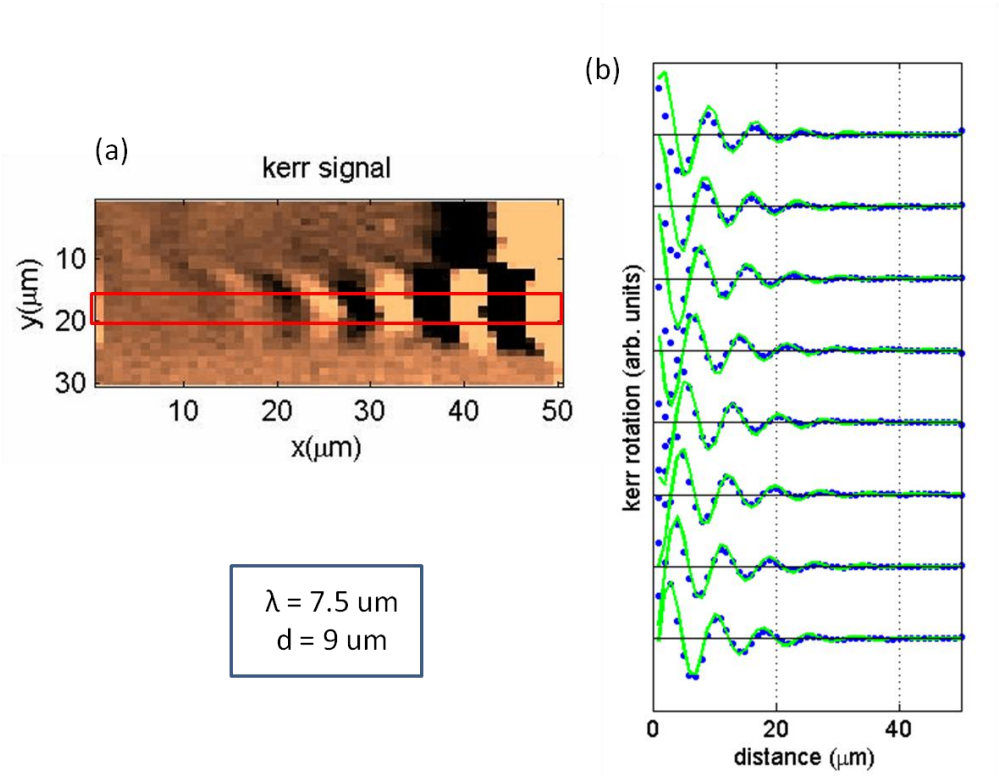

Figure 4.4.1 – Fitting of the 30x50 μm scan taken at 4.4GHz on the binary sample. The rectangle in (a) denotes the region over which the line scan was averaged. In (b) the data points (blue dots) and the line of fit (green line) are shown. The bottom fit corresponds to the first image ‘a’ and the top fit represents the final image ‘h’.

The propagating spin wave shown in figure 4.4.1(a) is fitted in figure 4.4.1 (b). The fitting parameters are determined visually, a so-called 'eye-ball' fit. The data in figure 4.4.1(b) is easy to fit due to the multiple oscillations. For other lines scans such as shown in figure 4.4.2; the fitting of the data is more difficult due to the lack of complete spatial oscillations. The mode is shown from two different views, figure 4.4.2 (a) and 4.4.2 (b) and the fitted data is shown for the wavelength and decay constant of 15 μm and 4 μm respectively.

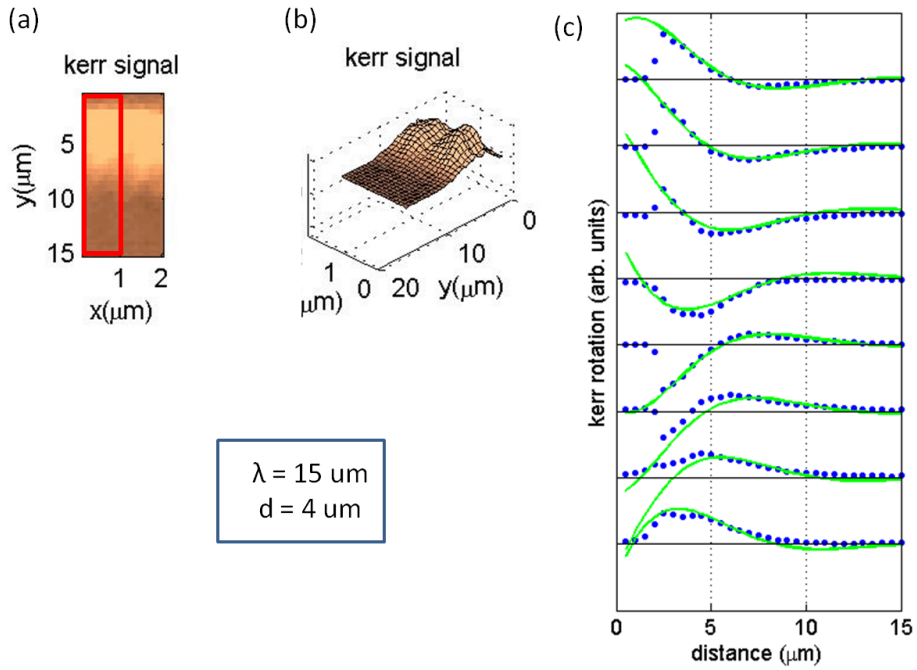

Figure 4.4.2 – The best 'eye-ball' fit for binary sample at 4.4GHz.The 2 x 15μm scan data was found with 15 μm and 4 μm for the wavelength and decay constant. The 4.4GHz mode was found to be of propagating character.

Due to the nature of this fitting procedure, the uncertainty of the decay constant and the wavelength is of the order of several microns. For this situation the fits never ideally match the

experimental data points and there is ‘artistic license’ to the best values of fitting parameters. The parameters obtained from the fitting procedure are consistent with qualitative observations from the images.

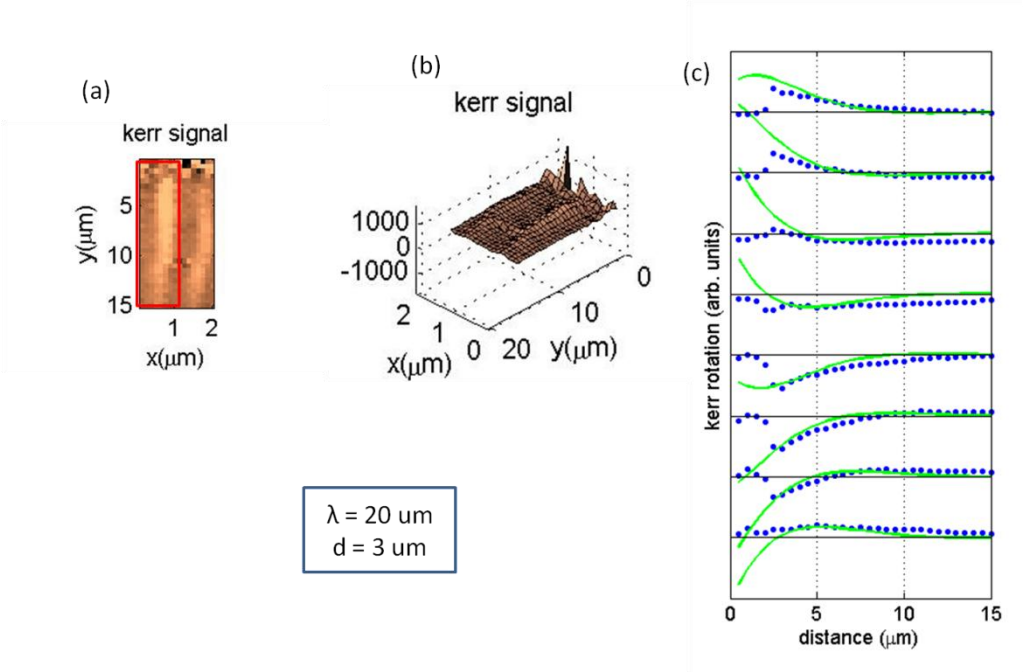

Figure 4.4.3 – For the 3.04GHz excitation on the cobalt dot sample, the values of 20 and 3μm for the wavelength and decay constant were determined respectively. The 3.04 GHz mode has the appearance of a driven standing wave character and is non-propagating.

The fitting performed on the binary sample gives consistent values of the decay constant of 3 and 4 μm for the 3.04 and the 4.4GHz respectively. In the un-patterned permalloy, the decay constant is 9 μm. The effect of the cobalt filled anti-dots reduces the decay constant by a factor of two. In the un-patterned permalloy the wavelength is 7.5 μm, the wavelength increases from 7.5 μm to 15 μm in the patterned region. At identical frequency, the wavelength has doubled. At the lower frequency (3.04GHz), the wavelength is even longer at 20 μm. In the patterned region

the decay constant is consistent at 4 μm, the two wavelengths are 15 and 20μm for the 4.4 and 3.04GHz modes respectively.

The Anti-dot Ref Sample

The same fitting procedure is performed on the air-filled anti-dot reference sample. Only the 2 x 15 μm scans for the 3.84 and 4.7GHz modes respectively have been fitted. The best fit parameters for the 3.84GHz propagating mode are λ = 15 μm and d = 4 μm.

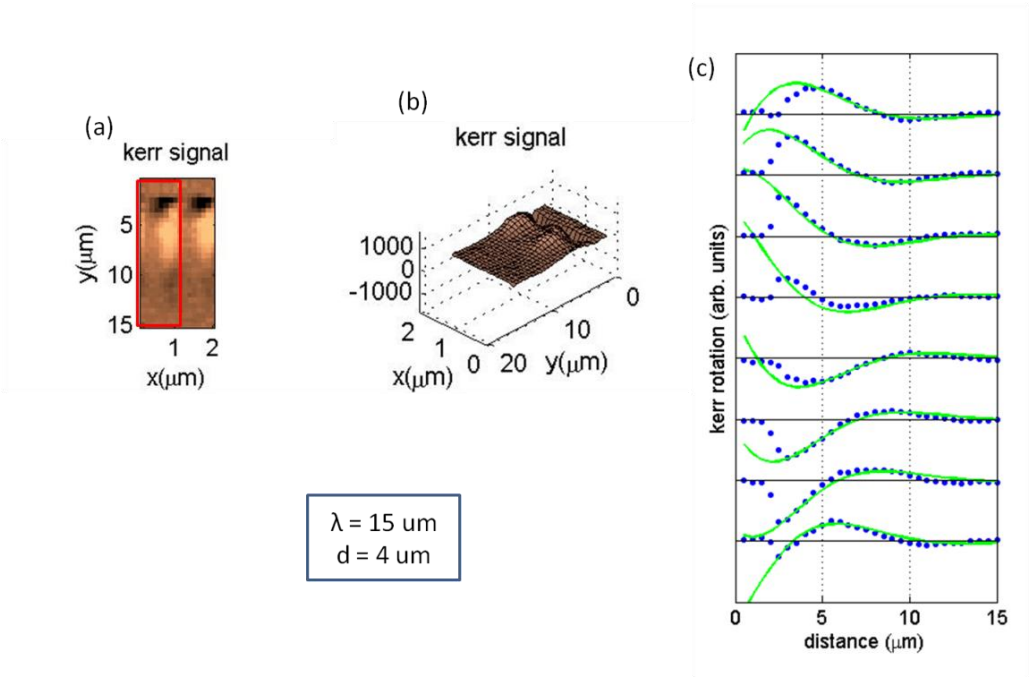

Figure 4.4.4 – The 3.84GHz mode of the anti-dot ref sample. This is the anti-dot ref samples propagating mode, with two alternative views shown in (a) and (b), the fitting shown in (c) yields the values of 15 and 4 μm respectively.

The propagating modes in both samples have the same wavelength. This could be coincidental; a consequence of the error in the fitting procedure or it could be fundamentally related via the dispersion associated with the 1 μm periodicity in both samples.

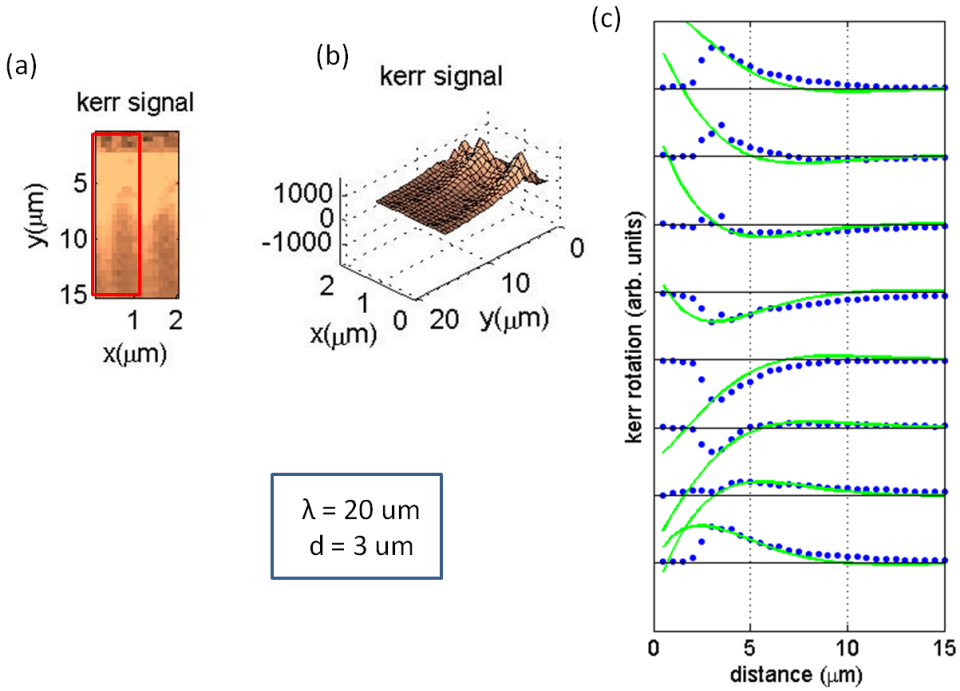

Figure 4.4.5 – The 4.7GHz mode in the air-filled anti-dot reference sample, showing a driven standing wave character, from different perspectives (a) and (b). The fitting for the stated parameters are shown in (c) for a 20 μm wavelength and 3 μm decay constant.

In figure 4.4.5 the fitted wavelength of 20 μm is identical to the wavelength of the driven standing wave mode of the cobalt dot sample. Table 4.5.1 shows a summary of the fitting parameters, including the frequency, wavelength and decay length for the cobalt dot and air-filled anti-dot sample.

4.5 Discussion and Analysis

In the air-filled anti-dot reference sample, the 4.72 GHz mode exhibits non-propagating character. Contrastingly, the lower frequency mode (3.8GHz) has propagating character. In the binary sample this trend is reversed and it is the higher frequency (4.4GHz) mode that exhibits propagating character, while the lower (3.04GHz) mode has the non-propagating character. The propagating mode swaps from the higher frequency in the binary sample to the lower frequency in the anti-dot ref sample. The lower 3.04GHz mode in the binary sample increases its frequency to 4.72GHz in anti-dot reference sample.

This behaviour is explained in terms of the modification of the internal field by the presence of the cobalt / air-filled patterning. In figure 4.5.1 (a), cobalt has a greater saturation magnetization than permalloy, the applied bias field 'polarises' the cobalt's magnetisation, creating fictional magnetic charges diametrically opposed along the field axis. These uncompensated magnetic charges give rise to a demagnetizing field $\mathbf{H}_D$ parallel to the applied bias field, which enhances the internal magnetic field between the Co dots. The 4.4 GHz mode propagates through this region between the dots and experiences this increased internal field, which raises the mode frequency.

The same explanation also holds for the 3.04 GHz binary mode in 4.5.1 (b), the demagnetizing field is anti-parallel to the applied field lowering the internal field through the dots. The driven standing wave 3.04GHz mode experiences a lower internal field between the dots and consequently has a lower frequency. In the binary sample, the applied field creates uncompensated charges on the cobalt dots which give rise to a static demagnetizing field which

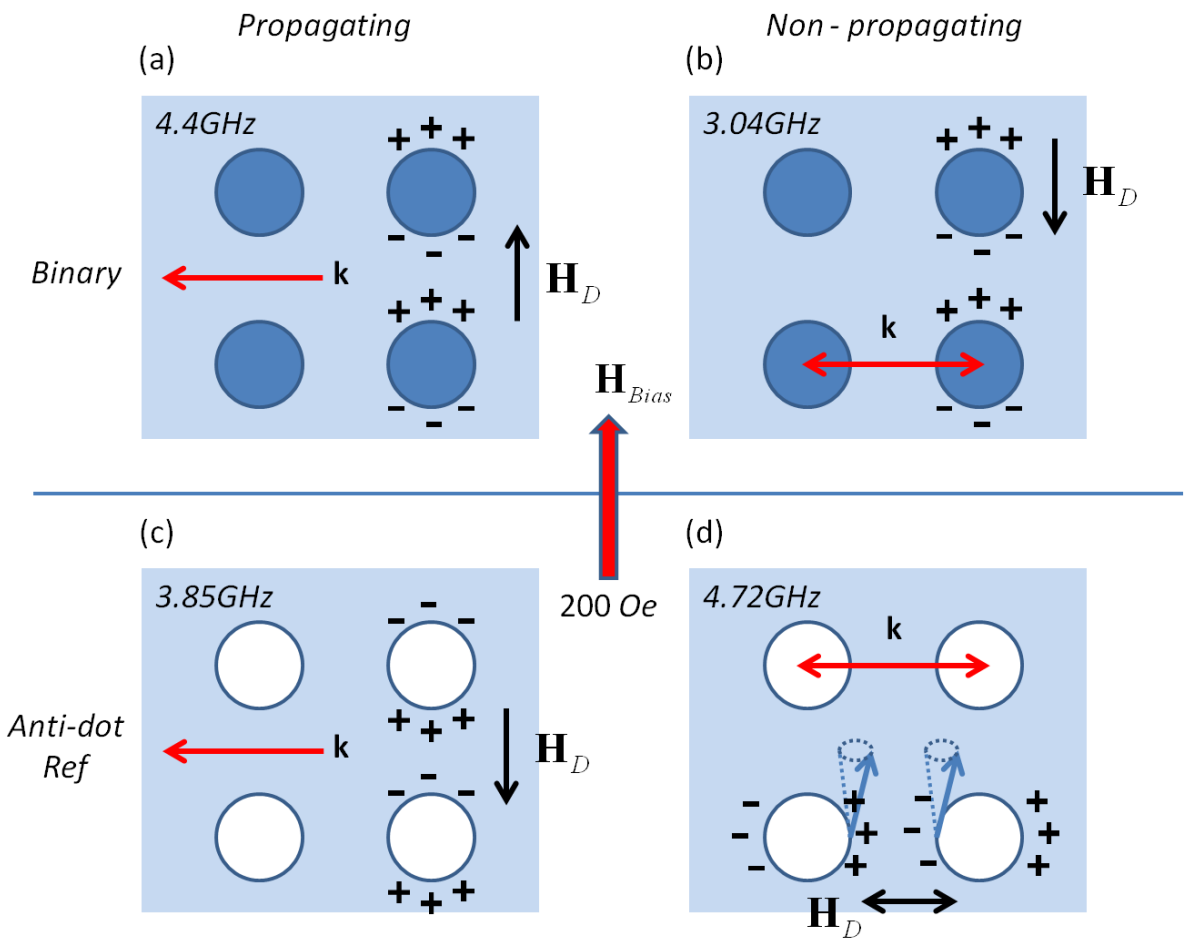

Figure 4.5.1 – Schematic showing the demagnetising effect the cobalt (solid blue circles, top images) and air-filled anti-dots (empty circles, bottom images) have by inducing a demagnetizing field which alters the internal field and mode frequency. The induced demagnetising field increases the internal field between the cobalt dots in (a) and reduces the internal field in the cobalt dots in (b). The internal field is reduced in the permalloy between the air-filled anti-dots in (c). In a direction parallel with the applied microwave field magnetic charges are driven back and forth between the air-filled anti-dots in (d). In (a), (b) and (c) the demagnetising field phenomenon is static, while in (d) the demagnetising field between through the dots is of dynamic origin. The applied bias field at 200 Oe is for panels (a) to (d) inclusive. The waveguide is located right of each image.

gives rise to the increased and decreased internal fields between and through the dots respectively.

In figure 4.5.1 (c), the air filled anti-dots give rise to uncompensated magnetic charges in the permalloy, generating a net static demagnetizing field anti-parallel to the applied field in the region between the dots. This reduction of the internal magnetic field reduces the propagating frequency between the anti-dots to 3GHz. The standing wave mode existing through the anti-dots at 4.72GHz in 4.5.1 (d) is a result of a dynamic demagnetizing field generated by the transient magnetic charges 'sloshing' back and forth between the anti-dots. This increases the internal field, raising the mode frequency. For the non-propagating standing wave modes, the mode frequency increases from 3.04 to 4.72GHz due to the enhancement of the internal field by the dynamic demagnetizing field brought about by the air-filled anti-dots.

To determine the effective damping parameter(s) the group velocity is required. From the fitting in section 4.4, the decay length and wavelength are obtained. The dispersion relation measured using Brillouin light scattering by our collaborators is shown in figure 4.5.2. The red and green dots in the dispersion represent the location of the Brillouin light scattering peaks in the frequency domain obtained at different scattering angles, which translate into the spin wave wavevector (k). Figure 4.5.2 illustrates two bands of dispersion for both samples at small wave vectors (long wavelengths). This is consistent with the time-resolved Kerr measurements and the Fourier spectra show in figure 4.2.3 and figure 4.3.3, where two dominant modes are visible. At wavelengths of 15 and 20 μm the wave vectors are 0.042×10^5 and 0.031×10^5 cm^{-1} respectively. The group velocities (i.e. dispersion slope) remain constant for wave vectors up to 0.4×10^5 cm^{-1}, estimated to be 2.5 km/sec. The group velocity of the un-patterned permalloy film can be

calculated using the Damon-Eshbach formula (equation 2.11.2), calculated to be 6.6 kms^{-1}. The resultant values for the five different cases of spin wave are displayed in Table 4.5.1. Using these values, the Gilbert damping factor can be extracted. It is known the Gilbert damping factor (α) is related to the angular frequency ($\omega=2\pi f$) and the relaxation time of the magnetic precession (τ) as $\alpha = (\omega\tau)^{-1}$. The spin wave decay length is given by $d = \tau v_g$, where v_g is the group velocity. After rearranging the effective damping parameter can be written as equation 4.5.1.

$$\alpha = \frac{v_g}{2\omega f d} \tag{4.5.1}$$

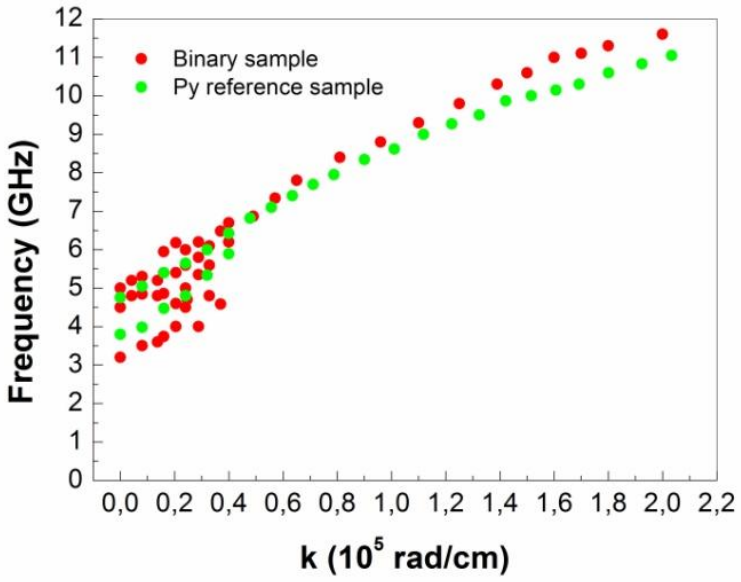

Figure 4.5.2 – The measured dispersion relation for both the binary (red dots) and anti-dot sample (green dots).This dispersion relation was measured by our collaborators using Brillouin light scattering.

The fitted parameters and the calculated values of damping are tabulated in table 4.5.1. The effective damping factor (α_{eff}) lies within the same range 0.023 to 0.028 for (a), (b), (d) and (e) of table 4.5.1. Table 4.5.1 (c) exhibits an exceptionally high value of 0.044. The effective damping parameter depends heavily on the medium through which the spin wave propagates. The localisation of the mode shown in table 4.5.1(c) is the only case in which the spin wave has to travel through the cobalt. In the other cases, the spin waves propagate through the permalloy. The Gilbert damping of cobalt is greater than permalloy giving rise to an extraordinary high value of α_{eff} in case (c) of table 4.5.1.

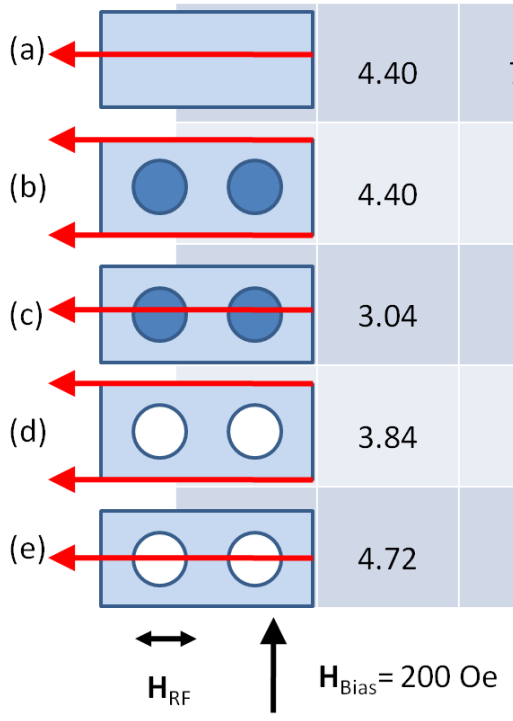

	f (GHz)	λ (μm)	d (μm)	v_g (km/sec)	v_p (km/sec)	α_{eff}
(a)	4.40	7.5	9	6.6	32	0.027
(b)	4.40	15	4	2.5	66	0.023
(c)	3.04	20	3	2.5	60	0.044
(d)	3.84	15	4	2.5	57	0.026
(e)	4.72	20	3	2.5	94	0.028

Table 4.5.1 – Tabulated results of the fitting procedure for the un-patterned region of the sample (a) (continuous film), between dots in the binary sample (b), through the dots in the binary sample (c),

between the anti-dots in the reference sample (d) and through the anti-dots in the reference sample (e). The frequency refers to the driving microwave frequency.

The effective damping factor of magnonic crystals has been studied for some time [86]. Analytical expressions for the effective damping coefficient of propagating spin waves in magnonic crystals have been obtained previously [87], where the effective damping coefficient depends strongly upon the spin wave frequency and the applied magnetic field. This dependence was enhanced in the vicinity of magnetic interfaces. There are two possible ways to interpret the data observed in table 4.5.1. One interpretation is spatial dephasing.

The dispersion in figure 4.5.2 is flat in the vicinity of small wave vectors. Propagating spin waves of the same frequency possessing different wave vectors initially propagate together in phase. Since they have different wave vectors superposition causes the total amplitude to undergo destructive interference. At a later point in space, constructive interference will occur, but since the spin wave modes are subject to inherent damping they decay before this is observed. The net effect of this 'dephasing' is to damp the total spin wave amplitude faster than individual modes subject to their own inherent damping. Spatial dephasing of the propagating spin waves essentially gives rise to an enhanced effective damping in the patterned structure. This process has been observed previously in 10μm permalloy squares, albeit in the time rather than space domain [88, 89].

A secondary interpretation is called the 'Borrmann effect', where spin waves in a periodically structured material propagate with less than normal absorption when spin waves

undergo Bragg diffraction. The effective damping parameter depends heavily on the medium through which the spin wave propagates.

4.6 Summary

In this chapter measurements of cobalt and air-filled anti-dot lattices have been presented using time-resolved scanning Kerr microscopy. In both samples the dominant mode(s) were measured and the wavelength and decay length were determined from fitting. The measured dispersion relation from our collaborators was used to determine the group velocity, and the effective Gilbert damping constants were determined. Two possible interpretations of the data can be put down to spatial dephasing of the propagating spin waves and the Borrmann effect. Anti-dot lattices show great future potential in magnonic devices and the understanding of spin wave dynamics in periodic structures remains of fundamental importance if such devices are to be realised in practice.

Chapter 5: Time-resolved Optically pumped Scanning Optical Microscope measurements of a Permalloy film

5.1 Introduction

In chapter 3, the setup and experimental development of the optical microscope was discussed. In this chapter preliminary measurements of the time-resolved optically pumped scanning microscope on a 20 nm continuous permalloy film are presented. This chapter is divided into two parts, the first part presents preliminarily data measured on the microscope. This data is not fully understood and was acquired in the early days of the optical microscope's construction. The second part presents data measured over a year later by Dr. Yat-Yin Au of the magnetic materials group in Exeter. This data is used to interpret the preliminary data measured previously.

Ultrafast Magnetisation dynamics has been subject to intense research since the discovery of ultrafast demagnetisation in nickel films by *Beaurepaire et al* in 1996 [90]. Until this time, little attention was paid to the study of magnetic effects on femtosecond timescales after irradiation by an ultrashort optical pulse. Previously, optical pump-probe techniques were used to investigate electronic relaxation processes in metallic materials. The absorption of intense laser pulses by a ferromagnet causes a highly non-equilibrium rearrangement of electrons and magnetic moments via fundamental microscopic physical processes [91], such as electron-electron scattering, electron-phonon scattering and magnon generation. All these processes occur on sub-picosecond timescales. On a nanosecond timescale the time evolution of the magnetisation is described by the Landua-Liftshitz-Gilbert equation. The transition between the two regimes of ultrafast sub-picosecond relaxation and nanosecond coherent precessional motion

is not fully understood [92,93]. The increasing speed and storage capability of modern electronics motivates the search for faster approaches to magnetically stored information. This quest has attracted many researchers with the aim of understanding both the fundamental mechanisms and control of magnetic properties on a femtosecond timescale. For the simplest itinerant ferromagnet, such as nickel, the underlying elementary mechanisms leading to the macroscopic demagnetisation on a sub-picosecond timescale has not been identified [94].

The difficulty lies in the complexity of a parallel dynamic treatment of photons, electrons, phonons and magnetic correlations of the spin system on different length and time scales. Optical pulses can serve as an alternative stimulus to the magnetisation. Laser induced changes in the anisotropy field due to thermal effects have been observed to trigger coherent precession of the magnetisation [95,96]. Magnetisation reversal has been observed using circularly polarised light in the rare-earth transition metal GdFeCo [97,98], where left and right optical pulses act as magnetic fields of opposite sign via the Inverse Faraday effect. However, this is now in doubt given recent work [99], in which optical switching in ferromagnetic GdFeCo with polarised femtosecond laser pulses is subject to a threshold of absorbed fluence, independent of wavelength and polarisation. Also they provide a quantative explanation of the intensity window in which all-optical helicity dependent switching occurs. Opto-magnetic effects have also been observed in media possessing strong magneto-optical effects such as anti-ferromagnetic dielectrics $DyFeO_3$ [100], $(LuYBi)_3$ $[FeGa_5]O_{12}$ [101], $FeBO_3$[102] and the paramagnetic ion LuIG [103].

In conventional optically-pumped time-resolved magneto-optical Kerr effect measurements a probe beam is focused on the sample and reads out the state of the magnetization after perturbation by an optical pulse. Pump-probe methods utilising the Kerr

effect are well established and possesse very high sub-ps temporal resolution. Using an optical pump-probe approach, coherent precessional modes can be excited [104,105]. Conventional optical pump-probe techniques lack spatial resolution and cannot investigate the distribution of magnetization dynamics in the vicinity of the pumped region. The time-resolved optically pumped scanning optical microscope combines the ability to perform scanning into a conventional optically-pumped time-resolved magneto-optical Kerr effect setup. This is achieved using two high numerical-aperture objective lenses mounted on xyz translation stages either side of the sample. Existing optical microscope(s) of similar design have observed ultrafast photoinduced magnetisation reversal in TbFeCo on a micron/sub-micron scale [106]. The authors utilise the polar Kerr effect using oppositely mounted high numerical aperture objectives to observe magnetisation reversal after being subjected to a femtosecond optical pulse and observed switching taking place between 3-4 ns down to 750 ps depending on the initial domain size. The experimental setup and geometry of the optical microscope in Exeter was discussed in chapter 3, followed by a discussion of experimental development. In this chapter results measured on the time-resolved optically pumped scanning optical microscope are presented.

5.2 Experimental Results – Preliminary optical microscope data

Hysterisis Loops of 20nm Permalloy film (NiFe) measured using Simple Bridge & Balanced Detector

Hysteresis loops were measured utilising the magneto-optical Kerr effect. Hysteresis loops were performed on the optical table and inside the optical microscope using the high numerical aperture probe objective. Both 400 and 800 nm light were used to measure loops in a transmission (Faraday) and reflection (Kerr) geometries for both the simple bridge and the

balanced detector on the optical table. The loops measured in transmission were qualitatively similar to those measured in reflection and are not presented in this Thesis. For measurements inside the microscope only 400 nm light was used and half of the beam was blocked to observe the longitudinal Kerr effect.

A small magneto-optical Kerr effect experiment was set up on the optical table next to the optical microscope. A linearly polarised laser beam is incident on the sample which is placed between the poles of an electromagnet. The reflected beam is directed to the detector which measures the rotation of the polarisation when the applied field is varied. This was done to ensure the Kerr effect could be observed before mounting the sample in the microscope. Loops on the optical table were initially measured using the simple bridge detector. The simple bridge is an established detector in the group and can measure static loops and time-resolved signals. The Thorlabs balanced detector was new and unfamiliar at the time of measurement. Initially, it was impossible to measure hysteresis loops using the balanced detector. This was due to either the low detector transimpedance gain or being aligned improperly. After sections of die cast housing were removed from the detector it was then possible to measure hysteresis loops. The low detector gain might still be a problem for dynamic measurements, estimated to be about an order of magnitude lower than that of the simple bridge detector.

In figure 5.2.1 (a) a hysteresis is measured using the simple bridge detector. The loop height is approximately 60 mDeg. The loop measurement was repeated using the balanced detector in figure 5.2.1 (b). The loop signal-to-noise has reduced and the measured loop height is 60mDeg. In both figure 5.2.1 (a) and (b) the hysteresis loops were measured on the optical table without using microscope objectives. In figure 5.2.1(c) the permalloy film was measured using

the probe objective in the optical microscope with the balanced detector. To measure the longitudinal Kerr effect with microscope objectives requires half of the incident beam to be

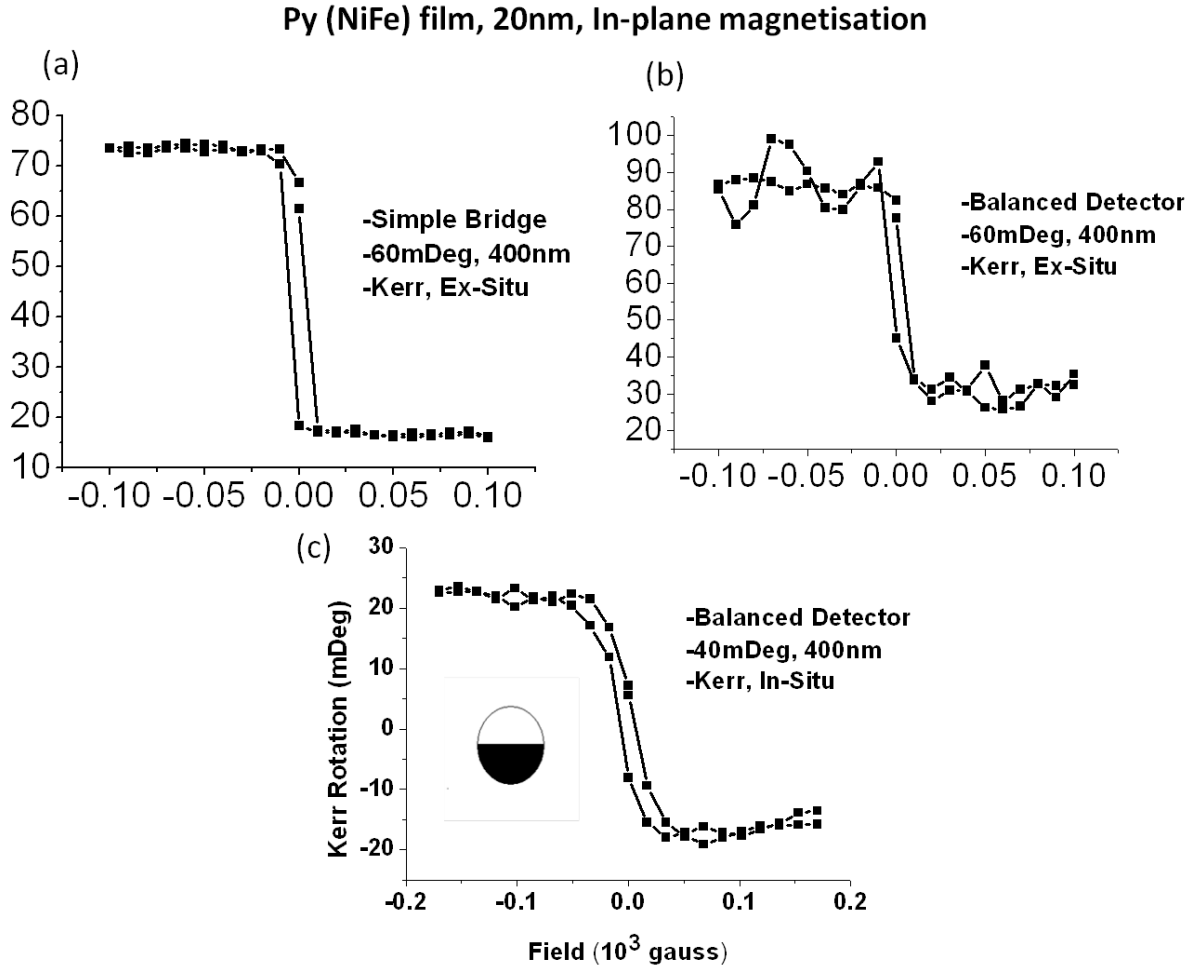

Figure 5.2.1 – Longitudinal Kerr loops measured for the 20 nm continuous permalloy film featuring in-plane magnetization using the 400nm probe beam. In-situ refers to measurement inside the microscope. Ex-situ refers to measurements made on the optical table.

blocked. This avoids cancelation of the Kerr rotation in the detector. The bottom half of the beam was blocked indicated by the half filled circle in figure 5.2.1 (c). The loop height is 40 mDeg or two-thirds of the loop height in figure 5.2.1 (a) and (b). The loop is more rounded indicating

either a hard axis loop or a measurement artefact of the optical microscope. A study of the easy and hard axis directions was not done. In (a) to (c) inclusive, the horizontal axis is the applied field in KG and the vertical is the Kerr rotation in milli-degrees.

Measurements on the 20nm Py (NiFe) film – Sapphire substrate

In this section, initial results from the optical microscope are presented. The presented data consists of time-resolved signals and scanning Kerr images on a 20 nm thick continuous film featuring in-plane magnetisation, mounted on a sapphire substrate. Initial use found the optical microscope to be unreliable and difficult to operate. Mechanical drifts made observing reproducible signals impossible. Further modification and refinement of the optical microscope is required to give it reliable operational service. This includes improving the thermal stability of the surroundings and re-constructing from a material with a material with a low co-efficient of thermal expansion.

The optical microscope is constructed of aluminium, which has one of the highest coefficients of linear thermal expansion of all the metals (~ 23 $\mu m.K^{-1}m^{-1}$). The optical microscope is located under the lab air conditioners. The temperature at the Tsunami laser cavity has been measured to fluctuate between 14 and 19^{o}C over a period of 30 minutes. In addition to compromising the mechanical stability, the temperature changes have created 1 Watt changes in the laser output power. The position of the air conditioners was eventually raised, partly alleviating the aforementioned problems.

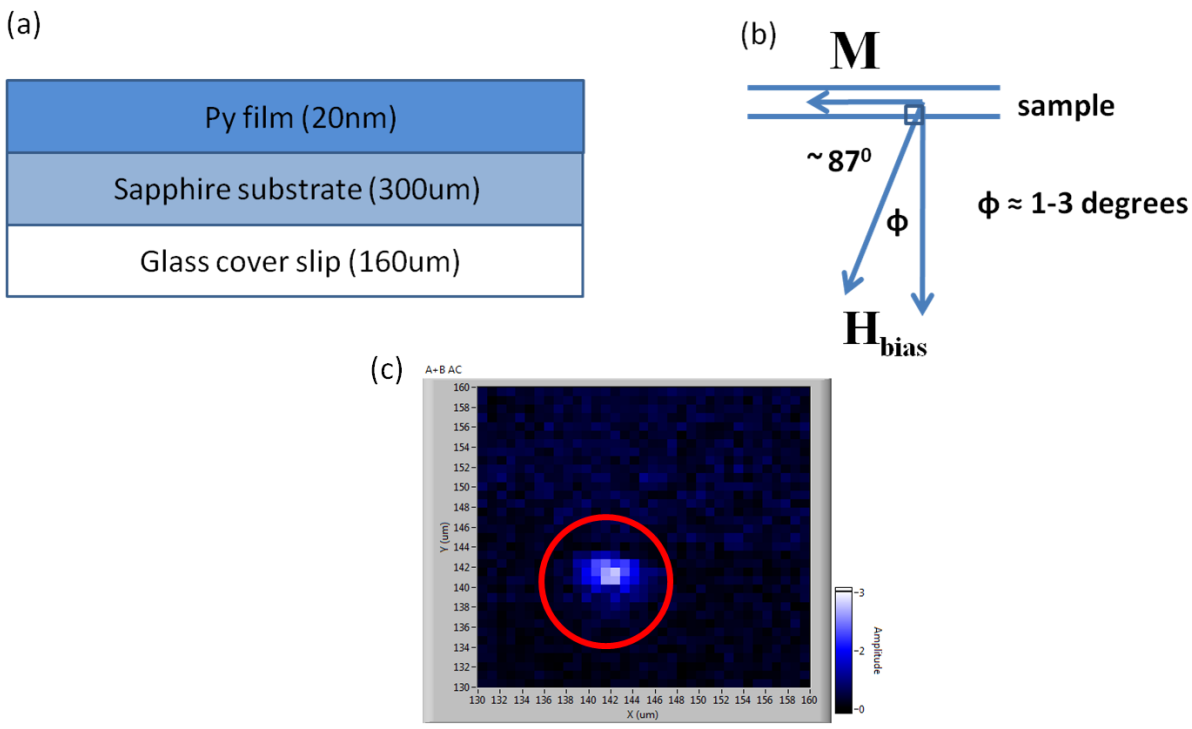

Figure 5.2.2 – Schematic in figure (a) of the sample and direction of the applied field (b). An AC scan of the pump spot is shown in (c).

In figure 5.2.2 (a) the 20 nm permalloy film is on a 300 μm sapphire substrate mounted on a conventional 160 μm glass microscope cover slip. Sapphire is present due to its high thermal conductivity (roughly 30 times higher than glass) to reduce the time-average heating from the pump pulses to reduce the probe signal background. In the experiment (b) a permanent magnet is used to apply an out-of-plane field several degrees from normal, enough to align the magnetization in-plane and provide a canting field. The field strength is 500Oe in the sample position and this is estimated to cant the magnetization about 2 – 3 degrees. In 5.2.2 (c) a 30 x 30 μm lock-in scan of the pump spot, the probe spot is placed on the pump spot maxima at coordinates 142(x), 141(y). The pump spot spot has a 1um wide central maximum.

Time-Resolved Signals from the 20nm Py (NiFe) film – Sapphire substrate

Permalloy has a saturation magnetisation of 10KOe. Considering the demagnetizing and bias fields, the angle the magnetisation departs from the in-plane direction can be calculated and is estimated at 2.8 degrees from the in-plane direction. The out-of-plane field is tilted several degrees φ to dictate the initial direction of magnetisation. The angle the field can be altered from the normal is limited by the pump and probe objectives and can be no greater than 10 degrees. Before using Sapphire as a substrate material, the background in the probe channel was of the order of 100 μV. The background generated using the Sapphire as a heat conducting substrate is now only a few μV.

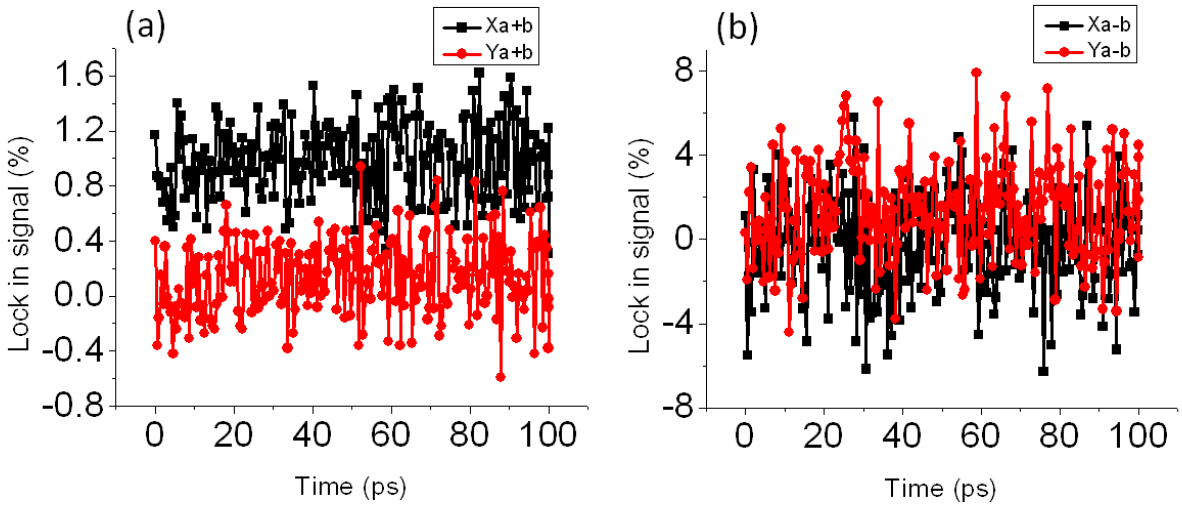

Figure 5.2.3 - The lock-in noise floor can be estimated for both the rotation and reflectivity channels, the sensitivity for both (a) and (b) is 100uV. The peak-to-peak noise amplitude is 2% or 2μV. The black line (square data points) is the X component of the signal in (a) and (b), the Y component the red line (circular data points). Here the probe spot is positioned over the pump spot. The pump spot position is determined from a lock-in scan of the pump spot shown in 5.2.2 (c).

Using figure 5.2.3, the reflectivity A+B signal in (a) has a noise amplitude of 1 μV in both the X and Y channels. In (a) the X and Y signal components have an off set of 1 μV. The rotation signal has larger amplitude noise of about 8 μV. The time-resolved scan in 5.2.3 is a 100 ps scan over the expected zero-time delay position. A spatial filter and two 400 nm bandpass filters are used in all time-resolved scans. A 200 ps time-resolved scan with a 1ps step size is performed over the zero-time delay position in figure 5.2.4. Backgrounds are seen in the signal on both detector channels.

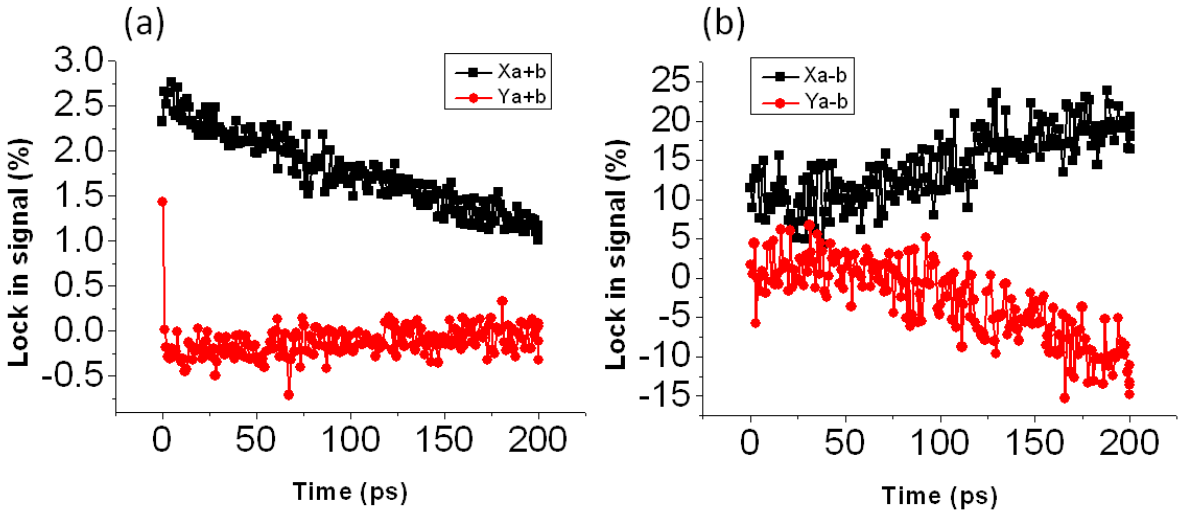

Figure 5.2.4 – Longer 200 ps time-resolved scan for both channels over the pump-probe spatial overlap position at 100 μV sensitivity in both (a) and (b). Backgrounds are seen in both rotation and reflectivity channels, the source of which is not fully understood.

In almost a trial and error process, a time-resolved signal eventually is observed in the reflectivity channel shown in figure 5.2.5 (a). The corresponding rotation signal is shown in figure 5.2.5 (b). The zero-time delay position is at 17 ps, a sudden step can be seen in the X channel (black line, square data points). Small amplitude oscillations are observed extending to

200 ps. The scan depicted in 5.2.5 (a) and (b) was repeated to ensure the signal in 5.2.5(a) is reproducible and is shown in 5.2.5(c) and (d). The reflectivity signal is replicated upon repeating the scan, shown in 5.2.5 (c).

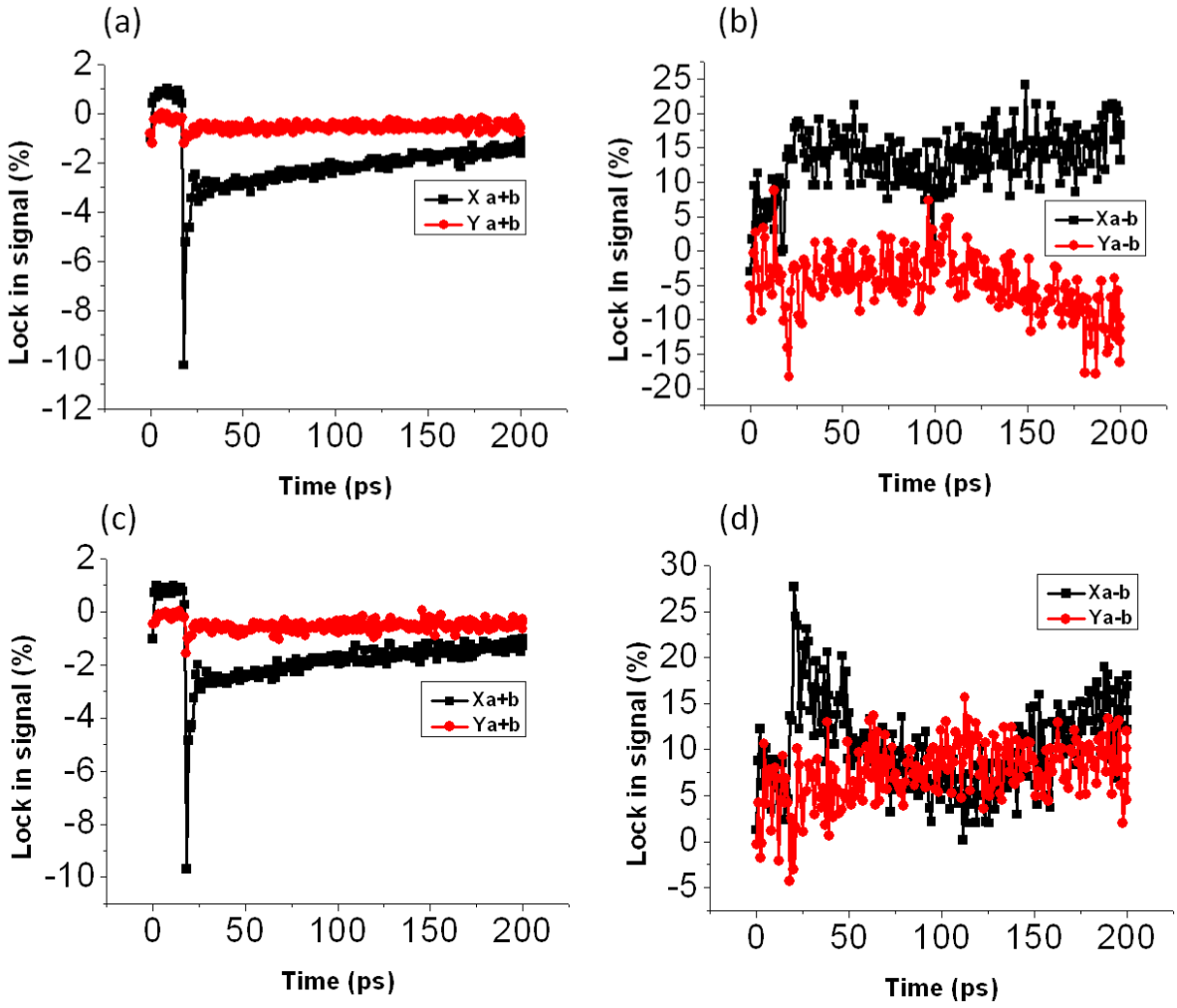

Figure 5.2.5 – A convincing pump-probe reflectivity signal seen in (a), with the corresponding rotation signal seen in (b). The signal in (a) looks genuine and the scan was repeated, shown in panels (c) and (d) which represent the reflectivity and rotation signals respectively. In (a) and (c) from delays of 17 ps onwards, relaxation of the signal continues for the 200 ps scan duration. The 'jump' in the signal occurs at the same temporal position, the reflectivity (A + B) signal peak amplitude is identical at 10 μV and the signal has the same shape.

The rotation signals in 5.2.5(b) and (d) have no correspondence. In 5.2.5(d), a step like jump is seen at 17 ps, followed by an undulation of the signal, whether these 'oscillations' are genuine is unknown. The reflectivity signals in 5.2.5 (a) and (c) are genuine; the rotation signals in 5.2.5 (b) and (d) are not.

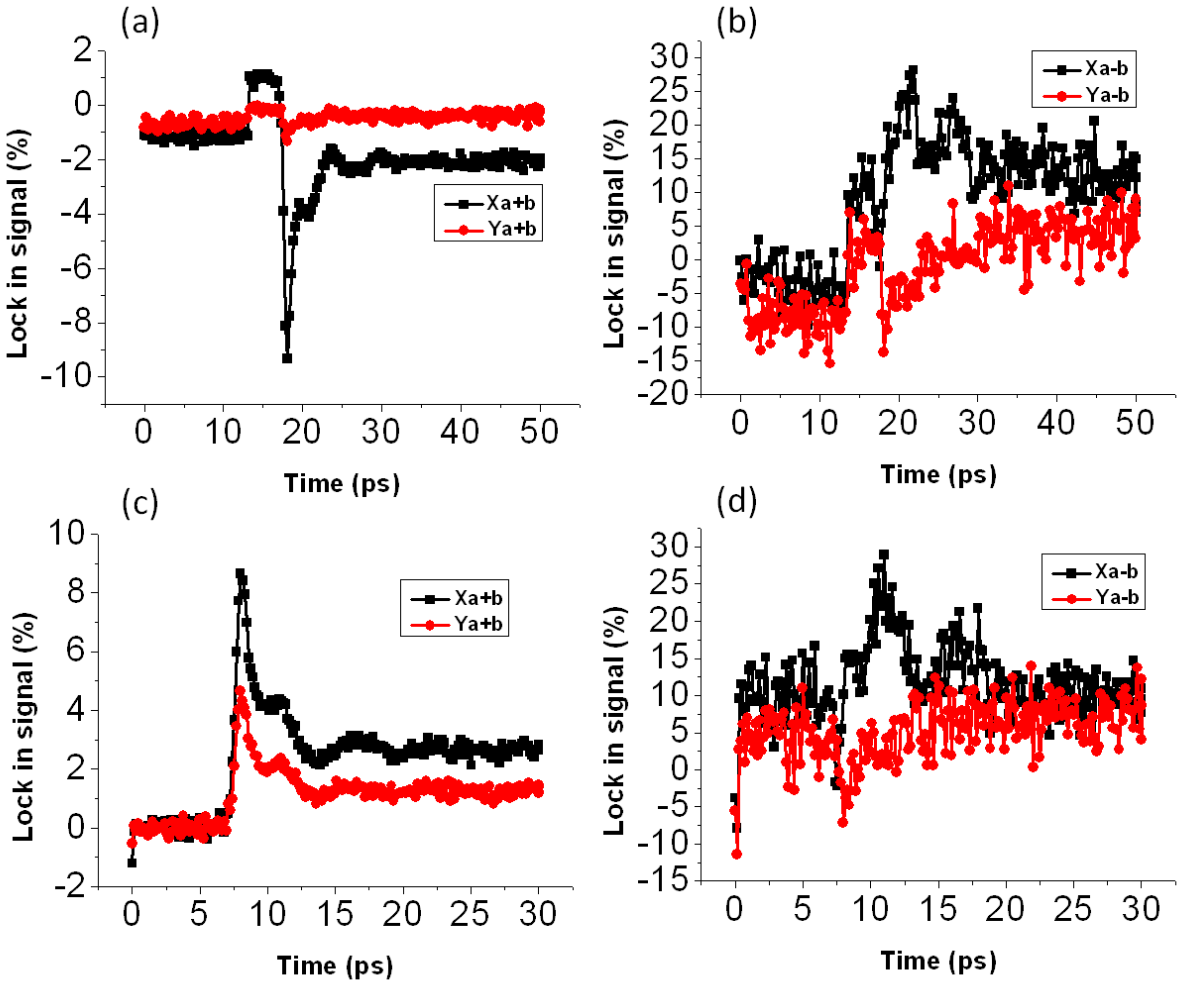

Figure 5.2.6 – A reproducible signal is observed in the reflectivity channel and is the only reproducible signal in this set of time-resolved measurements. The signal changes sign becoming positive in figure 5.2.6 (c). The rotation channel is unable to reproduce a consistent signal.

The scan from 5.2.5 (c)-(d) was repeated and the pump-probe time delay reduced from 200 ps to the first 50 ps of the signal, shown in figure 5.2.6 (a), with the corresponding Kerr (A -

B) rotation signal shown in 5.2.6 (b). The step between 10 - 15ps is from auto-phasing the lock-ins manually. The signal peak amplitude in 5.2.6(a) is reduced to 8 μV.

To observe in more detail the zero-time delay signal, a repeat scan of figure 5.2.5 (c) and (d) is performed for a delay of 30ps, shown in figure 5.2.6(c) and (d). The pump-probe overlap was adjusted manually and the new zero-delay position is 7ps. The signal polarity has reversed and is now positive in figure 5.2.6(c). The magnitude of the signal in figure 5.2.6 (c) is comparable to the magnitude of 5.2.6 (a) at 9 μV. The lock-in sensitivity in figure 5.2.7 has been reduced by an order of magnitude to 10 μV for 5.2.7 (a) to (c) inclusive.

In figure 5.2.7 (b) the Kerr channel saturates between 7 – 12 ps, the sensitivity was changed manually to reduce saturation of the signal. In (c) and (d), the time-constant is increased from 1 to 5 seconds. Up to figure 5.2.7 (b) the rotation signals have had no well-defined shape or reproducibility. Figure 5.2.7 (c) is the first instance of the signal showing an oscillatory character. The origin of the oscillations in (c) is unknown. The reflectivity signals in figure 5.2.7 (a) and (c), show small ripples or steps between 10 and 25 ps. They are observed in the previous reflectivity signals and their origin is unknown. The amplitude of the peak reflectivity signal in 5.2.7(a) is -7 μV, this reduces -6 μV in 5.2.7 (c). The reflectivity signal shape remains reproducible.

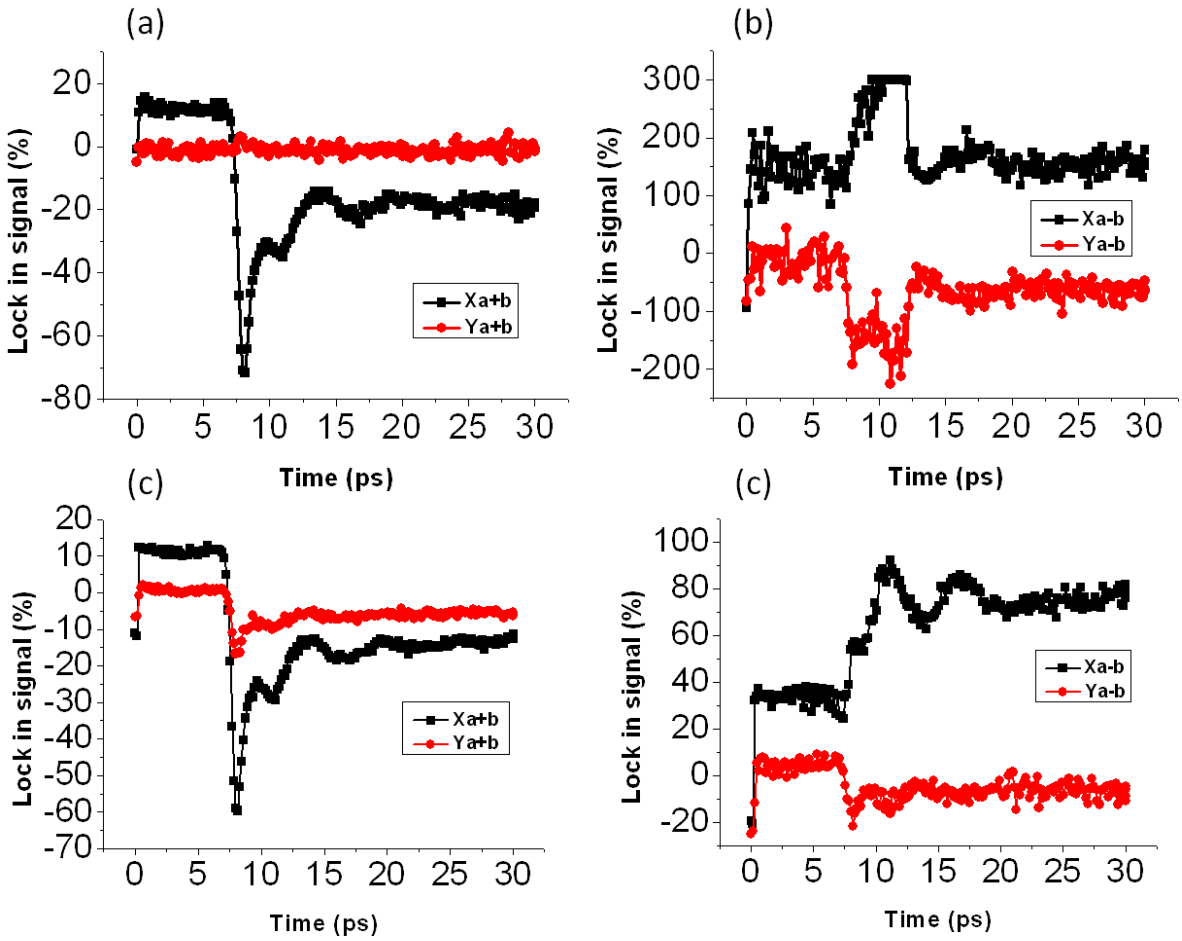

Figure 5.2.7 – Repeat time-resolved signals. The sensitivity for panels (a) to (c) inclusive is 10 μV, in (d) it is 50 μV.

In figures 5.2.3 to 5.2.7 inclusive, the measured time delays did not exceed 200ps. Longer delays of 2 ns are shown in figure 5.2.8. The lock-in integration time was 10 seconds and each curve consists of a 1ps temporal step. In figure 5.2.8 clear oscillations in the reflectivity and rotation channels can be seen. In figure 5.2.9 the FFT spectra of figures 5.2.8 are presented.

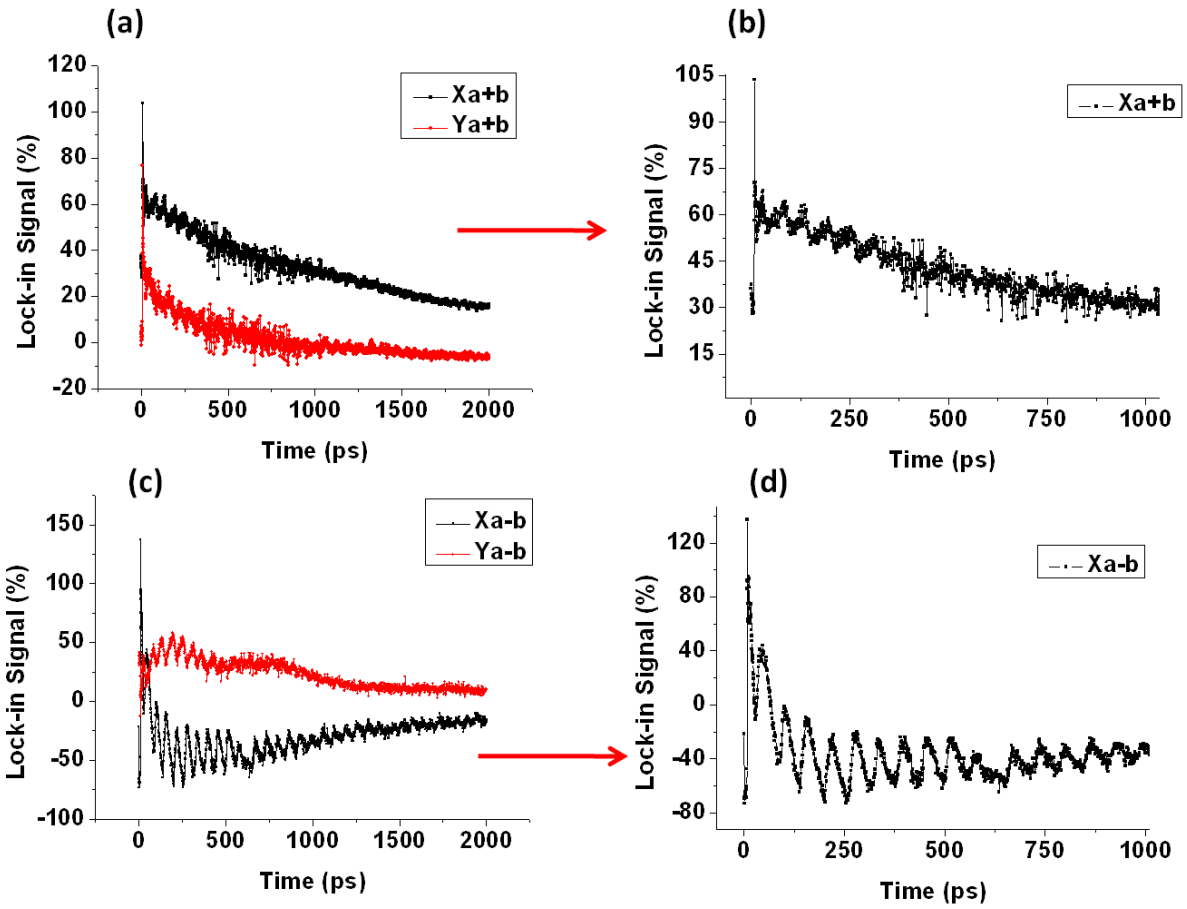

Figure 5.2.8 – Time resolved reflectivity and Kerr signals shown in figure 5.2.8 (a) and (c) respectively. The first nanosecond of figures 5.2.8 (a) and (c) are shown in figure 5.2.8 (b) and (d) respectively. For the reflectivity signals in figure 5.2.8 (a) and (b) the lock-in sensitivity is 20 μV. The sensitivity in the Kerr signals in figure 5.2.8 (c) and (d) is 50 μV. The pump and probe spots are overlapped and are circularly and linearly polarised respectively.

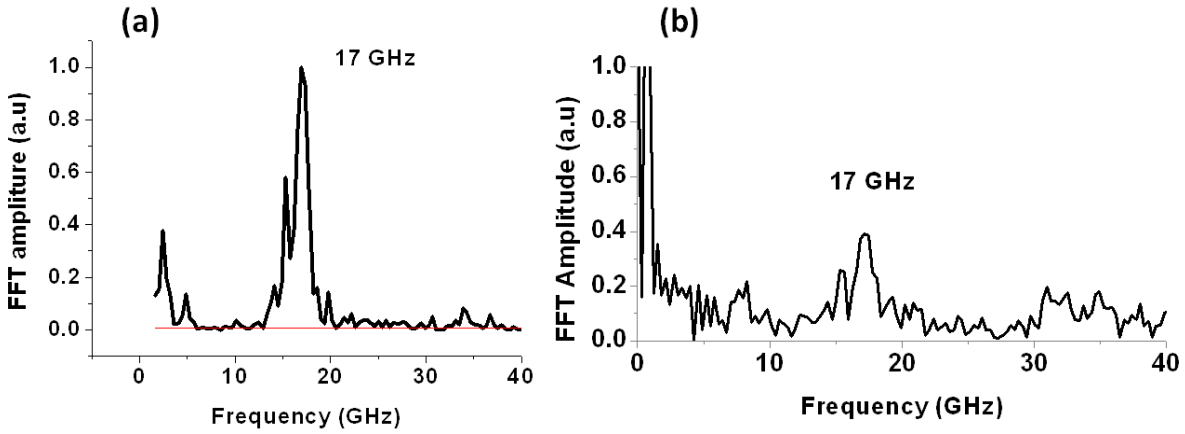

Figure 5.2.9 – Figure 5.2.9(a) is the corresponding FFT of figure 5.2.8 (c). A well resolved main peak is observed at 17 GHz and in figure 5.2.9(b) the FFT spectra of figure 5.2.8 (c) is shown. The spectra is noisy with a main peak at 17 GHz. Improper subtraction of the background gives rise to the piling up of the signal at DC in figure 5.2.9 (b).

Kerr Images from the 20nm Py (NiFe) film – Sapphire substrate

In the last section preliminary time-resolved signals of the 20 nm permalloy film with an out-of-plane field were presented. In this section Kerr images were measured for several different time delays in the vicinity of the pump spot. Initially Kerr images were performed to locate the pump spot after failing to observe a time-resolved signal. In the Kerr channel interesting circular-crescent shaped patterns were observed. The scans were performed for a time delay spanning 62ps. If the observed crescent patterns are spin waves, the spinwave group velocity is too small to see any propagation in the 62 ps interval. Considering spin waves with a group velocity of the order 1km/sec or 1 μm per ns, any propagation would only travel 60 nm in this time, a distance irresolvable in the images.

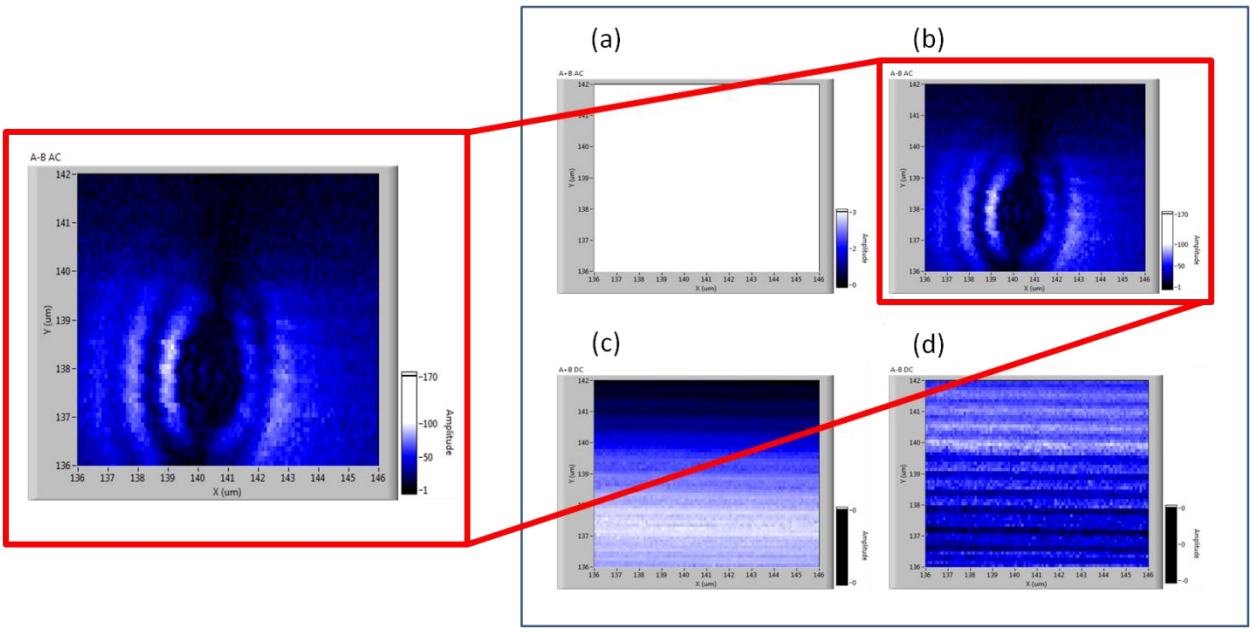

Figure 5.2.10 – Scan windows of the lock-in reflectivity and rotation in (a) and (b) respectively. In figure 5.2.8(c) and (d) the un-modulated reflectivity and rotation respectively. The labview software did not permit the panel in figure 5.2.8 (a) to be displayed. In (c) and (d), the un-modulated images should show no evidence of the pump spot due to the bandpass filters and the images consist of noise. Ideally images 5.2.8 (c) and (d) would have uniform contrast. Panel (b) has been shown in a highlighted view, showing the potentially interesting polarization response from the pumped region. Figure 5.2.10 (b) is a 10 x 6 μm scan (horizontal and vertical axes respectively) with a 0.1 μm step for both directions.

In figure 5.2.10, a 500 Oe magnetic field was applied several degrees from the normal, as in the time-resolved measurements ($\varphi \sim$ 1-3deg). The delay line position for the scans in figure 5.2.10 was -155.969 mm. Scans were performed, with delay positions varying from -158.5 mm to -140 mm. In figure 5.2.7, the pump-probe overlap is at 7 ps, the start position on the stage for the time-resolved scan is -158.5 mm and 7 ps corresponds to a 2.1 mm distance. The delay line must advance 1.05mm to temporally advance 7ps, giving an expected overlap position of -157.45

mm. Images were taken at negative ('-ve') delays, then close to the expected overlap position. Figure 5.2.11 shows the rotation channels for various delay positions and the corresponding pump-probe time delay.

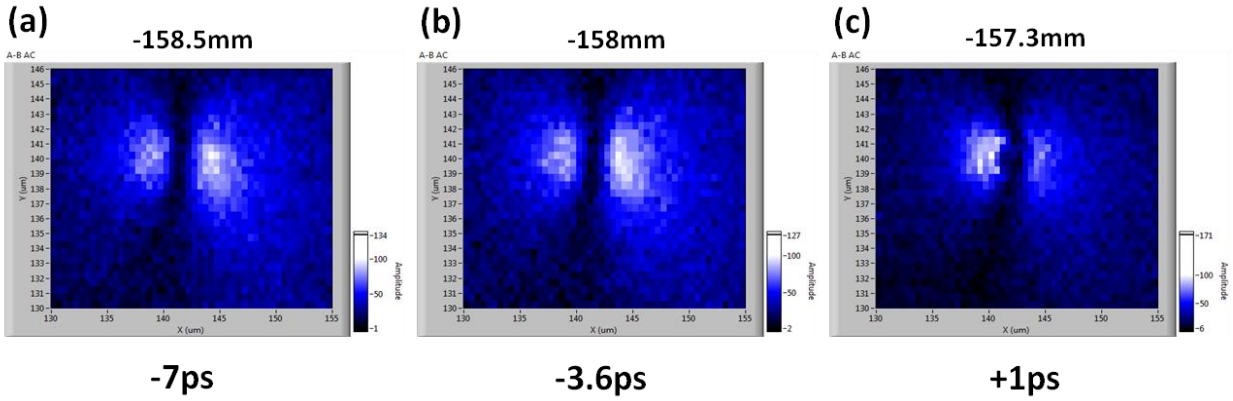

Figure 5.2.11 – Kerr rotation scans for various delay line positions on the 20 nm Py film sapphire substrate. At negative delays in (a) and (b) two circular-lobe shaped hemispheres are observed, featuring a line of symmetry in the vertical or 'y' direction of the scans. A similar pattern is seen at +1ps in (c), in the left hand lobe the emergence of ripple like structures can be seen. The horizontal axis is 25 μm and the vertical axis is 16um for all images (a) to (c) respectively.

Later delays from figure 5.2.11 are shown in figure 5.2.12. The chronology of the images is continued through figure 5.2.11 through to figure 5.2.14 inclusive, retaining the lettering (a) to (k) respectively. From figure 5.2.12 (f), scans are continued for a further 100 ps of time delay up to image (k) in figure 5.2.14. The images show the repeatable ripple structure and the vertical line of symmetry. The central region of figure 5.2.12 (f) is circular, having a width of 1 μm in either direction. This is the same size as the pump spot seen in 5.2.2 (c).

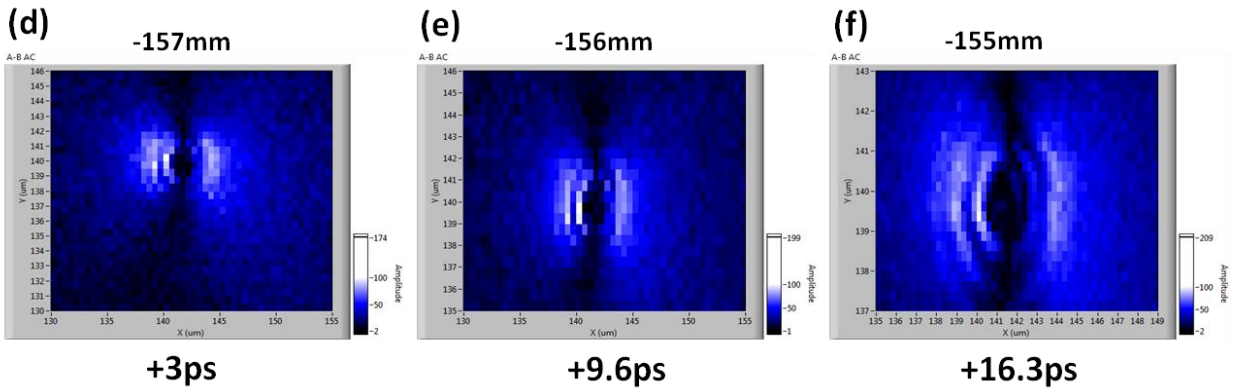

Figure 5.2.12 – Later delays of several picoseconds, a ripple structure can be seen to emerge from the lobe structure seen in the earlier image of 5.2.11 (c). The vertical line of symmetry remains and is a repeatable feature of the image(s). In figure 5.2.12 (d) the scan range is 25 x 16 μm, in (e) it is 25 x 11 μm and the scan range in (c) was altered to 15 x 6 μm for the horizontal and vertical axis respectively. Figure 5.2.12 (f) shows a clear ripple structure developing from the previously seen symmetric side-lobes in 5.2.12 (e).

An interesting feature is the vertical line of symmetry in images (a) to (k), figure 5.2.11 to 5.2.14 respectively. The field direction lies normal to the sample plane, tilted by about 3 degrees. The Hysteresis loop reveals a saturation field of no greater than 10Oe for the hard axis and 3Oe for the easy axis. The in-plane field points in the horizontal ‘x’ direction of all the images. In the images the horizontal axis represents the real-life horizontal. The in-plane applied field is normal to the line of symmetry seen in images (a) to (k).

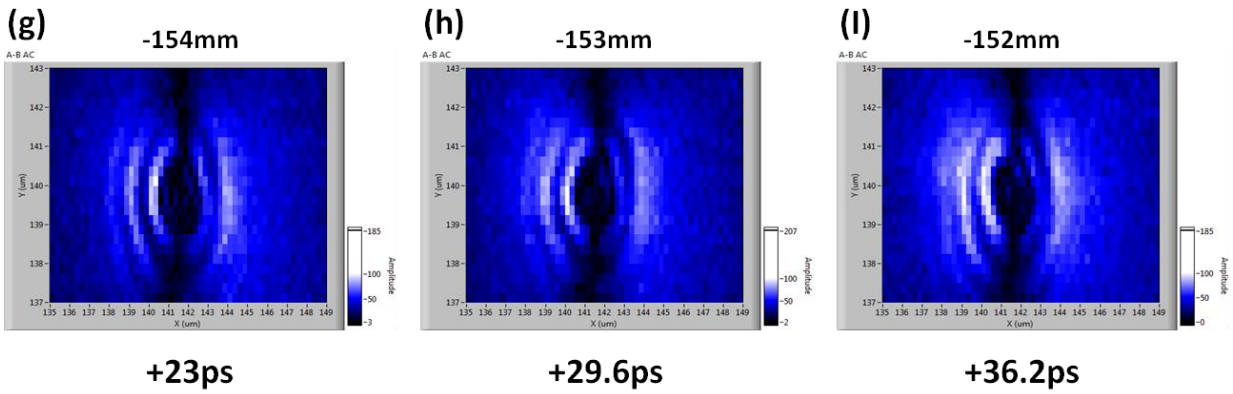

Figure 5.2.13 – Images (g) to (I) have the range 15 x 6 μm along the horizontal and vertical axes respectively.

The effect of the applied field on the direction of the symmetry axis is interesting. If the excitation is of magnetic origin and such a spin wave radiation pattern was excited by the pump pulse, in what direction would one expect such a symmetry axis to exist? The excitation could be non-magnetic and the polarization response could be generated by some additional means. Thermal effects and induced strain waves are going to be induced by absorption of the pump energy, to what extent this could manifest itself in the Kerr channel is an interesting question and currently unknown. In figure 5.2.13 and 5.2.14, the image aspect ratio is 6:14 resulting in the images appearing elliptical.

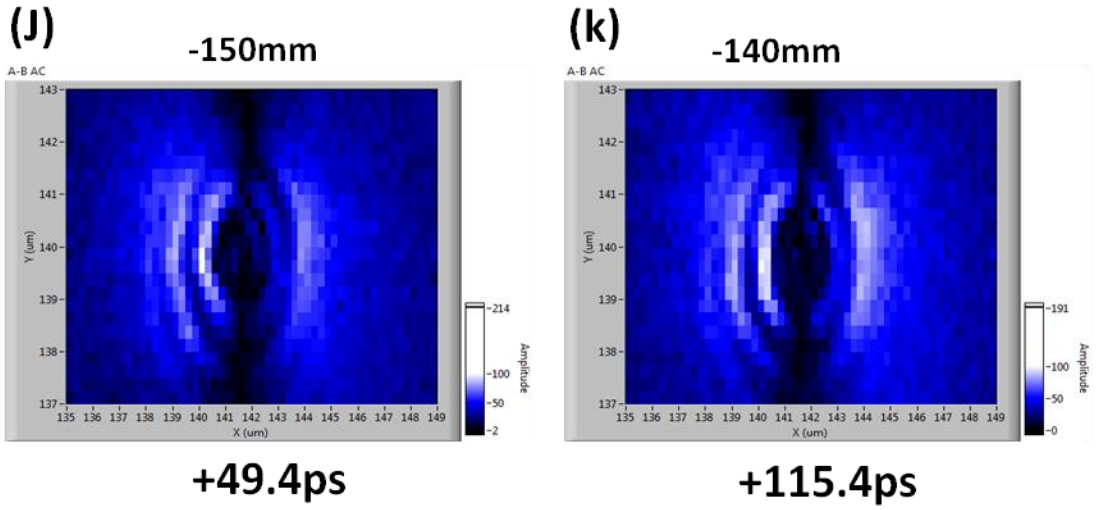

Figure 5.2.14 – The total time delay for 5.2.14 (k) is +115.4ps from the estimated pump-probe overlap. From figure 5.2.12 (f), the ripple pattern is fully visible remaining so until figure 5.2.14 (k). The limited time delay spanning 5.2.12 (f) to 5.2.14(k) does not allow the ripples to move significantly if they are a propagating magnetic disturbance. It is not clear whether the ripples move outwards as a wave front over this time interval. If the pattern is of magnetic origin and the ripples are propagating spin waves, typical group velocities of spin waves are too slow to be able to resolve this distance in 100ps.

Discussion

By using an ultrashort optical pulse to excite the sample, many other sub-systems are excited within the sample simultaneously. In addition to the spin system, which is responsible for the magnetic properties, the electron and phonon systems are also perturbed and excited on sub-ps timescales. In contrast, the field-pumped Kerr microscope couples directly to the magnetic system using pulsed or harmonic excitation. The sample remains in thermal equilibrium and secondary thermal effects are not present to alter the magnetization dynamics. In the optical process, many interacting systems are excited simultaneously and the spin system is indirectly

excited by the optical pulse. Due to thermal effects, strain waves can be generated, local compression of the sample can change band structure which may alter state-filling effects.

In this section the time-resolved signals and the images are discussed. In figure 5.2.5 (a), (c) and figure 5.2.6(a) reproducible time-resolved reflectivity signals are presented. The time-resolved signals show inconsistencies between repeats under the same conditions. The pump and probe spots were overlapped for each signal. The reflectivity signals in figure 5.2.5 (a), (c) and figure 5.2.6 (a) are reproducible and at 17 ps the pump-probe overlap position is observed. During the first 10-15ps oscillations are observed and die away. The signals then relax over the course of several hundred picoseconds. In figure 5.2.6 the time delay is reduced from 200 ps in figure 5.2.5 to 50 ps to observe the zero delay position in more detail. In figure 5.2.6 (c) the reflectivity curve inverts itself and is positive, despite being inverted the signal shape is the same as in figures 5.2.5 and figure 5.2.6. In figure 5.2.7 (a) and (c), the reflectivity curves change their sign again, becoming negative. The changes in the sign of the reflectivity are related to the pump-probe overlap. Any drifts in the pump-probe overlap on the order of the spot size which is a micron will cause a change in the observed signal. The lack of consistency and reproducibility of the rotation signals in figures 5.2.5 to figure 5.2.7 inclusive can be explained by relative drift of the pump-probe overlap.

In figure 5.2.7(d) several oscillations are observed in the first 20ps of zero-delay. In figure 5.2.8 longer 2 ns time resolved signals are shown with clear oscillations. In figure 5.2.8(a) the reflectivity signals show a constant relaxation over the timescale of 2 ns. In the rotation signal in 5.2.8(c) the signal features a background which after the first 500 ps starts to increase. The origin of the background stems from laser power fluctuation over the course of the time-resolved scan(s). The Fourier spectra in figure 5.2.9 of the oscillations in figure 5.2.8 give a

frequency of 17 GHz in both the rotation and reflectivity channels respectively. The origin of the oscillations could be either magnetic (magnons) or lattice modes (phonons). Cross talk or reflectivity breakthrough between the rotation and reflectivity channels would imply oscillations in both channels are identical. This could be spin waves in the rotation channel being detected and imposed on the reflectivity signal or phonons being measured in the reflectivity channel and imposed on the rotation signal.

The experimental challenge is consistently overlapping the sub-micron pump and probe spots. Mechanical drift can ruin the focus and overlap of the pump or probe spots. In the measured Kerr images presented in figures 5.2.11 to 5.2.14 inclusive, the observed pattern arises from spin waves generated in the pumped region. The time delay between figures 5.2.11 and 5.2.14 is only 100 ps, in this time distances travelled at typical spin wave group velocities are too small to be resolved. Pump defocusing during the course of multiple consecutive scans alters measured images. When the focus remains constant a measured image looks identical to the previous image.

5.3 Experimental Results - Recent optical microscope Data

In the last section, preliminary data were presented. The origin of the oscillations in the time-resolved signals is due to magnons or phonons, there is reflectivity breakthrough in the rotation and reflectivity signals. The changes between consecutive measured images are due to drifts of the pump focus position. In figure 5.3.1 the dependence on the measured image(s) is shown for various positions of the pump objective. In figure 5.3.1(a) and (f) there is a 20μm change in the pump objective, resulting in a drastic change to the observed image. The observed pattern depends strongly on the pump focus position. From figure 5.3.1 (a) the image evolves

from a blurry spec to a symmetrical circular pattern resembling the images presented in figure(s) 5.2.13 and 5.2.14.

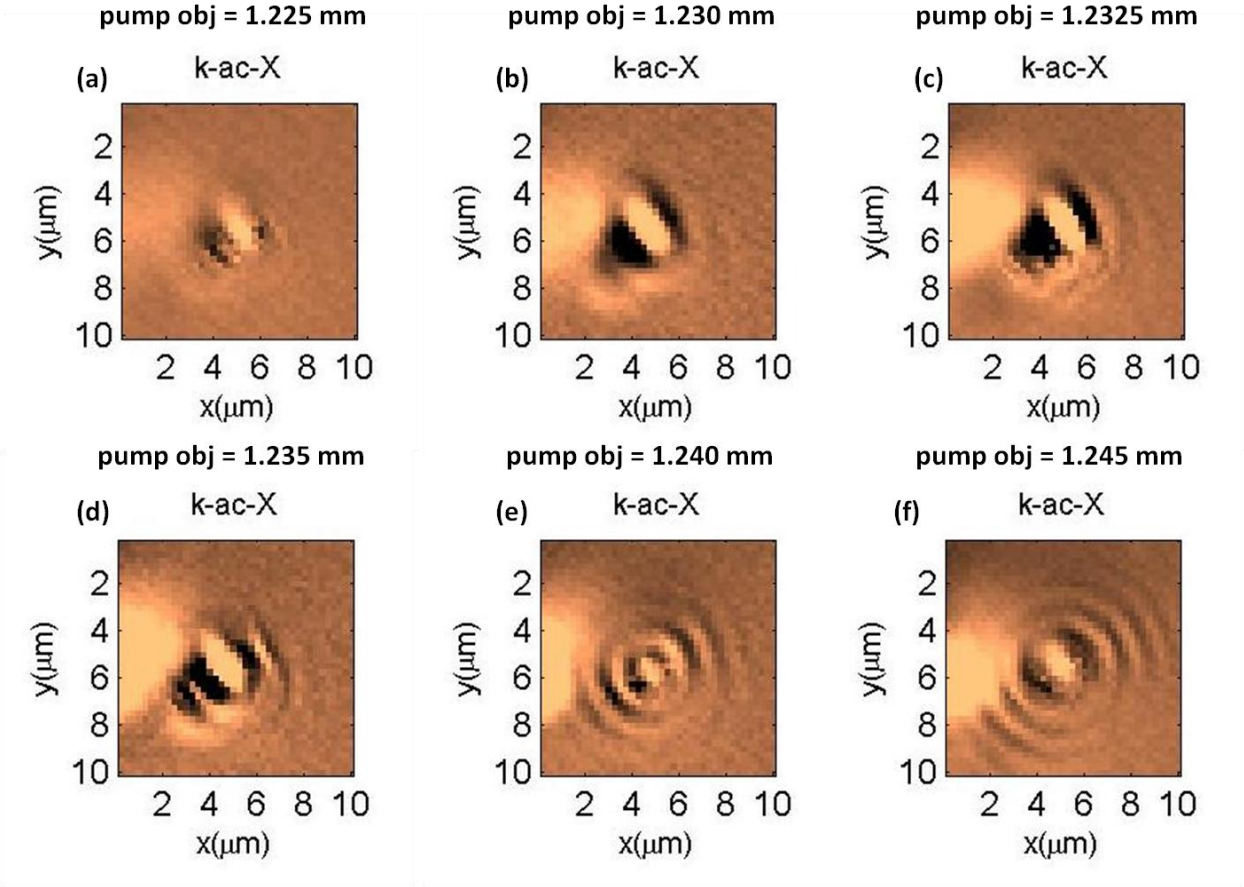

Figure 5.3.1 – Kerr images measured at different pump objective positions at several micron steps over a 20μm interval. The pump objective distances refer to the pump stage position. Images measured by Dr. Yat-Yin Au.

Due to the sensitivity of the pump focus position, it is almost impossible to tell whether changes are due to drifting of the pump focus or changes due to temporal evolution of the signal at different time delays. In figure 5.3.2, spin waves are observed propagating away from the pumped region. The zero-delay position is shown at 1 ns in figure 5.3.2(a), from 1ns onwards circular wave fronts can be seen in figure 5.3.2 (b) and (c). The wave fronts continue to

propagate away from the pump region in figure 5.3.2 (d) and (e) respectively. In figure 5.3.2 (e) the trailing edge of the propagating spin waves is observed.

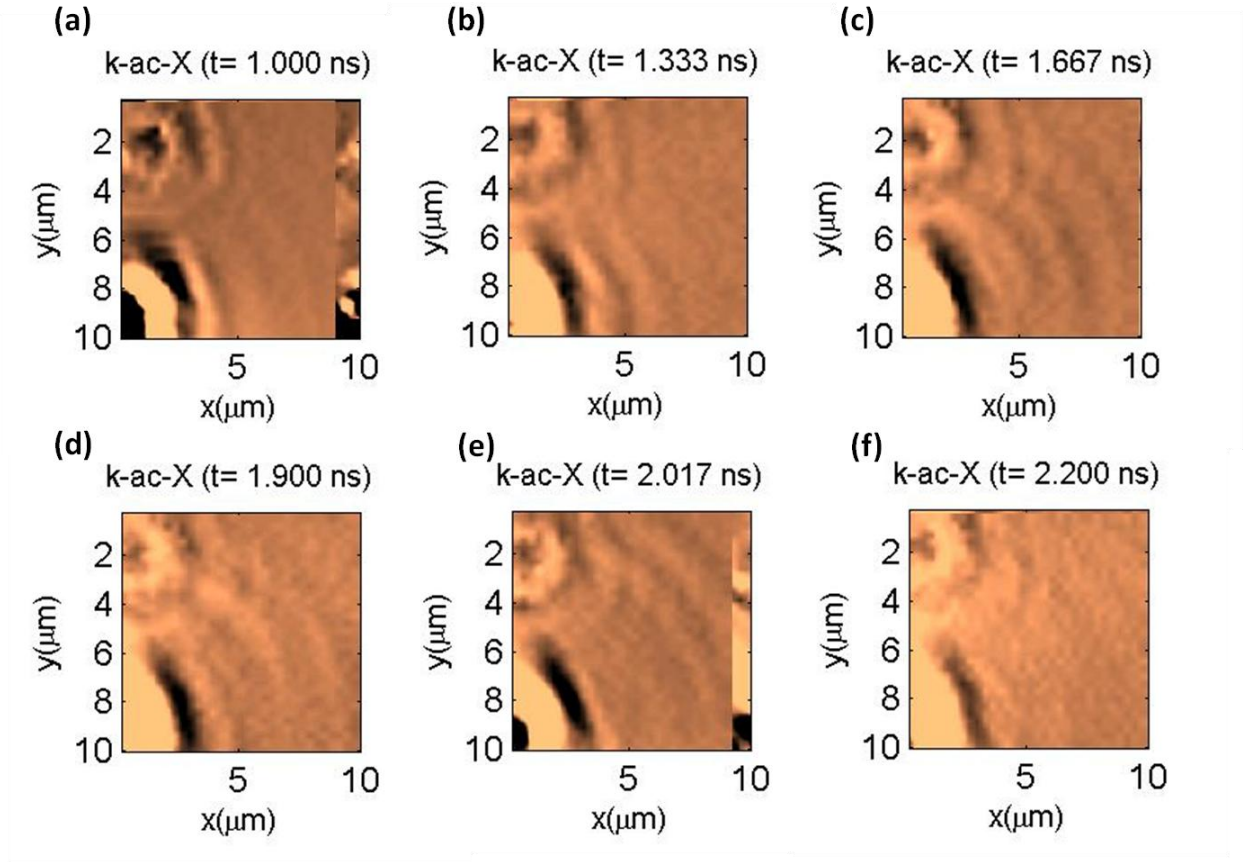

Figure 5.3.2 – Propagating spin waves travelling away from the pumped region (bottom left corner) from the zero-delay position at 1ns. The dark circular region in the top left of the image is a burn from previous optical exposure. The applied field is 500Oe directed out-of-plane. Images measured by Dr. Yat-Yin Au.

In figure 5.3.2 (f) the spin waves are no longer observed in the image as they have travelled away. The wavelength extracted from peak-to-peak distance in figure 5.3.2 (b) and (c) is 2.5μm. By comparing consecutive images, the period of the excitation is determined to be 0.25 ns, giving a frequency of 4GHz. A distance of one wavelength is traversed during this time, giving a phase velocity of 10km/sec.

Discussion

In figure 5.2.9 the Fourier spectra revealed a frequency of 17 GHz. This is much higher than the 4 GHz obtained from figure 5.3.2. The magnitude and direction of the applied field in both figures 5.2.9 and figure 5.3.2 is identical and any deviations in field will not give rise to a factor of 4 up shift in the precession frequency. The origin of the 17 GHz signal in figure 5.2.9 is probably an acoustic phonon mode measured in the reflectivity channel and being passed onto the rotation channel via reflectivity breakthrough. From figure 5.3.1, the observed images are strongly sensitive to the position of the pump objective relative to the sample, i.e. the focus position.

The images depicted in figure 5.3.1 are of magnetic origin and the resulting pattern is dependent on the focal quality of the exciting stimulus. Although of magnetic origin, the patterns observed in figure 5.3.1 are not propagating spin waves. In figure 5.3.2, spin waves are observed propagating away from the point of optical excitation. The separation of the ripple structures in figures 5.2.13 and 5.2.14 is 1μm. The wavelength observed from figure 5.3.2 was 2.5μm. The frequencies and wavelengths observed from the propagating spin waves in figure 5.3.2 are not reconcilable with the frequencies and wavelengths observed in Fourier spectra and images in figures 5.2.9, 5.2.13 and 5.2.14 respectively.

5.4 Summary

In this chapter, initial results from the time-resolved optically pumped scanning optical microscope have been presented. Time-resolved signals and images have been presented from a 20nm permalloy continuous film. The initial time resolved signals and images were subject to mechanical drift of the pump focus and in-plane drift which hindered the reproducibility of the

signals. Data acquired with a drift correction routine withing the magnetic materials group at Exeter (data presented) observed propagating spin waves and a strong dependence of the observed image on the pump objective position. Using the images obtained with the drift correction propagating spin waves were observed with a frequency of 4GHz and a wavelength of 2.5μm. This frequency is not comparable to the 17GHz observed previously in the Fourier spectra, leading one to assume that this is likely to be an acoustic phonon mode. The time-resolved optically pumped scanning optical microscope is in its infancy and has a great future potential once initial teething problems are addressed. Efforts in this direction will form much of the future work on this technique.

Chapter 6: Magnetic Transmission X-ray Microscopy (M-TXM) of Cobalt Nano-structures

6.1 Introduction

In this chapter Magnetic Transmission X-ray microscopy (M-TXM) measurements on Cobalt nanostructures are presented. The measurements were made at the Advanced Light Source (ALS), at the Lawrence Berkeley National Laboratory (LBNL) in Berkeley, California. The set of data was collected over two separate beam times in Nov, 2010 and June, 2011. The same sample set was measured at both beam times. The samples consist of a close packed array of cobalt anti-dots overlaid on a continuous permalloy film. The cobalt anti-dot layer and the permalloy film are separated by a silicon-nitride (SiN) layer. The silicon-nitride layer is thicker than the exchange length, designed to decouple the exchange interaction from the two magnetic layers. Not all samples in the measured set contained the silicon-nitride layer. The silicon-nitride layer was used to observe the effect of the stray dipolar fields from the cobalt on the permalloy film.

The focus of this chapter relates images acquired in California to the hysteresis loops measured in Exeter. This experimental technique is a static technique which uses X-ray magnetic circular dichroism (XMCD) as a contrast mechanism to image the ground state magnetisation. The resulting data are a set of grayscale images taken with a soft X-ray CCD detector. The importance of magnetic X-ray microscopy is its ability to image close to fundamental length scales in magnetism, the exchange length down at 10 nm. The current spatial resolution of the XM-1 microscope is around double this at around 20nm [107]. With future advances in zone plate patterning and lithography, the spatial resolution is closing in on the exchange length itself

[108]. The inherent timing structure of the synchrotron gives sub-100ps temporal resolution for current time-resolved (TR) X-ray measurements. To approach the fundamental time scale in magnetism, which is the time over which the exchange interaction dominates, the synchrotron timing structure needs to be reduced. The spatial duration or temporal width of circulating electron bunches in the storage ring determine the duration of the x-ray 'flashes' in the beam line end stations and consequently the experimental time resolution.

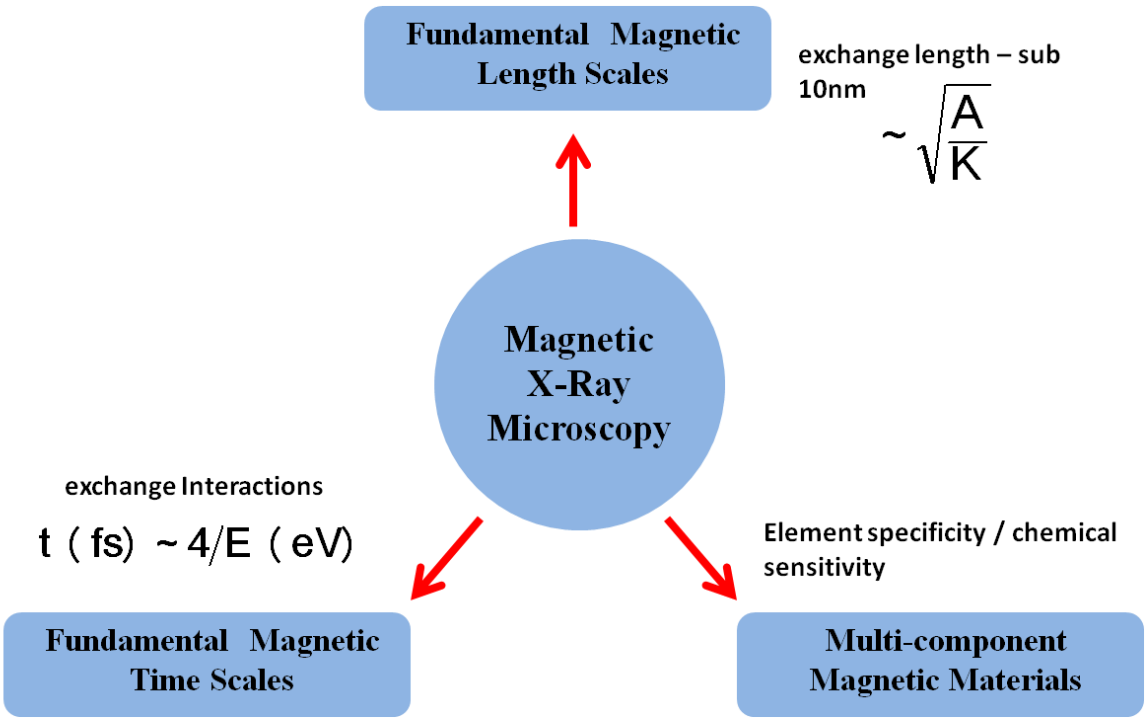

Figure 6.1.1 – Magnetic microscopies are closing in on fundamental magnetic length and time scales, which lie in the nanometer and femtosecond regions. The tunable X-ray energy gives preferential selection over the chemical species one chooses to study in composite magnetic samples. The exchange interaction lies at the heart of the fundamental length and time scales in modern magnetism. Currently the experimental spatial resolution is several factors out; the temporal resolution must be improved significantly to home in on the time the exchange interaction dominates.

Magnetism on the nano-scale and its spin dynamics on sub-nanosecond timescales is currently a highly attractive research topic [109, 110] since it addresses both fundamental length and time scales of magnetism. Interesting time scales of magnetism are precessional and relaxation phenomena , domain wall and vortex dynamics [111-113]. The fundamental timescale in magnetism is given by the time required to transfer energy and momentum from the electronic system to the spin system [114]. There is also a strong technological interest in fundamental magnetic processes due to current developments in ultrahigh density magnetic storage media and miniaturized magnetic sensor technology.

New technological concepts such as spintronics, require the understanding of spin dynamics in addition to the electronic charge of the electron. There is a variety of powerful techniques available to image magnetic nanostructures. They can be categorised by the probes they use, such as optical or electron based microscopies such as Kerr microscopy or Scanning Electron Microscopy with Polarisation Analysis (SEMPA) or Lorentz-transmission electron microscopy. Additionally, there are scanning probe microscopies such as magnetic force microscopy. Magnetic microscopies have largely contributed to the current level of understanding of magnetic phenomena. Spin-polarised scanning tunnelling microscopy provides static images with almost atomic level resolution [115].

Conversely, time-resolved Kerr microscopy images down to the femtosecond regime utilising an inherent diffraction limited spatial resolution in the sub-micron range only. The ultimate question of how magnetism behaves when both the fundamental magnetic length and time scales are approached cannot be addressed today and a thorough understanding of the nature of the exchange interaction is still missing. The grand challenge of modern magnetism is to achieve sub-10nm spatial resolution with elemental specificity and simultaneously having

femtosecond temporal resolution. Figure 6.1.1 depicts these experimental goals in x-ray magnetic microscopy.

6.2 Experimental Setup

In this section the experimental geometry and setup will be described. The (XM-1) X-ray microscope sits at beam line 6.1.2 at the ALS synchrotron, part of the Centre for X-ray optics and is a full-field soft X-ray transmission microscope [116]. Soft X-ray photons have energies extending from 250eV (just below the carbon K-edge) up to several keV, with wavelengths ranging from about 10nm down to 0.1nm. This is the soft X-ray region of the electromagnetic spectrum, wavelengths shorter than 0.1nm are classed as hard X-rays and wavelengths longer than 10nm are ultraviolet. There are a large number of atomic resonances, leading to absorption of soft X-rays in very short distances, typically nm to um in all materials. These elementally specific atomic resonances provide chemical specificity and the nm wavelength affords a high spatial resolution, ideal for microscopy. The K and L absorption edges are associated with the removal of core 2p electron by photo absorption, which is excited to a valence 3d state [117].

This core-to-valence electron transition is the origin of the X-ray magnetic circular dichroism contrast mechanism. Figure 6.2.1 shows a schematic drawing of the XM-1 soft X-ray microscope, which is modeled from a conventional bright field visible light microscope. Broadband soft X-ray radiation comes from a bending magnet source from the ALS synchrotron, being directed to the beam line end station by a plane X-ray mirror. As in a conventional light microscope, the X-rays are focused onto the sample by the condenser zone plate (CZP) and then pass through a pinhole which features a 100nm silicon nitride vacuum window. The condenser zone plate and pinhole act as a linear monochromator, due to the condenser zone plate's

wavelength dependent focal length. A particular wavelength is chosen by moving the condenser zone plate along the X-ray optical axis and a spectral resolution of about 1eV is possible, in an energy range 250 – 1.8keV (5 to 0.7nm).

Bending magnet radiation viewed at an angle to the orbital plane of the storage ring provides circularly polarized x-ray photons; a movable aperture upstream of the condenser zone plate allows the choice of a given helicity. The degree of polarization of a given helicity varies between 60 – 70% [118]. The X-rays are transmitted through the sample which sits in air. In the vicinity of element specific resonant X-ray absorption edges e.g. the 3d transition metals, large values of circular dichroism up to 25% can be observed [119]. The sample is illuminated by a 10 μm field-of-view by X-rays tuned to a specific absorption edge. The sample which features a ground state magnetic configuration with a spatially varying magnetization will impart a locally varying photon intensity to the transmitted X-rays. The X-rays then pass through another silicon-nitride vacuum window to a second Fresnel zone plate, the micro zone plate (MZP), which acts as a collecting objective and images the transmitted photons onto a two-dimensional charge coupled device (CCD) detector.

The spatial resolution of the XM-1 x-ray microscope is determined by the outermost zone width Δr of the micro zone plate. The soft X-ray CCD detector is a back-thinned, back-illuminated 2048 x 2048 pixel array, each pixel is 13.5 x 13.5 μm, which gives the total detector size as a 27.6 x 27.6mm. Having a10um field-of-view gives a single pixel in a recorded image a size of 5nm. The CCD detector can be operated in one, two and four binning modes, in which the recorded image resolution becomes 2048 x 2048, 1024 x 1024 or 512 x 512 pixels respectively. Given the inherent spatial resolution is no less than 20 nm, 4-binning mode is used to give a 20nm image pixel size. Using a lower binning mode will increase the individual image exposure

time. The detector quantum efficiency is approximately 60 – 80% and requires about 1000 photons per pixel. The total number of photons per image is around 4.2 x 10^9 photons. Typically in the storage ring, there are around 10^{17} electrons per bunch; to get 10^9 photons for a single image gives a 10^{-8} photon per electron probability for circulating electrons. The X-ray optics and the beam line itself are under vacuum due to the strong absorption of soft X-rays in air.

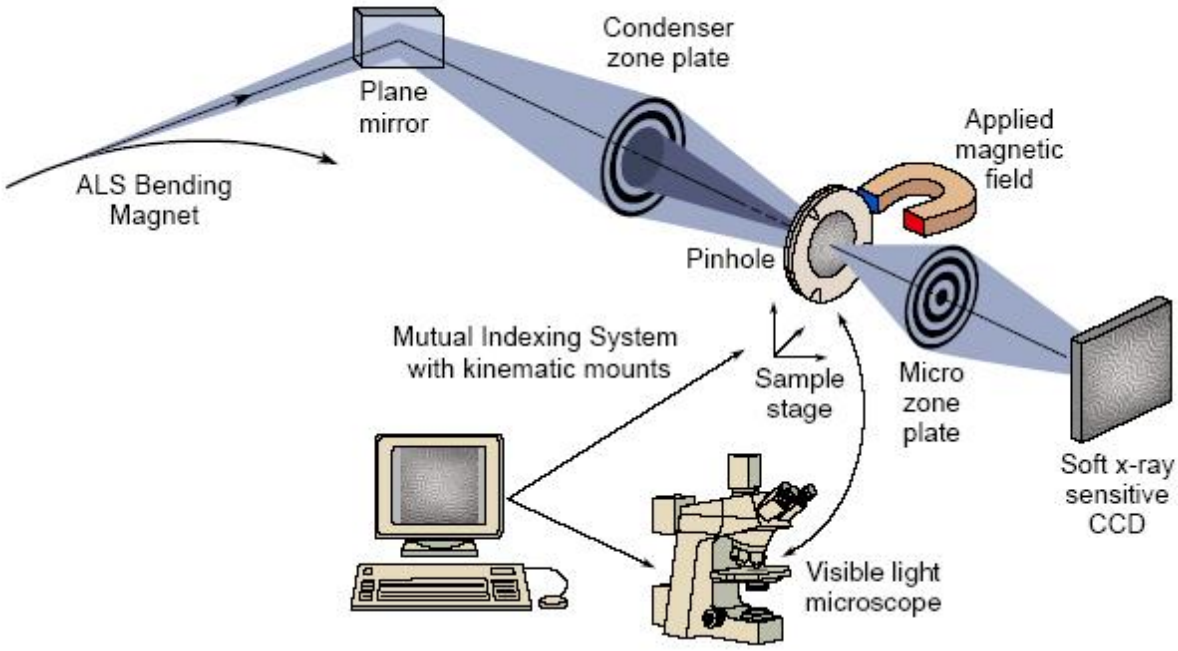

Figure 6.2.1 – Schematic of the XM-1 microscope at beam line 6.1.2. Image taken from [116]

The aligning light microscope (ALM) or visible light microscope in figure 6.2.1 is used to align the X-ray microscope once a new sample is mounted. The sample stage, the condenser zone plate and micro zone plate sit on kinematic xyz stages. As a pure photon in/photon-out technique, in principle magnetic fields of any strength and direction can be applied. In practice, fields up to 2 – 3kOe can be applied in a perpendicular geometry and fields of 1 -2kOe can be applied in the

sample plane. This allows samples with both in-plane and out-of-plane magnetization to be studied. To image the in-plane component of magnetization, the sample has to be tilted about an axis perpendicular to the x-ray optical axis. The tilt angle is typically 30 degrees; larger angles dramatically increase the effective thickness of the sample, at 30 degrees the effective thickness is increased by a factor of 2.

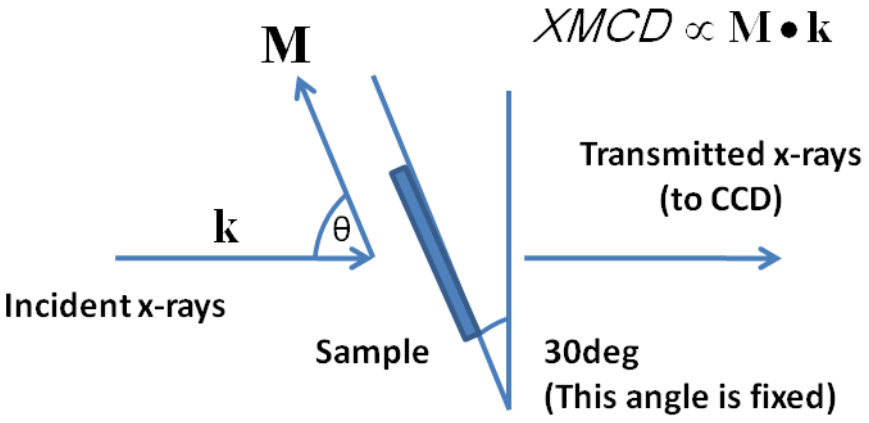

Figure 6.2.2 – Schematic view of the sample orientation and its in-plane magnetistion in the XM-1 microscope. Special pole pieces allow the bias magnetic field to be applied in the plane of the sample. The sample can be rotated in its own plane; this is dependent on the available recesses in the sample holder. These angles were fixed at 0 and 30deg.

Fresnel Zone Plate Optics

For visible light microscopes, transparent materials such as glass use refraction to manipulate light. In the X-ray region, the refractive index of matter including glass is so close to unity that X-rays experience negligible amounts of refraction. This initially prevented X-ray microscopes from being realized for almost 80 years after W. Roentgen's initial discovery in 1895. Rather than use refraction, X-ray 'lenses' use diffraction and are called Fresnel zone plates

(FZP). Fresnel zone plates are circular diffraction gratings, featuring a radially increasing line density. In its simplest form, a transmission Fresnel zone plate consists of alternate transparent and opaque rings. High quality Fresnel zone plates are fabricated by state-of-the-art nanotechnology tools, such as e-beam lithography. The Fresnel zone plates used on the XM-1 microscope are built in-house at the centre for X-ray optics in Berkeley. A zone plate lens is fully specified by 3 parameters. Spatial resolution is set by the wavelength λ and the outer zone width Δr. To avoid chromatic blurring, the number of zones N, must be less than the inverse relative spectral bandwidth λ / Δλ, such that N < λ / Δλ. For many applications, λ, Δr and N constitute a natural set of zone plate-defining parameters [120]. In terms of these parameters, the other parameters of the zone plate are given by equations 6.2.1 to 6.2.4 inclusive.

$$D = 4N\Delta r \tag{6.2.1}$$

$$f = \frac{4N(\Delta r)^2}{\lambda} \tag{6.2.2}$$

$$F^{\#} = \frac{\Delta r}{\lambda} \tag{6.2.3}$$

$$NA = \frac{\lambda}{2\Delta r} \tag{6.2.4}$$

Where D is the zone plate diameter, f is the Fresnel zone plate focal length, $F^{\#}$ is the lens f-number and the zone plate numerical aperture is denoted by NA. For uniform plane wave illumination the Rayleigh criterion sets the diffraction limited spatial resolution of a perfect lens, given by equation 6.2.5.

$$R = \frac{0.610\lambda}{NA} = 1.22\Delta r \tag{6.2.5}$$

The condenser zone plate has a diameter of 11mm, an outer zone width of 55 nm and 50,000 zones. Using equations 6.2.2 to 6.2.4, the condenser zone plate focal length is 30cm and has a numerical aperture of 0.014. The condenser zone plate has a centre-stop providing hollow cone illumination of the pinhole and sample, the former of which helps to limit the spectral bandwidth of the impinging X-rays. The micro zone plate has 500 zones and a 50 μm diameter, giving Δr as 20 nm a focal length of 500 μm, a numerical aperture of 0.04 and a spatial resolution of 25 nm. By using the most advanced zone plates, the maximum possible spatial resolution of the XM-1 is 0.8Δr [121].

6.3 Sample Description

Sample 13 (S2H2S2)

In this chapter, data are presented for three different samples measured at the Advanced Light Source in Berkeley. The sample set taken to Berkeley consisted of 15 cobalt structures, labelled sample 1 to sample 15. The cobalt thickness, permalloy thickness, presence of the silicon nitride layer, sphere diameter and structure type (either zig-zag or anti-dot) varied between samples. In this chapter data are presented on samples 9, 11 and 13. These samples are presented because of the measured set they are the only samples to show any result. Sample 9 features a 20 nm thick (continuous) permalloy film, on top of which sits an 11.7nm thick cobalt anti-dot layer. Separating the cobalt and permalloy layers of sample 9 is a 5-7 nm thick silicon-nitride layer, the anti-dot diameter is 700nm. Sample 11 features 10.8 nm thick cobalt anti-dots 705 nm in diameter on 40 nm of continuous permalloy. Sample 13 has 60 nm of continuous

permalloy, with a 10.8nm thickness of 700nm diameter cobalt anti-dots. Samples 11 and 13 both feature the silicon-nitride layer.

The cobalt thickness of the three samples is nominally identical at *circa* 10 nm. All presented samples feature the silicon-nitride sandwich layer. The permalloy thicknesses are 20, 40 and 60nm for samples 9, 11 and 13 respectively. Samples 11 and 13 measured on the iron edge reveal the sudden switching behaviour of the permalloy, Sample 9 measured on the cobalt edge reveals the magnetisation reversal to occur slowly. The hysteresis loops were measured using the magneto-optical Kerr effect (MOKE) in Exeter. The original experimental aim was to observe the influence of the dipolar fields from the cobalt nanostructures on the magnetic groundstate of the permalloy film. This aim was not achieved. The acquired images are being used in conjunction with the hysteresis loop to explain the reversal process.

In figure 6.3.1(a) annotations to the SEM images show the angles 86.5 and 86.7 degrees, this angle is the first line of symmetry of the anti-dot pattern with respect to the horizontal edge of the sample holder. The size markings in figure 6.3.1 (b) denote the centre to centre separation as 777.4 nm, the Co thickness between the anti-dots is 100 nm wide and the length of these regions is of the order of 540 nm. In figure 6.3.1 (a) and (b) the scale bars are 3 and 1μm respectively. The field direction is in the plane of the sample, which is along the horizontal axis of images figure 6.3.1(a) and (b), along the 0 degree direction.

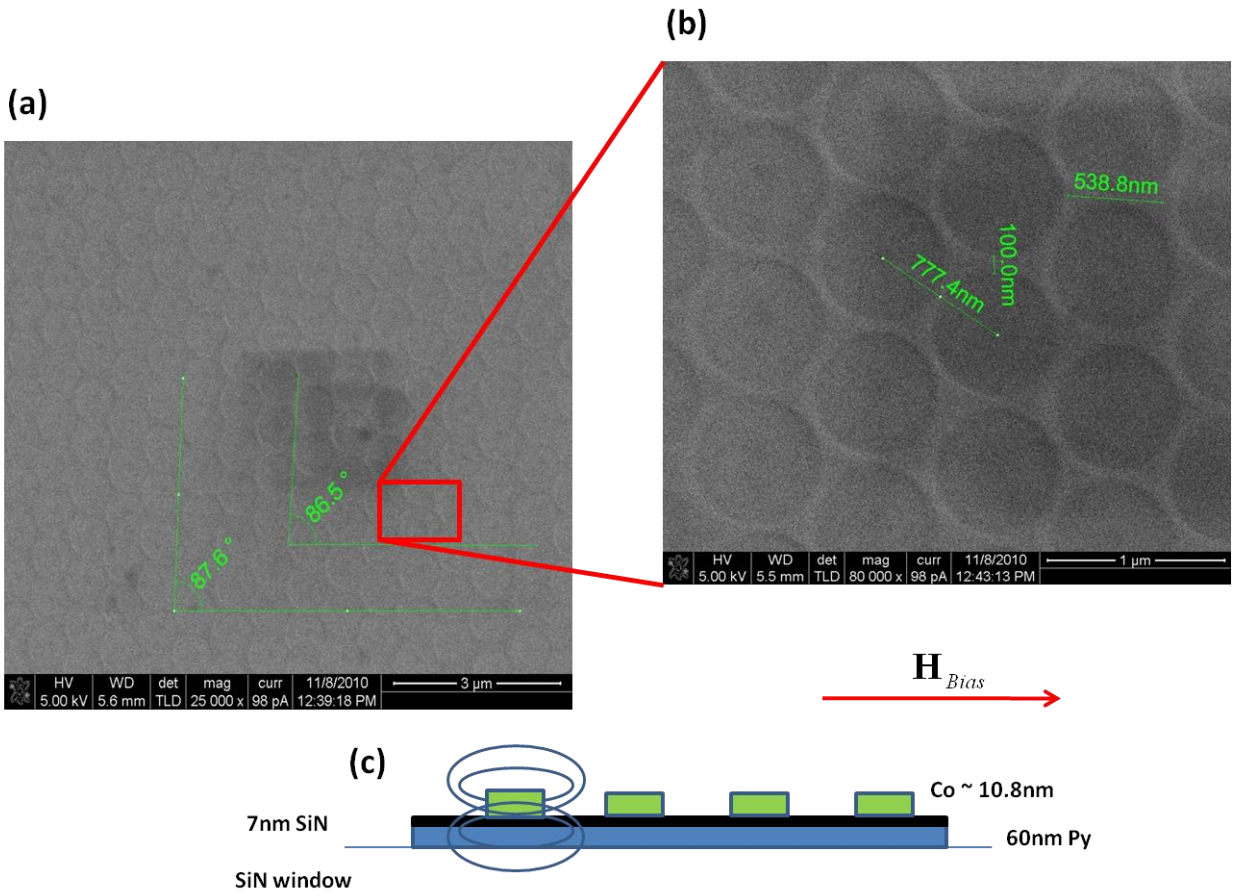

Figure 6.3.1 – Scanning electron microscope (SEM) images (a & b) of the cobalt anti-dots and permalloy film. Figure 6.3.1(c) illustrates the side view of the cobalt anti-dot matrix overlaid on the continuous peramlloy film.

In figure 6.3.1, the close-packed array of the cobalt anti-dots can be clearly seen, the circular regions in the SEM images are negatives in the cobalt and hence the permalloy film underneath. The webbing region between the circular areas is the cobalt structure itself. The tessellation of the close-packed nano-spheres during fabrication leaves lines of symmetry in the resulting anti-dot pattern, when the field direction lies along a particular line of symmetry one would expect this to be an easy axis of magnetization. Conversely, when the field direction lies at an angle to a given line of symmetry, the resulting hysteresis loop would be along a hard(er)

axis of magnetization. The SEM images of the presented samples were taken by Dr. Ehsan Ahmed here in Exeter, who also measured the hysteresis loops.

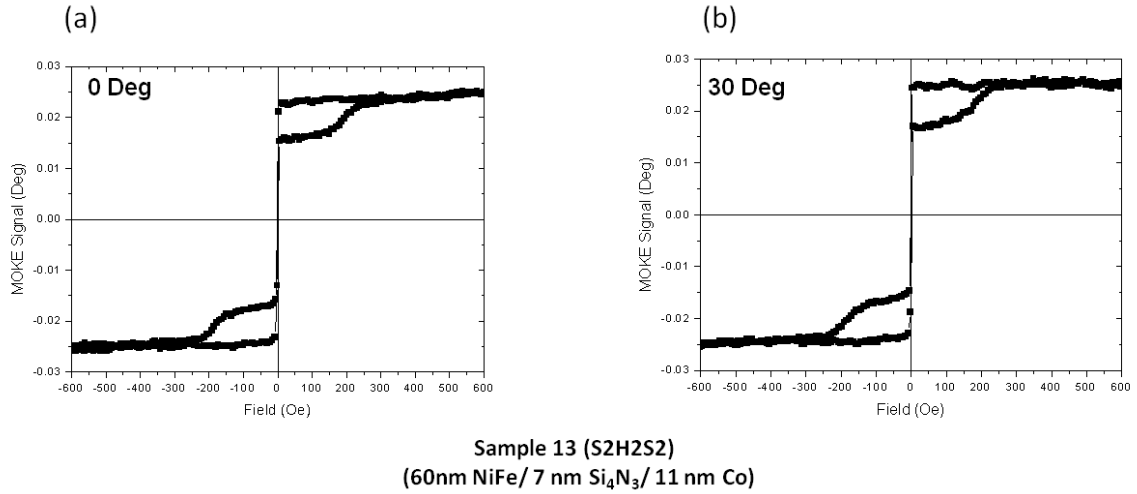

Figure 6.3.2 – Hysterisis loops of sample 13 measured in Exeter prior to the June, 2011 beam time.

In figure 6.3.2(a) the loop is measured at 0 degrees, corresponding to the field along the first line of symmetry of the cobalt structures and the saturation field is ± 250 Oe. In (b) the sample has been rotated 30 deg with respect to the applied field. The hysteresis loop shape is similar and the saturation field remains at ± 250 Oe. In figure 6.3.1(a) the SEM image shows an 87degree angle from the horizontal line, this horizontal line serves as the zero line for the applied field in hysteresis loop and synchrotron measurements. The vertical axis is the Kerr rotation in degrees and the horizontal axis is the applied magnetic field in Oe. The loop height is the order of 50mDeg for both loops in figure 6.3.2 (a) and (b).

Two contributions to the hysteresis loop can be seen in figure 6.3.2 from the permalloy and cobalt layers. The optical spot in the hysteresis loop measurements is millimetre sized. Such a spot samples many sphere diameters periods and an ‘averaged’ response is measured from the

sample. The sharp switching close to zero field originates from the permalloy layer, which has a characteristically low switching field of 10 to 20Oe. The sharp switching from the permalloy accounts for about 60% of the rotation signal as seen from figure 6.3.2. At larger fields the rotation signal gradually increases as the cobalt magnetisation in the anti-dot structure starts to reverse. This reversal appears linear in field up to about ±200Oe. For larger field values the cobalt reversal accelerates as the loop gets steeper, finally saturating at ± 250Oe. Due to the narrow and complex shape the corresponding shape anisotropy of the cobalt structures will be large. As the magnetization departs from its ground state equilibrium, demagnetizing fields fight the applied field to reduce the magnetic charges built up over the cobalt structure.

Sample 11 (S2H3S2)

In sample 13, the permalloy thickness is 60 nm. This is relatively thick compared to the other samples measured; the permalloy thickness was varied for different samples of the same (*circa* 10 nm) cobalt thickness. This was to investigate of the extent of 'magnetic printing' from the cobalt structures on the permalloy layer underneath and how this varied with permalloy thickness. Sample 11 has 10.8 nm of cobalt and 40 nm permalloy (2/3 the thickness of sample 13). Sample 11 contains a silicon-nitride exchange decoupling layer and has a sphere diameter of 700 nm. The SEM images of sample 11 in figure 6.3.3 (a)-(b) are shown. At certain points on the sample(s) vacancies were observed in the anti-dot structure. Vacancies leave islands of cobalt surrounded by anti-dots. At the beam line during measurement, dislocation or vacancy points were specifically sought for their potentially interesting behaviour. Potentially they could be domain nucleation points or sites where magnetisation reversal is initiated.

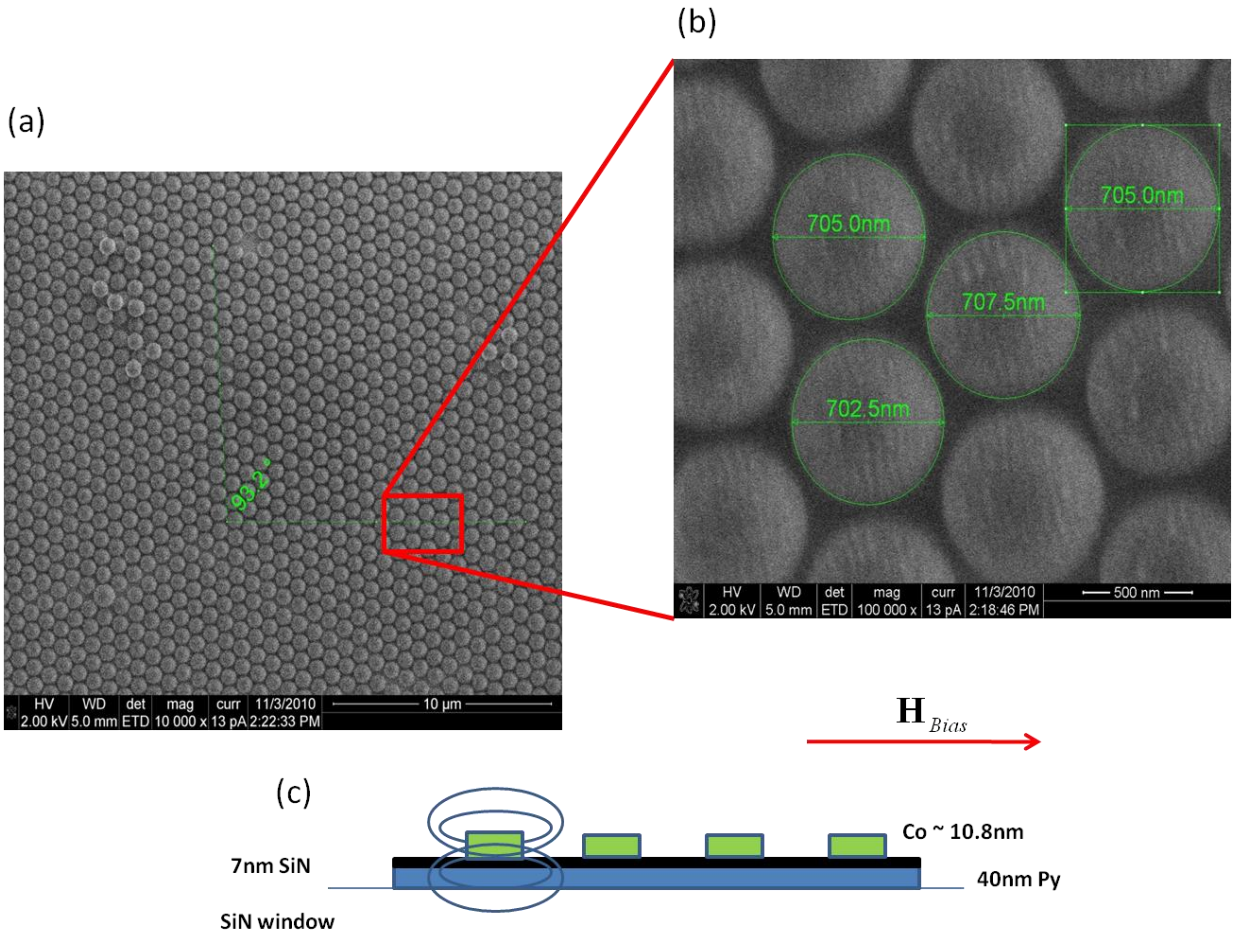

Figure 6.3.3 – In figure 6.3.3(a) the denoted angle is 93.2 degrees from the zero field direction (along the horizontal). Several self-assembled nano-spheres can be seen, they were not fully removed during the lift-off process. In (b) the anti-dot sphere diameter is measured at about 700nm (702.5nm). The light grey circular regions are negatives in the cobalt (permalloy film), the dark grey regions are the cobalt structures. The field direction in (c) remains in plane. In (a) and (b) the SEM scale bars are 10µm and 500nm respectively.

In Figure 6.3.4, the measured hysteresis loops for sample 11 are shown. Qualitatively, they appear similar to the measured loops in figure 6.3.2. The permalloy reverses sharply at low field, constituting the initial step / jump in the rotation signal, which is followed up by a slower more gradual reversal from the Cobalt structures. In the 0 degree loop in figure 6.3.4(a), after the

sudden switch of the permalloy at low field, the loop remains almost flat up to ±100 Oe. The cobalt interstices starts to gradually reverse from this field range onwards. From ±100 Oe to ±200 Oe the cobalt reverses in an almost linear fashion until reaching full saturation at ±250Oe. A similar process happens in figure 6.3.4(b), however the field is along a 'harder' direction, the cobalt reversal starts at a higher field of 200 Oe, followed by full saturation at 350 Oe.

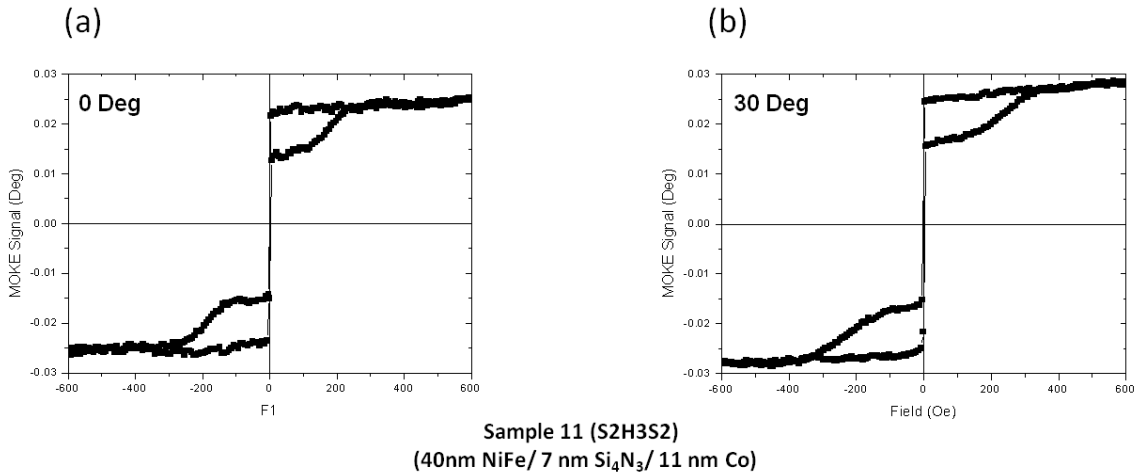

Figure 6.3.4 – Hysteresis loop measurements of sample 11 at 0 Deg (a) and 30 Deg (b). The vertical axis is the Kerr rotation in degrees and the horizontal axis is the applied magnetic field in Oe. The loop height is the order of 50mDeg for both loops in (a) and (b).

Sample 9 (S2H4S3)

The original experimental aim during the Nov, 2010 beam time was to observe the effect of 'magnetic printing' on the permalloy film; to do this a variety of batch file scripts were used. Scripts called batch files are simply text files which dictate the current to the magnet (and hence field) for each measured image. It was later found during the June, 2011 beam time this phenomenon of 'magnetic printing' was not observed on the permalloy layer and a different

variety of scripts focusing on iron edge reversal were performed. Previously scripts focusing on a variety of field histories were used. Sample 9 has the thinnest permalloy layer of 20nm and 11.7 nm of cobalt thickness.

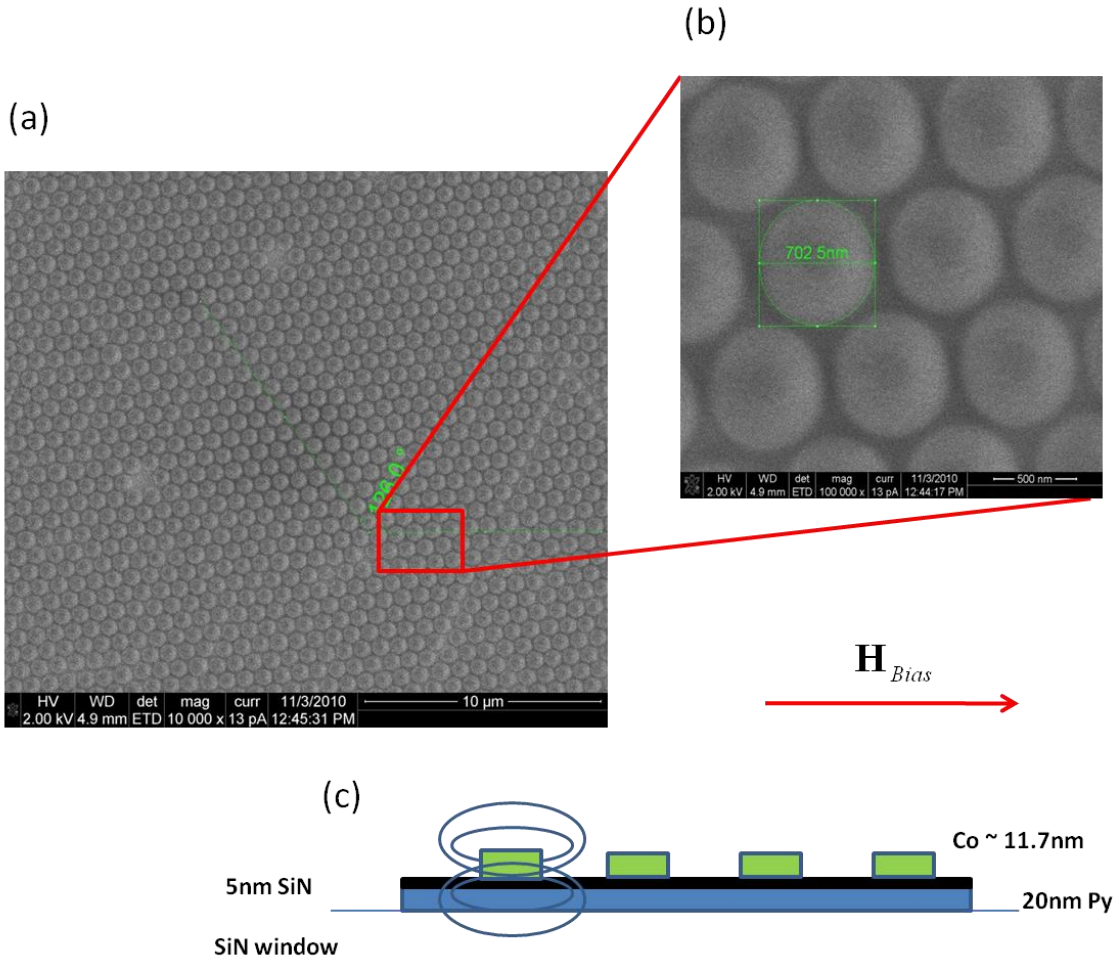

Figure 6.3.5 – Sample 9 SEM images in (a), where the angle from the horizontal (bottom edge) side of the sample mount to the first line of symmetry is 126 degrees. In (b) the anti-dot structure appears visually similar to samples 13 and 11. The sphere diameter is measured in the annotation as 702.5nm. The scale bars in images (a) and (b) are 10 µm and 500 nm respectively.

The reversal process was observed on samples 11 and 13 on the iron edge, check contrast scripts revealed contrast on the cobalt edges; however the cobalt reversal process was not

observed due to the applied field size being too small (typical batch files went up to 50 Oe, insufficient to cause saturation). Data on the cobalt edge were obtained on sample 9 during the first beam time. Since sample 9 contains the same thickness cobalt layer (± 1 nm) as samples 11 and 13, it can serve as an estimator for the cobalt edge reversal process in sample 11 and 13. The hysteresis loops of sample 9 are shown in figure 6.3.6.

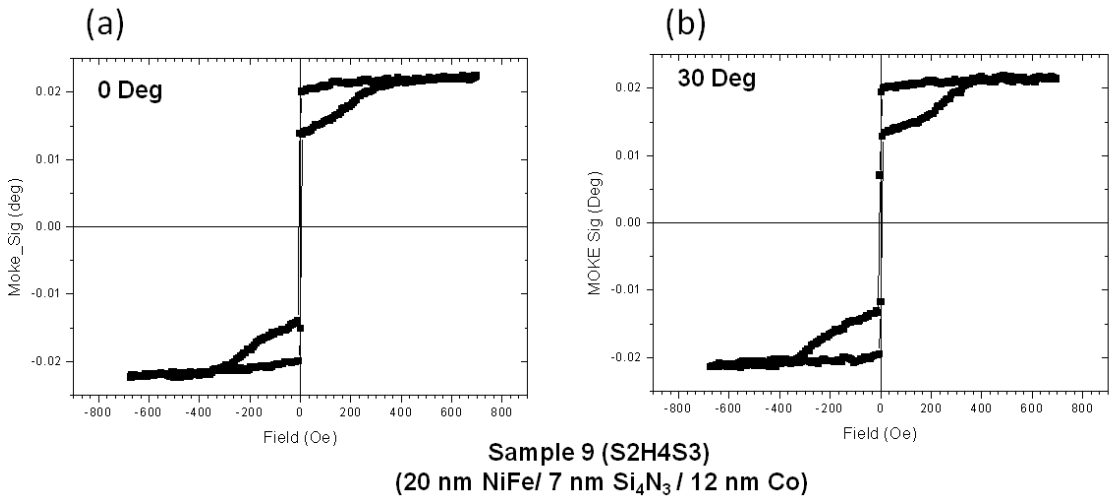

Figure 6.3.6 – Hysteresis loops for sample 9, for the 0 degree (a) and 30 degree (b) directions respectively.

The loop shape in figure 6.3.6 appears unchanged by the reduced permalloy thickness. The sharp switching features of the loops in figures 6.3.2 and 6.3.4 are also present in figure 6.3.6; sharp reversal from the switching of the permalloy at low field, followed by gradual reversal from the cobalt structures. From figure 6.3.6 (a) and (b) the saturation field is 400Oe, the cobalt reversal process in (a) is almost completely linear with field until saturation.

6.4 Experimental Results

L_3 Fe edge (707eV, 1.754nm)

Sample 13 (S2H2S2)

In this section iron edge data is presented for both samples 13 and 11. By selecting a particular absorption edge the experiment has chemical sensitivity of the individual elements in the sample. By tuning the x-ray energy to the iron edge at 707eV allows direct observation of the iron layer itself. Other chemical species such as nickel or cobalt have different core to valence state transition energies and consequently will not be 'seen' by x-ray photons at 707eV. In this section, data is presented from batch file scripts focusing on the reversal mechanism of the iron, such as that shown in 6.4.1 (a).

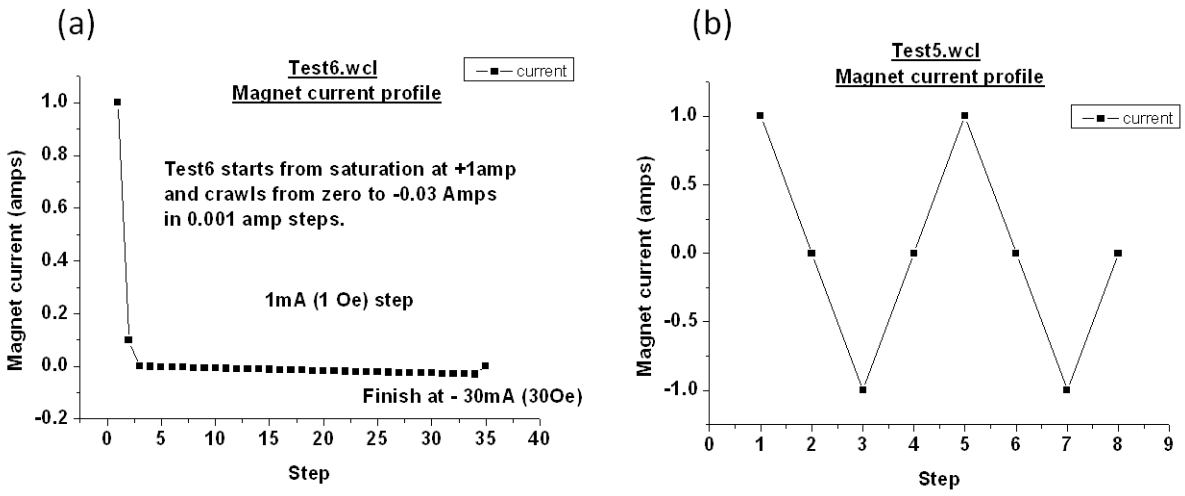

Figure 6.4.1 – Batch files Test 6 (a) and Test 5 (b) performed on sample 13. An image is taken on each data point in (a) and (b). The step number is arbitrary, representing the number of images in a particular scan. Informally it represents magnet current with time.

In 6.4.1 (a), the Test 6 batch file sets the magnet current to +1 amp and an image is taken, the magnet current reduces to +0.1 amp and an image is taken, the next current value is 0 amps

where another image is taken and so on. From zero amps the current steps in 1mA (1 Oe) steps to a final value of -30 mA or -30 Oe. Test 5 in 6.4.1 (b) alternates the magnet current between +1 amp and -1amp, the field calibration is 1mA per Oe (1KOe per amp). The magnet core saturates at ±1amp and this current value corresponds to ± 1KOe. From the hysteresis loops shown in the last section, this field value is sufficient to saturate the sample(s).

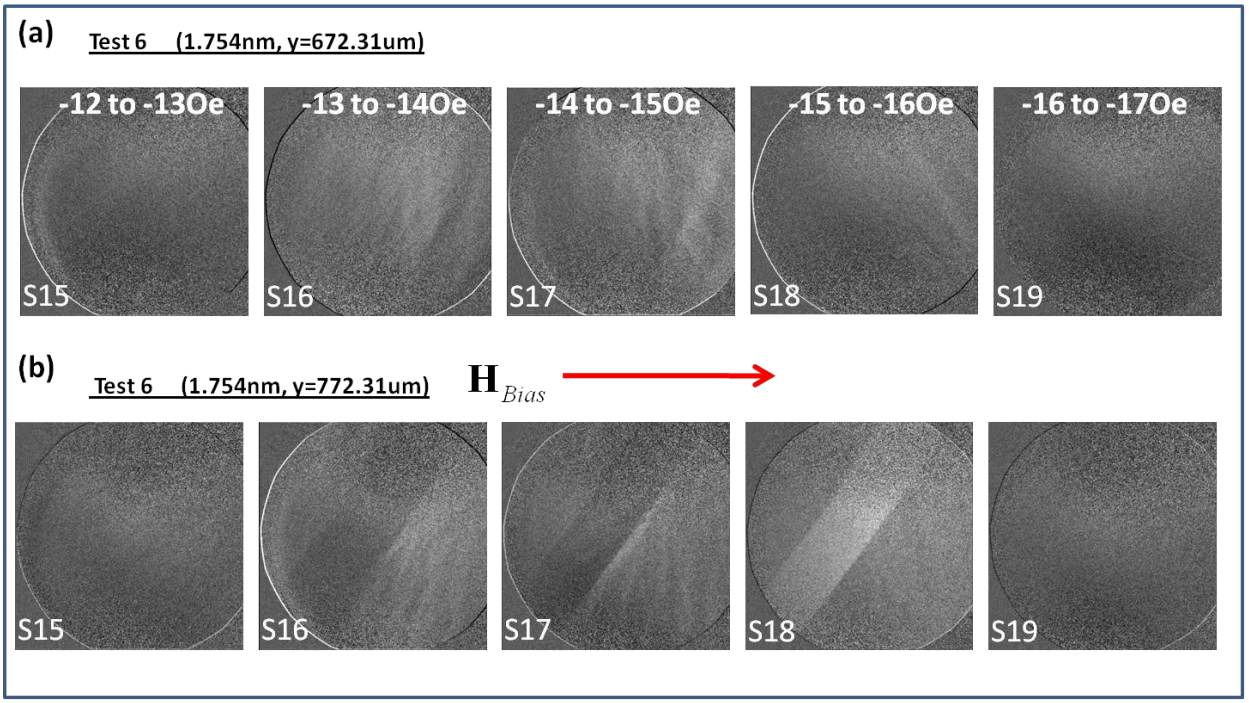

Figure 6.4.2 – Test 6 Fe edge (1.754nm) results from sample 13 (S2H2S2) at two differing positions in (a) and (b). The 'y' coordinate differs in (a) and (b), 'x' and 'z' are identical. The images seen here are the difference of two images taken at the shown field values. The 'S' value in the bottom left corners correspond to the image sequence number from the batch file, for Test 6 this goes from S1 to S33. The images less than S15 or higher than S19 showed no contrast (blank images, such as S19 where no further changes take place) and are not presented here.

Test 5 was predominantly used as a check contrast script for samples or particular regions of a sample, if no contrast is seen between field values of +1KOe to -1KOe then no further

measurements are performed on that region. Tests 5 and 6 were both performed on samples 11 and 13, the Test 6 script (-30 Oe) did not reveal results on the cobalt edge and the large field (±1KOe) script of Test 5 did not show any contrast on the iron edge. Both these results are expected from the hysteresis loop and the data is not presented here in this thesis. The Test 6 iron edge and Test 5 cobalt edge is presented from samples 11 and 13 in this thesis.

In the grayscale images presented in this thesis, each individual image is a difference of two images taken on a single 'data' point of the batch file scans, such as those in figure 6.4.1. One image is used as a reference for the second; any contrast seen once the images have been properly overlaid is the 'magnetic difference' of the two images at a particular absorption edge and field value. The same image (e.g. the first image at +1KOe) can be used as a reference for all the following images or the last image can serve as a reference for the next. This latter technique follows the change between each successive image and is ideal for determining the reversal and saturation field. The images in figure 6.4.2 (a) and (b) show reversal starting at -12 to -13Oe, and fully completing by -16 to -17Oe. This is consistent with the low field switching observed in the hysteresis loop in figure 6.3.2 and the characteristic values expected from permalloy.

The domains seen in figure 6.4.2 (a) are several microns across and are randomly distributed. In figure 6.4.2(a) images S16 and S17 show domains orientated vertically, in S18 the domains are now orientated diagonally. In 6.4.2 (b) the iron domains are 10's of microns in size (the image field-of-view is 10 μm) and appear consistently orientated along the same diagonal until the film saturates and becomes a single domain state at field from -18Oe onwards. From figure 6.4.2, the iron edge contrast shows no resemblance to the cobalt pattern above and the iron domain reversal mechanism appears stochastic in nature and happens consistently over a specific field window of -15 to -20Oe. Further measurements were made at various randomly chosen

positions on the sample 13 surface. Figure 6.4.3 displays this data. To observe contrast with in-plane magnetization, the sample holder is deliberately tilted at 30deg, as shown in 6.2.1.

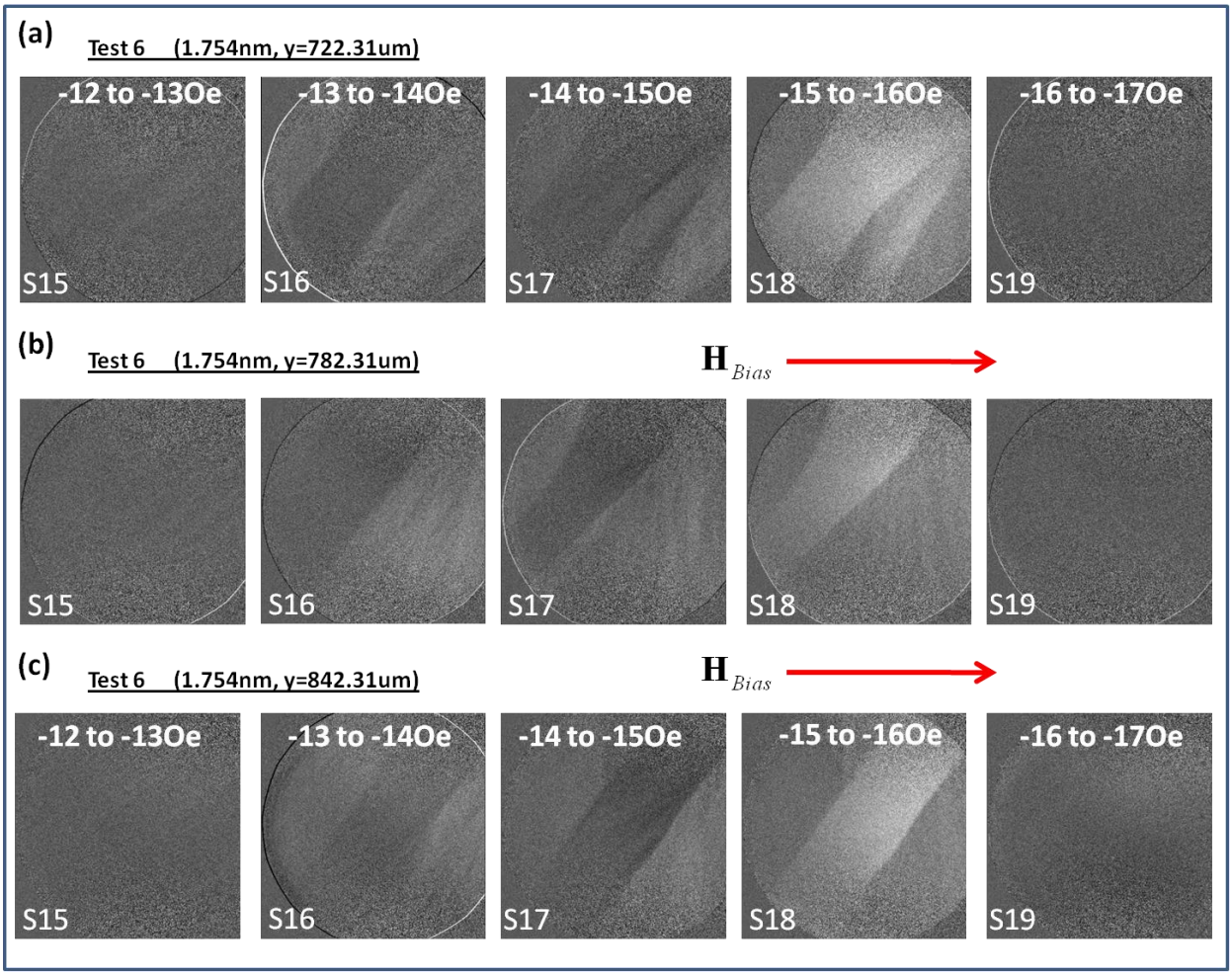

Figure 6.4.3 – Repeat measurements of the Test 6 batch file on randomly chosen points on sample 13. Reproducible results confirming the lack of cobalt influence, reproducible switching field range and random nature of the domain reversal process. The seemingly reproducible diagonal orientation of the large domains is an interesting feature.

The sample can move in the x-y plane, because the sample is tilted any motion in the x-direction changes the x-ray focus, the condenser moves toward or away from the sample in this case. Therefore any alteration of the x-coordinate has to be followed by a correction in the

sample's z-coordinate to preserve the focus. A simpler way to location find on the sample is to alter 'y' only, which moves the sample in a vertical plane. This requires no secondary alterations to the sample stage.

Figure 6.4.3 (a) – (c) inclusive shows large domains, a given domain shape does not appear to be reproducible, but large straight domains seem to be favoured in the iron. The sample is initially in a single domain state at +1KOe, at zero field the domain configuration remains unchanged and remains so until image S15 in the -12 to -13Oe range. This single domain state then fragments or splits into large area micron sized domain regions which feature opposite magnetization. Regions of unchanged magnetization still remain and can be seen with opposite (light vs dark) contrast. The diagonal orientation is perhaps favoured because having opposite magnetization domains along the field direction is energetically unfavorable and the minimum in this case selectively points along a diagonal direction. As the field increases to larger negative values, the reversed domains grow in size as they start to nucleate from un-switched regions. This process occurs in a series of sudden jumps over a narrow field range, until the entire film consists of a single domain state of opposite magnetization.

Sample 11 (S2H3S2)

In addition to the sample 13 iron edge data shown previously in the last section, iron edge reversal was also seen on sample 11. These data corroborates the findings from sample 13's. The permalloy layer in sample 11 behaves identically the permalloy layer in sample 13, reversal occurs at the same field values and over the same field range. The reduction in contrast is explained by the reduced permalloy thickness of sample 11. The thinner layer reduces the selective absorption in the XMCD contrast mechanism. The reduced sample 11 contrast is shown

in figure 6.4.4; faint contrast can be seen in images S14 to S16 inclusive in (a) and (b) respectively. In figure 6.4.4 (a) the lower hemisphere of the images has darker shading than the upper hemisphere; this is partly caused by shifting of the beam and can be corrected by adjusting the (KZP) microscope zone plates. When the contrast is faint, the contrast can be partially hidden by this effect.

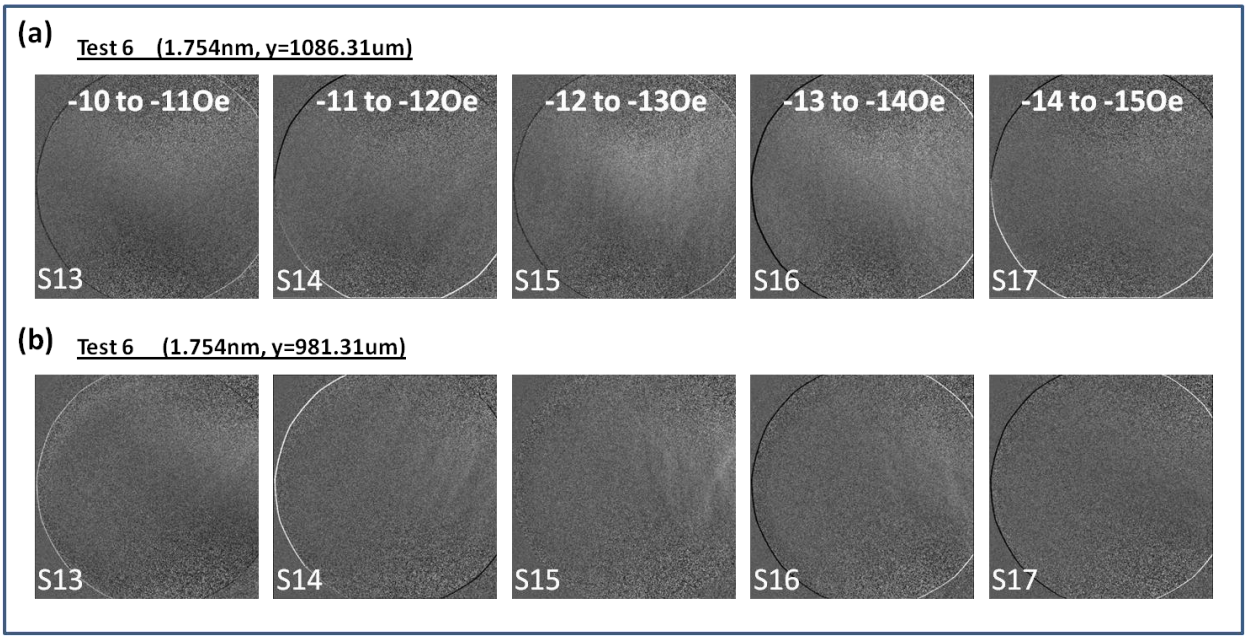

Figure 6.4.4 – The limited iron edge contrast seen on the thinner 40nm permalloy film of sample 11 in (a) and (b). Images S13 and S17 in both cases shown no contrast, very faint contrast can be seen in images S14 to S16. When the contrast is faint, it can be difficult to differentiate the contrast from variations in the x-ray illumination between consecutive images, as in (a). The field in these images is horizontal as displayed in 6.4.2 and 6.4.3.

Faint contrast seen in figure 6.4.4 occurs at repeatable field values, the switching starts in the region -11 to -12Oe and completes at saturation between -14 to -15Oe. The domain size seems characteristically smaller, only several microns in size, rather than extending for several

10’s of microns in figures 6.4.2 and 6.4.3. Figure 6.4.5 shows for various different positions the same trend in domain size and switching field. In 6.4.5 (a) contrast can be seen in the -14 to -15Oe image, the reversal process has completed by this point when compared to the other images.

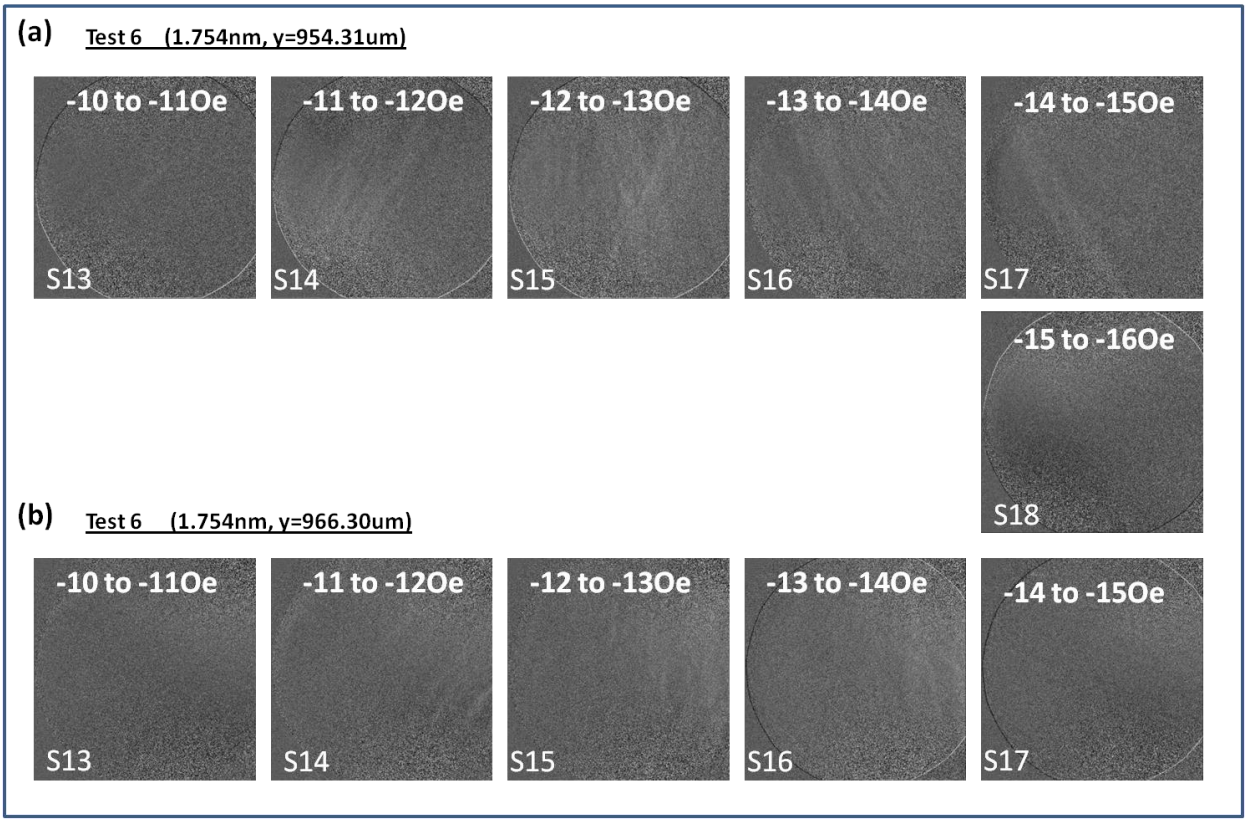

Figure 6.4.5 – Faint striations seen in (a), in images S14 and S15 the domain orientation appears diagonal, in consecutive images S16 and S17 the domain patterns have accumulated together into long narrow domains orientation diagonally in the opposite direction to the previous two images. No such behavior is seen in (b), where throughout S14 to S16 inclusive the reversing domains remain small and irregular in shape, finally magnetisation reversal completes. The field in these images is horizontal as displayed in figures 6.4.2 and 6.4.3.

Sample 11 shows the same behaviour as sample 13 on the iron edge. Domains observed in figure 6.4.6 are characteristically larger than that previously seen in figures 6.4.4 and 6.4.5. The domains have formed into longer linear type patterns observed on sample 13 in figures 6.4.2 and 6.4.3, the direction of the linear type domains also switches orientation before reversal completes. The reversal process in samples 11 and 13 is stochastic in nature and undergoes reversal independently of the cobalt. The reversal process itself occurs suddenly, starting and finishing at repeatable field values, a characteristic which is universal to both samples. Switching in sample 13 generally starts at 13-14Oe and finishes at 15-16Oe. In Sample 11, the switching process starts at 11-12Oe and finishes at 13-14Oe, the switching field is a few Oersted lower in sample 11 than sample 13.

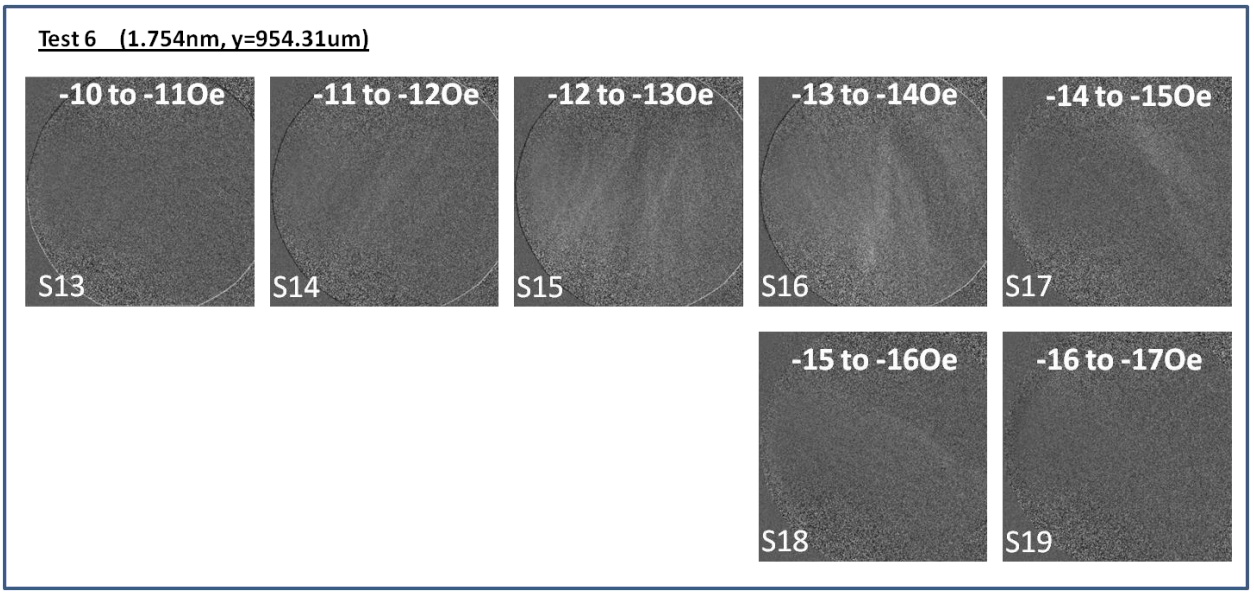

Figure 6.4.6 – Weak magnetic contrast seen as the Test 6 batch file was repeated at the same position as 6.4.5 (a). The domain patters have different shape and comparable size. The field in these images is horizontal as displayed in figures 6.4.2 and 6.4.3.

L_3 Co edge (778eV, 1.594nm)

Sample 13(S2H2S2)

The batch files Test 5 and Test 6 were performed on the cobalt edge. In the following images, the x-ray energy is tuned to the cobalt L_3 absorption edge at 778 eV.

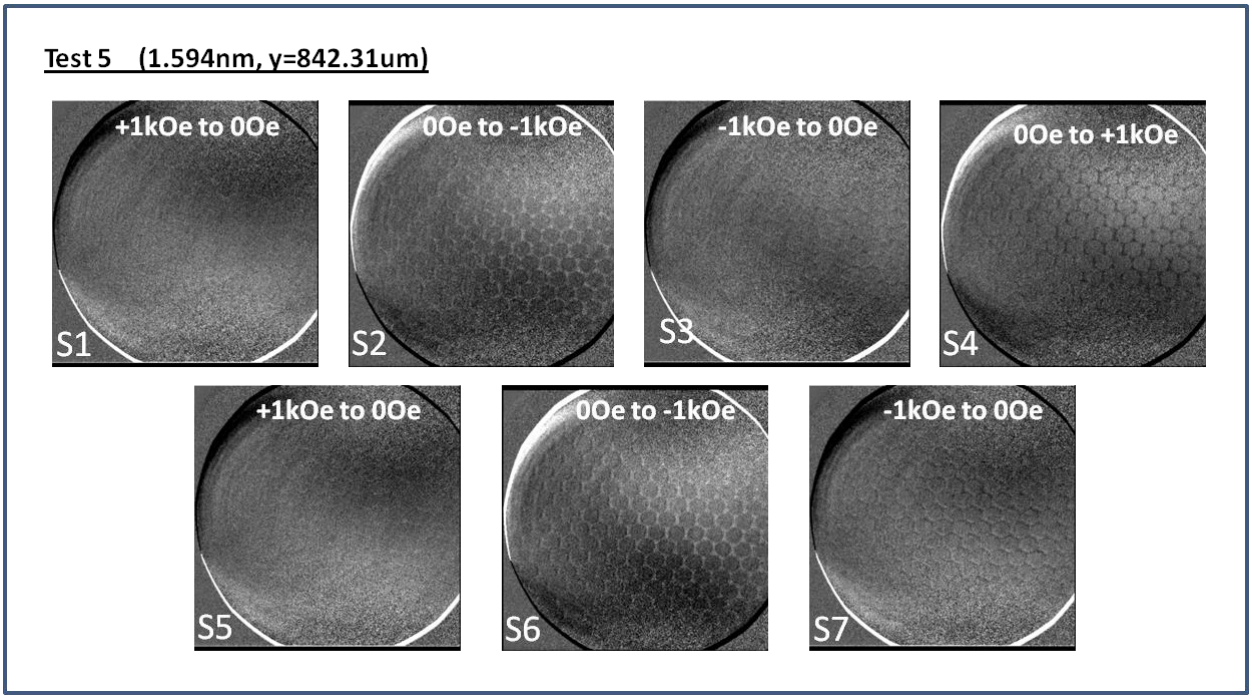

Figure 6.4.7 – Test 5 cobalt edge check contrast data performed at the same position as figure 6.4.3 (c). Contrast is not observed between ±1KOe and 0Oe, only between the field values 0Oe and ±1KOe where the magnetization reverses completely. The field in these images is horizontal as displayed in 6.4.2 and 6.4.3.

In the test 5 batch file the field profile starts at +1KOe, then 0Oe then to -1KOe, this cycle is repeated. In figure 6.4.7, no contrast or change is observed in S1, at +1KOe when the cobalt structures are saturated and at zero field there is no detectable change to the magnetization. The cobalt does not relax from its saturation direction when the field goes to zero.

This behaviour is seen in figure 6.4.7 S1, S3, S5 and S7 respectively. From the zero field state to -1KOe in S2 strong contrast is observed, here the magnetization is in the zero field state with '+ve' magnetization, a -1KOe field reverses magnetization. This is seen as white contrast in figure 6.4.7 S2. In figure 6.4.7 S4 the reverse process happens and the observed contrast is dark. Lastly in figure 6.4.7 S6 white contrast is seen as the difference between zero field magnetization in the '+ve' direction is reversed to the '-ve' direction. This observed pattern of switching in figure 6.4.7 is reproduced below at a different point on the sample in figure 6.4.8.

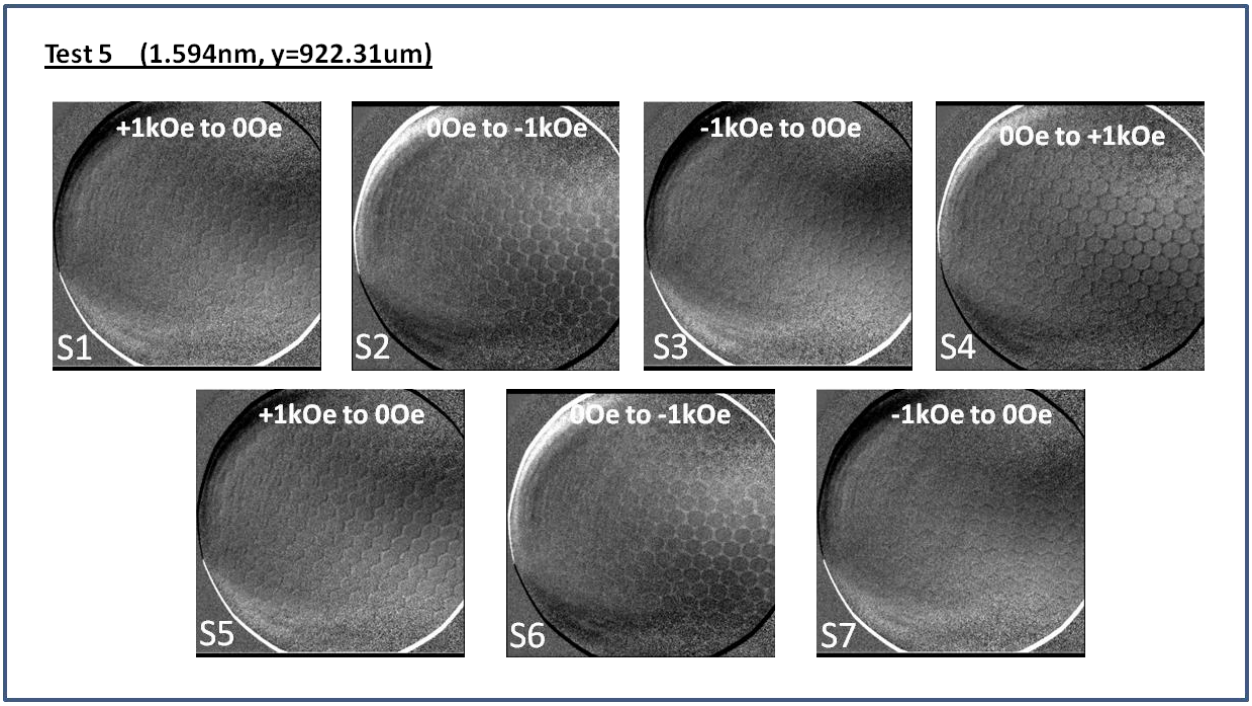

Figure 6.4.8 – Reproducible switching observed between the field values ± 1KOe and zero. The reversal mechanism itself is not expected to be deterministic, but stochastic in nature. For field values large enough to saturate the sample completely, the path of reversal is not known but the end point is the same in each case. The field in these images is horizontal as displayed in 6.4.2 and 6.4.3.

Sample 11 (S2H3S2)

The Test 5 and 6 scripts were performed on the cobalt and iron edges of sample 11. Figure 6.4.9 and 6.4.10 show test 5 cobalt edge data at two different positions. Figure 6.4.9 features a vacancy located centre image, light and dark contrast is seen where the vacancy magnetization is reversed in images S4 and S6 of figure 6.4.9. A thickened stripe region is visible in figure 6.4.10.

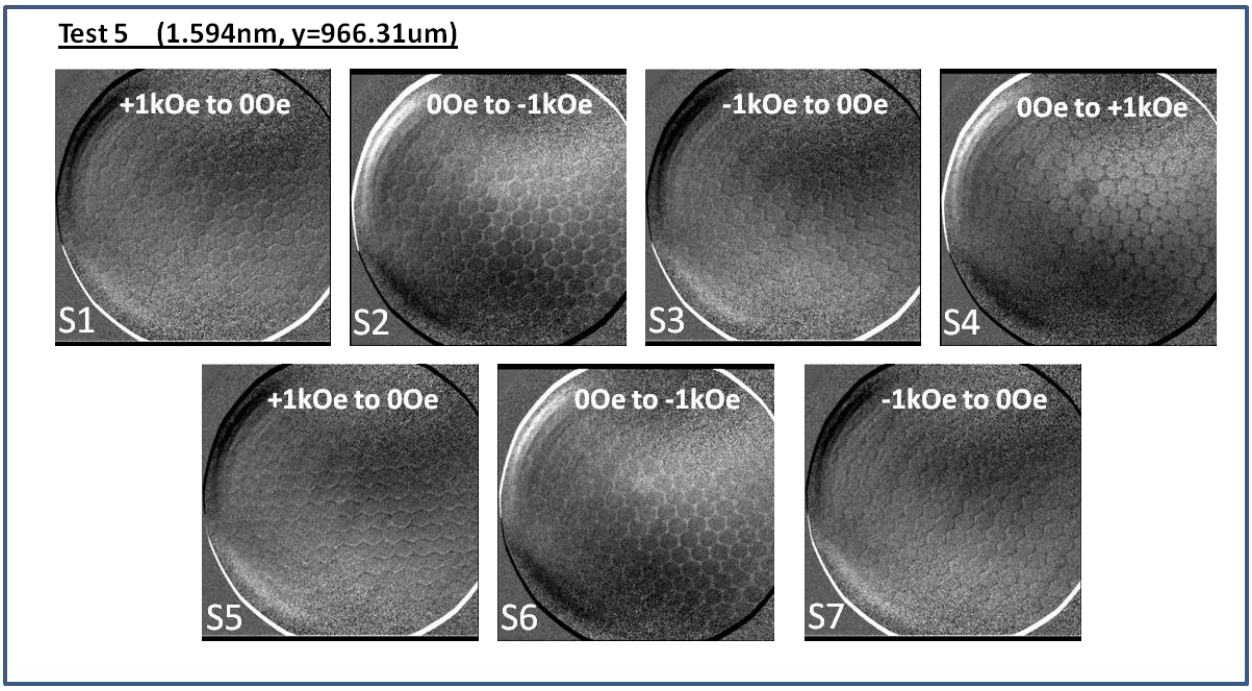

Figure 6.4.9 – An anti-dot vacancy is observed. The behaviour of the cobalt contrast observed in this figure is identical to figure 6.4.8. Above the saturation field contrast is seen in images S2, S4 and S6. The field in these images is horizontal as displayed in 6.4.2 and 6.4.3.

On samples 11 and 13, both the Test 5 and 6 scripts were used. Test 5 (±1KOe) showed no contrast on the iron edge. Similarly, Test 6 showed no contrast on the cobalt edge. The applied field in test 6 is not high enough (-30Oe) to initiate reversal in the cobalt, since no changes occur to the magnetisation there is no change and hence contrast observed in

consecutive images. Reversal in the permalloy occurs at low fields (< 20Oe), the difference between the zero field state and +1KOe and -1KOe is a uniform contrast image of dark or light illumination. The cobalt pattern has a distinct shape and is easy to distinguish from a uniform background, this is not the case of the permalloy layer.

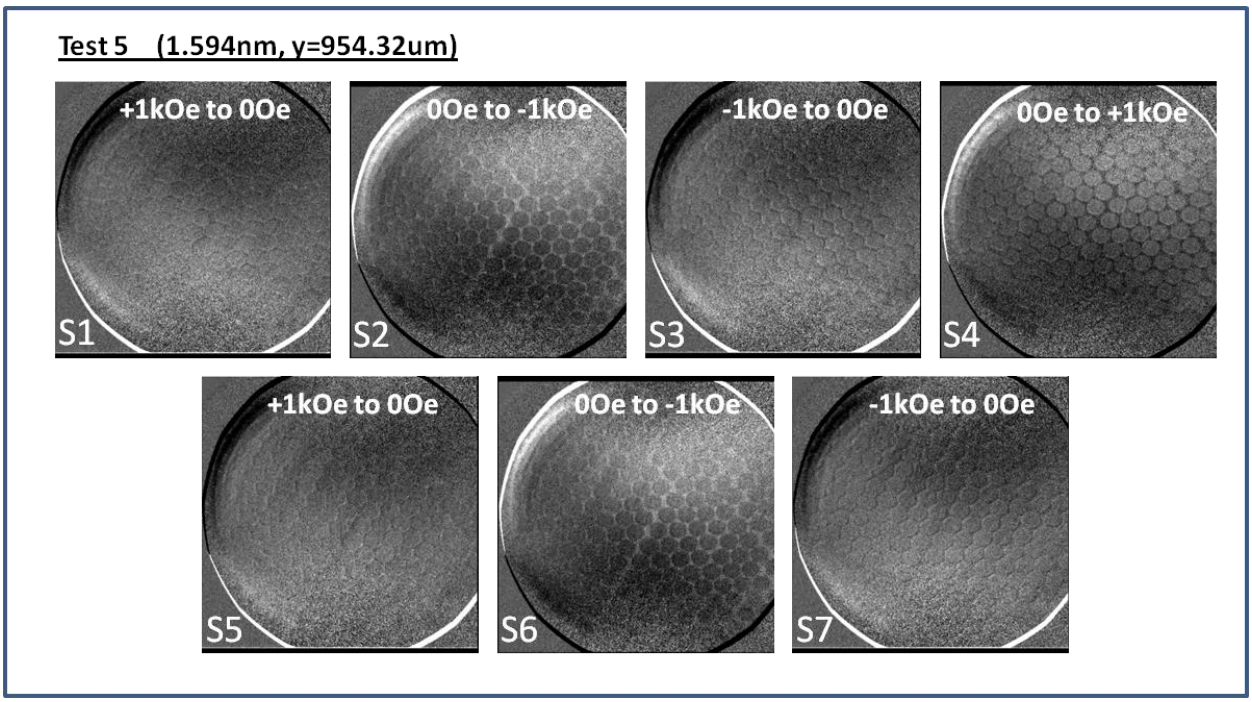

Figure 6.4.10 – Test 5 performed at a different position to figure 6.4.9, repeatable behaviour is observed above the saturation field. The field in these images is horizontal as displayed in figure 6.4.2 and 6.4.3.

Sample 9 (S2H4S3)

The iron edge data of samples 11 and 13 reveals sudden switching of the permalloy layer at low fields (15-20Oe). This is consistent with the hysteresis loops measured in Exeter, which shows the initial sudden switching to occur at this field range. The same batch file script (Test 6)

applied on the cobalt edge reveals no contrast; the cobalt does not begin reversal at a bias field of -30Oe. Measurements were performed on the cobalt edge of sample 9.

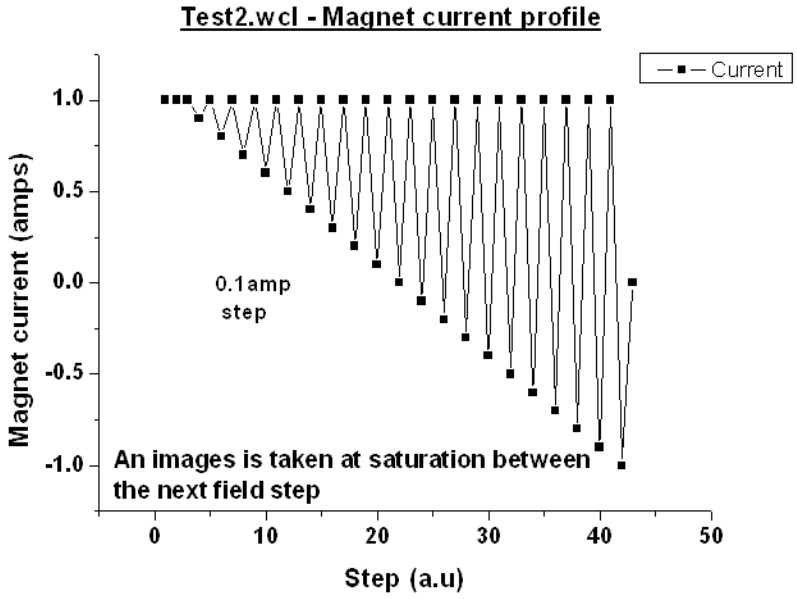

Figure 6.4.11 – The batch file scan for Test 2 used on sample 9. A reference images is taken at +1KOe between each stepped field value. The field is stepped in 0.1 Amp or 100Oe steps from +1KOe to -1KOe. An image is taken on each data point.

In the Test 2 batch file an image is taken every 100Oe, the cobalt reversal process is obtained and shown in figures 6.4.12 and 6.4.13. Reversal in the cobalt layer starts to occur at 200Oe in figure 6.4.12. Here the shape anisotropy of the cobalt is high and reversal would be expected to start at higher fields than a continuous film. This effect can be seen in figure 6.4.12 where contrast in a vacancy appears at -100Oe. The vacancy is of the order 1um (~700nm) and compared to the cobalt interstitial thickness of 100nm, the vacancy is almost a continuous film.

The shape anisotropy of the vacancy is less and switches at a lower field than the surrounding cobalt structure.

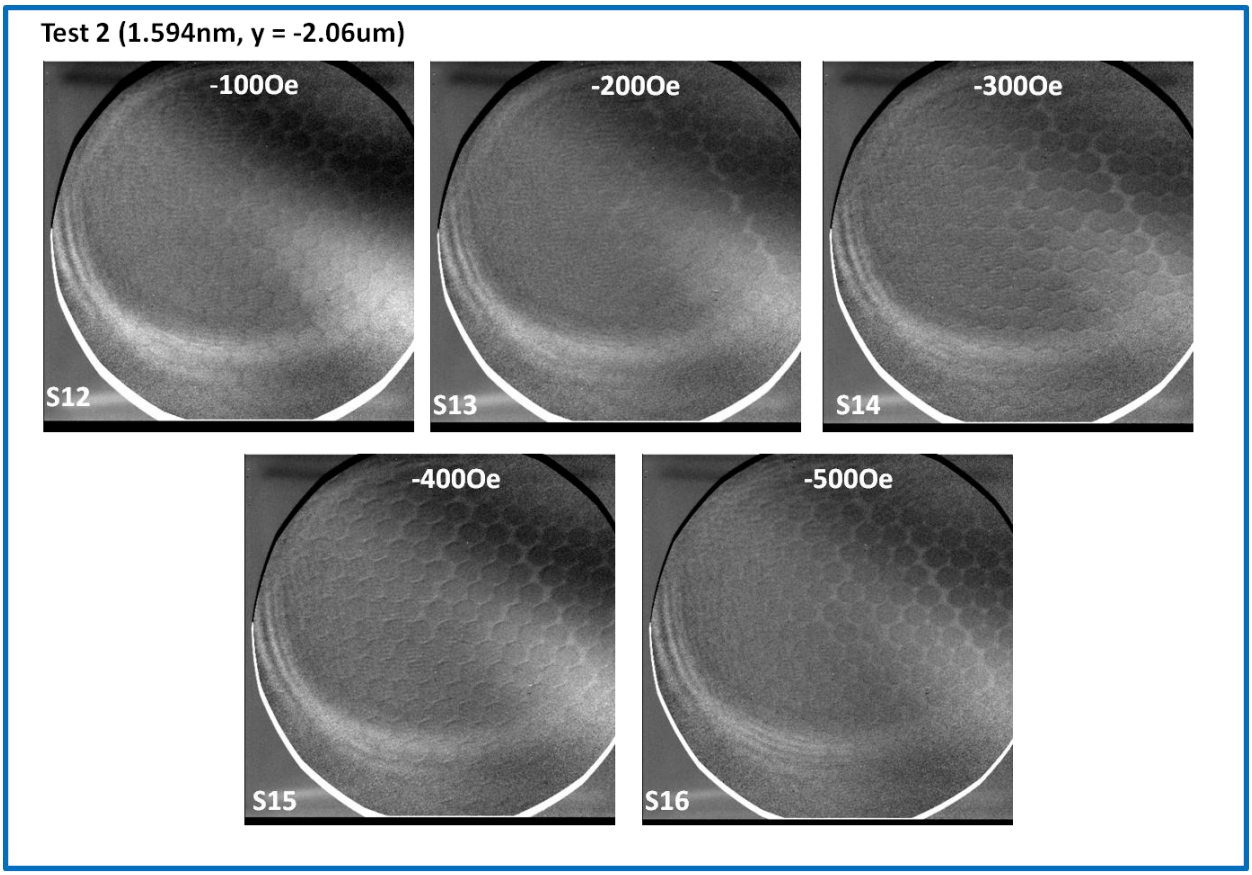

Figure 6.4.12 – Cobalt edge measurements on sample 9, showing initiation and completion of the reversal process for a sequence of decreasing values of the applied field. The reversal does not initiate until -200Oe and is fully completed by -500Oe.

In 6.4.12, a strip region of cobalt webbing can be seen where contrast in S13 first becomes apparent. As the applied field increases, regions close to this initial nucleation site undergo sudden jumps of reversed magnetization in S14. In images S15 and S16 of figure 6.4.12, the magnetization reversal process completes as regions of reversed magnetization branch out. This style of process is seen repeated again in figure 6.4.13. No contrast is initially visible in

figure 6.4.13 S11, in S12 only a vacancy is observed at -100Oe. At -200Oe the thickest / widest regions reverse after the initial vacancy, from here onwards through S13 to S16 magnetization completes reversal.

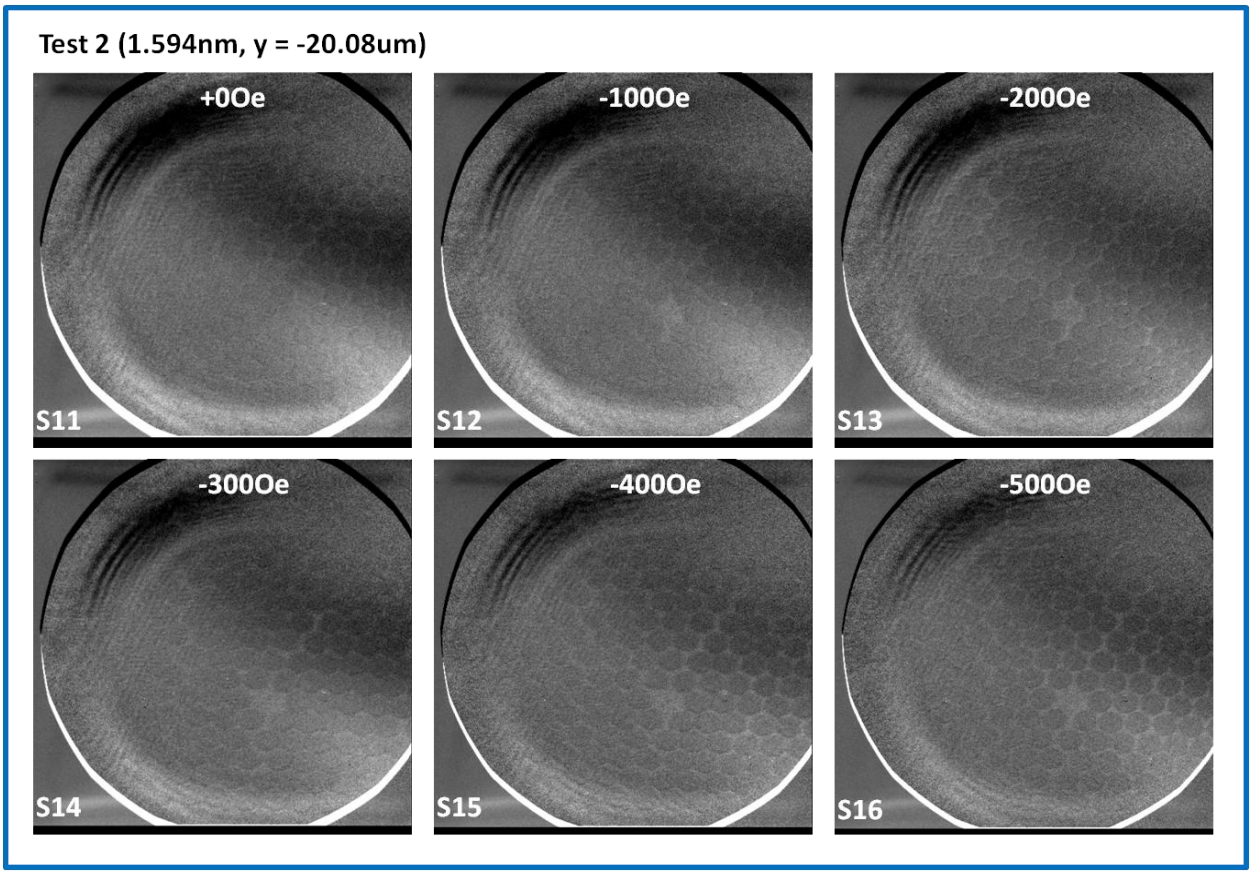

Figure 6.4.13 – The reversal process appears to nucleate around vacancies or discontinuities on the cobalt. In image S12 contrast is seen 10 Oe earlier than in figure 6.4.12 where contrast is first observed at 200Oe.

The contrast in image S16 of figure 6.4.13 is not expected to reveal a uniform contrast pattern due to differing widths of the cobalt and the microscope sensitivity. The orientation of adjacent magnetic moments is important in determining the XMCD contrast signal. Strong contrast is observed for larger angles between magnetic moments, moments orientated 90deg

from each other will show strong magnetic contrast, two moments 10 deg apart would show weak contrast.

In the anti-dot structure the local moments are unlikely to depart more than several 10's of degrees. Coupled with the inherent spatial resolution of the XM-1 at 20nm, fine features in the anti-dot structure will not be observed.

6.5 Discussion

The aim of this chapter is to use the images measured at the Advanced Light Source to explain the hysteresis loops of the samples. All three of the samples discussed here have similar loop shape and saturation fields, of the order 400Oe. Samples presented in this chapter, samples 11, 13 and 9 featured the silcon-nitride layer, no evidence was found on the iron edge of these samples indicating any interaction with the cobalt structures. The iron and cobalt components of the sample structure behave independently and switch independently at field values consistent with the field ranges observed in the hysteresis loops.

In most of the samples measured without the silicon-nitride layer no pattern in the iron was observed. The reason for this is an interesting question, although this data is not presented in this thesis, it was initially thought without the silicon-nitride layer the exchange interaction would directly 'impart' the cobalt magnetisation direction on the permalloy due to the interlayer exchange interaction. The permalloy ground state would then be studied in samples featuring the silicon-nitride layer. Comparison could be made of the magnetic ground states of samples with direct and in-direct coupling between the layers. One particular sample revealed on the iron edge what appears to be evidence for magnetic printing from the cobalt structures. This sample (sample 2) features 20nm of permalloy with 23 nm thick cobalt anti-dots without a silicon-nitride

layer. The layers should be exchange coupled and the observed contrast is very weak and barely visible. Either the experiment technique lacks the sensitivity to observe such a pattern or something such as an oxide layer has formed at the elemental interface preventing an effective exchange coupling between the layers. The explanation of the lack of cobalt induced iron contrast is not understood.

The data acquired from the Advanced Light Source presented in this chapter displays the switching of the Iron layers of samples 11 and 13 and the characteristic field values at which they happen. This behavior was universal to samples 11 and 13 and occurred independently of position. Using images from sample 9 showed the reversal process of cobalt to be slow and gradual. The Advanced Light Source images can be described with respect to several aspects of the measured hysteresis loops. There are two contributions to the hysteresis loop(s), the sharp switching seen at low field (<30Oe) from the permalloy, which gives about 50-60% of the initial loop height. The permalloy reversal starts and finishes reproducibly within a 5Oe window.

As the applied field increases the cobalt layer adds to the rotation signal as it gradually reverses its magnetization. The slower reversal of the cobalt is due to the intricate shape of its structure, the shape anisotropy fights any changes to the ground state magnetization by the build-up of magnetic charges creating strong demagnetizing fields within the structure. The applied field is always fighting the magnetisation in the shape of the structure, there is no characteristic point on the hysteresis loop where the cobalt starts to reverse. For a 100Oe field range after the reversal of the permalloy, the cobalt magnetisation is linear with field and steepens from 100 to 250Oe, here it is more expensive from an energy point of view to orientate the magnetisation. For field values greater than 250Oe the loop(s) have reached saturation. The iron edge images in figures 6.4.2 and 6.4.3 show reversal starting at the field range 12-13Oe, from 13-15Oe the

domain patterns suddenly and stochastically jump to new configurations over 1Oe steps. At fields of 16-17Oe the reversal process is complete. The iron edge data shows this behavior to be reproducible on both samples measured and to occur independent of position. The iron edge reversal process stops and starts at reproducible ranges of the field. The reversal process shown in the images is fast and sudden, which is entirely consistent with the measured hysteresis loops.

The cobalt data shown in figures 6.4.12 and 6.4.13 shows reversal advancing over a field range of several hundred Oersted. The images in figures 6.4.12 and 6.4.13 are separated by 100Oe each, reversal can initially be seen to start at 200Oe in figure 6.4.12 and then at 100Oe in figure 6.4.13. The images show domain nucleation starts at points featuring the lowest shape anisotropy, such as the thickest regions of the cobalt or vacancies in the anti-dot structure. Once nucleation has begun at these points, domains grow and suddenly jump outwards stochastically from the initial nucleation sites. This process continues as the applied field increases until saturation is complete.

The stochastic effects of reversal are not observable in the hysteresis loops due to the size of the optical spot. The endpoints of the reversal process are always identical; the exact path taken to get to the anti-parallel state is stochastic in nature and not reproducible. The optical spot in the loop measurements is millimetre sized; the measured response is the averaged Kerr response of millions of anti-dot periods. The stochastic effects of magnetisation reversal are 'averaged' out and become invisible on this length scale.

The XM-1 microscope at the Advanced Light Source has been used to study previous sub-micron size structures. Time and space-resolved magnetic transmission x-ray microscopy was used to study vortex core gyrations in a pair of dipolar coupled 50 nm thick permalloy disks

[122] utilising a stroboscopic pump-probe technique. The quoted spatial and temporal resolution was 20nm and 70ps respectively. The disks each had a radius of 2.4 μm and an edge-to-edge separation of 120nm. By acquiring images at given time delays following pulsed excitation the dynamics of the vortex core can be imaged. The vortex cores could be resolved in the acquired images, with a size estimated to be sub-100nm. The x-rays strike the disks normal to their surface so that the x-ray wave vector is parallel to the vortex core magnetisation. This geometry provides maximum contrast signal despite being sub-100nm in size. The core is several pixels across in the measured images. The size of their vortex core is comparable to the width of the cobalt anti-dot region in the samples presented in section 6.4. Despite being of similar size to our sample's features the direction of magnetisation of the vortex core relative to the x-rays strongly favours an increased contrast signal compared to the geometry used in our study.

Films of TbFeCo have been imaged in the XM-1 microscope where the (maze) domain pattern is visible with 100nm wide domains [107]. The magnetisation of the TbFeCo film was out-of-plane. High resolution images have been obtained on films of CoCrPt with perpendicular magnetisation [123], the domain pattern was clearly observed with strong contrast and domains widths smaller than 100nm. Studies on the XM-1 microscope which resolved sub-100nm features have been achieved using samples with perpendicular magnetisation. This provides the maximum magnetic contrast signal.

Samples have also been measured which possess in plane magnetisation. Investigating current driven domain wall dynamics, a figure-eight shaped permalloy element was measured using time-resolved x-ray microscopy [124]. The element is 4μm long and 2μm wide. At the domain wall edges in the centre of the figure-eight, magnetisation is anti-parallel; each half of the figure-eight has strong opposite contrast. The in-plane magnetisation of the figure-eight

sample requires it to be mounted identically to our samples (samples 9, 11 and 13). The size of the figure-eight sample is microns with magnetisation at large relative angles (180 degrees) to generate a large contrast signal. The cobalt anti-dot structures are much smaller in size at around 100nm and the departure of magnetisation between local moments is small, not more than 20 degrees maximum. From comparison with contemporary literature, the samples that we measured at the Advanced Light Source did not offer large enough angles of magnetisation to fulfil the original experimental aim. Structures on the sub-100nm length scale can be observed by using out-of-plane magnetisation which maximises the magnetic contrast signal.

6.*6 Summary*

In this chapter measurements from the Advanced Light Source have been presented. The original experimental aim of the measurements was to investigate the permalloy ground state in the presence of dipolar fields from the cobalt anti-dots. The original aims were never achieved experimentally. This chapter has presented the acquired images to compliment the already measured hysteresis loops. The x-ray images represent a spatial hysteresis loop of the sample at a particular absorption edge. The data shown in the images is consistent with the hysteresis loops measured in Exeter and agreement is found on both absorption edges independent of position.

The images have given a spatial insight to the reversal mechanism on both the iron and cobalt components of the sample. From the inherent element specificity and the high spatial resolution, magnetic transmission x-ray micrsocopy is a unique and powerful tool to study nanoscale magnetism. The current spatial resolution is the order of 20 nm, which lies just outside the exchange length (~10nm) which is fundamental length scale of magnetism. The timing structure of the synchrotron limits the temporal resolution to about 70ps. This is orders of

magnitude slower than the fundamental time scale in magnetism, which is the time scale over which the exchange interaction acts, typically on the order of femtosceonds. Currently, contemporary magnetism does not understand magnetic phenomena on such small length and time scales. The spatial resolution is closing in faster than temporal resolution; the best theoretical resolution of the XM-1 is quoted at 15nm [124], while the temporal resolution is several orders of magnitude too large. This development requires improvements to the entire synchrotron timing structure of the electron bunches, while the spatial resolution is limited by the zone plate fabrication by nanolithography.

Chapter 7 - Conclusion

In this thesis, data is presented from a variety of experimental techniques. The general background theory of magnetism is given in chapter 2, with the sections on spin waves in periodic magnetic structures being particularly relevant to the thesis. In chapter 3, the experimental background of both the time-resolved scanning Kerr microscope ("field-pumped microscope" or TRSKM) and the time-resolved optically pumped scanning optical microscope ("optically-pumped microscope" or TROPSOM) is discussed. The experimental development of the optically pumped microscope is also briefly mentioned. Chapter 4 reports results of time-resolved imaging on bi-component ("binary") 2D magnonic crystals using time-resolved scanning Kerr microscopy. The measurements were intended to elucidate the character (either stationary or propagating) and the effective damping of the magnonic modes of the patterned structures. In chapter 5, time-resolved signals and images acquired from a 20nm continuous permalloy film were presented. The measurements serve as an initiation of the newly constructed time-resolved optically pumped scanning optical microscope. Early images and time-resolved signals were presented and compared with images measured later on. In chapter 6, magnetic transmission x-ray microscopy measurements were performed on composite samples of cobalt nanostructures overlaid on continuous permalloy films at the Advanced Light Source in Berkley, California, USA. The measurements revealed the magnetic ground state of the nanostructures and provided reversal fields consistent with hysteresis loops measured in Exeter.

In chapter 4, bi-component 400 nm anti-dot lattices with both air and cobalt filling were studied at a bias field of 200 Oe with the applied field directed along a square edge of the anti-dot lattice. The anti-dot lattice spacing was 1μm. The mode characters (either propagating or

non-propagating) was determined for both patterned structures. The air-filled anti-dot sample revealed two modes at 4.72 and 3.8 GHz. The 4.72 GHz mode exhibited non-propagating character. The 3.8 GHz mode has a propagating character. In the cobalt filled anti-dot sample (the "binary sample"), this trend is reversed, and the higher frequency (4.4 GHz) mode exhibits propagating character, while the lower (3.04 GHz) mode has non-propagating character. The modification of the internal field by the anti-dot filling induces an upshift of the frequency of the propagating mode in the cobalt sample. The spatial distribtution of the modes was observed and the spatial profiles were fitted to extract the wavelength, decay constant and effective damping parameter for the patterned structures. The effective damping of the patterned region is heavily dependent on the material through which the spin waves propagate. The values of damping are fairly similar throughout (0.023~0.028), the mode which propagates through the cobalt dots experiences the highest value of damping.

In chapter 5, time resolved signals and scanned images were acquired from a 20 nm thick continuous permalloy film mounted on a 300 μm thick sapphire substrate under a 500 Oe nearly out-of-plane magnetic field. Initial time resolved signals revealed a 17 GHz mode and images revealed crescent shaped ripples with 1 μm wavelength. Further measurements revealed propagating spin waves with a frequency of 4 GHz and wavelength 2.5μm. The observed propagating spin wave frequency and wavelength are not therefore consistent with the previous measurements, which were subject to mechanical drift of the pump focus position. The origin of the oscillations in the time-resolved signals is not fully understood and could originate from either spin waves or phonons. Further measurements revealed that the observed magnetic images were sensitive to the 'quality' of the pump focus. In particular, drastic changes were observed

for changes of several microns in the distance between the pump focusing objective and the surface of the sample.

In chapter 6, magnetic transmission x-ray microscopy was used to study the magnetic ground states of nanostructures consisting of cobalt anti-dots 700 nm in diameter and a continuous permalloy film of various thicknesses ranging from 20 to 60 nm. The data was acquired at the Advanced Light Source at the Lawrence Berkeley National Laboratory in Berkeley, California. The sample was illuminated with circularly polarized x-rays at an element specific L_3 absorption edge, i.e. 707 and 778 eV for iron and cobalt respectively. The contrast was generated due to magnetic x-ray circular dichroism. The acquired images were used in conjunction with hysteresis loops measured in Exeter to extract the switching fields for each sample. The reversal in the soft permalloy layers occurred suddenly over a narrow field window between 13 – 17 Oe for all samples measured. The reversal in the cobalt was slow and gradual, since the complex shape of the nanostructures meant the applied field had to compete with the demagnetizing field. The full saturation was observed in the field range of 250-350 Oe on the cobalt edge. The initial experimental aim was to observe the permalloy ground state in the presence of the dipolar fields from the cobalt structures. The samples have a 7 nm silicon nitride layer between the cobalt and permalloy to decouple the exchange interaction between the layers. The previous studies on the microscope used samples with large angles of magnetisation between adjacent micron sized domains. In our samples, cobalt sections were sub-100 nm in size and the local angle of magnetisation was small. This could explain why only limited magnetic contrast was observed on the permalloy film from the cobalt layers, even in samples where the silicon nitride layer was absent. The contrast most probably exists but is beyond the current sensitivity of the X-ray microscope.

Bibliography

[1] E. Segre, *From Falling Bodies to Radiowaves – Classical Physicists and their Discoveries* (Freeman, New York, 1984)

[2] Stohr and Siegmann, *Magnetism: From Fundamentals to Nanoscale Dynamics*,Pages 1-15 (Springer-Verlag Berlin Heidelberg, 2006)

[3] E. Segre, *From X-rays to Quarks – Modern Physicists and their Discoveries* (W.H Freeman and Company, San Francisco, 1980)

[4] G.L. Verschurr, *Hidden Attraction, The Mystery and History of Magnetism* (Oxford University Press, Oxford, 1993)

[5] J.D. Livingstone, *Driving Force, The NaturalMagic of Magnets* (Harvard University Press, Cambridge, Massachusetts, 1996)

[6] P.A.M Dirac, Proc.R. Soc. A **117**, 610 (1928)

[7] W. Heisenberg, Z. Phys. **49**, 619 (1928)

[8] L. Neel, Ann. De Phys. **18**, 5 (1932)

[9] N.F. Mott, Proc. Phys. Soc. (London) **47**, 571 (1935)

[10] J.C. Slater, Phys. Rev. **49**, 537 (1936)

[11] J.C. Slater, Phys. Rev. **49**, 931 (1936)

[12] E.C. Stoner, Proc. Phys. Soc. (London) A **154**, 656 (1936)

[13] B. Lenk, H. Ulrichs, F. Garbs, M. Münzenberg, Physics Reports, **507**, 4 (2011)

[14] V. V. Kruglyak, S. O. Demokritov, and D. Grundler, J. Phys. D: Appl. Phys. 43, 264001 (2010).

[15]. A.H.Morrish, The Physical Principles of Magnetism, John Wiley & Sons (1965)

[16]. The Feynman Lectures on Physics, Addison-Wesley (1964)

[17]. A.I.M Rae, Quantum Mechanics , McGraw-Hill (1985)

[18]. R. L.Liboff, Introductory Quantum Mechanics, Addison Wesley, (1991)

[19]. Google Images, http://chem4823.usask.ca/nmr/larmor.gif

[20] M.L Plumer, J.van Ek, D.Weller, The Physics of Ultra High-Density Magnetic Recording, Springer-Verlag Berlin Heidelberg, (2001)

[21] B.Hillebrands, K.Ounadjela, Spin Dynamics in Confined Magnetic Structures, Springer-Verlag Berlin Heidelberg New York, (2001)

[22] Stohr and Siegmann, *Magnetism: From Fundamentals to Nanoscale Dynamics* ,p.480-490, Springer-Verlag Berlin Heidelberg, (2006)

[23] Stohr and Siegmann, *Magnetism: From Fundamentals to Nanoscale Dynamics*, p.170-180, Springer-Verlag Berlin Heidelberg, (2006)

[24] G.E. Uhlenbeck, S. Goudsmit, Nature **117**, 264, (1926)

[25] W. Heisenberg, P. Jordan, Z. Phys. **37,** 263 (1926)

[26] P. Strange, *Relativistic Quantum Mechanics - with Applications in Condensed matter and Atomic Physics* Cambridge University Press, (1998)

[27] Stohr and Siegmann, *Magnetism: From Fundamentals to Nanoscale Dynamics*, p.203-209, Springer-Verlag Berlin Heidelberg, (2006)

[28] E. Beaurepaire, H. Bulou, F. Scheurer, J. Kappler, *Magnetism: A Synchrotron Radiation Approach*, Springer, Berlin Heidelberg (2006)

[29] M. Faraday: Phil. Trans. R. Soc. **136**, 1 (1846)

[30] J. Kerr: Philos. Mag. **3**, 321 (1877)

[31] H. R. Hulme: Proc. R. Soc. (London) Ser. A **135**, 237 (1932)

[32] P. N. Argyres: Phys. Rev **97**, 334 (1955)

[33] B. R. Cooper: Phys. Rev. **139**, A1504 (1965)

[34] R. Kubo: J. Phys. Soc. Japan **12**, 570 (1957)

[35] C. S. Wang and J. Callaway: Phys. Rev. B **9**, 4897 (1974)

[36] M. Singh, C. S. Wang and J. Callaway: Phys. Rev. B **11**, 287 (1975)

[37] W. H. Kleiner: Phys. Rev. **142**, 318 (1966)

[38]N. Bloembergen: *Nonlinear Optics* (Benjamin, New York, 1965)

[39] A. Cracknell: J. Phys. C **2**, 1425 (1969)

[40] B. Lenk, H. Ulrichsa, F. Garbs, M. Munzenberg, Physics Reports 507 (2011)

[41] M. Krawczyk and H. Puszkarski, Phys. Rev. B 77, 054437 (2008)

[42] D. D. Stancil and A. Prabhakar, *Spin Waves. Theory and Applications* (Springer, 2009).

[43] S. Neusser, H. G. Bauer, G. Duerr, R. Huber, S. Mamica, M.L. Sokolovskyy, G. Woltersdorf, M. Krawczyk, C. H. Back, and D. Grundler, Phys. Rev. B **84**, 184411 (2011).

[44] Stohr and Siegmann, *Magnetism: From Fundamentals to Nanoscale Dynamics*, p.679-690, Springer-Verlag Berlin Heidelberg, (2006)

[45] B.Hillebrands, K.Ounadjela, Spin Dynamics in Confined Magnetic Structures, Springer-Verlag Berlin Heidelberg New York, (2001)

[46] , A.V. Kimel, A. Kirilyuk, and T. Rasing, Laser & Photon. Rev, **3**, (2007)

[47] B. Koopmans, J. J. M. Ruigrok, F. Dalla Longa and W. J. M. de Jonge, Phys. Rev. Lett **95** (2005)

[48] N. Kazantseva, U. Nowak, R. W. Chantrell, J. Hohlfeld and A. Rebei, European Physical Letters **81** 27004 (2007)

[49] E.Beaurepaire, J.-C.Merle, A.Daunois and J.-Y.Bigot Phys.Rev.Lett **76** (1996)

[50] D. Attwood, Chapter, Soft X-rays and Extreme ultraviolet Radiation: Principles and Applications, Cambridge University Press, (1999)

[51] M. C. Martin, W. R. McKinney, Applications of Synchrotron Radiation Techniques to Materials Science IV, Materials Research Society, (1998)

[52] E. Beaurepaire, H. Bulou, F. Scheurer, J. Kappler, *Magnetism: A Synchrotron Radiation Approach*, Springer-Berlin Heidelberg (2006)

[53] J. L. Erskine and E. A. Stern: Phys.Rev. B **12**, 5016 (1975)

[54] B. T. Thole, G. Van der Laan and G. A. Sawatzky: Phys. Rev. Lett. **55**, 2086 (1985)

[55] G. Van der Laan, B. T. Thole, G. A. Sawatzky, et.al:Phys. Rev. B **34**, 6529 (1986)

[56] G. Schutz, W. Wagner, W. Wilhelm, et al: Phys. Rev. Lett. **58,** 737 (1987)

[57] H. Ebert, P. Strange and B. L. Gyorffy: J. Appl. Phys. **63**, 3055 (1988)

[58] C. T. Chen, F. Sette, Y. MA et al: Phys. Rev. B **42**, 7262 (1990)

[59] G. Van der Laan and B. T. Thole: Phys. Rev. B **43**, 13401 (1991)

[60] Stohr and Siegmann, *Magnetism: From Fundamentals to Nanoscale Dynamics,* p.389-400, 437, Springer-Verlag Berlin Heidelberg (2006)

[61] http://ssrl.slac.stanford.edu/stohr/xmcd.htm

[62] http://xraysweb.lbl.gov/peem2/webpage/Project/TutorialContrast.shtml

[63] Y. Au, T. Davison, E. Ahmad, P. S. Keatley, R. J. Hicken and V. V. Kruglyak, Appl. Phys. Lett. 98, 122506 (2011).

[64] Spectra Physics, Millennia Pro s-series User's manual

[65] Spectra Physics, Tsunami User's manual

[66] http://en.wikipedia.org/wiki/File:Stimulated_Emission.svg

[67] http://bme240.eng.uci.edu/students/10s/mwinkle1/basics.html

[68] http://inst.eecs.berkeley.edu/~ee236a/fa02/TsunamBroch0180.pdf

[69] http://www.olympusmicro.com/primer/techniques/microscopylasers.html

[70] C. Sykes, J. Adam and J. Collins, Appl. Phys. Lett. **29,** 388 (1976)

[71] M . Krawczyk and H. Puszkarski, Phys. Rev. B **77**, 054437 (2008)

[72] S. A. Nikitov, Ph. Tailhades, C.S. Tsai. J. Magn. Magn. Mater. 223 (2001).

[73] J. O. Vasseur, L. Dobrzynski and B. Djafari-Rouhani, Phys. Rev. B **54**, 2 (1996)

[74] B. Lenk, H. Ulrichsa, F. Garbs, M. Munzenberg, Physics Reports 507 (2011)

[75] S. Neusser, G. Duerr, S. Tacchi, M. Madami, M. L. Sokolovskyy, G. Gubbiotti, M. Krawczyk, and D. Grundler, Phys. Rev. B **84**, 094454 (2011)

[76] S. Tacchi, F. Montoncello, M. Madami, G. Gubbiotti, G. Carlotti, L. Giovannini, R. Zivieri, F. Nizzoli, S. Jain, A. O. Adeyeye, and N. Singh, PRL 107, 127204 (2011)

[77] R. Zivieri, F. Montoncello, L. Giovannini, F. Nizzoli, S. Tacchi, M. Madami, G. Gubbiotti, G. Carlotti, and A. O. Adeyeye, Phys. Rev. B **83**, 054431 (2011)

[78] S. Neusser, B. Botters, M. Becherer, D. Schmitt-Landsiedel, and D. Grundler, Appl. Phys. Lett. 93, 122501 (2008);

[79] A. Y. Toporov, R. M. Langford, and A. K. Petford-Long, Appl. Phys. Lett. **77**, 3063 (2000)

[80] C. C. Wang, A. O. Adeyeye, and N. Singh, Nanotechnology **17**, 1629 (2006)

[81] R. Hertel, W. Wulfhekel, and J. Kirschner, Phys. Rev. Lett. **93**, 257202 (2004)

[82] T. Schneider, A. A. Serga, B. Leven, B. Hillebrands, R. L. Stamps, and M. P. Kostylev, Appl. Phys. Lett. **92**, 022505 (2008).

[83] V. E. Demidov, S. O. Demokritov, K. Rott, P. Krzysteczko, and G. Reiss, Appl. Phys. Lett. **92**, 232503 (2008)

[84] 14J. Topp, J. Podbielski, D. Heitmann, and D. Grundler, Phys. Rev. B **78**, 024431 (2008)

[85] G. Duerr, M. Madami, S. Neusser, S. Tacchi, G. Gubbiotti, G. Carlotti and D. Grundler, Appl. Phys. Lett. **99**, 202502 (2011)

[86] V. V. Kruglyak and A. N. Kuchko, *The Physics of Metals and Metallography*, Vol **92**, No. 3 (2001)

[87] V. V. Kruglyak and A. N. Kuchko, J. Magn. Magn. Mater, 272 (2004) 302

[88] A. Barman, V. V. Kruglyak, R. J. Hicken, and J. M. Rowe, Phys. Rev. B **69**, 174426 (2004)

[89] A. Barman, V. V. Kruglyak, R. J. Hicken, A. Kundrotaite, and M. Rahman, Appl. Phys. Lett. **82**, 18 (2003)

[90] E. Beaurepaire, J. C. Merle, A. Daunois, and J. Y. Bigot, Phys. Rev. Lett. **76,** 4250 (1996)

[91] M. Djordjevic, G. Eilers, A. Parge, and M. Munzenberg. J. Appl. Phys, **99,** 08F308 (2006)

[92] B. Koopmans, M. Van Kampen, and W. J. M de Jonge. J. Phys. Condens. Matter **15** (2003)

[93] B. Koopmans, M. Van Kampen, J. T. Kohlhepp and W. J. M de Jonge. Phys. Rev. Lett **85** 0844 (2000)

[94] U. Ataxia, O. Chubykalo-Fesenko, J. Walowski, A. Mann, and M. Munzenberg. Phys. Rev. B **81**, 174401 (2010)

[95] M. van Kampen, C. Jozsa, J. T. Kohlhepp, P. LeClair, L. Lagae, W. J. M. de Jonge, and B. Koopmans. Phys. Rev. Lett **88,** 227201 (2002)

[96] G. Ju A, V. Nurmikko, R. F. C. Farrow, R. F. Marks, M. J. Carey, and B. A. Gurney. Phys. Rev. Lett **82,** 3705 (1999)

[97] C. D. Stanciu, F. Hansteen, A. V. Kimel, A. Kirilyuk, A. Tsukamoto, A. Itoh, and Th. Rasing, Phys. Rev. Lett. **99,** 047601 (2007)

[98] C. D. Stanciu, F. Hansteen, A. V. Kimel, A. Tsukamoto, A. Itoh, A. Kirilyuk, and Th. Rasing, Phys. Rev. Lett. **98,** 207401 (2007)

[99] A. R. Khorsand, M. Savoini, A. Kirilyuk, A.V. Kimel, A. Tsukamoto, A. Itoh, and Th. Rasing, Phys. Rev. Lett **108**, 127205 (2012).

[100] A. V. Kimel, A. Kirilyuk, P. A. Usachev, R. V. Pisarev, A. M. Balbashov, and Th. Rasing. *Nature* **435**, 655 (2005)

[101] F. Hansteen, A. Kimel, A. Kirilyuk, and Th. Rasing. Phys. Rev. Lett. **95,** 047402 (2005)

[102] A. M. Kalashnikova, A. V. Kimel, R. V. Pisarev, V. N. Gridnev, A. Kirilyuk, and Th. Rasing, Phys. Rev. Lett. **99**, 167205 (2007)

[103] A. H. M. Reid, A. V. Kimel, A. Kirilyuk, J. F. Gregg, and Th. Rasing. Phys. Rev. Lett **105,** 107402 (2010)

[104] Benjamin Lenk, Gerrit Eilers, Jaroslav Hamrle, and Markus Münzenberg, Phys. Rev. B **82**, 134443 (2010)

[105] Y. Liu, L. R. Shelford, V. V. Kruglyak, R. J. Hicken, Y. Sakuraba, M. Oogane, Y. Ando, and T. Miyazaki. J. Appl. Phys. **101**, 09C106 (2007)

[106] T. Ogasawara, N. Iwata, Y. Murakami, H. Okamoto, and Y. Tokura, Appl. Phys. Lett **94**, 162507 (2009)

[107] P. Fischer, T. Eimüller, G. Schütz, G. Denbeaux, A. Pearson, L. Johnson, D. Attwood, S. Tsunashima, M. Kumazawa, N. Takagi, M. Köhler, and G. Bayreuther, Rev. Sci. Instrum. **72**, 2322 (2001)

[108] Weilun Chao, Jihoon Kim, Senajith Rekawa, Peter Fischer, and Erik H. Anderson, Optics Express, **17**, 20 17669 (2009)

[109] J. Militat, A. Thiaville, *Science* **290,** 466 (2000).

[110] M.R. Freman, B. C. Choi, *Science* **294**, 1484 (2001)

[111] S. B. Choe, Y. Acreman, A. Scholl, A. Bauer, A. Doran, J. Stohr and H. A. Padmore, *Science* **304** 420 (2004)

[112] Y. Acreman et. Al, *Science* **290** 490 (2000)

[113] W. K. Hiebert, G. E. Ballentine, L. Lagae, R. W. Hunt, M. R. Freeman, J. Appl. Phys **92(1)** 392 (2002)

[114] J. Stohr and H. C. Siegmann, *Magnetism,* Springer (2006)

[115] M. Bode, *Rep. Prog. Phys*, **66** 523 (2003)

[116] http://www.cxro.lbl.gov/BL612/

[117] D. Attwood, Soft X-rays and Extreme ultraviolet Radiation: Principles and Applications, Cambridge University Press (1999)

[118] P. Fischer, IEEE Transactions on Magnetics, **44**, 7 (2008)

[119] C.T. Chen, F. Sette, Y. Ma and S. Modesti, Phys. Rev. B **42** 7262 (1990)

[120] X-Ray Data Booklet, Centre for X-Ray optics and Advanced Light Source, October 2009

[121] P Fischer, D Kim, Brooke L Mesler, W Chao, Anne E Sakdinawat, Erik H Anderson, **601**, 20, p4680, Surface Science (2007)

[122] H. Jung, Y.Sang. Yu, K.Suk Lee, M.Young Im, P. Fischer, L. Bocklage, A. Vogel, M. Bolte, G. Meier and S. K. Kim, Appl. Phys. Lett **97** , 222502 (2010)

[123] P. Fischer, AAPPS Bulletin, **18,** 6 (2008)

[124] P. Fischer, Materials Today, **13**, 9, (2010)